INFORMATION TO USERS

While the most advanced technology has been used to photograph and reproduce this manuscript, the quality of the reproduction is heavily dependent upon the quality of the material submitted. For example:

- Manuscript pages may have indistinct print. In such cases, the best available copy has been filmed.
- Manuscripts may not always be complete. In such cases, a note will indicate that it is not possible to obtain missing pages.
- Copyrighted material may have been removed from the manuscript. In such cases, a note will indicate the deletion.

Oversize materials (e.g., maps, drawings, and charts) are photographed by sectioning the original, beginning at the upper left-hand corner and continuing from left to right in equal sections with small overlaps. Each oversize page is also filmed as one exposure and is available, for an additional charge, as a standard 35mm slide or as a 17"x 23" black and white photographic print.

Most photographs reproduce acceptably on positive microfilm or microfiche but lack the clarity on xerographic copies made from the microfilm. For an additional charge, 35mm slides of 6"x 9" black and white photographic prints are available for any photographs or illustrations that cannot be reproduced satisfactorily by xerography.

Chen, Dong Min

A 2D-ACAR STUDY OF POSITRON INTERACTIONS WITH SURFACES OF ALUMINUM AND SILICON

City University of New York PH.D. 1987

PLEASE NOTE:

In all cases this material has been filmed in the best possible way from the available copy. Problems encountered with this document have been identified here with a check mark ✓.

1. Glossy photographs or pages _____
2. Colored illustrations, paper or print _____
3. Photographs with dark background ✓
4. Illustrations are poor copy _____
5. Pages with black marks, not original copy _____
6. Print shows through as there is text on both sides of page _____
7. Indistinct, broken or small print on several pages ✓
8. Print exceeds margin requirements _____
9. Tightly bound copy with print lost in spine _____
10. Computer printout pages with indistinct print _____
11. Page(s) _____ lacking when material received, and not available from school or author.
12. Page(s) _____ seem to be missing in numbering only as text follows.
13. Two pages numbered _____. Text follows.
14. Curling and wrinkled pages _____
15. Dissertation contains pages with print at a slant, filmed as received ✓
16. Other _____

_____

_____

A 2D-ACAR STUDY OF POSITRON INTERACTIONS WITH SURFACES OF ALUMINUM AND SILICON

by

DONG MIN CHEN

A dissertation submitted to the Graduate Faculty in Physics in partial fulfillment of the requirements for the degree of Doctor of Philosophy, The City University of New York.

1987

This manuscript has been read and accepted for the Graduate Faculty in Physics in satisfaction of the dissertation requirement for the degree of Doctor of Philosophy.

Feb. 10, 1987
Date

Leonard O. Roellig
Chair of Examining Committee

Feb. 11, 1987
Date

Joel I. Gersten
Executive Officer

Stephan Berko

Joseph L. Birman

Marten L. den Boer

Herman Z. Cummins

Kelvin G. Lynn

Supervisory Committee

The City University of New York

Abstract

A 2D-ACAR STUDY OF POSITRON INTERACTIONS WITH SURFACES OF ALUMINUM AND SILICON

by

Dong Min Chen

Advisor: Professor L. O. Roellig

Using a high intensity slow positron beam and an UHV surface chamber constructed at Brookhaven National Laboratory, we have applied the well established technique of 2-Dimensional Angular Correlation of Annihilation Radiation to study the interactions of positrons with three low index surfaces of aluminum, Si(111)-(7×7), and Si(100)-(2×1) surfaces. Effects of the adsorption of oxygen on Al surfaces and hydrogen on a Si(111)-(7×7) surface have also been explored. Our measurements confirmed three important processes: spontaneous positronium(Ps) formation and emission, positrons bound in a surface state, and thermally desorbed as Ps atoms. A method has been developed to accurately separate these components. The Ps momentum distributions exhibit some unique structures that are sensitive to the surface conditions, and are found to reflect the electron density of states near the surfaces thus suggesting a new surface spectroscopy: angle-resolved Ps spectroscopy. The positron surface state spectrum has an essentially isotropic distribution with respect to the components perpendicular and parallel to the surface, indicating lateral localization of the surface state positron. This is inconsistent with either the image potential induced positron surface state model, or the physisorbed Ps surface state model for ideal surfaces. The extracted thermal Ps momentum distributions are in good agreement with the theoretical description of a thermodynamical emission process. This thesis provides the first systematic discussion of these extended techniques, and the important results obtained to date.

Acknowledgement

I wish to express my sincere appreciation to Professor S. Berko, Dr. K. G. Lynn, Professor L. O. Roellig, and Professor R. N. West for their profound guidance, support, careful reading of the manuscript and helpful comments, and for their personal interest for my general welfare. I am especially grateful to Dr. A. P. Mills, Jr. and Dr. K. F. Canter for there incisive suggestions; and to Dr. M. Weinert for providing me the Al band structure program. This work would not have been possible without the high intensity slow positron beam constructed at the High Flux Beam Reactor of Brookhaven National Laboratory. I am indebted to my colleague M. Weber for his major contribution in building the beam. Special thanks are extended to J. Ruthford, J. Zahradka, P. Schnitzenbaumer and S. Z. Tang for their great effort to keep the beam operating; and to the HFBR operators, especially to T. Homquist, for their collaboration in the routine preparation of ^{64}Cu isotope. Dr. P. Sferlazzo and Dr. A. Viescas are also thanked for valuable discussions and assistance. I am grateful to J. Hurst for cutting the samples and taking the x-ray pictures; to Dr. A. Moodenbaugh for his assistance in setting up the data acquisition and transformation system; and to both of them for the fabrication of ^{63}Cu pellets and irradiation capsules. Mrs. M. Mckeown is thanked for her work on the early version of the data analysis programs. Much of the data analysis has been carried out in the ACAR Lab. of Brandeis Univ., the help from Dr. R. Lee in many occasions is gratefully acknowledged. It is my pleasure to thank all the members in the BNL Low-Energy-Particle group for their numerous help, friendship, and above all, for their good senses of humor, which made my life there cheerful. As a CUSPEA student, I would like to express my gratitude to Dr. T. D. Lee, the founder of the CUSPEA program. Thanks are also due to J. C. Zhang, F. Q. Nan, and Z. Wei, whose encouragement during my college years had helped me succeeded in the first phase of the CUSPEA program. Finally, I wish to thank Ms. Bei Ru Jia for her patience and careful help in the final preparation of this thesis. This work was supported in part by the National Science Foundation (Grant No. DMR-8315691) and the U.S. Dept. of Energy Division of Material Sciences(Contract No. DE-AC02-76CH00016).

Table of Contents

List of Tables

List of Figures

Chapter 1. Introduction

In the last few years, a new field of positron surface physics has been opened and advanced rapidly with the development of slow monoenergetic positron beams[1,2]. Most of the research in this field were directed toward understanding the basic interactions of positrons with surfaces and identifying some of the areas where positrons might eventually make a complementary surface probe. When positrons impinge on a target surface(see Fig. 1.1) a number of interesting phenomena occur: diffraction, reemission of low energy positrons, spontaneous emission of positronium(Ps), positrons bound in surface states and thermally desorbed as Ps, trapping of positrons by surface defects or impurities, etc. These phenomena are sensitive to the sample material, sample temperature, crystalline perfection, surface orientations, and contaminations. Many of these phenomena were newly revealed and their physical mechanisms still await for further investigations and more complete understanding both experimentally and theoretically.

The technique of angular correlation of annihilation radiation(ACAR) has long been used in the study of interactions of positrons with electrons in condensed matter[3-5]. The advent of two-dimensional position sensitive γ-detectors and computer-assisted image reconstruction algorithms has made it become one of the most important means of studying bulk electronic structures and defects. It is one's natural desire to extend these techniques to study various interactions of positrons with surfaces, in particular, surface electronic structures. Due to the nature of this particular application, however, a high flux($>10^7$ particles/sec.) low energy positron source is required. Only until very recently such high intensity positron beams have come into being and surface 2D-ACAR technique is finally applicable[6-8]. The pioneer measurements of this kind were conducted about a year ago by Howell *et al*.[7] on a Cu(121) surface at Lawrence Livermore National Lab., and by Lynn *et al*.[8] on an Al(100) surface at Brookhaven National Lab.(BNL). These preliminary work has opened a new chapter of the positron surface physics.

At BNL, this important investigation has being continued. The experimental technique has been greatly improved, and the 2D-ACAR measurement has been performed for all three low

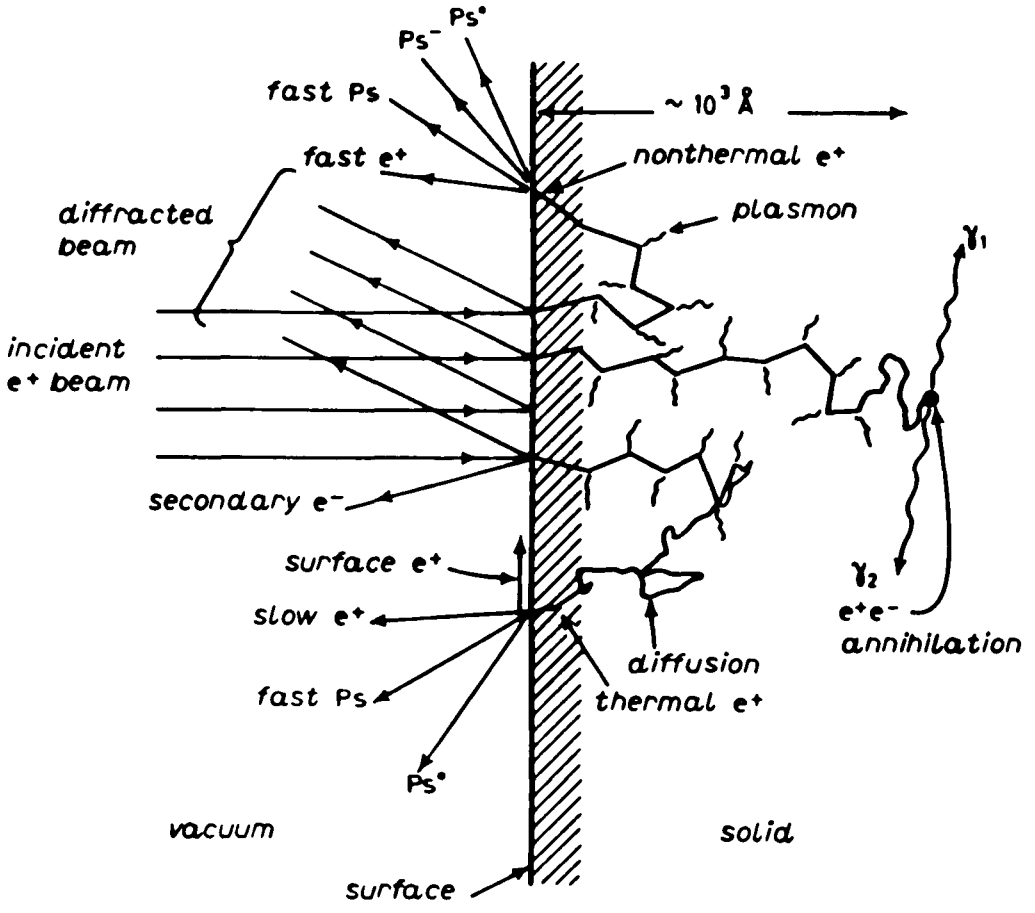

Figure 1.1. Positron interactions with a surface (from Ref. 1).

index surfaces of aluminum and two important reconstructed surfaces of silicon. These studies have shed new light on some areas of this field and opened a promising future. It is the goal of this thesis to present the first systematic discussion of the surface 2D-ACAR technique and some important results obtained up to date. In the first chapter we should provide a brief introduction to various aspects related to this study, the principle of this technique and some general theory.

§ 1.1 Positron Interaction with Solids*

The commonly used primary positron sources are isotopes,† e.g. ^{64}Cu , ^{22}Na , ^{58}Co , which emit positrons via β^+-decay. The energy distribution of the emitted positrons is the associated β^+-spectrum ranging from zero to the order of MeV. After being injected into a solid sample, the positrons lose energy rapidly by ionization, electron-hole excitation and finally by positron-phonon scattering. Within a few tens of picosecond positrons reach thermal equilibrium with the lattice and their spatial distribution forms the implantation profile, the shape of which depends on the incident-energy spectrum and on the sample material. The thermalized positrons subsequently diffuse inside the sample. For β^+-decay positrons, the diffusing length($\sim 10^3$ Å) is much shorter compared with the mean implantation depth($10\sim100\mu m$). Most of the incident positrons eventually annihilate with bulk electrons via the emission of energetic photons. Prior to annihilation, positrons are subject to various fates characterizing their environment. In a single crystal, the positron can form a ground state (e^+-energy band minimum) delocalized Bloch wave with large amplitude present at the interstitial sites due to the repulsion of the ion cores, and interacting strongly with the conduction electrons or valence electrons. If a positron encounters a vacancy, a dislocation or a microvoid, it has a finite probability being trapped in such region. In some material containing open volume or large voids, the positron may become bound to an electron and form the neutral positronium atom localized in the voids or delocalized in an open volume insulator crystal.

---

* For more detailed discussion of this subject see Refs.[3-5] and references therein.

† Another practical way of producing positrons is the 'pair production', see references cited in Ref.[7].

When a positron finally annihilates, the annihilation products are governed by the QED selection rules: in spin singlet e^+-e^- overlap, annihilation proceeds predominantly via the 2γ channel, while spin triplet overlap produces mainly 3γ photons. Single-photon annihilation is only possible in the presence of an electron or nucleus which can absorb the recoil momentum. The ratios of the cross sections for the respective processes are $\sigma_{3\gamma}/\sigma_{2\gamma} \approx \alpha$, $\sigma_{1\gamma}/\sigma_{2\gamma} \approx \alpha^4$, $\alpha = 1/137$ being the fine structure constant. Thus the annihilation occurs mainly via 2γ channel. On the other hand, if Ps atoms are formed in the ground state, 3/4 of the population will be in the triplet state and undergoes 3γ annihilation, while the other 1/4 in the singlet state participate in 2γ annihilation. In either case the annihilation characteristics of the γ-photons, their energies, momenta, and time of emission (or the lifetime of e^+ or Ps) reflect the initial state of the one-positron-many-electron system. Thus these antiparticles of electrons provide us with an useful probe for the study of condensed matter.

§ 1.2 Positron Interaction with Surfaces*

1.2.1 Implantation and Diffusion - Positron implantation profile is similar to that of electron and can be expressed with an empirical formula[9]:

$$P(z) = \frac{m z^{m-1}}{z_0^m} \exp[-(z/z_0)^m] \qquad 0 \le z < \infty, \tag{1.1}$$

where

$$z_0 = \bar{z}/\Gamma(1+1/m), \tag{1.2}$$

and

$$\bar{z} = \alpha E^n, \tag{1.3}$$

is the mean implantation depth at incident energy E, m,n and α are experiment-determined parameters. Most earlier studies for positrons[10] used $m = 1$, $n \approx 1.6$ and in general found good agreement with experiments. For $m = 1$ Eq.(1.1) leads to an exponential profile:

$$P(z) = \frac{1}{\bar{z}} \exp[-z/\bar{z}] \qquad 0 \le z < \infty. \tag{1.4}$$

* Also see the review articles [1,2] and references cited.

Recent Monte Carlo computations[11] have shown that for positrons $m = 1.9$ provides better agreement with experiments for Al, Si, Cu, and Au from 0 to 10 keV.

The relative number of the implanted and thermalized positrons diffusing back to the surface or annihilating in the bulk is ruled by the diffusion process. This can be described by a simple one dimensional diffusion equation[12]

$$\frac{\partial n(z,t)}{\partial t} = D_+ \frac{\partial^2 n(z,t)}{\partial^2 z} - \lambda n(z,t) \qquad 0 \leq z \leq \infty, \tag{1.5}$$

subject to an initial condition

$$n(z,0) = P(z), \tag{1.6}$$

and to a perfect absorption boundary condition*

$$n(0,t) = 0, \tag{1.7}$$

where $n(z,t)$ is the positron density, D_+ the diffusion coefficient and $\lambda = 1/\tau$, the positron bulk annihilation rate. Thus the fraction returning to the surface

$$\begin{aligned} F &= -J(0) = D_+ \frac{\partial n}{\partial z}\Big|_{z=0} \\ &= \int_0^\infty P(z) exp[-z/L_+] dz \ , \end{aligned} \tag{1.8}$$

which is simply the Laplace transform of the implantation profile and $L_+ = \sqrt{D_+/\lambda}$ is the positron diffusion length. Using the exponential profile Eq.(1.8) yields

$$F = \frac{1}{1 + (E/E_{\frac{1}{2}})^a}, \tag{1.9}$$

where $E_{\frac{1}{2}}$† is defined by

$$L_+ = \alpha E_{\frac{1}{2}}^a \tag{1.10}$$

and is the incident energy at which half of the implantation positrons diffuse back to the surface.

As an example, Fig. 1.2a shows four implantation profiles with $m = 1.9$ for Al and Si at few typical positron energies used in the present 2D-ACAR study. Figure 1.2b plots the mean implantation depth, $\bar{z}$, fraction diffusing to the surface, F, and the fraction annihilating in the

* A more general boundary condition given in Ref.[12] is: $D_+ \partial n/\partial z \mid_{z=0} = \nu n(0)$, where ν is the total rate of removing e^+ from the bulk. Finite ν implies the internal reflection at the surface, while for a perfectly absorbing boundary as Eq.(1.7) ν would tend to infinity.

† $E_{\frac{1}{2}}$ was denoted as E_0 in most of the literatures.

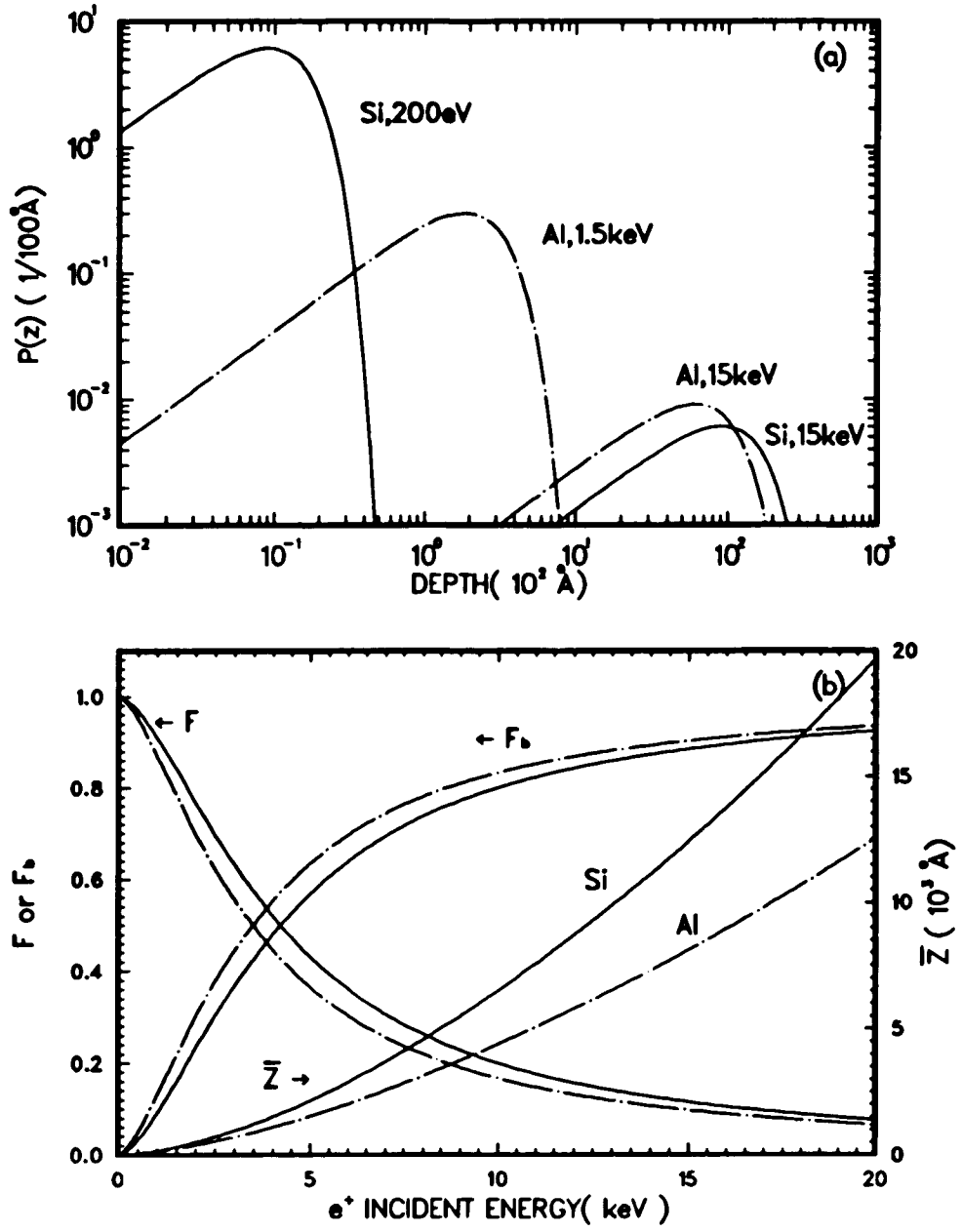

Figure 1.2. (a). Positron implantation profiles generated from Eq. (1.1)-(1.3) with $m = 1.9$ at four typical incident energies used in the experiment; (b). Positron mean implantation depth $\bar{Z}$, the fractions diffusing back to the surface F and annihilating in the bulk F_b vs incident energy as expressed in Eq. (1.3) and Eq. (1.9)-(1.10), respectively. Other parameters for both figures are associated with Al and Si and listed in Table 1.1.

Table 1.1 Parameters used in Eq.(1.1)-Eq.(1.10) to illustrate in Fig. 1.2 positron implatation and diffusion in Al and Si(selected from Refs. 11,13).

	τ (ps)	α ($\AA/keV^n$)	m	n	D_+ (cm^2/sec)	L_+ ($\AA$)	E_k (keV)
Al	166	132	1	1.52	0.45	864	3.47
			1.9	1.52	0.60	998	
Si	220	163	1	1.60	1.19	1619	4.2
			1.9	1.60			

bulk, $F_b = 1-F$, vs the positron implantation energy for Al and Si, respectively. F and F_b are calculated for the exponential profile(Eq.(1.4) and Eq.(1.9)) and have small deviations from results calculated using $m = 1.9$. Other parameters are listed in Table 1.1 correspondingly. At 200eV incident energy the fraction returning to the surface is 99% for both Al and Si, and hence the bulk annihilation is negligible, while at 15keV only 9% incident positrons comes back to the Al surface and 12% to the Si surface thus the annihilations occur mostly inside the bulks. The capability of controlling the implantation depth as well as these relative fractions F and F_b are essential for surface studies.

Upon reaching a surface, positrons interact strongly with the surface via multiple channels. Those that have been widely studied are shown schematically in Fig. 1.1, and are to be reviewed below.

1.2.2 Positron Emission from Surfaces. - For a number of materials such as single crystal *Cu*, *W*, *Ni*, *etc.*, positrons can be reemitted from the surface into vacuum because their work function Φ_+ are negative[1,14]. This is a contrary behavior to that of their counterpart, electrons. An electron work function Φ_- can be expressed as the minus sum of the bulk chemical potential μ_- and the dipole potential ϕ_D introduced by the atomic termination at a surface[15]:

$$\Phi_- = -\mu_- - \phi_D \tag{1.11}$$

It is readily seen that the dipole layer contribution to the positron work function Φ_+ should be equal in magnitude and opposite in sign to ϕ_D [16,17], thus:

$$\Phi_+ = -\mu_+ + \phi_D \tag{1.12}$$

The dipole potential depends upon the material, surface orientation and surface conditions(*e.g.* roughness and contaminations), and hence play a very important part in the electron and positron work functions. The bulk chemical potential $\mu_\pm$, in general, includes the zero-point energy E_0, the correlation energy E_c and the exchange energy E_{xc}. Since the positron is distinguishable from electrons, the Pauli repulsion force between e^+ and e^- does not exist and E_{xc} vanishes. The opposite sign of the charge gives rise to the opposite contributions of E_0 and E_c to μ_+ and to μ_-. Consequently, for most simple metals and transition metals, positron work functions are negative and thermalized positrons diffusing to the surface are emitted into the vacuum with a narrow energy width at $-\Phi_+$(on the order of eV), and with a small angular spread caused by the transverse thermal energy[18,19].

The most important application of the reemission of positrons from surfaces is the production of the slow positron beams and the brightness enhancement of these beams[20,21]. It also has been determined[19] that with high energy-resolution analyzers the reemitted positrons energy loss spectroscopy(REPELS) can be utilized to study adsorbates, interactions of adsorbates with the substrate, and other inelastic processes taking place at a surface.

1.2.3 Spontaneous Ps Emission from Surfaces - When a positron is bound with an electron forming a ground state Ps atom in vacuum, the binding energy gained by the system is $\frac{1}{2}Ry = 6.8\ eV$, which is, for many cases, greater than $\Phi_-(4 - 5\ eV)$, the energy needed to remove an electron from a solid. Consequently, it is energetically more favorable for a positron to leave a solid by picking up an electron and forming Ps atom than to leave the surface as a bare positron. The Ps work function Φ_{Ps} is thus defined as:

$$\Phi_{Ps} = \Phi_+ + \Phi_- - \frac{1}{2}Ry \tag{1.13}$$

The maximum energy of the emitted Ps is equal to $-\Phi_{Ps}$ [22]. When Φ_{Ps} is positive the spontaneous emission of Ps atoms is forbidden. Φ_{Ps} is expected to be negative for most metals except possibly the alkali metals because of the small E_0 and ϕ_D [17]. Furthermore, Ps^- negative ions and

the first excited state Ps^* atoms can possibly be formed at W and Cr surfaces[1,23].

The medium-vacuum interface plays another important role here. It provides a low electron density environment necessary for Ps to be formed and to escape. Inside metals the strong screening effects prevent Ps formation[24]. Ps formation were only observed in metals containing large voids[5,25], in insulators with open volume crystalline structure like quartz, ice and alkali halides[26], and in low density gases[27]. The common nature of these material is the existence of the low electron density region. In the solid, a host electron of opposite spin can replace the electron in the triplet Ps state(*i.e.* , spin exchange), or can overlap with the positron in the triplet Ps state(*i.e.* , pickoff), leading to a higher decay rate than the ortho-Ps. Ps formed near the surface of some insulators can diffuse back to the surface and be emitted into vacuum with a characteristic energy[28]. Two mechanisms for the spontaneous Ps emission has been proposed[22,29-31]. They will be discussed in §1.5.3 and §4.9.

1.2.4 Thermal Emission of Ps - At elevated sample temperatures, additional Ps of thermal energies are emitted from some metal and semiconductor surfaces[32,34]. The yield increases as a function of temperature, and is shown[33-36] to be related to the total thermal emissivity

$$\iota = \frac{4K_B T}{h}\exp[-E_a/K_B T], \tag{1.14}$$

where K_B and h are the Boltzmann's and Planck's constance; and E_a is the characteristic activation energy. The velocity distribution normal to the surface also follows Maxwell-Boltzmann's distribution[34](also see §4.10 and §5.6). The activation energy E_a is typically on the order of a tenth of an eV, and depends on the material and the surface conditions. In particular, some surface adsorbates can cause substantial reduction of E_a and lower the desorption temperatures[37].

In addition to the proposed thermodynamical process for the Ps desorption at elevated sample temperature, quantum tunneling model has also been shown to predict a similar temperature and activation energy dependence of the total activation rate[29,38].

1.2.5 Positron Surface State - The experimental evidence of thermal desorption of Ps from surfaces has led to the belief of that at low temperature($<300^\circ$K) a fraction of positrons,

responsible for the thermal Ps, reside in some bound states at the surface, where they annihilate with a unique lifetime characteristic of a low electron density[39]. Two theoretical models have been proposed to account for these observations.

1). Positron-image induced surface state: This earlier picture is described as follows[40,41]. In close vicinity outside the surface there exists a bound state due to the attraction between a positron and its image charge, known as positron-image induced surface state. A simple approximation is to take the static image potential $V=-1/4z$ for large distance, and terminate it with the vacuum e^+-e^- correlation energy E_{P_s}. A more realistic potential is formed by merging a *screened* static image potential $V=-1/4(z-z_1)$ into a electron density dependent e^+-e^- correlation energy near the surface. The screening of the positron induces an effective image plane located at a small distance z_1 outside the jellium edge[45]. These two potentials are shown schematically in Fig. 1.3a. Thermalized positrons diffused to the surface can undergo some inelastic scattering and become bound in such a state where the positron lives with a longer lifetime[39-44], because of the less overlap of the localized positron wave function with the decaying electron wave function tail extenting into the vacuum. For many materials $\Phi_- < \frac{1}{2}Ry$, the activation energy is therefore substantially decreased when Ps atom is formed. As a result, positrons bound in the surface states escape as a Ps atoms when thermally activated. The positron surface state binding energy E_b is typically 2-3eV[33,34], and is related to the activation energy by

$$E_b = E_s - \Phi_- + \frac{1}{2}Ry. \tag{1.15}$$

It is shown[37,41] that in some cases surface adsorbate shallows the surface potential well and causes the desorption of Ps atom from the surface states even at room temperature.

2). Physisorbed Ps state: When proposing the first model, the possibility of the bound Ps state was also mentioned, but dismissed[40]. Recently, this model has been re-emphasized[46-48]. This model[46], illustrated in Fig. 1.3b, views a positron trapped in the surface state as forming Ps with an electron which exchanges rapidly with the host material. The Ps at large distances is

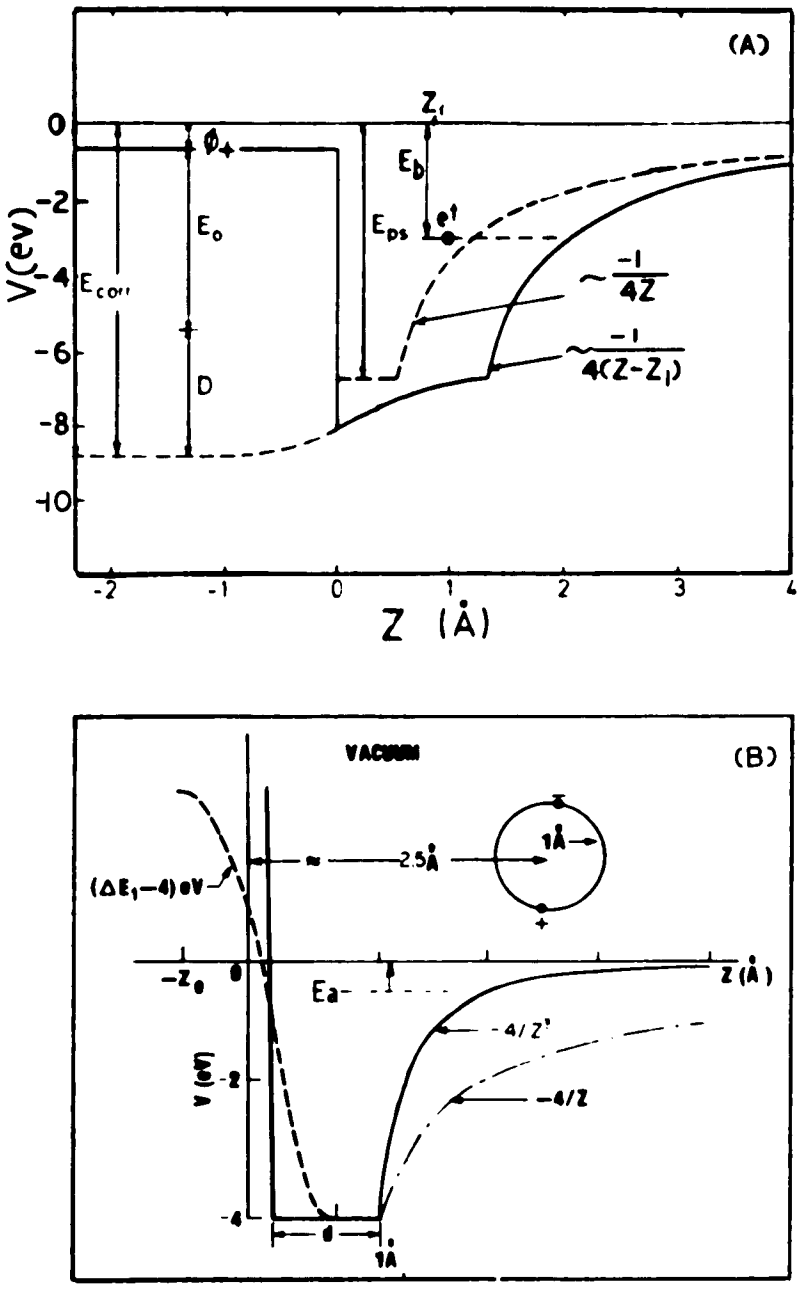

Figure 1.3. Potentials for two positron surface state models: (a). the static image potential $-1/4Z$, and the screened static image potential $-1/4(Z-Z_1)$, Z_1 indicating the position of the effective image plane(from Ref.41); (b). Physisorbed Ps induced dipole potential $-4/Z^3$, the image potential $-4/Z$ is plotted for comparison, the dashed curve is explained in the text(from Ref. 46).

attracted to the surface by a weak $-1/z^3$ van der Waals polarization potential. At short distances, the singular potential begins to level off and ultimately become repulsive due to the short-range repulsion between electrons in the host material of the same spin as the one on the Ps. Electrons of the opposite spin feel a net weak attraction characteristic of Ps^-. From the point of view of the uncertainty principle, $E_s \approx few\, 10^2 meV$ (the binding energy of the Ps atom to the surface) implies that the mean distance from the surface of Ps is 2.5 Å , while the vacuum Ps binding energy E_{Ps} =6.8eV indicates that the radius of the Ps is about 0.5 Å. Thus it is reasonable to imaging a somewhat stable weakly bound Ps state.

Detailed comparisons between the above two models have also been made within the same theoretical framework[48]. The results indicate that the surface Ps state can not be ignored in the description of the positron binding to the surface. The above two models predict a positron or Ps wave function delocalized in the surface plane but localized perpendicular to the surface. This leads to an anisotropic momentum distribution, which is in disagreement with experimental observations[7,8].

1.2.6 Other Interaction Processes - The above are the dominate processes which occur in a wide incident energy range for various surfaces. Other interaction processes shown in Fig. 1.1 are less important to the ACAR study and will only be briefly mentioned.

When a low energy ($\sim 10^2\, eV$) beam of positrons impinge on a target, some of the incident positrons will be scattered elastically or inelastically from the target surface. If the beam is coherent the elastically-scattered beams will obey the Bragg condition[49] and can form, on some position sensitive detector, the low-energy positron diffraction(LEPD) pattern[21] similar to low-energy-electron-diffraction (LEED) pattern. Together with the I-V measurement[50] LEPD provides informations about the crystal surface structure. The advantage of LEPD over LEED is that the lack of e^+–e^- exchange interaction reduces the theoretical computation effort for the structural interpretation of these I-V curves[50]. The surface scattering process can also be accompanied by picking up an electron and form a scattered Ps atoms whose energy can be much greater than the Ps work function[51].

Positrons diffusing through the bulk lattice toward a surface are likely to be trapped by vacancies, dislocation loops, surface steps and other defects. The relative yields of those processes discussed before can be altered substantially by the presence of these defects. The great sensitivity of these surface interaction processes to the defects provides another method to study crystalline imperfections near a surface and in the interface regions[52].

When positrons are implanted with low energy ($< 100eV$), a significant fraction of them can be scattered back to the surface before establishing thermal equilibrium with the bulk[53,54]. These nonthermal positrons can be emitted into vacuum with an energies higher than $-\Phi_+$ when Φ_+ is negative. In some cases nonthermal positrons can even overcome a small positive Φ_+ barrier and escape into vacuum. This effect is more pronounced for insulators, because when the positron energy is reduced to the order of the electron band gap the electron-hole excitation cross section will drop dramatically. Nonthermal positrons can participate in all the interactions with the surface and the effects can not be ignored.

All the above processes can occur independently or simultaneously depending upon the type of material under study and the incident positron energy. The competition between the processes when they are permitted to take place at the same time is complicated and can only be described by empirical parameters, the branching ratio B_i s.

§ 1.3 The Principle of 2D-ACAR Technique[3]

When a positron annihilates with an electron or a para-Ps annihilates two γ-photons are created. In the center-of-mass frame, the conservation of momentum and energy requires that the two photons are emitted at an angle of 180°, with total energy $E_t = 2m_e c^2 - E_B$, E_B being the binding energy of the electron and positron in the solid. In the laboratory frame, however, the two photons are not necessarily anticolinear and their energy is Doppler shifted, because the initial momentum p of the annihilation pair is generally finite. In the geometry given in Fig. 1.4,*

* The perpendicular and parallel subscripts denote the directions perpendicular and parallel to the surface, respectively.

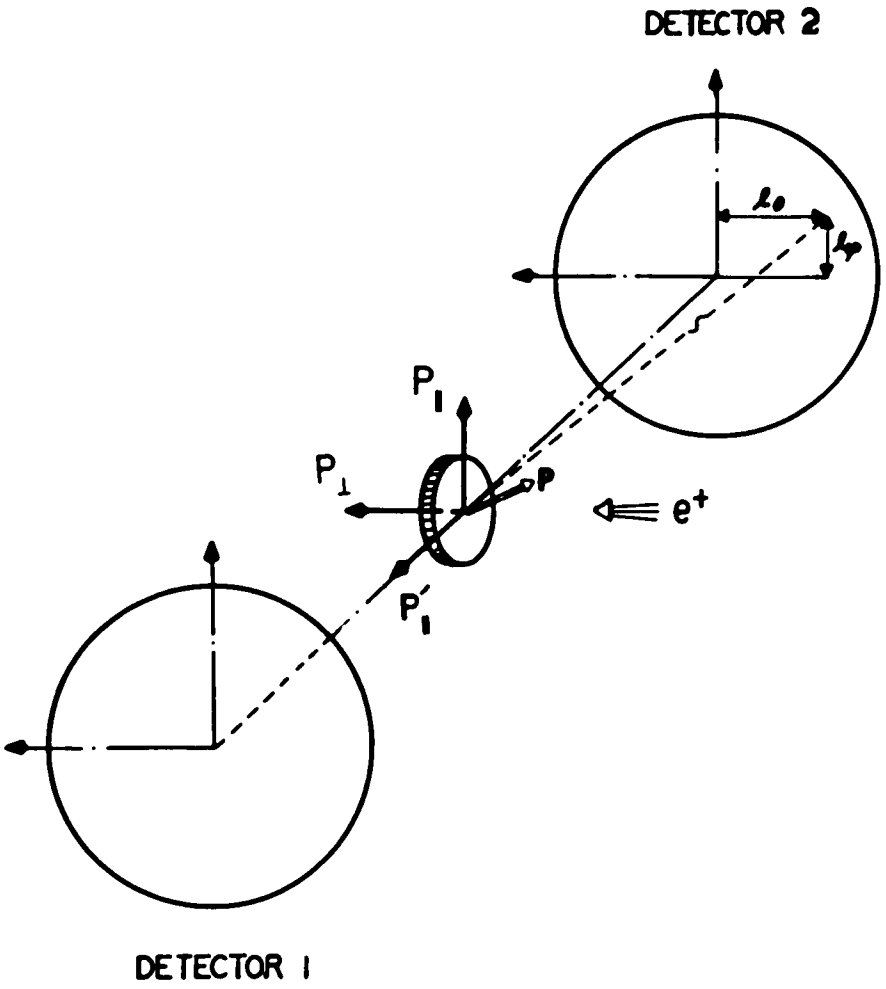

Figure 1.4. The geometry of the present 2D-ACAR experiment.

the angular deviation of the two photons from the anticolinear and energy of the two photons can be expressed as

$$\theta = p_\perp / m_e\, c\,, \qquad \phi = p_\parallel / m_e\, c\,, \tag{1.16}$$

$$E_{1,2} = m_e\, c^2 - E_B\,/2 \pm c\, p_\parallel'\,/2. \tag{1.17}$$

A momentum p corresponding to one atomic unit (*i.e.* $|\vec{p}\,| = 1$ *a.u.* ,$m = 1, c = 137$) produces an angular deviation of 7.297 mrad, when p is perpendicular to the 2γ axis, and an energy shift of $\pm$ 1.86 keV (from $mc^2 = 511\ keV$) when parallel to the 2γ axis(neglecting the smaller E_B term, few eV).

In principle, simultaneous measurements of both angular deviation θ , ϕ and the Doppler shift could provide through Eq.(1.16) and Eq.(1.17) the partial three dimensional momentum density $\rho(\mathbf{p})$ of the annihilation pair in the initial state of the one-positron-many-electrons system. Practically, such ideal experiment is not feasible because of the restricted signal intensity. Instead, modern two dimensional position sensitive detectors have made it possible to measure the two-dimensional projection of the 2γ-angular correlation

$$N(p_\parallel,\, p_\perp) = \int \rho(\mathbf{p})\, d\, p_\parallel' \,. \tag{1.18}$$

When the projection is taken along sufficient number of different angles, the reconstruction of the original three-dimensional momentum densities from the measured projections can be accomplished with the assistance of some computer algorithm.

In order to implement the measurements of 2D-ACAR from surfaces, positrons of controllable energies (from 1 to $10^4 eV$) are implanted in the near surface region. It is clear from the discussion of §1.2 that the 2γ annihilations from a surface are contributed essentially from three parts:

i). $N_{s.s.}\,(p_\parallel,\, p_\perp)$: positrons residing at the surface and annihilate with surface electrons;

ii). $N_{Ps}\,(p_\parallel,\, p_\perp)$: para-positronium emitted from the surface which annihilate within few tenth of a mm from the surface because of the short lifetime(125ps);

iii). $N_{bulk}\,(p_\parallel,\, p_\perp)$: positrons diffusing inside the lattice and annihilate with bulk electrons.

Thus the total measurement

$$N_{tot}(p_{\parallel}, p_{\perp}) = N_{Ps}(p_{\parallel}, p_{\perp}) + N_{s.s.}(p_{\parallel}, p_{\perp}) + N_{bulk}(p_{\parallel}, p_{\perp}). \quad (1.19)$$

The relative contribution of each term is dependent of the incident positron energy, the sample temperature and other experimental conditions. It will be shown in chapter 3 that these components can in fact be decoupled by virtue of their underlying symmetries. Therefore various mechanisms can be studied using the surface 2D-ACAR technique.

§ 1.4 2D-ACAR Spectra

A two dimensional ACAR spectrum is defined by Eq.(1.18) and Eq.(1.19). As an example, here we show tow sets of the spectra for Al and Si in Fig. 1.5 and Fig. 1.6, respectively. They are peak-normalized and are presented in a perspective view, in which the vertical axis is the intensity $N(p_{\perp}, p_{\parallel})$. For all our measurement the geometry was the same as Fig. 1.4. The integration(or projection) is taken over $p_{\parallel}'$, parallel to the surface.

Fig. 1.5a is a bulk Al spectrum from an Al(111)-^{22}Na-Al(111) sandwich sample, which contains only the bulk annihilation. Fig. 1.5b shows the results of a 1.5 keV positron beam impinging on an Al(100) surface. In this spectrum more than 70% of the contribution comes from the annihilation taking place at the surface. The asymmetry between $p_{\perp}>0$ and $p_{\perp}<0$ arises form the fact that Ps atoms formed at the surface are emitted into vacuum with $p_{\perp}\leq 0$. Fig. 1.5c is from a measurement similar to Fig. 1.5b but with the sample temperature being raised up at 600° K. The large reduction of the contribution at $p_{\perp}>0$ region indicates that positron trapped in surface states were thermally desorbed from the surface as Ps atoms.

Figure 1.6 is a similar set of spectra for a Si(111)-(7×7) surface. Fig. 1.6a was taken at 15 keV incident positron energy, hence 90% annihilation occurred inside the bulk. In Fig. 1.6b the incident energy was reduced to 200 eV, and when the sample temperature was increased from 300° K to 870 ° K it changes to Fig. 1.6c.

The effects observed in these spectra due to the change of the incident positron energy and sample temperature are anticipated from the previous discussions. A perspective view offers good

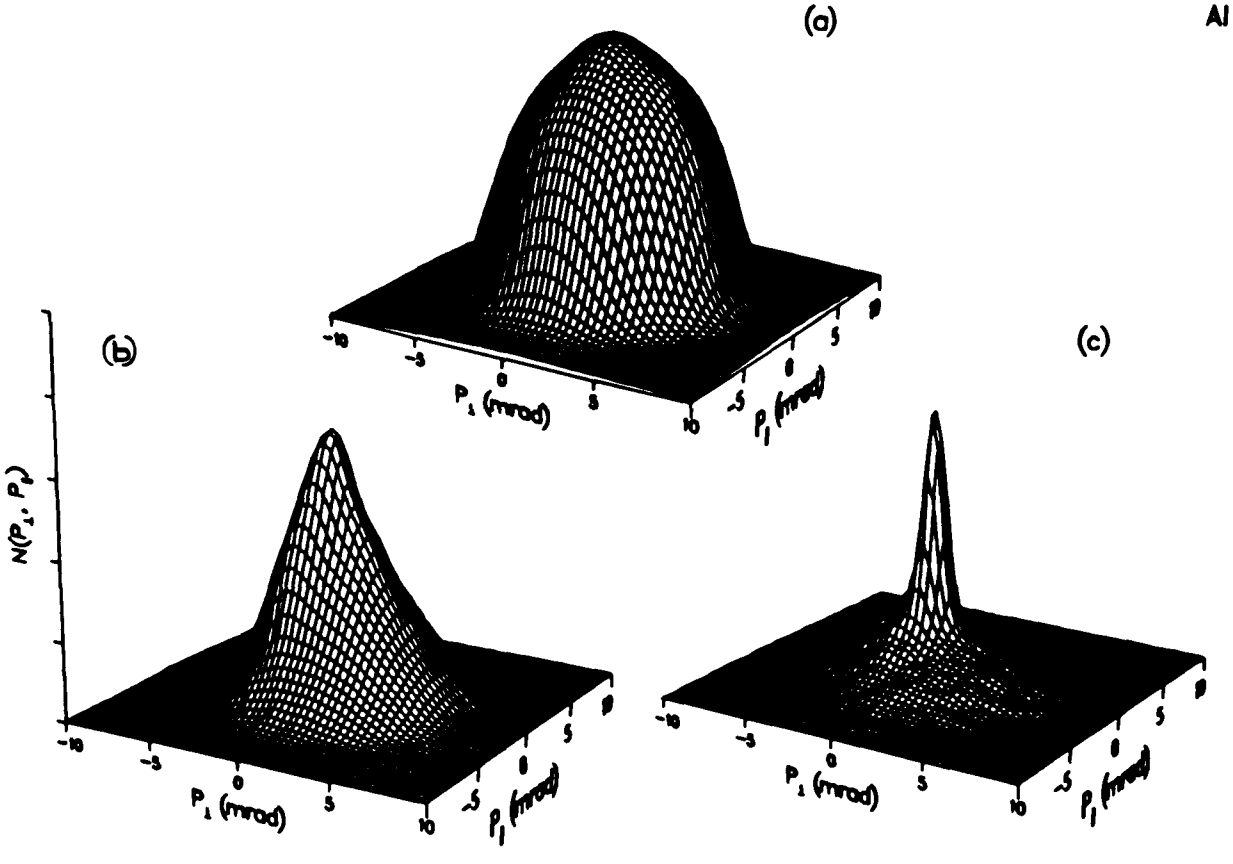

Figure 1.5. Peak-normalized 2D-ACAR spectra for (a). a Al(111)-^{22}Na-Al(111) sample; (b). an Al(100) surface with 1.5keV positron beam energy at room temperature; (c). an Al(100) surface with 1.5keV beam energy at 600° K.

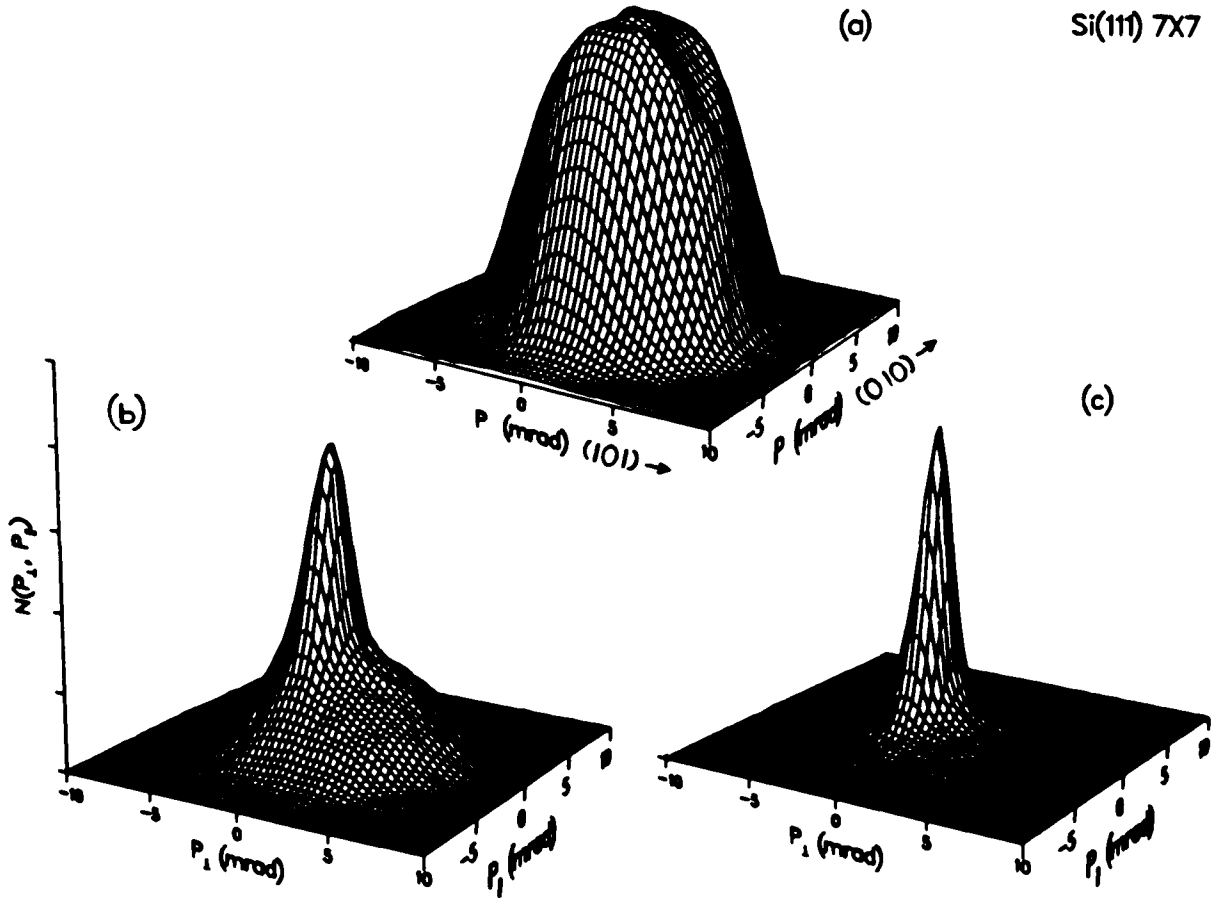

Figure 1.6. Peak-normalised 2D-ACAR spectra for a Si(111)-(7×7) surface, the incident positron energies and sample temperatures are respectively: (a). 15keV, 300° K; (b). 200eV, 300 ° K; and (c). 200eV, 870° K.

visual effect, but to extract the information embedded in an ACAR spectrum, the spectrum is often examed with its contour plot and one dimensional cuts at various directions. We will encounter these when we return to more discussions of the surface ACAR results in Chapter 4 and Chapter 5.

§ 1.5 Momentum Density Functions of 2γ Annihilation

To gain insight into a system under study from 2D-ACAR measurements, further theoretical considerations are necessary. This is in general a nontrivial many-body problem, which is further complicated by the presence of the positron. Fortunately, many important features can already been drawn from some general inspections.

1.5.1 2γ-Annihilation in Bulk Crystal * - The general theoretical description of positron annihilation in condensed matter have been achieved by several researchers[55]. In the independent-particle model(IPM), for a positron in state $\psi_+(\mathbf{r})$ annihilating in a system of electrons described by a Slater determinant of single-particle states $\psi_{-j}(\mathbf{r})$, the momentum distribution of the 2γ annihilation is given by:

$$\rho^{2\gamma}(\mathbf{p}) = const \cdot \sum_j \left| \int d\mathbf{r}\, e^{-i\mathbf{p}\cdot\mathbf{r}} \psi_+(\mathbf{r})\psi_{-j}(\mathbf{r}) \right|^2 . \tag{1.20}$$

The integral in Eq.(1.20) is the momentum spectrum of the overlap between the single-particle positron wave function and electron wave function. In momentum representation it becomes a convolution between the single-particle positron momentum wave function $\phi_+(\mathbf{p}')$ and electron momentum wave function $\phi_{-j}(\mathbf{p}')$:

$$\rho^{2\gamma}(\mathbf{p}) = const \cdot \sum_j \left| \int d\mathbf{p}'\ \phi_+(\mathbf{p}')\, \phi_{-j}(\mathbf{p}-\mathbf{p}') \right|^2 . \tag{1.21}$$

For a periodic system with lattice vector $\mathbf{R}$ and the corresponding reciprocal lattice vector $\mathbf{G}$, $\psi_+(\mathbf{r})$ and $\psi_{-j}(\mathbf{r})$ obey the Bloch theorem[56]:

$$\psi_+(\mathbf{r}) = u_{\mathbf{k}^+}(\mathbf{r})\, e^{i\mathbf{k}^+\cdot\mathbf{r}} \qquad \text{and} \qquad \psi_{-j}(\mathbf{r}) = u_{\mathbf{k}^-,l}(\mathbf{r}) e^{i\mathbf{k}^-\cdot\mathbf{r}} , \tag{1.22}$$

where l is a band index and

* We follow the derivation given by S. Berko in Ref.[3].

$$u_{k^{\pm},l}(r) = u_{k^{\pm},l}(r+R). \tag{1.22}$$

For a single-electron Bloch wave we have

$$\rho^{2\gamma}_{k^+,k^-,l}(p) = const \cdot \left| \int dr\, e^{-i(p-k^+-k^-)\cdot r} u_{k^+}(r) u_{k^-,l}(r) \right|^2. \tag{1.24}$$

The total momentum density becomes the statistical sum of Eq.(1.24) weighted by a Boltzmann distribution f_{B^+} for the positron near the bottom of its band and the usual Fermi distribution f_{F^-} for electrons:

$$\rho^{2\gamma}(p) = \sum_{k^+,k^-,l} f_{B^+}(k^+,T)\, f_{F^-}(k^-,T)\, \rho^{2\gamma}_{k^+,k^-,l}(p) \tag{1.25}$$

For zero temperature we set $k^+ = 0$, $k^- = k$, then

$$\rho^{2\gamma}(p) = \sum_{k,l} n_l(k)\, \rho^{2\gamma}_{k,l}(p)\,, \tag{1.26}$$

where $n_l(k)$ is the occupancy number equal to zero for states above Fermi level, and one otherwise. The momentum representation of $\rho^{2\gamma}_{k,l}(p)$ is obtained by inserting into (1.24) the periodic expansion:

$$u_{k^{\pm},l}(r) = \sum_G c_l{}^{\pm}(k,G) e^{iG\cdot r}, \tag{1.27}$$

and denoting

$$\phi_l{}^{\pm}(k,G) = \sum_{G'} c^{+}(G')\, c_l{}^{-}(k,G-G')\,. \tag{1.28}$$

Thus,

$$\rho^{2\gamma}_{k,l}(p) = const \cdot \sum_G \left| \phi_l{}^{\pm}(k,G) \right|^2 \delta(p - k - G), \tag{1.29}$$

which is equivalent to the integral in Eq.(1.21).

Two important features can be immediately deduced from these derivations. First, we note that the important dependence of $\rho^{2\gamma}(p)$ on the Fermi surface appears in Eq.(1.26) via the $n_j(k)$'s. The momentum spectrum should have a cut off at Fermi momentum k_F if the ACAR detectors have infinite resolution; Second, Eq.(1.29) shows that an electron associated with crystal momentum k will contribute not only at $p=k$ but at all $p=k+G$, with amplitude $\left| \phi_l{}^{\pm}(k,G) \right|^2$, known as umklapp annihilation components(or high momentum components). The electronic structure within a Brillouin zone is fully contained in the amplitude function which drops rapidly as the zone extended into higher zones[57].

1.5.2 Annihilation Near Crystal Surface - Near a crystal surface, the translational symmetry in the direction perpendicular to the surface is broken. The truncation of a bulk crystal in many cases also results in the relaxation and reconstructions of a few top atomic planes in order to obtain a more stable structure than a perfect bulk crystal termination[58]. Additionally, surface adsorbates can also form some ordered overlayers commensurate or incommensurate with the substrate. In general, the salvage form its own two dimensional periodic net with a two dimension lattice vector $\vec{R}$ * and the associated reciprocal lattice vector $\vec{g}$, defined in analogy to the bulk case[56,58]:

$$\vec{R} = n\vec{a}_1 + m\vec{a}_2, \tag{1.30}$$

$$\vec{g} = h\vec{b}_1 + k\vec{b}_2, \tag{1.31}$$

and

$$\vec{b}_i \cdot \vec{a}_j = 2\pi\delta_{ij}. \tag{1.32}$$

where n, m, h, and k are integers. The transformation between the surface geometrical structure and its substrate structure can be expressed as

$$\vec{a}_1 = m_{11}\vec{a}_1' + m_{12}\vec{a}_2', \tag{1.33}$$

$$\vec{a}_2 = m_{21}\vec{a}_1' + m_{22}\vec{a}_2', \tag{1.34}$$

where $\vec{a}_i'$ stands for the substrate lattice unit vector. Thus the relative structure of the surface with respect to the substrate is uniquely defined by the transformation matrix M. For instance, Si(111)-(7×7) structure is associated with $m_{11} = 7$, $m_{22} = 7$, and $m_{12} = m_{21} = 0$.

The notion of the Bloch theorem can be extended to describe the states near the surface. For instance,

$$\psi_+(\mathbf{r}) = u_{\vec{k}^+}(\mathbf{r})e^{i\vec{k}^+\cdot\mathbf{r}} \qquad \text{and} \qquad \psi_{-j}(\mathbf{r}) = u_{\vec{k}^-,l}(\mathbf{r})e^{i\vec{k}^-\cdot\mathbf{r}}, \tag{1.35}$$

where

$$u_{\vec{k}^\pm,l}(\mathbf{r}) = u_{\vec{k}^\pm,l}(\mathbf{r}+\vec{R}), \tag{1.36}$$

is the analogy to Eq.(1.23) in the two dimensional case. It evolves into the form of $u_{k^\pm,l}(\mathbf{r})e^{ik_z z}$ as z moves into the bulk ($z \to \infty$) and vanishes as $z \to -\infty$. The periodic expansion can only be

* We denote a three dimensional vector as $\mathbf{x}$ and a two dimensional vector as $\vec{x}$.

carried out parallel to the surface while the perpendicular should be written in a Fourier transform form, i.e.

$$\psi_{\vec{k}^{\pm},l}(\mathbf{r}) = \sum_{\vec{g}} \left[\int c_l{}^{\pm}(\vec{k},\vec{g},p_\perp) e^{ip_\perp \cdot z} \, d\, p_\perp \right] e^{i\vec{g}\cdot\vec{r}}. \tag{1.37}$$

Thus for the zero temperature approximation,

$$\rho^{2\gamma}_{\vec{k},l}(\mathbf{p}) = const \cdot \sum_{\vec{g}} | \phi_l{}^{\pm}(\vec{k},\vec{g},p_\perp) |^2 \delta(\vec{p}-\vec{k}-\vec{g}), \tag{1.38}$$

$$\rho^{2\gamma}(\mathbf{p}) = \sum_{\vec{k},l} n_l(\vec{k},p_\perp) \rho^{2\gamma}_{\vec{k},l}(\mathbf{p}), \tag{1.39}$$

where

$$\phi_l{}^{\pm}(\vec{k},\vec{g},p_\perp) = \sum_{\vec{g}'} \int d\, p_\perp' \; c^{+}(\vec{g}',p_\perp') c_l{}^{-}(\vec{k},\vec{g}-\vec{g}',p_\perp-p_\perp'). \tag{1.40}$$

Clearly we can make parallel remarks on Eq.(1.39) and Eq.(1.40) as we did on Eq.(1.26) and Eq.(1.29). The Fermi cutoff and umklapp will still exist in the direction parallel to the surface. Perpendicular to the surface the situation is more complicated and depends on the specific picture of the positron surface state. Nevertheless, in many cases near a surface the wave functions of the z-component $\psi_{\pm}(z)$ can be approximately separated from the total wave functions $\psi_{\pm}(\mathbf{r})$[42,44]. Hence

$$\psi_{\vec{k}^{\pm},l}(\mathbf{r}) = \left[\int \chi^{\pm}(p_\perp) e^{ip_\perp \cdot z} \, d\, p_\perp \right] \cdot \sum_{\vec{g}} c_l{}^{\pm}(\vec{k}^{\pm},\vec{g}) e^{i\vec{g}\cdot\vec{r}}, \tag{1.41}$$

$$\rho^{2\gamma}_{\vec{k},l}(\mathbf{p}) = const \cdot \left| \int \chi^{+}(p_\perp') \chi^{-}(p_\perp - p_\perp') \, d\, p_\perp' \right|^2 \cdot \sum_{\vec{g}} | \phi_l{}^{\pm}(\vec{k},\vec{g}) |^2 \delta(\vec{p}-\vec{k}-\vec{g}), \tag{1.42}$$

where $\chi^{\pm}(p_\perp)$ is the Fourier transform of $\psi_{\pm}(z)$, and

$$\phi_l{}^{\pm}(\vec{k},\vec{g}) = \sum_{\vec{g}'} c^{+}(\vec{g}') c_l{}^{-}(\vec{k},\vec{g}-\vec{g}'). \tag{1.43}$$

The $p_\perp$ dependence of the momentum density function is determined by the integral in Eq. (1.42). Since the positron is confined in the direction perpendicular to the surface it's momentum component $p_\perp$ is substantially larger compared with a delocalized thermal positrons in the bulk or with the other two momentum components $p_\parallel$ and $p_\parallel'$[42]. Thus $\chi^{+}(p_\perp')$ will play an important role in the convolution and introduces substantial anisotropy in the momentum distributions with respect to the two orthogonal directions, parallel or perpendicular to the surface.

1.5.3 Ps Momentum Distributions - The angular distribution of 2γ annihilation from Ps formed at a surface reflects the momentum distribution of the center of mass motion of these Ps atoms. This is determined by the initial state of the system and the formation mechanism which is not fully understood. However, a plausible picture consistent with experimental observations is that as the thermalized positron approaches the vacuum it carries with it a correlated cloud of electrons, at low enough density ($r_s = n^{-1/3}/a_0 \approx 6$), this cloud begin to resemble vacuum positronium and in the presence of the surface it is liberated from the solid leaving behind the single hole required by the charge conservation[22]. The momentum distribution for the Ps emission can be described by the Fermi golden rule:

$$\rho_{Ps}(\mathbf{q}) \sim \sum_j |\, M_j \,|^2 \, n_j \, \delta(E(\mathbf{q}) + (E_F - E_j) + \phi_{Ps}), \tag{1.44}$$

where $\mathbf{q}$ is the Ps momentum, n_j and E_j are the occupation number and energy of the jth electron, and M_j is the matrix element. For a sudden formation process,

$$M_j = \int d\mathbf{r}^+ \, d\mathbf{r}^- \, \psi^*_{Ps}(\mathbf{r}^+, \mathbf{r}^-) U(|\mathbf{r}^+ - \mathbf{r}^-|) \psi_+(\mathbf{r}^+) \psi_{-j}(\mathbf{r}^-). \tag{1.45}$$

In the first order approximation the initial state is described by independent particle wave functions of Eq.(1.35-1.37) and the interaction Hamiltonian $U(|\mathbf{r}^+ - \mathbf{r}^-|)$ is a bare[22] or screened[31] Coulomb interaction near the surface leading to the Ps bound state which is represented by a free Ps wave function[31]

$$\psi_{Ps}(\mathbf{r}^+, \mathbf{r}^-) \sim e^{-i\mathbf{q}\cdot(\mathbf{r}^+ + \mathbf{r}^-)/2} e^{-|\mathbf{r}^+ - \mathbf{r}^-|/2a_0}. \tag{1.46}$$

where a_0 is the 'Bohr radius' of the Ps atom. The overlap between the initial state and the final state is restricted to a small region near the surface. For a surface with translational symmetry parallel to the vacuum interface, we can proceed further by carrying out implicitly the integral over $\mathbf{r}^+$ and setting the temperature to zero. Thus

$$M_j = \int \psi_j(\mathbf{r}) \varsigma(\mathbf{r}) d\mathbf{r}, \tag{1.47}$$

where $\mathbf{r} = \mathbf{r}^-$ and

$$\varsigma(\mathbf{r}) = \sum_{\overline{\gamma}} \varsigma_{\overline{\gamma}}(z) e^{-i(\overline{\gamma} - \overline{\gamma})\cdot\overline{\gamma}} \tag{1.48}$$

In momentum space Eq. (1.47) becomes

$$M_l(\vec{k},q_\perp) = \sum_{\vec{g}} \phi_l^{\pm}(\vec{k},\vec{g},q_\perp)\delta(\vec{q}-\vec{g}-\vec{k}). \tag{1.49}$$

Here

$$\phi_l^{\pm}(\vec{k},\vec{g},q_\perp) = \sum_{\vec{g}'} \int d\, q_\perp' \;\xi(\vec{g}',q_\perp')\, c_l^{-}(\vec{k},\vec{g}-\vec{g}',q_\perp-q_\perp'), \tag{1.50}$$

and $\xi(\vec{g},q_\perp)$ is the Fourier transform of $\varsigma_{\vec{g}}(z)$. Substituting Eq.(1.49) into Eq. (1.44) we obtain

$$\rho_{Ps}(\mathbf{q}) = const \cdot \sum_{\vec{k},l,\vec{g}} |\, \phi_l^{\pm}(\vec{k},\vec{g},q_\perp)\,|^2\, n_l(\vec{k},q_\perp)\delta(\vec{q}-\vec{k}-\vec{g})\;\delta(E(\mathbf{q})+(E_F-E_l(\vec{k})+\Phi_{Ps}). \tag{1.51}$$

The occupation number and the delta-functions imply the conservation of energy and momentum parallel to the surface. Ps atoms can be formed with electrons in an energy range from E_F to $E_F+\Phi_{Ps}$. As suggested by the first delta-function Ps can also be formed with surface umklapp electrons, (and perhaps can be named umklapp Ps), as long as the energy conservation is also satisfied.

Ion-neutralization process also has been extended to describe the Ps formation mechanism at a surface[29, 30]. A more detailed discussion is given in §4.9.6. Despite the different mechanism, the above general conclusions such as the conservation of energy and parallel momentum, and the possible umklapp Ps are retained in this model.

Chapter 2. Experimental

The surface 2D-ACAR measurement system, as illustrated schematically in Figs. 2.1-2.3, consists of a high intensity slow positron beam, a surface chamber, a pair of two dimensional position-sensitive detectors(Anger cameras in this case) and the associated data acquisition system. The surface chamber(Fig. 2.2) is equipped with a low energy electron diffraction(LEED) and retarding field Auger analyzer,† a mass spectrometer, a gas manifold, an ion sputtering gun, and an electron gun heater. In a typical experiment, the sample surface is prepared and characterized in the surface chamber; a slow monoenergetic positron beam produced in the source chamber is accelerated to the desired energy and guided to bombard the prepared surface; annihilation signals are detected by the 2D-Anger cameras; the angular correlation signals of a pair γ-rays created from the same annihilation event is then extracted and sent to the data acquisition system(Fig. 2.3).

The set-up here is different from traditional 2D-ACAR system in the following two aspects:

i). A conventional positron emitter with a β^+-spectrum(0 – 1 MeV) energy distribution is replaced by a high intensity, energy tunable, monoenergetic beam of positrons. This, as demonstrated in §1.2.1, is essential for controlling the positron implantation depth, and hence the fraction of the thermalized positrons which diffuse back to and interact with the surface under study.

ii). As seen in Fig. 2.1 the target chamber, the positron source chamber and the beam line are join together and form an ultra-high-vacuum(UHV) system. The UHV environment is necessary both for the surface studies and for the positron source evaporation, energy moderation and the beam transportation.

Perhaps, the biggest challenge encountered in performing this type of experiment is to be able to accumulate data of high resolution and good statistics within a time scale of one hour or less so that the sample surface condition will not alter during the whole measurement. This

† In later stage of this work the surface chamber has been supported with a double pass cylindrical analyzer.

demands an excellent vacuum ($\sim 10^{-11}$ Torr), a strong e^+-beam intensity ($> 1\times10^7 e^+/sec$) and detectors of good spatial resolution ($10\ mm^2 <$) and high detecting efficiency ($>15\%$). (These parameters are, of cause, strongly coupled and compensate each other.) These necessities are, in fact, responsible for the delay of the application of 2D-ACAR technique to studies of positron interactions with surfaces. In the present work, using a beam of initial intensity $\approx 7\times10^7\ e^+$/sec, 15 cps coincident rate was achieved with the Anger cameras located 10 meters away from the sample which results in an overall resolution of 1 mrad FWHM by 1 mrad FWHM. Typically, an elapsed-time of three hours was necessary to yield 1000 counts at the peak channel as a result of positron source decay.

The evolution of the ACAR technique has been well documented[3,5] and will not be provided in this chapter. We will confine ourselves mainly to the new aspects mentioned above.

§ 2.1 High Intensity Slow Positron Beam

The high intensity slow positron beam used for the present work was constructed at High Flux Beam Reactor (HFBR) of Brookhaven National Laboratory. Here 'high intensity' implies an incident count rate close to $10^8\ e^+/sec$ which is one to two order of magnitude higher than any other e^+-beams from radioactive sources. The design, performance and future improvement of this beam has been discussed in great detail by Weber *et al.* [59]. The basic components of this beam is shown schematically in Fig. 2.1. Briefly, a ^{64}Cu β^+-decay source is produced in the core of HFBR by irradiating ^{63}Cu with a high flux of thermal neutrons ($8.3\times10^{14}\ n_e/cm^2$ sec). A typical source of 22 Ci β^+-activity is obtained in 48 hours irradiation. The ^{64}Cu source is then introduced, through a pre-evacuation chamber (labeled as air lock in Fig. 2.1), into a crucible in the source chamber where it is evaporated onto a single crystal W(110) substrate. After some careful annealing about 100 μm thick, 1 cm^2 area single crystal Cu(111) film is formed on the W(110)-substrate. This Cu film plays two important roles. It is a strong positron emitter as well as a positron energy moderator, which converts $\approx 0.01\%$ of the high energy positrons into a monoenergetic positron source with a narrow energy width and small angular spread($\sim 30^e$). Ini-

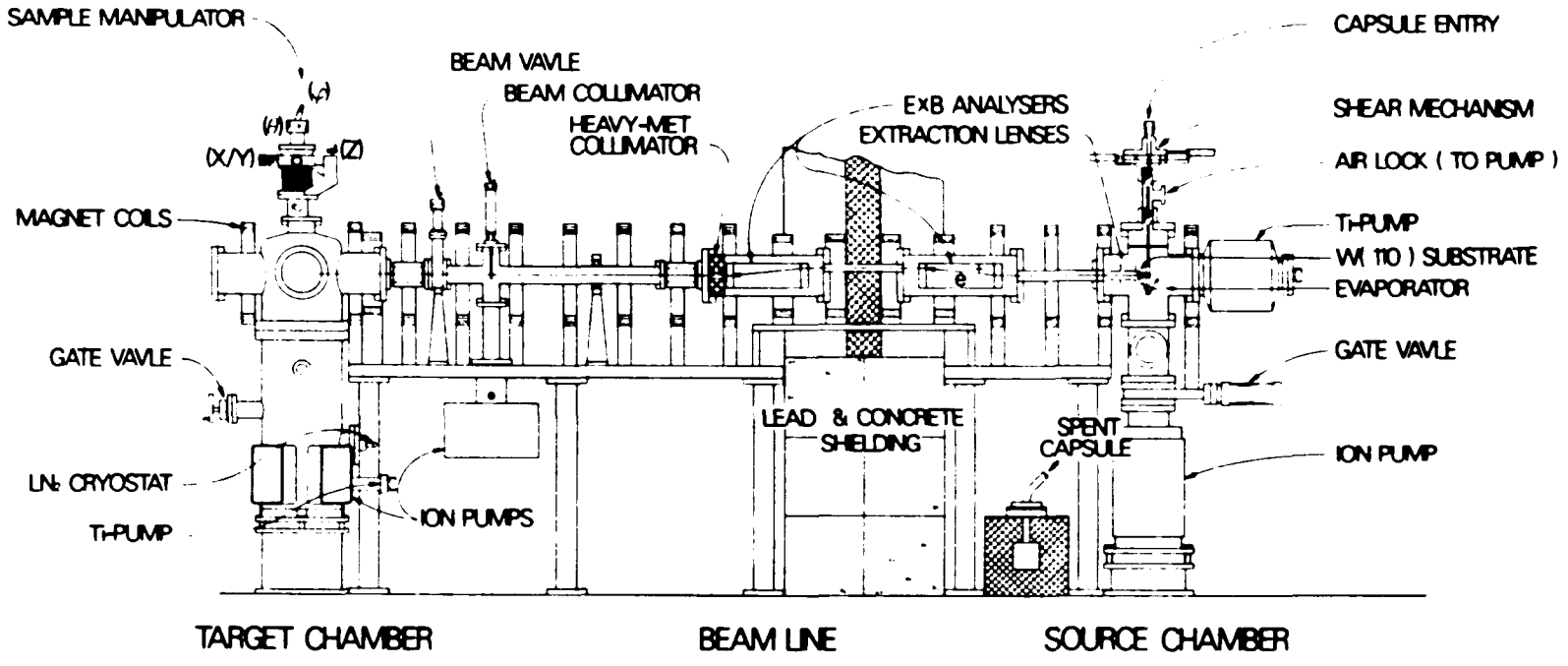

Figure 2.1. Side view of the 2D-ACAR experimental setup at HFBR of Brookhaven National Laboratory.

tially a slow positron intensity of $7\times10^7 cps$ can be obtained from this self-moderator. However the beam intensity decreases exponentially with a half-life of 12.8 hours, characterising the ^{64}Cu isotope. Consequently, the preparation of a fresh Cu film using a new ^{64}Cu source becomes one of the important routine steps of the experiment.

The emitted positrons are extracted away from the source by two serial electrical static lenses and filtered by a set of $\mathbf{E}\times\mathbf{B}$ energy analyzers. An axial **B** field is generated to guide the beam transportation. In order to obtained a better focusing effect the **B** field is increased adiabatically from 20 gauss at the source end to 80 gauss at the target end[60]. A linear accelerator was installed at the entrance of the surface chamber(Fig. 2.2), which accelerates the incident positrons to the desired energy and focus the beam on the target surface. At 200 eV the beam size is about 8 mm in diameter as displayed on a micro-channel-electron-multiplier-array(CEMA).

§ 2.2 Sample Surface Preparation

All the samples used for the present investigations were cut into discs of 1 mm thick, 6.35 mm in diameter and were polished to a mirror finish. X-ray Laue pictures were taken for each sample to ensure a good single crystal quality and an accuracy of selected crystalline orientations to 2°. As shown in the inset of Fig. 2.2, the sample was carefully mounted with hidden wires on a Ta-pedestal which was attached to the heater stage of a sample manipulator. The manipulator is capable of x,y,z translation, polar(θ) rotation as well as azimuthal(ϕ) rotation. This allows the sample to be located in various positions for sputtering, annealing with e^--gun, displaying LEED patterns, taking Auger spectrum and choosing the ACAR projection angle. The heater stage could heat the sample to a temperature up to $\sim 900^\circ$K. A type-K thermal couple was attached to the reverse side of the sample to monitor the sample temperature during annealing or high temperature runs. To avoid alloying a W-foil was inserted between the thermal-couple and the back of the sample.

A pressure in 10^{-10} Torr range could be obtained for the entire UHV system after roughing followed by about 48 hours baking at $\approx 150^\circ$C chamber temperature. This pressure was further

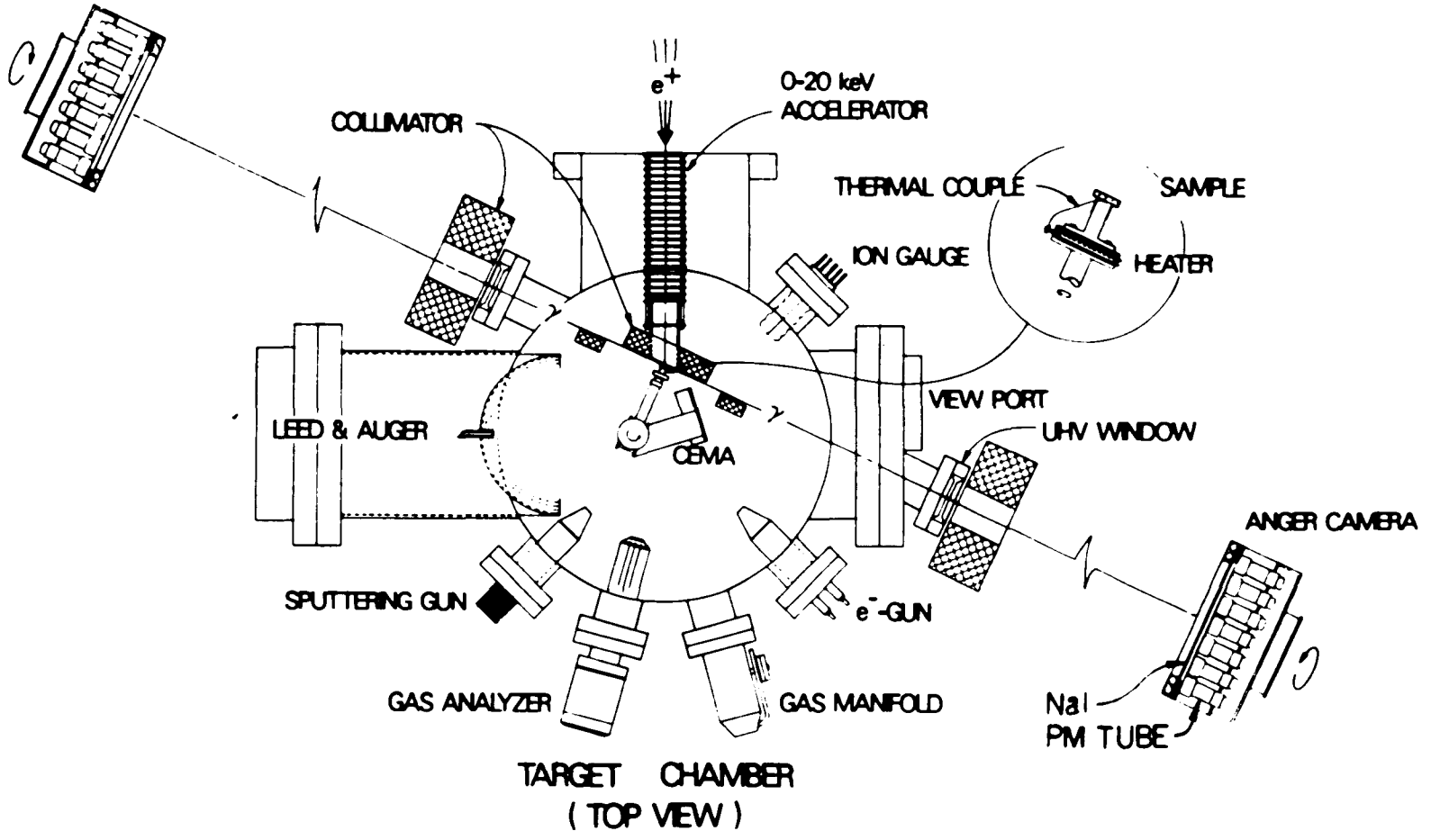

Figure 2.2. Top view of the target chamber and the Anger cameras. The blow up shows the sample holder.

improved and maintained through the constant operation of the ion-pumps and partially the Ti-sublimation pumps. The mass spectrometer was used to analyse the residual gas elements. Due to the special procedures of the e^+-source preparation the source chamber and the beam line pressures were usually an order of magnitude higher than that of target chamber. When preparing the sample surface, the beam valve was closed and the pressure in the target chamber could reach 7×10^{-11} Torr. During measurements, however, the target chamber pressure rose to $2\text{-}3\times10^{-10}$ Torr, due to the pressure in the beam line and sources chamber. Liquid nitrogen was circulated through a cryostat installed in the target chamber, which could reduce the pressure to $1\text{-}2\times10^{-10}$ Torr.

Further preparation of the specimen surfaces were conducted *in situ* (the UHV target chamber), *i.e.* , surface cleaning(sputtering and annealing), surface characterization and controlled gas exposure. When a sample was introduced into the target chamber it was first outgassed and sputtered with $\sim$ 1-2kV Ar^+ for 2-3 hours. During the sputtering the ion-pump portion of the chamber is isolated from the Ar gas and an external turbo-pump was used to keep a constant flow of the Ar gas inlet from a leak valve. The Ar flow was determined by the pressure difference between the chamber (1×10^{-4} Torr) and the turbo-pump (1×10^{-6} Torr). The incident angle of the Ar^+-beam was about 15° with respect to the sample surface. The ion-current received by the sample was typically 10-15 $\mu A/cm^2$ with 1kV, 25 mA emission current ion-beam in 1×10^{-4} Torr Ar gas. At the end of the sputtering, the chamber was first evacuated using the turbo pump to 1×10^{-7} Torr before the gate valve isolating the ion-pump was open again. The damage of the sample surface resulted from ion-bombardment was removed by annealing at some high temperature according to the sample material. It should be emphasized that thermalized and/or pre-thermalized positrons are inclined to be trapped with a very high probability in vacancies, voids, dislocations and some impurities[18,52]. It is, therefore, important to eliminate these possible effects which might be caused by the imperfection of the crystal structure at the surface as well as in the bulk. Thus each sample was subject to prolonged annealing(at least 12 hours) before measurements were performed. High temperature annealing(i.e. close to melting point) plus

slow cooling usually leads to a good bulk crystal ordering. However, it could also introduce surface roughness(e.g. facets). Therefore, we have chosen to use some moderate heating temperatures which will be given later. Below 900° K the annealing could be accomplished using the sample heater stage, while above this temperature the e^--gun was employed. Prior to each run the sample was retreated for one or more cycles of sputtering at lower energy(500– 750 eV) to reduce the damage, and annealed for shorter time (30 min.–1 hour).

The surface condition was monitored by the LEED and Auger spectroscopy. The coherent pattern of LEED is associated with long range interaction of the incident electron wave with a few top layer lattice planes and hence provides information about the crystallographic ordering of the crystal surface[58]. The characteristic Auger peaks on the other hand uniquely identify the species adsorbed at the surface[61,62]. For the present investigation the surface was considered to be clean when a correct LEED pattern of high quality(i.e. sharp and good contrast) was observed and impurity intensities detected by the Auger analyzer were below the noise level. In most of our work, we used a four grids retarding field Auger analyzer which has a noise-to-signal(main peak) ratio $N/S \approx 1/500$. For later experiments a double pass cylindrical analyzer was added into our system and hence much higher noise-to-signal ratio($>1/2000$) was obtained. The Auger spectra taken with the double pass cylindrical analyzer were also used to confirm the impurity levels estimated with the four grids retarding field Auger analyzer.

In principle, the evolution of a sample surface can be recorded. However, due to reasons given in next chapter, each surface run was followed by a bulk run and our sample position could not be disturbed in between. Thus the surface could be examined only after the bulk run and the accumulation of impurities during the surface run could only be estimated. To gain more control of the situation, the data were stored frequently during the measurement and were carefully compared afterwards. In addition, similar experimental conditions were simulated when positron beam was not in operation, and surface conditions were monitored after similar time durations. These findings will be incorporated in our data interpretations.

The above are the common procedures for preparing various surfaces. There are of course

differences among these surfaces. We will postpone the discussion of their chemical properties to Chapter 4 and 5, and only summarize below the technical aspects for those surfaces whose ACAR results are to be discussed later.

Clean Al Surfaces - Polished Al surfaces become oxidized rapidly in the ambient. The oxidized surfaces in turn protect the bulk Al from being further oxidized. During baking contamination of C increases significantly for large amount of CO and CO_2 are released from the chamber wall and W-filaments.† Most of the carbon could be removed after first hour sputtering, while complete removal of the oxide layers usually required an additional 1–2 hours sputtering. After the initial treatment, all three low index surfaces of Al could be cleaned routinely by 1 or 2 cycles of sputtering and annealing. Very sharp LEED pattern could be obtained with annealing temperature of $\sim$620° K. Prolong heating of the Al sample close to melting temperature ($\sim$ 870° K) also resulted in a fairly clean surface. However, after several hours heating the sample surface looks less shining, perhaps indicating the growth of facets in a microscopic scale[63]. Thus high temperature annealing was not favored. For our cleaned surface the remaining impurities were estimated to be less than 0.03% of C_{KLL} ($\sim$ 0.01ML) and 1% of O_{KLL} ($\sim$ 0.03ML)[62].

The difficulties arose from the re-contamination of the cleaned surface, especially, the oxidation. Common residual gas in our UHV chamber were found to be H($M/e=2$), methane($M/e=16$), H_2O($M/e=18$), N_2 or CO($M/e=28$) and CO_2 ($M/e=44$). Since the sticking coefficient of H_2 on Al is much smaller compared with rest of the gasses, H_2 contamination is ignored even though its partial pressure is highest ($\sim 4\times10^{-11}$ Torr). The other three gasses had similar partial pressure ($\sim 1\times10^{-11}$ Torr). It has been reported[64] that the oxidation rate of Al surfaces with H_2O is four times higher than with pure O_2. Thus residual H_2O in the system could be a serious problem and should not be acceptable for the study of Al surfaces. A prolong bake with uniform chamber temperature can reduce effectively the H_2O level. Indeed, our ACAR data show a high sensitivity to contaminations associated with different background pressures.

† This is true in general for most of surfaces.

Monolayer oxygen on Al(100) - The early stage of oxidation processes for the three low index Al surfaces were reported[65,66] to be different because of their different atomic configurations at the surface layers. For Al(100) and Al(110), due to the open structures oxygen atoms penetrate into sublayers and form Al-oxide islands at the very beginning of the O_2 exposures. For Al(111) on the other hand there exists two phases: a chemisorbed phase at lower coverage ($<$ 150L) and oxidation at higher exposure. Additionally, for clean surfaces the sticking probability of oxygen is highest on Al(110) and lowest on Al(100). Consequently, it is harder to keep Al(110) clean compared with other two faces during measurements, which is consistent with our experiences.

The monolayer oxygen on Al(100) was prepared by first cleaning the surface, and then checking it with LEED and Auger analyzer before exposing it to 2×10^{-7} Torr 99.999% pure oxygen for 12 minutes. This led to a total exposure of $\approx$ 150 L (1L $=1\times10^{-6}$ *Torr* ·sec), and corresponded to a coverage of $\sim$ 1 monolayer[65,66]. After the exposure we observed a uniform fading of the original LEED pattern of the clean surface and the Auger spectrum showed a reduction of the 68eV peak associated with clean Al and an increase of 51eV peak indicating the presence of oxygen on Al surfaces. These observations were in agreement with the results of Refs.[65-67].

Oxide layers on Al(111) - Two different exposures were studied. The thin layers oxide on Al(111) was the result of an exposure of $\approx 3\times10^4$ L. The LEED pattern was completely extinguished after the exposure. The sample was heated to 430 °K for 1 hour in an attempt to recrystalize the oxide layers[68]. However no sign of any LEED pattern was observed afterwards. In addition to the oxygen peak at $\sim$ 510eV, the Auger spectrum showed a larger Al peak at 51eV than 68eV.

The thick layer oxide were obtained from continuous O_2 exposure of the thin layer oxide sample to O_2. The total exposure was increased to 1×10^6 L which last about another 60 hours, and in between the oxygen gas was replaced three times. In this case the Auger spectrum displayed a vanishing clean Al_{KLL} signal, implying that the thickness of the oxide layer was $\approx$ 10 Å, the mean escaping depth of the 68eV Auger electrons[58,61].

Si(100)-(2×1) Surface - The Si(100) sample was cut from a silicon wafer with p-dopant and a resistivity of 15–30$ohm \cdot cm$. After heating at 1200° K the surface underwent a 2×1 reconstruction. Sharp LEED pattern was observed without ion-bombardment. The LEED pattern suggested that there were domains of 2×1 superlattice rotating 90° relative to each other. This typical result was found in many previous studies[69]. The impurities remained on the heated surface was mainly carbon which was reduced to ~1% of a monolayer by sputtering and annealing. It has been reported[70] that at base pressure better than 1×10^{-10} Torr common residual gasses do not stick on Si surfaces efficiently ($<10^{-4}$ monolyer/day) and a Si surface can stay clean for more than 24 hours. The Auger spectra and LEED pattern taken after some 36 hours ACAR experiment did demonstrate very little changes.

Si(111)-(7×7) - The Si(111) sample was cut from a detector-grad intrinsic silicon crystal. It is well established[69] that 7×7 reconstruction takes place as a result of the annealing at 1000° K or higher. In our case the first 7×7 LEED pattern emerged after 2 hour sputtering and annealing. The higher order spots were found to be sensitive to the contaminations. A clean and well reconstructed Si(111)7×7 surface could be reproduced by routine sputtering and annealing. At base pressure better than 1×10^{-10}Torr the 7×7 LEED pattern could exist for at least two days, although the higher order spots gradually became more diffusive.

H on Si(111)-(7×7) - The monolayer atomic hydrogen on Si(111) was obtained by first preparing a clean and ordered surface then exposing it to high purity hydrogen gas. During the exposure the sample was placed near a hot W-filament (≈2000° K) to dissociate the molecule hydrogen. This also resulted in an elevation of the sample temperature to ≈400° K. After 30 minutes exposure with 5×10^{-7} Torr hydrogen gas a saturated monolayer coverage was expected in accordance with Refs.[70-72]. The LEED pattern observed afterwards exhibited enhanced intensities of the 1/7 order spots as consistent with these references.

§ 2.3 Anger Camera Detection System

The two dimensional position sensitive detector system used in the present project was the Anger-camera-based system developed at University of East Anglia[69]. The schematic of the camera head is shown in Fig. 2.2. It consists of a large area thallium-activated sodium iodide crystal of 12.7mm thickness and 50.8cm in diameter and of a hexagonal close-packed array of 37 photomultiplier tubes of 70mm diameter optically coupled to a perspex light guide which in turn is coupled to the crystal assembly. For optimal performance the photon accepting area of the camera is stopped down to a $0.11m^2$ circular area by a thick lead collar of 37cm inner diameter. The detector head also contains the primary electronic circuitry which output position and energy signals for each γ-ray detected.

The principle of operation is an extension of common scintillation detectors. The number of photons collected by each tube, hence the pulse height of the tube output, is proportional to the distance of the tube from the position of the scintillation in the crystal. Thus the energy of the γ-ray as well as the position registered by the γ-ray can be extracted from some combination of the outputs from all tubes. This is accomplished by the primary electronic circuitry which includes the E,X,Y,Z and the threshold circuit boards. The energy(E) mixer board collects the direct output from all the photo-multipliers and provides an summed-output E_{tot} , the energy of the detected γ-ray. The X/Y mixer boards produce two orthogonal position signals for each scintillation by applying the photo-multiplier tube outputs to summing resistor networks. Each tube has an associated resistor in the summing network, the value of the resistor being chosen to give the attenuation proportional to the position of the tube with respect to a reference point in the crystal. The X/Y signals for each scintillation are the sum of all the tube output after passing through the resistor networks, respectively. Due to statistical fluctuations in the scintillator and photomultipliers, successive γ-ray of same energy striking the same point on the crystal do not necessarily produce the same amplitude signals. The outputs from the X/Y mixer circuits form a Gaussian distribution with consequent loss of resolution. To overcome this problem, ratio circuits are used. In these circuits a Z mixer output proportional to the total energy and having the same Gaussian

distribution as the X/Y mixer board outputs is generated and is used to divide the X/Y mixer board outputs. This yields constant amplitude pulses of X/Y signals regardless the fluctuation of the detector. In addition, a threshold circuit is designed to set a threshold below which output pulses from the tubes are not input to the X/Y mixer circuits. The function of this circuit is to remove low amplitude events which are due to multiple reflections in the crystal and which would cause errors in the mixer output position signals.

The external electronic circuit and the data acquisition devices are shown in block diagram of Fig. 2.3. The X_1/Y_1 and X_2/Y_2 outputs from the two Anger cameras are carefully calibrated via linear amplification and offset and combined in the Mixer to give the position difference signals: $\Delta X = X_1 - X_2$ and $\Delta Y = Y_1 - Y_2$. These signals are then sent to two analog-to-digital converters(ADC). Meanwhile, the energy outputs from the detector heads are gated in the pulse height analyzers(PHA) with a $\sim$ 20% window set at the 511keV photopeak for the γ-pair created from the positron(or positronium) annihilation. Hence the background radiation and events arising from large angle scattering before entering the crystal are rejected. The accepted signals are transferred to a coincident circuit which generates a triggering signal when two input signals arrive coincidently from each of the energy channels associated with the same annihilation event. This triggering signal finally enables the ADCs to analyze the position difference signals, and the results are transmitted through the CAMAC Dataway to the PDP11 computer. Events that are valid in respect to both the timing and energy requirements are received and stored in the computer. Other usual computer peripherals provide for overall control, data displaying and transformation.

The performance of these detectors such as their uniformity of response, resolution and linearity highly depends on the final tuning, even though it is strictly limited by the detectors intrinsic properties. A theoretical discussion of this subject has been given by West *et al.* [73]. The tuning is pretty much empirical and in general it involves the following steps(not necessarily in that sequence):

1). constant gain adjustment for individual photomultiplier tube;

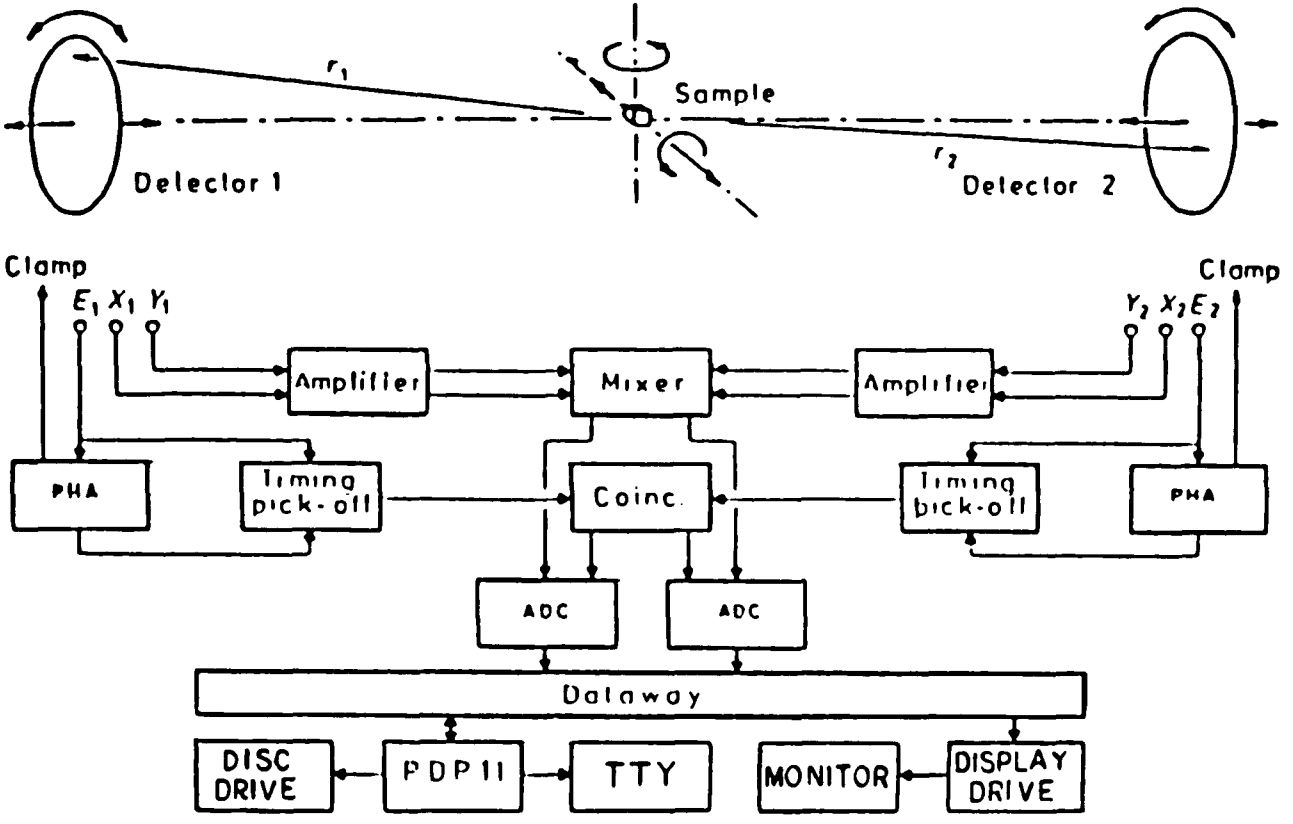

Figure 2.3. Block diagram of the 2D-ACAR data acquisition system.

2). mixer boards adjustment;

3). summing resistors adjustment for best linearity;

4). alignment of two camera's axes;

5). matching two camera's calibration;

6). timing adjustment for optimal counting rate;

7). overall resolution measurement;

8). coincident field calibration;

9). measurement of the sampling function.

More detailed explanations of these procedures can be found in Ref.[69]. Here we only summarize some of the important specifications of the present detector system:

Single camera detection area:	0.11 m^2
Single camera detection efficiency:	$\sim$ 17%
Overall spatial resolution:†	10.86 *mm*
Background coincident rate:†	$\sim$ 0 cps
ADCs gain:	128
Data array dimensions:	128$\times$128
Camera-to-sample distance:	11.14 *meters*

† in coincidence field

Chapter 3. Data Analysis

It is shown in the first chapter that surface 2D-ACAR measurement in general contains three contributions(Eq. 1.19): bulk annihilation, surface state annihilation, and annihilation of para-Ps formed at the surface. This implies that the usefulness of this technique relies very much on the possibility of separating the individual components. In this chapter we show that using the underlying symmetries of these contributions, and the well studied positron implantation and diffusion process in bulk material, the measured spectra can indeed be decomposed. In section two we discuss the detailed analysis procedures, and in section three we show the results of a simulation test of this analysis scheme. The error estimation is briefly discussed in the final section.

§ 3.1 The Analysis Scheme

3.1.1 Inversion Symmetry of Momentum Densities - We now show from time reversal symmetry[74] that the momentum density functions of the positron surface state annihilation and bulk annihilation possess inversion symmetry with respect to the momentum **p**. That is

$$\rho_{s.s.}(\mathbf{p}) = \rho_{s.s.}(-\mathbf{p}), \tag{3.1}$$

$$\rho_{bulk}(\mathbf{p}) = \rho_{bulk}(-\mathbf{p}). \tag{3.2}$$

In contrast,

$$\rho_{P_s}(\mathbf{p}) = 0 \quad \text{for } p_\perp > 0, \tag{3.3}$$

because the Ps atoms are emitted into vacuum.

A more general form than the independent particle approximation(Eq. 1.20) of the momentum distribution for the annihilation of a positron in a many electrons system is[3,5]

$$\rho^{2\gamma}(\mathbf{p}) = const \cdot \int d\tau \, | \int d\mathbf{r} e^{-i\mathbf{p}\cdot\mathbf{r}} \psi(\mathbf{r},\mathbf{r},\tau) \, |^2, \tag{3.4}$$

where $\psi(\mathbf{r}_+,\mathbf{r}_1,\tau)$ is the one-positron- many-electron initial state properly antisymmetric in all electron coordinates, $\mathbf{r}_+$, $\mathbf{r}_1$ are the coordinates of the positron and an electron, respectively, and τ stands for the remaining electrons coordinates $\{\mathbf{r}_2, \mathbf{r}_3, \ldots, \mathbf{r}_n\}$. It is obvious that apart from a constant phase factor $\psi(\mathbf{r}_+, \mathbf{r}_1, \tau)$ being real is *sufficient* to generate the inversion symmetry of

$\rho^{2\gamma}(\mathbf{p})$ with respect to $\mathbf{p}$.

The realness of a solution $\Psi(\mathbf{x},t)$ to a Schrodinger equation is closely related to the time reversibility of the quantum system. It is well established in quantum mechanics that a closed or isolated system is invariant under time reversal transformation. For a system in which spin can be neglected, time reversal symmetry requires that

$$\Psi_{rev}(\mathbf{x},t) = \Psi^*(\mathbf{x},-t), \tag{3.5}$$

is the solution of the time reversal transform of the Schrodinger equation. Therefore, for a stationary and nondegenerate state this implies

$$\Psi_{rev}(\mathbf{x}) = \Psi^*(\mathbf{x}) = C\,\Psi(\mathbf{x}), \tag{3.6}$$

where C is the constant phase factor. Thus the eigenstate of a bound stationary quantum system is a real function apart from the factor C.

In the absence of the spin-orbit coupling, these statements are still true for a many-body system, even though their spins can not be neglected for other considerations. For our one-positron-many-electron system, the interaction leading to the annihilation is dominated by the Coulomb interaction, the spin-orbit interaction can be neglected, and the effects of the spins are taken into account for the selection rules and for the exclusion principle. Consequently, time reversal symmetry leads to the inversion symmetry of the momentum density functions as stated in Eq.(3.1) and Eq.(3.2).

In general, however, for a system containing particles of spin 1/2, the consequence of time reversal transformation depends on the number of the spins under consideration, which is known as the Kramers theorem. For even numbers of spins 1/2, the system has at least one basis whose eigenvectors are all real, while for odd number of spins 1/2, the system is at least twofold degenerate, its degeneracy is necessarily of even order, and the orthonormal basis is made up of pairs of complex-conjugate vectors. This Kramers degeneracy can be removed by the introduction of an external magnetic field. The effects of the Kramers degeneracy on Eq.(3.1) and Eq.(3.2) need to be investigated further. It is noted, of course, that $\psi(\mathbf{r}_+,\mathbf{r}_1,\tau)$ being real(apart from a constant phase factor) is a *sufficient* but not *necessary* condition for Eq.(3.1) and Eq.(3.2).

3.1.2 The Analysis Scheme - Eq. (3.1)-(3.3) are the basic underlying symmetries that are of great importance to the data analysis scheme to be constructed below. 2D-ACAR measures the projection of momentum density function in a given direction:*

$$N(\vec{p}) = \int R(\vec{p} - \vec{p}')\rho(\mathbf{p}')d\mathbf{p}' , \tag{3.7}$$

where $\vec{p}$ is the projection of $\mathbf{p}$ on the plane containing $p_\parallel$ and $p_\perp$ axes(see Fig. 1.4), and $R(\vec{p}-\vec{p}')$ is the two dimensional detector's resolution function. Since the nonlinealities of the cameras can be adjusted to be sufficiently small[73], the resolution function can be regarded as homogeneous, *i.e.*, $R(\vec{p} - \vec{p}') = R(|\vec{p} - \vec{p}'|)$. Consequently, the inversion symmetry of $\rho(\mathbf{p})$ propagates via the homogeneous kernel into $N(\vec{p})$, except it is integrated over $p_\parallel'$. It is then followed from Eq.(3.1)-(3.2) and (3.7) that:

$$N_{s.s.}(\vec{p}) = N_{s.s.}(-\vec{p}), \tag{3.8}$$

$$N_{bulk}(\vec{p}) = N_{bulk}(-\vec{p}). \tag{3.9}$$

However, because of the smearing introduced by the finite detector resolution

$$N_{Ps}(\vec{p}) \neq 0 \quad \text{for } 0 \leq p_\perp \leq \epsilon, \tag{3.10}$$

where ϵ is on the order of the FWHM (full-width-at-half-maximum) of the overall detector resolution function. Only in an ideal situation has the resolution function become a δ-function and $\epsilon \to 0$. In this limit,

$$N_{tot}(\vec{p}) = \begin{cases} N_{s.s.}(\vec{p}) + N_{bulk}(\vec{p}) + N_{Ps}(\vec{p}) & p_\perp \leq 0 \\ N_{s.s.}(\vec{p}) + N_{bulk}(\vec{p}) & p_\perp > 0 \end{cases}; \tag{3.11}$$

thus

$$N_{Ps}(\vec{p}) = \begin{cases} N_{tot}(\vec{p}) - N_{tot}(-\vec{p}) & p_\perp \leq 0 \\ 0 & p_\perp > 0 \end{cases}. \tag{3.12}$$

The Ps component of a measured 2D-ACAR spectrum is therefore extracted from a simple 'inversion- subtraction', a name we will refer to the operation of Eq.(3.12) henceforth.

However, for finite detector resolution, $\epsilon \neq 0$, the direct inversion-subtraction of the measured spectrum leads to some inevitable distortions to the true spectra in the region $-\epsilon \leq p_\perp \leq \epsilon$. It

* This is an extension of Eq.(1.18), where we assumed a perfect detector resolution.

leaves some extra counts in $N_{s.s.}(\vec{p})$ and over subtracts $N_{Ps}(\vec{p})$. Nevertheless, outside this small region($\sim\pm$ 1.5 mrad) the extracted spectra are still accurate. In principle the distortion can be eliminated by employing some deconvolution technique[75] prior to the inversion-subtraction. Therefore we can separate the directly measured spectrum into a Ps component and a symmetrical(inversion symmetry) component.

The symmetrical part of the spectrum is the sum of the surface state annihilation and the bulk annihilation. We have shown in §1.2.1 that the relative contributions of these two components are determined by the incident beam energy, which is controllable. At low incident energy ($E < 100\ eV$) the bulk annihilation is negligible, while at high energy ($E > 15\ keV$) the annihilations occur mostly in the bulk. Thus it appears that separation of the bulk component can be avoided if one use a sufficiently low incident energy for the measurement. Unfortunately, at low incident energy ($E < 100eV$) the fraction of the nonthermal positrons returning to the incident surface can be significant, and it will contaminate our measurement of the Ps momentum distribution. Therefore in all our surface measurements, we have selected $E=200eV$ for Si samples, and $E=1.5keV$ for Al. In the latter case the bulk contribution can not be ignored(see § 1.2.1). However, using the diffusion equation one can determine the relative bulk fraction. Consequently, $N_{s.s.}$ can be extracted by subtracting a properly normalized high energy run from a low energy run(also see §3.2.6).

In the above scheme the price one pays in order to obtain the para-Ps annihilation spectrum is that the information of surface state annihilation and the bulk annihilation can be extracted from only half of the measured spectrum, *i.e.*, $N_{tot}(\vec{p})$ for $p_\perp \geq 0$, and the other half provides the Ps spectrum.

§ 3.2 Analysis Procedures

To implement the above scheme the following steps are taken sequentially:

1). Apply the camera sampling function to the raw spectrum;

2). Determine the position of $\vec{p} = 0$ and center the spectrum;

3). Symmetrize the spectrum (when allowed);

4). Deconvolute the spectrum;

5). Perform the inversion-subtraction;

6). Convolute the separated spectra;

7). Remove the bulk component(when necessary).

We now give more detailed explanation and justification below.

3.2.1 The Momentum Sampling Function - A rigorous discussion of this subject has been given by West *et al*.[73]. It is shown that in a particular case in which the camera adjustments are assumed to be exceedingly successful and the linearity is hence perfect, the recorded 2D-ACAR spectrum of a delta momentum density $\delta(\mathbf{p}'' - \mathbf{p}')$ takes the simple form

$$N_\delta(\vec{p}'',\vec{p}') = M(\vec{p}')R(|\vec{p}''-\vec{p}'|), \tag{3.13}$$

where

$$M(\vec{p}') = \int \epsilon_1(\vec{p}' + \frac{\vec{p}''}{2})\,\epsilon_2(\vec{p}' - \frac{\vec{p}''}{2})\,d\vec{p}'', \tag{3.14}$$

is the momentum sampling function, ϵ_i is the efficiency function of camera i ($i = 1,2$) and the integral is taken over all space.

The recorded spectrum of a general momentum density is, therefore, the convolution of $\rho(\mathbf{p}')$ with $N_\delta(\vec{p}'',\vec{p}')$. Thus Eq.(3.7) implies implicitly that the measured spectrum has already been divided by $M(\vec{p}')$.

The momentum sampling function $M(\vec{p}')$ corrects for the deviation of the detection efficiencies across the camera areas, and more importantly for the variation of coincidence field efficiency for different angular correlated γ-pairs associated with momentum $\vec{p}'$. Thus for perfectly uniform cameras(ϵ_i constant), the integral of Eq.(3.14) equals the overlapped area of two circles of the cameras radius P_0 on centers displaced by $\vec{p}''$, namely

$$M(\vec{p}') = M(|\vec{p}''|) = \frac{2M(0)}{\pi}[\cos^{-1}\xi - \xi(1-\xi^2)^{\frac{1}{2}}], \tag{3.15}$$

where $\xi = p''/2P_0$. Eq.(3.15) approximates to a right circular cone of base diameter $4P_0$. The deviation of the general $M(\vec{p}')$ from this ideal form is small as will be seen in Fig. 3.2b.

A true single camera efficiency $\epsilon_i(\vec{p})$ can be measured by illuminating the cameras with an Al-^{22}Na-Al sandwich source placed in the specimen position. To discriminate the background the signals being collected for camera 1 are gated by the coincident events detected by camera 2, which is set closer to the source to ensure larger subtending solid angle, and is rotated to a few different angles with respect to camera 1 during the measurement to reduce the coupling between the two cameras local efficiencies. Similar measurement is also performed for camera 2. The momentum sampling function is then obtained from overlapping the two measured camera efficiency functions(see Eq.3.14).

Figure 3.1a shows a measured efficiency spectrum along the $p_\parallel$ axis(i.e. $p_\perp$=0) and the solid curve is the averaged efficiency. Although the deviation of the data points from the straight line is within the statistical error bars, it shows that the left hand side is better tuned than the right hand side. A cut of the generated momentum sampling function at $p_\perp$=0 is shown in Fig. 3.1b. The solid curve represents the ideal expression of Eq.(3.15). The difference between the two is evidently small. Figure 3.1c is a contour plot of the generated momentum sampling function. It is fairly isotropic as suggested by Eq.(3.15). To demonstrate the effect of the momentum sampling function Fig. 3.2 shows cuts at $p_\parallel$=0 of the corrected(solid) and the uncorrected(dashed) bulk Al spectra. The corrected spectrum was obtained from dividing the uncorrected spectrum by a peak-normalized $M(\vec{p})$ shown in Fig. 3.1c.

3.2.2 Centering - Obviously, finding the origin of $\vec{p} = 0$ is crucial for the symmetrizing of step 3 and for performing the inversion-subtraction of step 4. In general, when the annihilation source is placed at the mid point of the axis joining the centers of two detectors, $\vec{p} = 0$ coincides with the origin of the detectors coincidence field coordinate system. A small shift of the source from the center point results twice the shift of the position of $\vec{p} = 0$ from the origin of the coincidence field. A physical alignment to a very high accuracy is usually not trivial given various constraints one has.

For the present study we take the advantage of the reflection symmetry of long slit spectra generated from measured 2D spectra:

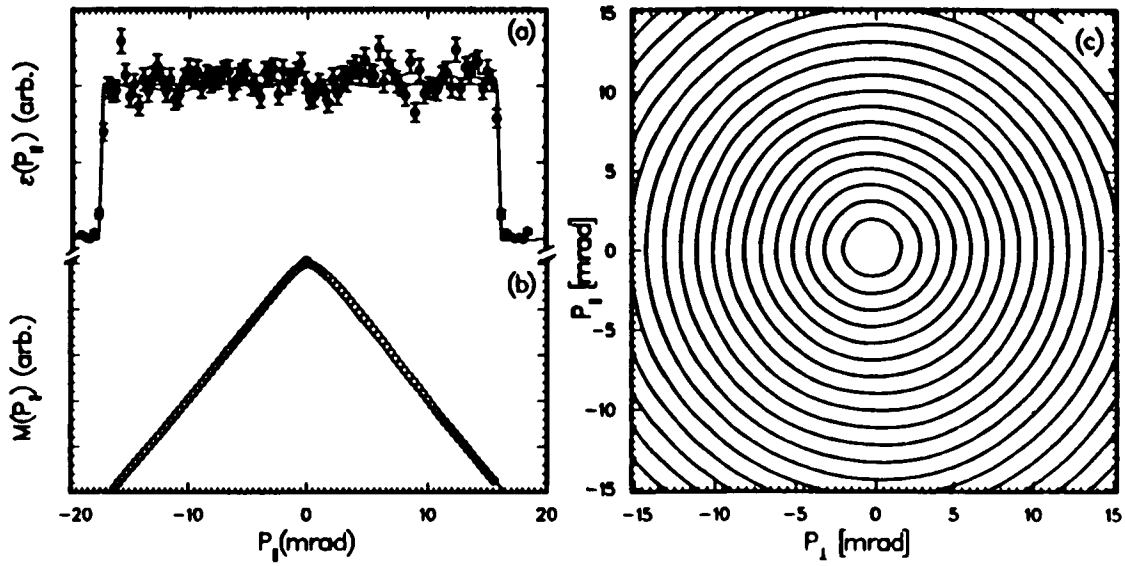

Figure 3.1. (a). Single camera efficiency function($\approx 100 counts/channel$) at $p_\perp=0$, the camera's radius is from the zero to the cut-off , the averaged constant efficiency is plotted in solid curve; (b). A cut at $p_\perp=0$ of the momentum sampling function generated from two single camera efficiency functions, only the upper half spectrum is shown, the solid curve is the ideal expression of Eq.(3.15) with the camera radius extracted from (a); (c). A contour plot of the momentum sampling function with constant contour step, the center corresponds to the peak in (b).

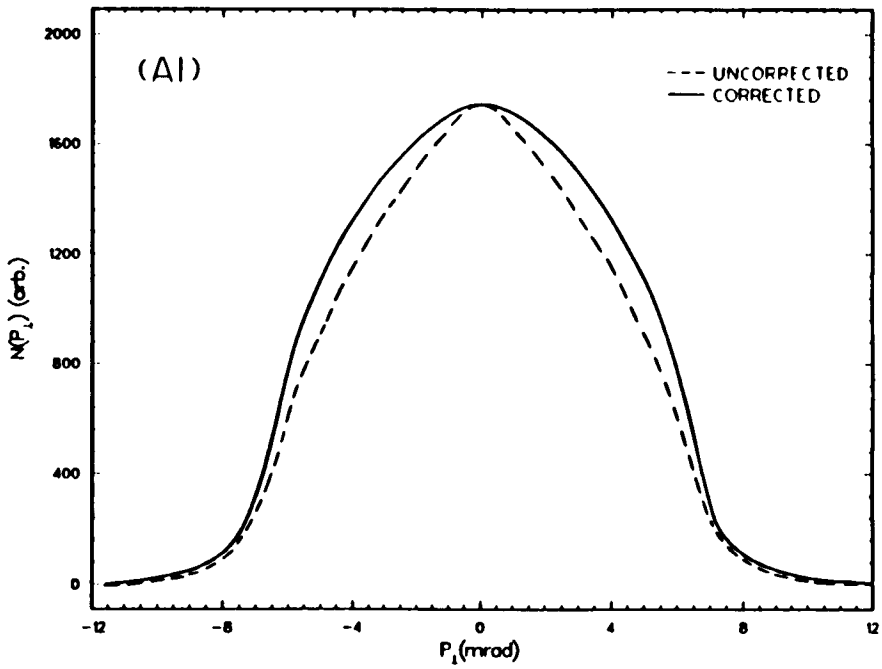

Figure 3.2. Sections at $p_\parallel=0$ of bulk Al 2D-ACAR spectra: the dashed curve is a raw spectrum; the solid curve is obtained from dividing the raw spectrum by the momentum sampling function(Fig. 3.1c) which is peak-normalized to one.

$$N(p_\parallel) = \int N(\vec{p})\, dp_\perp, \tag{3.16}$$

or

$$N(p_\perp) = \int N(\vec{p})\, dp_\parallel. \tag{3.17}$$

The reflection symmetry of $N(p_\parallel)$ and $N(p_\perp)$ exists in most of the bulk spectra. However for surface 2D-ACAR spectra only the integration over the perpendicular direction (Eq.3.16) might possess reflection symmetry. Thus in our measurements each surface run was followed by a bulk run without altering the sample position in between. The surface run then provides the position of $p_\parallel$=0, while the bulk run provides that of $p_\perp$=0.

Figure 3.3 illustrates a least-square fitting method that we used to extract these positions. The long slit spectrum is folded about a few selected centers(full or half channels); the χ^2(open square in Fig. 3.3a), defined as

$$\chi^2 = \frac{1}{n-1} \sum_{i=1}^{n} \frac{(N_i - N_i^{fold})^2}{N_i}, \tag{3.18}$$

($n <$ *center channel*) is computed for each selected center; a parabolic curve is then fitted to these χ^2-points using least-square method; finally the 'real center' is assigned to be the bottom of the fitted parabolic curve. Figure 3.3b offers a visual inspection* of the 'goodness of the fit' for a bulk Al data. The circles are the folded points of the right hand side data about the extracted center. As we can observe this method is rather successful. It is accurate to $<10\%$ of a channel(or $<$ 0.04mrad). However, the disadvantage is the lack of immediate examination of the sample contaminations accumulated during the run, because of the following bulk measurement, which also leads to some additional cost of run time and other expenses.

Because the spectrum is stored in a finite two dimensional array(128$\times$128), some interpolation scheme is needed to perform the point-by-point inversion- subtraction as the center point $\vec{p} = 0$ does not necessarily fall in either a full channel or a half channel. Furthermore, a deconvoluted spectrum is usually more noisy. It is, therefore, necessary to center the spectrum with respect to the two dimensional mesh before the deconvolution. In all the analysis we used a para-

* Note that a real χ^2 for the assigned center can not be obtained without interpolation.

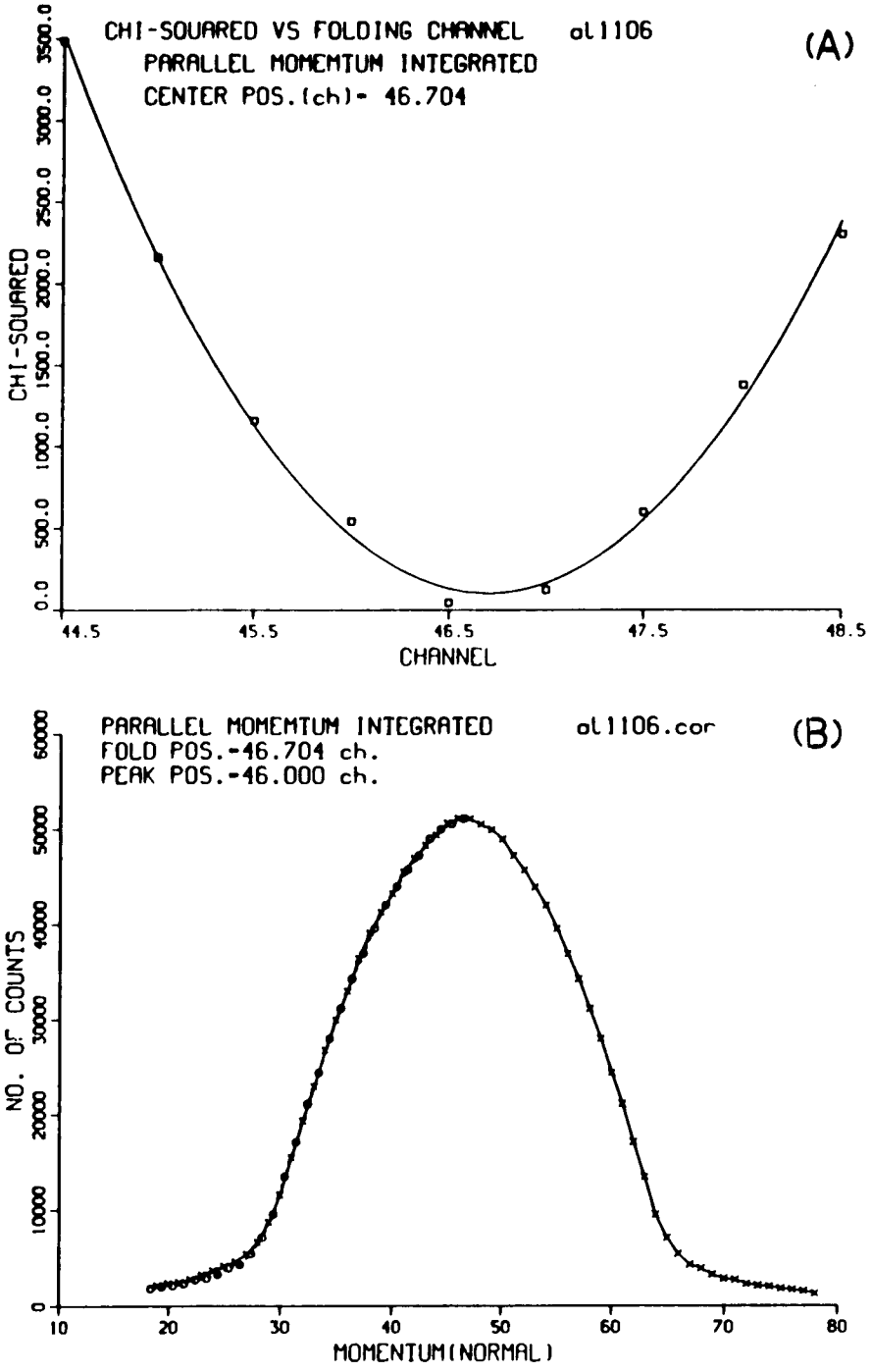

Figure 3.3. (a). χ^2 vs folding channel and the fitted parabolic curve(solid), see text for explanation; (b). Comparison of folded and unfolded long slit curve of bulk Al, the folding center is extracted from the minimum of the fitted parabolic curve in (a).

bolic interpolation within the nearest 3×3 sub-mesh. Figure 3.4 shows the sections through $p_\perp$=0 of a Si(100)-(2×1) 2D-ACAR spectrum before and after the interpolation. We choose to display this spectrum because it has an intense peak and hence is more sensitive to the possible smoothing due to the interpolation. The difference between the centered spectrum and the original one is negligibly small. Thus the interpolation does not cause significant damage to the original spectrum.

3.2.3 Symmetrizing - Although the symmetry of an ACAR spectrum is reduced due to the asymmetric Ps component, in many cases the system under study possesses a mirror plane parallel to the $p_\parallel'$ $p_\perp$ plane, thus the associated ACAR spectrum has a reflection symmetry with respect to the $p_\perp$ axis. In this case we can perform a two-fold symmetrization of the measured spectrum to reduce the relative error by a factor of $\sqrt{2}$. The two-fold symmetrized spectrum becomes†

$$N'(p_\parallel, p_\perp) = \frac{1}{2}[\, N(p_\parallel, p_\perp) + N(-p_\parallel, p_\perp)\,]. \tag{3.19}$$

Rigorously speaking, the operation of Eq.(3.19) is legitimate only if (*i*). the detectors have perfect linearity and uniformity; (*ii*). the crystal axis is perfectly aligned with the detectors axis; (*iii*). the position of the zero $|\vec{p}|$ is known exactly; and (*iv*). the crystal surface maintains the same symmetry as the bulk termination. In reality, these conditions can only be optimized and the symmetrized results should be inspected with caution, especially for data of low statistics.

In addition to the fine adjustment of the cameras and the overall geometry, we have used a χ^2 test in performing the symmetrization. The position of $p_\parallel$=0 of the spectrum and its small angle deviation with respect to the camera axes are fine tuned to minimize the antisymmetry:

$$\Delta N(p_\parallel, p_\perp) = N(p_\parallel, p_\perp) - N(-p_\parallel, p_\perp)\,, \tag{3.20}$$

or to optimize the χ^2, defined similarly to Eq.(3.18). Fig. 3.5 shows a resultant antisymmetric distribution summed over the significant region(from $p_\parallel$=0 to $p_\parallel$=10 mrad) of an Al surface spectrum with a total counts of $\sim 4\times10^5$. The χ^2 per degrees of freedom is 0.97, indicating the difference is well within statistical fluctuation as can be seen in the distributions of Fig. 3.5. We

† Henceforth unless specified a symmetrized spectrum is understood to be two fold in accordance with Eq.(3.19).

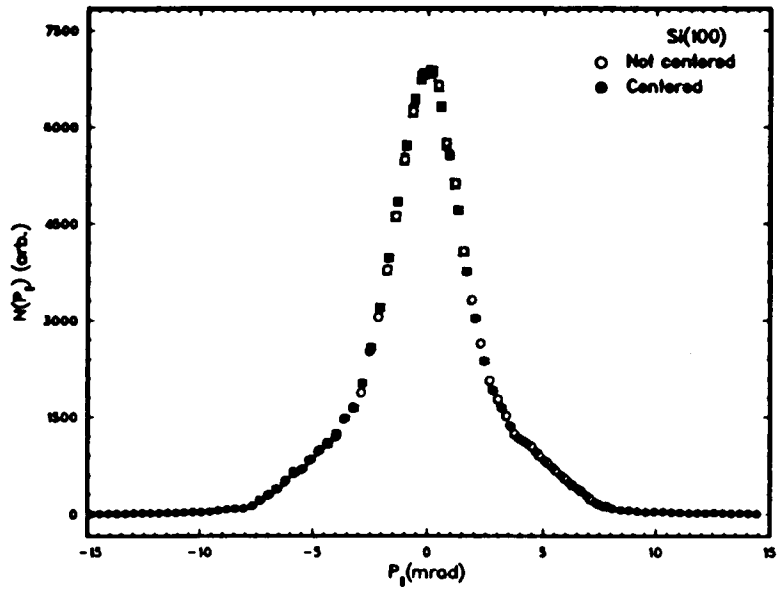

Figure 3.4. Sections at $p_\perp$=0 of a Si(100)-(2×1) spectrum taken with $200eV$ incident positron energy. Spectrum corrected with the momentum sampling function is drawn with open circles and filled circles represent the corrected spectrum being centered via parabolic interpolations.

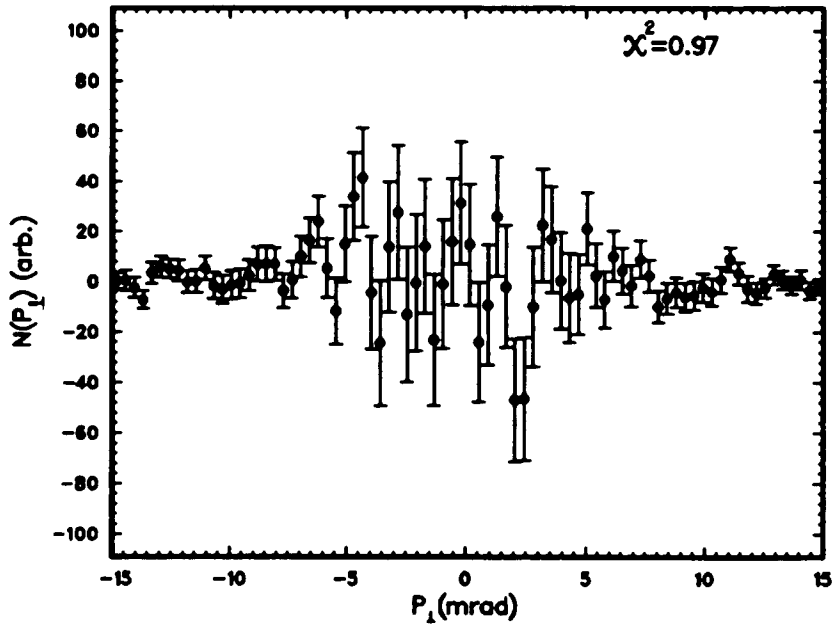

Figure 3.5. Antisymmetrical distribution(Eq.3.20) summed from $p_\parallel$=0 to $p_\parallel$=10mrad for an Al(100) surface ACAR spectrum. The χ^2 shown is defined by Eq.(3.18).

will inspect some symmetrized results in next section when we demonstrate the simulation test of our analysis scheme. Note that to optimize the conditions for symmetrization we automatically search for the best position for $p_{\parallel}=0$ and therefore it is closely related with the centering of step 2.

3.2.4 Resolution Function - A typical approximation of an Anger camera's resolution function is a Gaussian function. In Ref.[73] it is shown that when both cameras are proerly tuned, the overall resolution function in the coincidence field is approximated as a Gaussian as well, i.e.

$$R(\vec{p}-\vec{p}\,') \propto exp[-(\vec{p}-\vec{p}\,')^2/2\sigma_p^2]. \tag{3.21}$$

As an example in Fig. 3.6 we compare the normal section(dots) through the center of a measured resolution function for the present Anger cameras with that of a Gaussian function(dashed curve) whose width is the same as the measured one. The camera's resolution spectrum was measured with an Al-^{22}Na-Al source and setting the cameras closer than one meter. In this distance FWHM of the Al ACAR spectrum ($\sim$ 10mrad) corresponds to 5 mm spatial width, which is about half of the measured width.† We see that the agreement is excellent in the statistically significant region(-10mm to 10mm). In a real measurement the finite beam size or the sample size, which ever smaller, will worsen the resolution in the direction parallel to the surface. Consequently, the total resolution is the convolution of a square function, representing the sample or beam size, with the cameras resolution function. The results for our setup is shown with a dot-chained curve. With a sample diameter of 6.35mm the width is broadened by 30%. Since the Gaussian resolution function is completely uncoupled between the two orthogonal directions, we should see that the exact form of the resolution function in the parallel direction is not as important for the data separation.

3.2.5 Deconvolution - There are many well established and sophisticated deconvolution techniques available[75]. However the purpose of the deconvolution here is to perform a more accurate data separation. Thus the van Cittert's method is quoted for many of its merits[76],

† Ideally, we would like to have a δ-source, e.g., a quartz-^{22}Na-quartz sample.

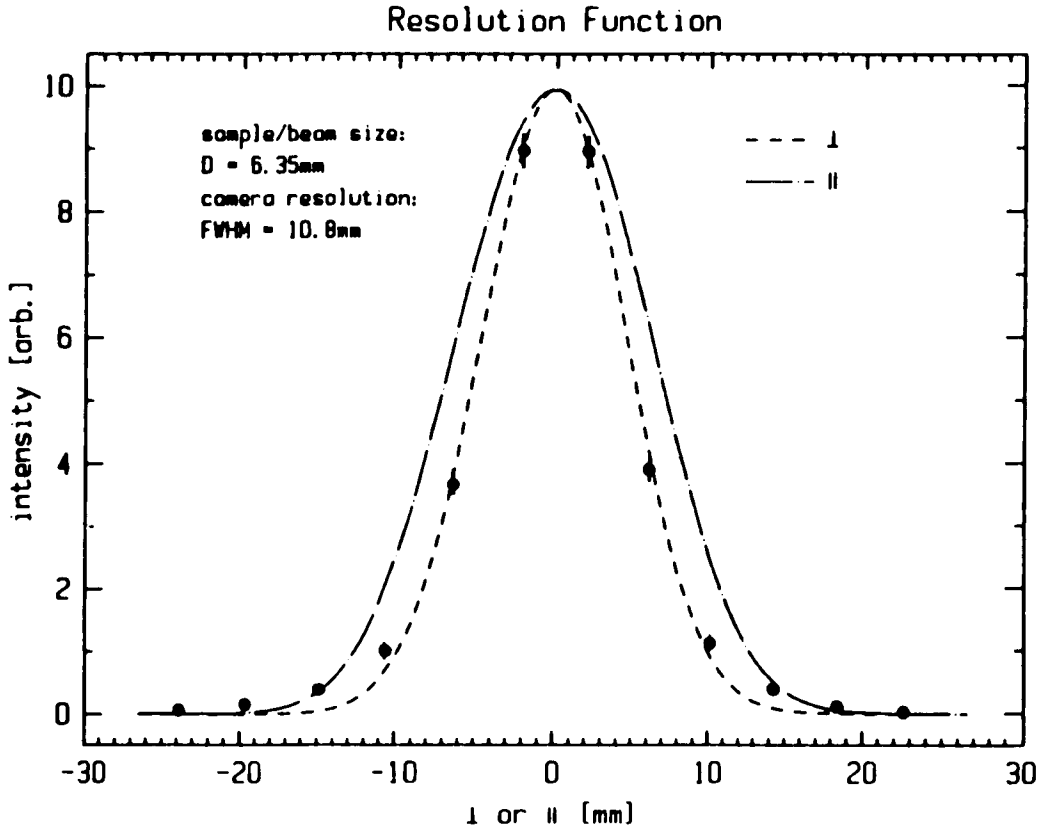

Figure 3.6. The solid dots are the measured coincidence field resolution function along $p_\perp$ axis, the dashed curve is a Gaussian function of the same FWHM as the measured one, the chain-dotted curve is obtained from convolving the Gaussian function(dashed curve) with a sample size square function, hence represents the overall resolution along $p_\parallel$ axis.

which will become more transparent as we proceed.

In this method the data are convolved with the resolution function, broadening further. The point-by-point differences between the original data and the broadened data are then added to the original data to construct the first-order solution. This is in turn convolved with the resolution, compared with the original data and the resulting correction applied to the first-order solution to obtain the second-order solution, *etc.* . This procedure may be expressed by

$$\Delta_i = N_0 - \int N_{i-1}(\vec{p}\,')R(\vec{p} - \vec{p}\,')d\vec{p}\,' , \tag{3.22}$$

$$N_i = N_{i-1} + \Delta_i , \tag{3.23}$$

where Δ_i and N_i are the i th order correction and solution, respectively. Obviously, it is easy to construct a computer algorithm for carrying out these iteration procedures. The Fourier transform of the above yields

$$\hat{N}_i = \hat{N}_0 + (1-\hat{R})\hat{N}_{i-1}, \tag{3.24}$$

where $\hat{N}_i$ is the Fourier transform of N_i *etc.* , and after n iteration it leads to

$$\hat{N}_n = \hat{N}_0\left[\frac{1-(1-\hat{R})^{n+1}}{\hat{R}}\right], \tag{3.25}$$

which provides the relationship between van Cittert's method and Fourier transform deconvolution. The numerator in the bracket is a modification to the inversed-filter function $\hat{R}$. For large n it approaches unity, provided $\hat{R}$ is not to small, and Eq.(3.25) becomes the direct Fourier transform of Eq.(3.7) the process converges to the desired answer because the correction make the convolute of the solution approach the data. On the other hand, however, for $\hat{R} \ll 1$ the bracket approaches $(n+1)$,i.e. the high frequency content of N_0 is simply amplified by $(n+1)$. This can also be seen directly from Eq.(3.22) -(3.23) because high frequency components in the intermediate solution are smoothed out in the convolution step, so that the noise in the data is added to the solution at each iteration. After sufficient number of iterations the correction of Eq.(3.22) contains essentially the noise component of the data. This immediately leads to the following interesting result:

$$N_e = N_0 - \Delta_{n+1} \tag{3.26}$$

$$= \int N_n(\vec{p})R(\vec{p}-\vec{p}\,')dp\,' , \tag{3.27}$$

i.e., when the n th order solution is convoluted back with the resolution function we obtain a smoothed version of the *original* data because the noise Δ_{n+1} has been removed. This particular feature is attractive to us since we plan to convolve the separated data later on. In addition, owing to the Gaussian resolution function and the linear operation of the van Cittert's method, the deconvolution could be restricted, if one wishes, to the perpendicular direction in order to meet our demands.

To illustrate the above discussion figure 3.7a compares an original Si(100) data cut at $p_{\parallel}$ with the smoothed one(dashed) according to Eq.(3.26)-(3.27) and using $n=5$. The two curves almost coincide with each other. This suggests that after convolution the separated data will be essentially the same as the real spectra being measured separately except in the region near $p_{\perp}=0$ in which some uncertainty may still remain even though the deconvolution has been applied. Figure 3.7b shows the same section of the Si(100) spectra deconvoluted with various numbers of van Cittert iterations. After five iterations the peak containing Ps does not increase and only the small oscillations are enhanced. Thus number of iterations used in our analysis did not exceed five.

3.2.6 Data Separation - The first step of the data separation is to apply the inversion subtraction of Eq.(3.12) to the deconvoluted spectrum and subsequently convolve the separated spectra. Figure 3.8 shows the perspective view of an original Si(100)-(2×1) spectrum(a) measured with 200 eV incident positron energy, the separated Ps spectrum (b), and surface state spectrum (c) in which the bulk annihilation is negligible.

The fraction of positronium emission can be readily calculated from the ratio:

$$\eta = \frac{V_{Ps}}{V_{tot}}, \tag{3.28}$$

where

$$V = \int N(\vec{p})\, d\, p_{\parallel} d\, p_{\perp}. \tag{3.29}$$

Since positronium atoms are formed both in singlet state and triplet states, presumably the total Ps fraction is four times the singlet which is detected in the 2D-ACAR measurement. Thus

$$F_{Ps} = \frac{4V_{Ps}}{V_{tot} + 3V_{Ps}}, \tag{3.30}$$

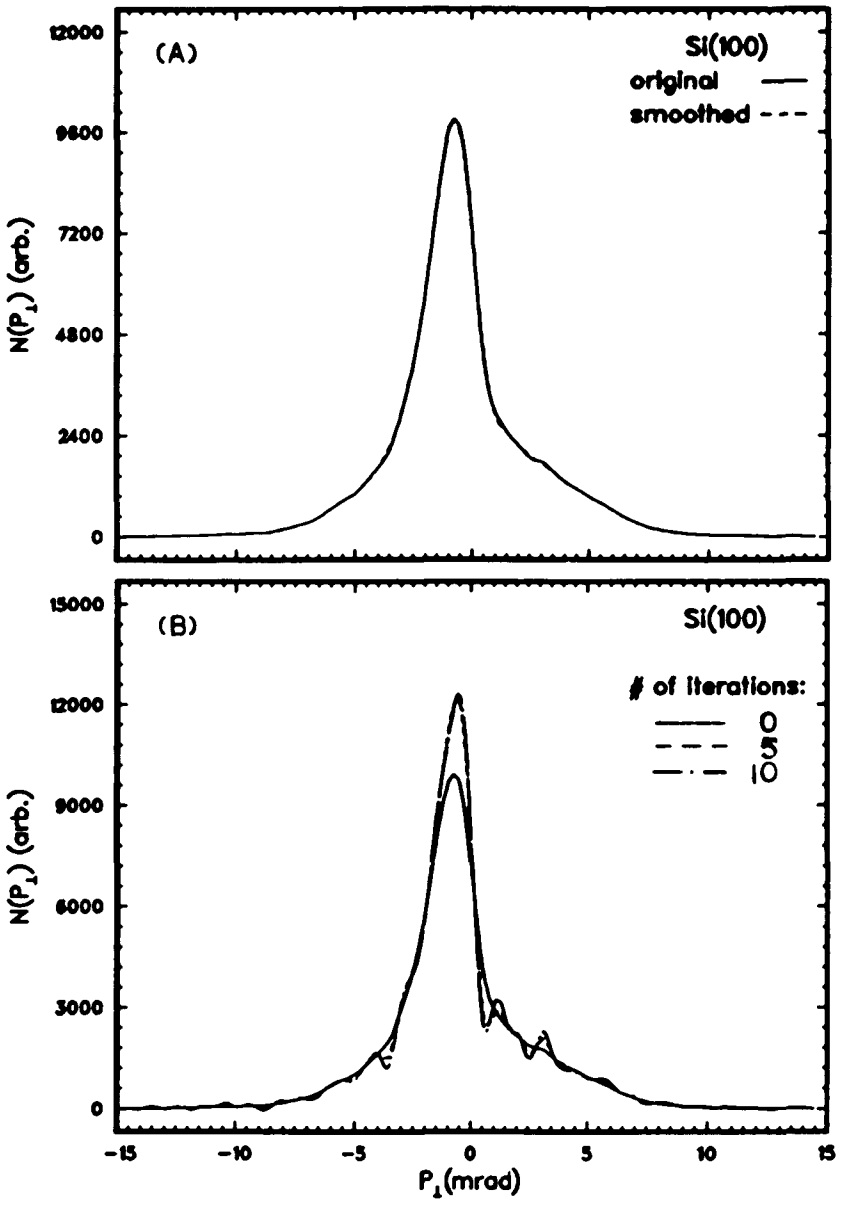

Figure 3.7. (a). The solid curve is a cut at $p_{\parallel}$=0 of a Si(100) spectrum measured using $200eV$ positron beam, the dashed curve coinciding with the solid curve is the result of the measured spectrum being first deconvoluted with five van Cittert's iterations and subsequently convolved back; (b). Cuts at $p_{\parallel}$=0 of the deconvoluted Si(100) spectrum using different numbers of van Cittert iterations as indicated in the figure.

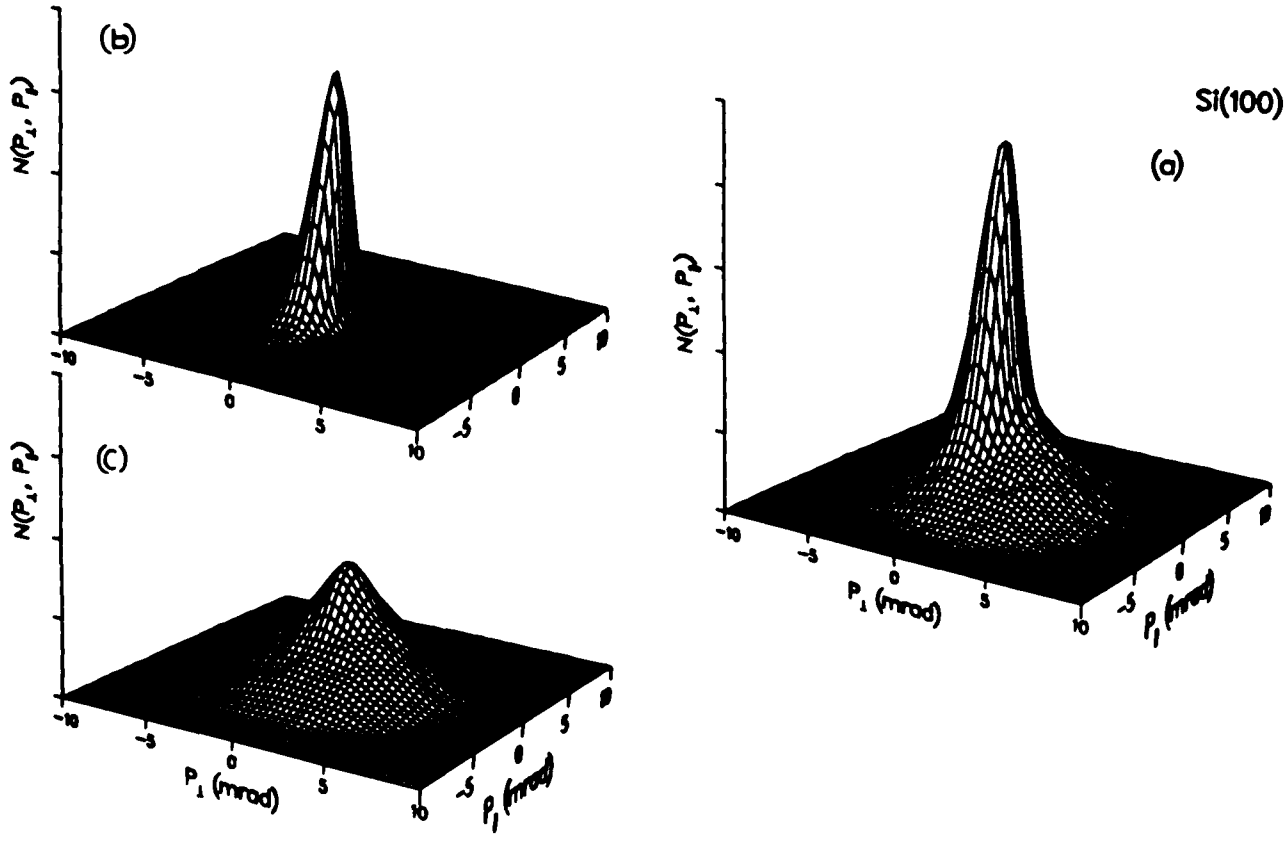

Figure 3.8. Perspective view of a centered Si(100) spectrum (a), the extracted Ps spectrum (b), and positron surface state annihilation spectrum(c). The technique employed to separate (a) into (b) and (c) is discussed in the text. The incident positron energy associated with these spectra is $200eV$ and hence the residual fraction of bulk annihilation embedded in (c) is negligible. Spectra are shown with the same intensity(vertical axis) scale.

$$= \frac{4\eta}{1 + 3\eta}. \tag{3.31}$$

If a retarding field is applied to repel the remitted slow positrons(if any) back to the surface, which was the case for the present work, then the fraction of slow positron emission $F_{e^+} = 0$, and

$$F = \frac{V_{s.s} + 4V_{Ps}}{V_{tot} + 3V_{Ps}}, \tag{3.32}$$

or

$$\frac{V_{s.s.}}{V_{tot}} = F(1 + 3\eta) - 4\eta. \tag{3.33}$$

Similarly,

$$F_{bulk} = \frac{V_{bulk}}{V_{tot} + 3V_{Ps}}, \tag{3.34}$$

or

$$\frac{V_{bulk}}{V_{tot}} = F_{bulk}(1 + 3\eta), \tag{3.35}$$

and

$$\frac{V_{bulk}}{V_{tot} - V_{Ps}} = F_{bulk}\frac{1 + 3\eta}{1 - \eta}. \tag{3.36}$$

From Eq.(1.8)-(1.9) and Eq.(3.28)-(3.36) we can calculate the relative fraction of bulk or surface state contributions to be removed.

§ 3.3 A Simulation Test

We shall now demonstrate a simulation test of the above discussed data analysis technique. In this test a Gaussian random deviate generator is used to create the statistical fluctuations in a perfect theoretical spectrum, which is subsequently shifted by 1 channel in both the $p_{\parallel}$ and $p_{\perp}$ directions, thus form a simulated 2D-ACAR spectrum. The procedures discussed in § 3.2 are then applied to this spectrum, and the output is compared with the theoretical spectra that we start with.

The theoretical Ps component, shown in the top-left frame of Fig. 3.10, is generated from a free electron model which will be discussed in detail in §4.9. The surface state component is

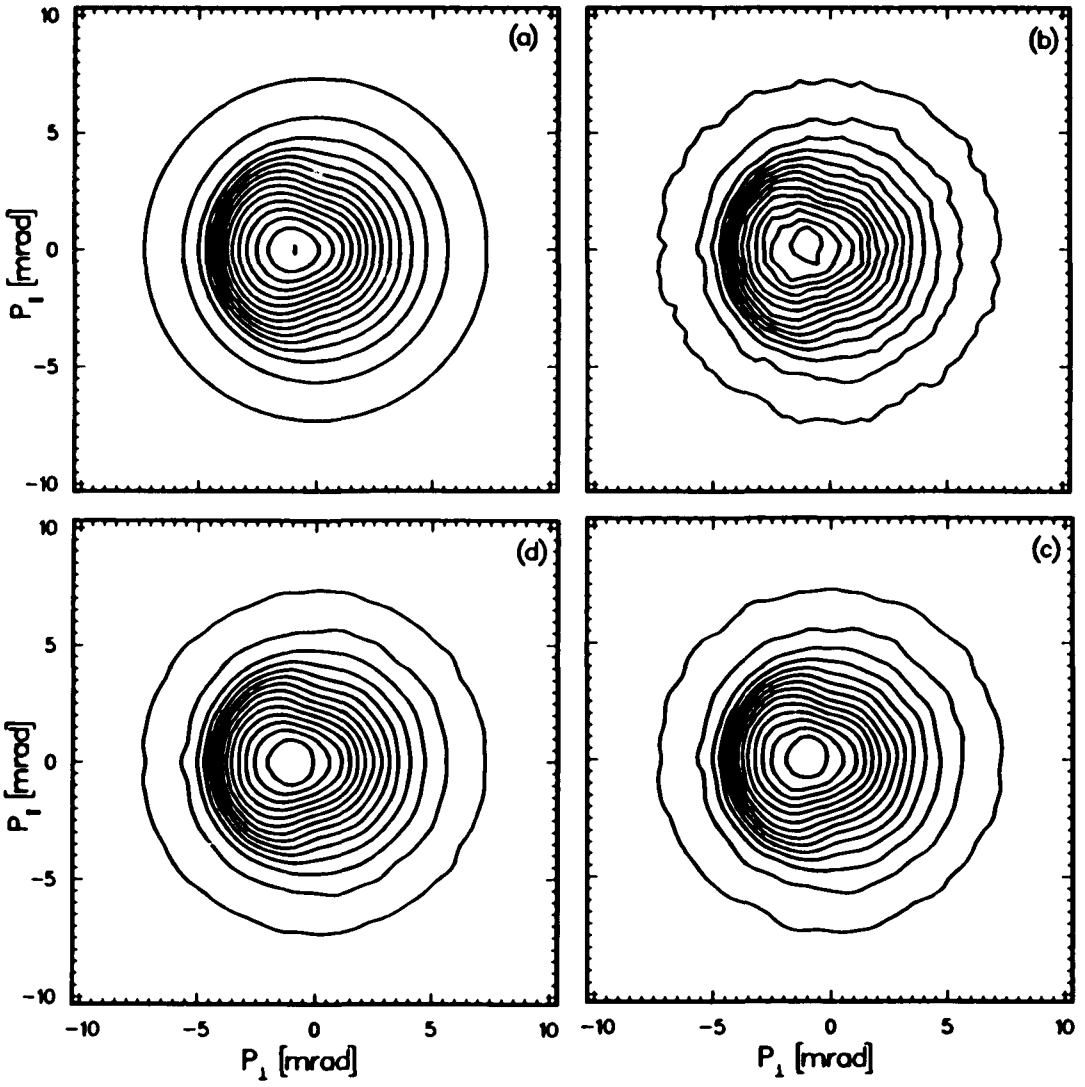

Figure 3.9. Contour plot for: (a). a perfect theoretical spectrum consisting of 32% of total Ps(Fig. 3.10a-left) and 68% of surface state(Fig. 3.10a-right); (b). same as (a) but including the random Gaussian deviation; (c). smoothed version of (b) using 5 van Cittert iterations; (d). same as (c) but with (b) being symmetrized prior to smoothing.

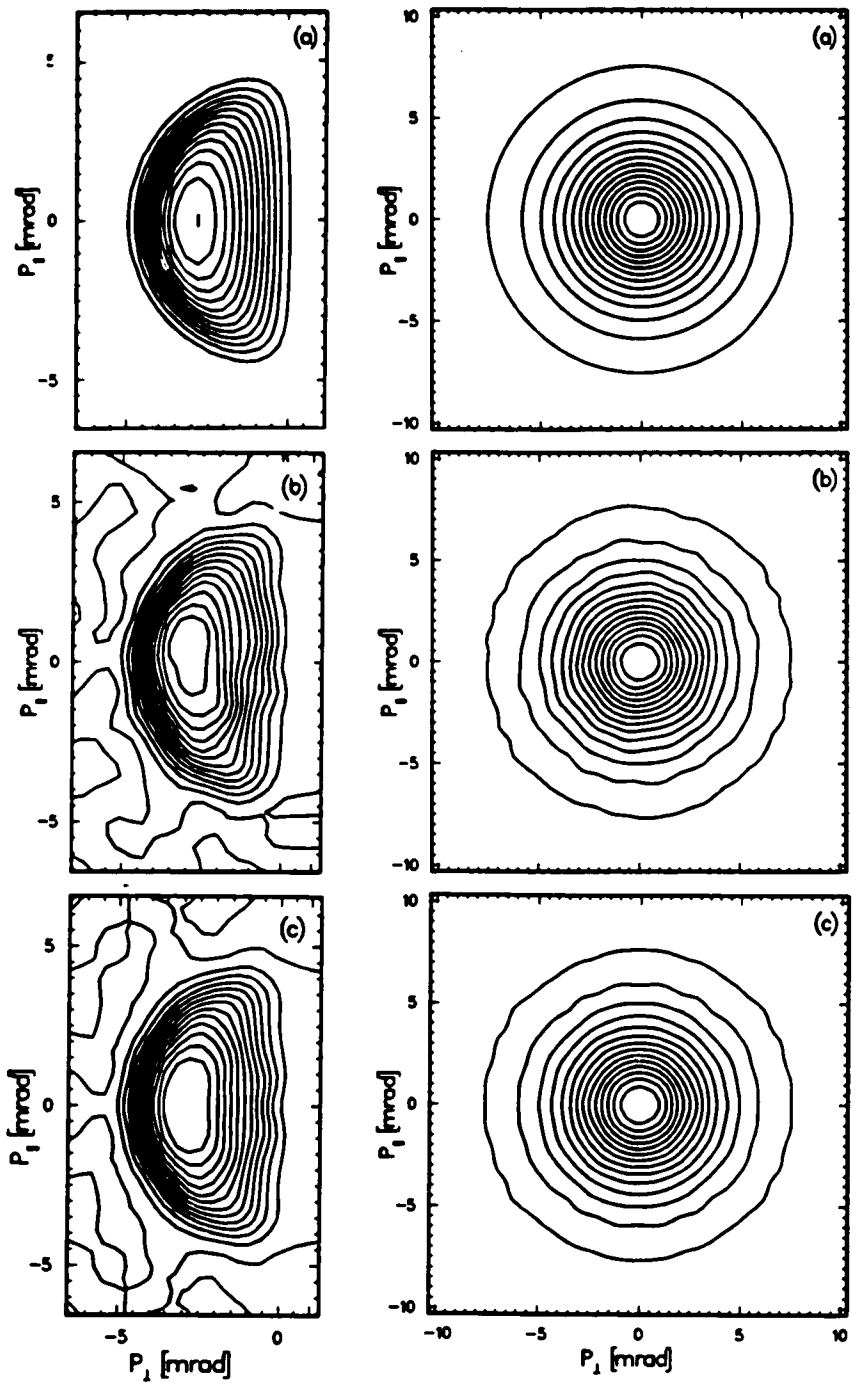

Figure 3.10. Left: Ps spectra; Right: surface state spectra. (a). theoretical spectra; (b). separated spectra from the simulated spectrum of Fig. 3.9b; and (c). separated spectra from the symmetrized version of Fig. 3.9b.

approximated by a Lorentzian-squared function shown in the top-right frame in Fig. 3.10, which fits the Al surface state spectrum reasonably well. 11 vol% of the Ps spectrum is then added to the surface state spectrum, leading to a total Ps fraction of 32%, similar to our measurement(see §4.9). The total spectrum is shown in Fig. 3.9a, which is somewhat similar to the measured Al spectra shown in Fig. 4.12. Fig. 3.9b is the full simulated noisy spectrum from Fig. 3.9a. The spectrum contains a total counts of 5×10^5, in comparable with most of our single measurement listed in Tbl. 4.2. Within this statistics the effect of the random fluctuation is still significant. Fig. 3.9c is the result of Fig. 3.9b being smoothed according to Eq.(3.26)-(3.27) with n =5. When Fig. 3.9b is first symmetrized then smoothed we obtain Fig. 3.9d. From the comparison of these four versions we can conclude: (*i*). Eq. (3.26)-(3.27) is a satisfactory algorithm for smoothing our 2D-ACAR spectrum; and (*ii*). the symmetrization indeed improves the agreement without introducing appreciable artifact.

Fig. 3.10 compares the separated spectra. The left column contains three Ps spectra, while the right column are the three corresponding surface state spectra. The top row is the perfect theoretical spectra, the middle is the results separated from Fig. 3.9b, and the bottom is the separated results from the symmetrized version of Fig. 3.9b. The agreement between (a) and (c) is striking, our data analysis technique is no doubt a rather successful one. In fact with an initial total counts of 1×10^6, the separated spectra are essentially identical with the input. In addition the total Ps fraction deduced from the separated spectra agrees with the input value within 1%. This accuracy is true only when the center of the spectrum is known exactly.

Although the symmetrization reduces the statistical fluctuation and improves the overall agreement, in the Ps spectrum (c) we can still observe a small artifact near the zero which is a result of the symmetrization. For lower statistical data this problem is enhanced, therefore, care must be exercised. However, a real structure can still be distinguished from their reproducibility. Structures due to the random fluctuation in general do not appear at the same position as concluded from our extensive test.

§ 3.4 Error Analysis

3.4.1 Statistical Error - The primary error of the raw spectrum is extracted according to the statistical fluctuation[77]

$$\Delta N = \sqrt{N_{raw}}. \tag{3.37}$$

The error propagation depends on the errors introduced by various sources and their correlation in the cause of analysis, in some cases it is complicated and can only be roughly estimated.

After the raw spectrum is divided by the momentum sampling function,

$$\Delta N = \frac{\Delta N_{raw}}{M} + \frac{\Delta M}{M}\frac{N_{raw}}{M} \tag{3.38}$$

The second term can be ignored if $\Delta M/M << \Delta N_{raw}/N_{raw}$, *i.e.*, the relative error of the momentum sampling function is much smaller than that of the raw data. This is up to the control of the experimenter and is easily obtainable. Since M is constructed from the single camera efficiency function measurement, we can estimate at the peak

$$M(0) \approx \sum_{ij}^{n} N_\epsilon^2, \tag{3.39}$$

$$= n^2 N_\epsilon^2, \tag{3.40}$$

where N_ϵ is the averaged counts/channel of the efficiency spectrum and n is the dimension of the array. Hence

$$\frac{\Delta M(0)}{M(0)} \approx \frac{2}{n\sqrt{N_\epsilon}}. \tag{3.41}$$

The criterion for this peak channel becomes

$$\frac{N_\epsilon}{N_{raw}} >> \frac{4}{n^2}, \tag{3.42}$$

or substituting n=128,

$$\frac{N_\epsilon}{N_{raw}} >> 2.5\times10^{-4}. \tag{3.43}$$

Near the edge of the spectrum ($\pm 15 mrad <$) the corresponding sampling function is roughly half the height of the peak(Eq. 3.15), and in Eq.(3.42) n is substitute by $n/\sqrt{2}$. Typically, N_{raw} is on the order of 10^3, and this condition is very easy to be met with N_ϵ as small as 100 counts/channel. Thus the error of the sampling function can be ignored most of the time.

The centering involves parabolic interpolation over a 3×3 sub mesh, therefore, the new data point is correlated to its neighboring points. In principle it is possible to propagate the errors in the same fashion. However it is tedious and cost too much computing time. In fact, linear interpolation with four nearest point is a much simpler but reasonable way to estimate the new error bars and hence has been used in our analysis.

For similar reason, the error propagation through the deconvolution and then convolution becomes even more difficult, (but not impossible because of the linear operations). Thus we assign the same error bars to the separated symmetrical spectrum. It is therefore appeared to be more smoother than the error bars suggest. For Ps spectrum obtained from the inversion-subtraction, the errors attached to the data points for $p_\perp > 0$ is set to be zero because of the full correlation, while for data points in region $p_\perp \leq 0$ the point-to-point subtraction is uncorrelated.

3.4.2 Other Sources of Error - The uncertainty of the position of $\vec{p} = 0$ is potentially another important cause of error which might be introduced during the inversion subtraction and should be always borne in mind. In addition to the technique of searching the center, one can inspect the result with other physical constraints. For instance, the separated Ps spectrum should not contain negative value beyond statistical fluctuation and the distribution should not extend too far than the maximum Ps energy allows. Figure 3.11 shows a set of cuts for Ps emitted from Si(100) surface which has been properly centered (solid curve), or offset in the perpendicular direction by ±0.1 mrad(dashed/dot-dashed). The arrow indicates the maximum Ps kinetic energy. The spectra are indeed sensitive to such a small deviation. Additionally, the Ps fraction calculated from Eq.(3.31) changes substantially with respect to a small offset of the center.

Since our experiment is performed in an UHV chamber, γ-rays must penetrate windows, the chamber walls or other type obstruction. In the present study we use conventional UHV windows on the 2¾ inches conflat flanges as shown in Fig(2.2). To be sure that no effect on measured spectra could be possibly caused from these windows we have measured bulk Al spectrum with and without the windows present in the γ-ray path. The result showed that the shape of the spectra were identical but the total counts reduced by 11% due to the absorption and scattering of the

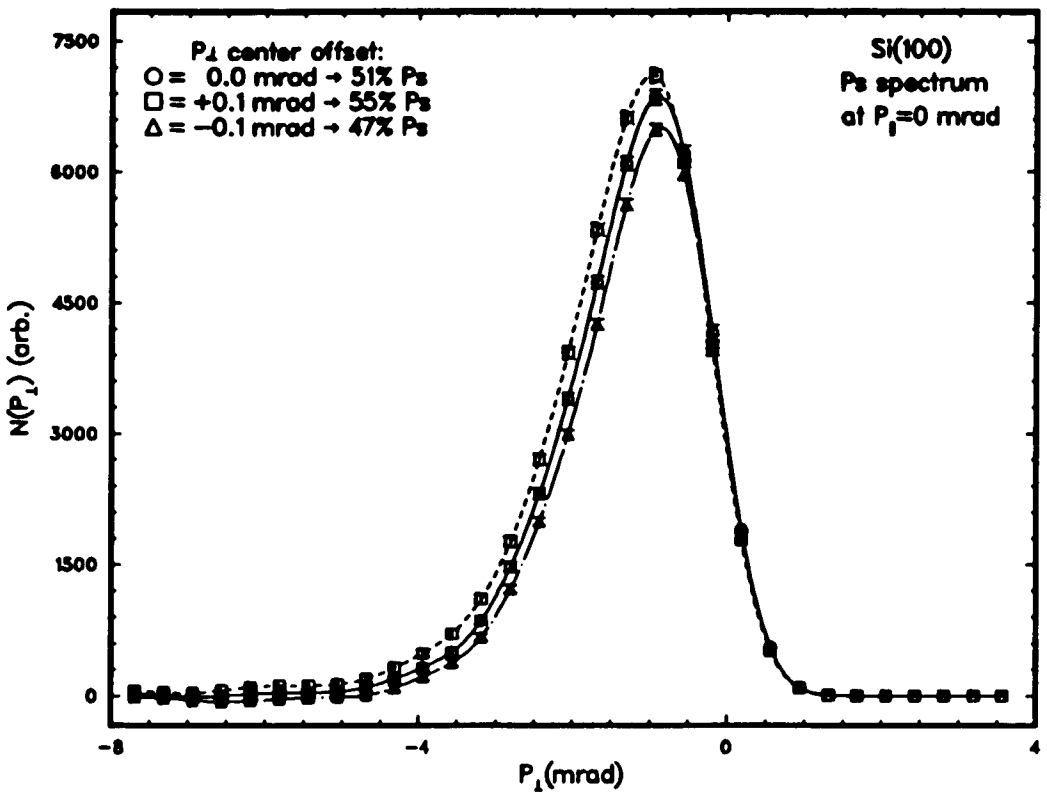

Figure 3.11. Sections at $p_{\parallel}=0$ of a Si(100)-(2×1) Ps spectrum obtained with and without a small offset on $p_{\perp}$ origin with respect to the position deduced from the associated high energy run. The total Ps fractions calculated from the separated spectra are also listed.

windows.

Chapter 4. 2D-ACAR Study of Al Surfaces

In this chapter we discuss the 2D-ACAR experiment on three low index surfaces of aluminum, i.e. Al(100), Al(110) and Al(111). Owing to the simple, nearly-free-electron nature, both bulk and surfaces of aluminum have served as a prototype model for extensive theoretical[78-95] and experimental[63-67,96-109] investigations. The interplay between theoretical calculations and the wealth of experiments using various conventional modern surface probes has provided us with better understanding of these surfaces and their interactions with adsorbates. Traditional positron annihilation technique as well as the newly developed slow positron beams have also been applied to study the interactions of positrons with the bulk and surfaces of Al, and have yielded vast experimental results[1-3,5]. Thus we have selected this widely studied simple metal for testing our application of surface ACAR technique, and for further understanding the mechanisms of positron interaction with metal surfaces.

This chapter is organized as follows. In the first four sections we review the surface structures and the surface reciprocal lattice structures; the bulk and surface electronic structures; oxidation of Al surfaces; and some previous positron studies on Al. In section 5 we compare the directly measured ACAR results under various conditions(before invoking the data separation). The decomposed results of positrons annihilation at the surfaces of Al are presented and discussed in section 6, while some examples of positron annihilation in vacancies and defects are given in section 7. Ps momentum distributions are shown in section 8, and some theoretical discussion about the Ps formation is followed in section 9. In the final section we discuss the thermal Ps emission spectra.

§ 4.1 Surface Atomic Structure and 2D-Brillouin Zone

The atomic configuration of aluminum is $[Ne]3s^2 3p^1$[56]. Single crystal Al has a face-centered cubic(FCC) structure with a conventional cubic cell of size a =4.06 Å . The corresponding reciprocal lattice has a body-centered cubic(BCC) structure with a conventional cubic cell size

$4\pi/a$.

Al(100), Al(110) and Al(111) surfaces are close to the simple terminations of the bulk crystal. There are no surface reconstructions as confirmed by LEED[66-67,96-98], but a few percent($<10\%$) of contraction or dilation of the (110) and the (111) surface layers have been reported[95,106]. Column (a) of Fig. 4.1 shows a hard sphere model of the top layer atom configurations of these three surfaces. The interplanar distance d and the unit cell of the surface periodic net defined by the two dimensional(2D) lattice vectors $\vec{a}_{ij}$ are indicated for each surface. In the (111) plane atoms are arranged with hexagonal symmetry. There are three types of layers that repeat in an ABCABC $\cdots$ order along the (111) direction. The (111) is the most densely packed face of the FCC crystal, and the distance between the layers is $a/\sqrt{3}$ which is largest compared with the (100) and the (110) direction. The 2D square unit cell of the (100) face is seen to be rotated 45° with respect to the conventional three-dimensional crystal axis and the sides to be of length $\bar{a}=a/\sqrt{2}$. The second layer is separated by $a/2$ from the top layer and the atoms appear in the fourfold hollow sites of the top layer while the third layer repeats the first layer. The (110) surface has a rectangular unit cell and atoms are packed in alternative layers similar to the (100) face but with a smaller layer separation $d=a/2\sqrt{2}$. The size of the unit cell indicates that the (110) is the most open surface among the three low index surfaces.

The first 2D Brillouin zone(BZ) of the surface reciprocal lattice defined by Eqs.(1.31)-(1.32) for each of these surface are shown in column (b) of Fig. 4.1. As can be seen the zone is largest for the (111) face and smallest for the (110), opposite to the relative sizes of the 2D unit cells in real space. The shape of the 2D BZ is simply the 90° rotation of the corresponding unit cell in real space. Fig. 4.2 shows the projections of the 3D-Brillouin zone onto the 2D-zones along the three directions. These projections will help us to understand the relationship between the bulk electronic structure and the surface electronic structures[85-89].

§ 4.2 Bulk and Surface Electronic Structures

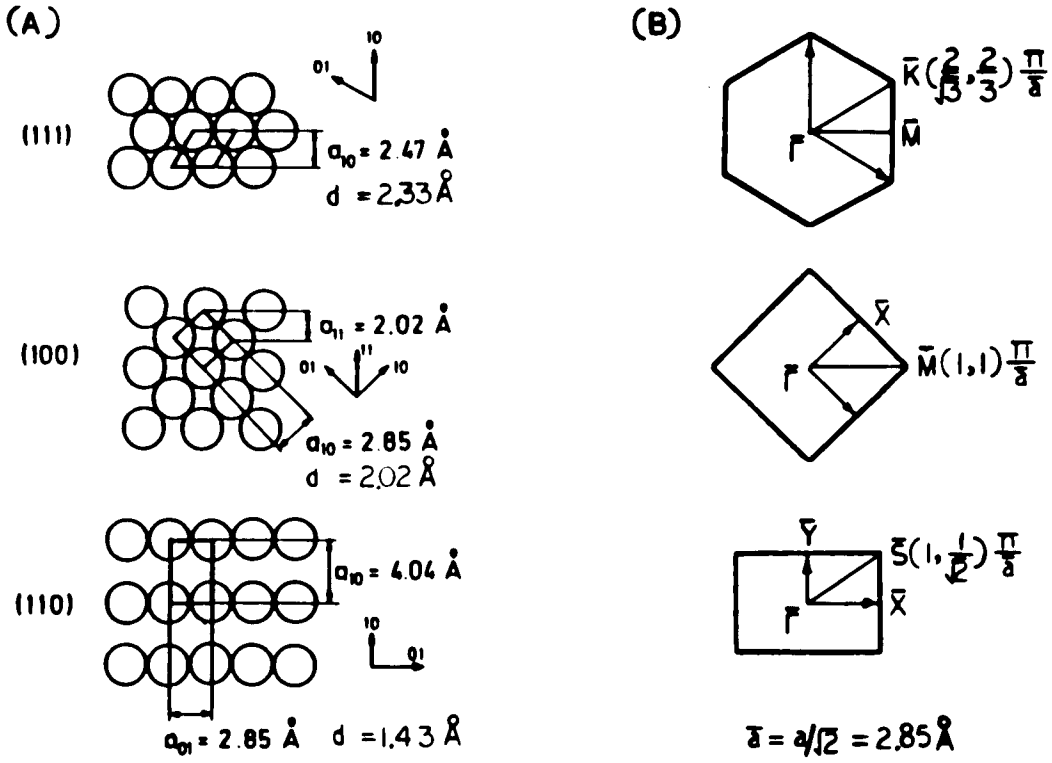

Figure 4.1. (a). Hard sphere model of top layer atomic configuration for three low index surfaces of aluminum, the 2D unit cell and the interplanar distance d are given for each face; (b). 2D Brillouin zones corresponding to the real space unit cell shown on the left.

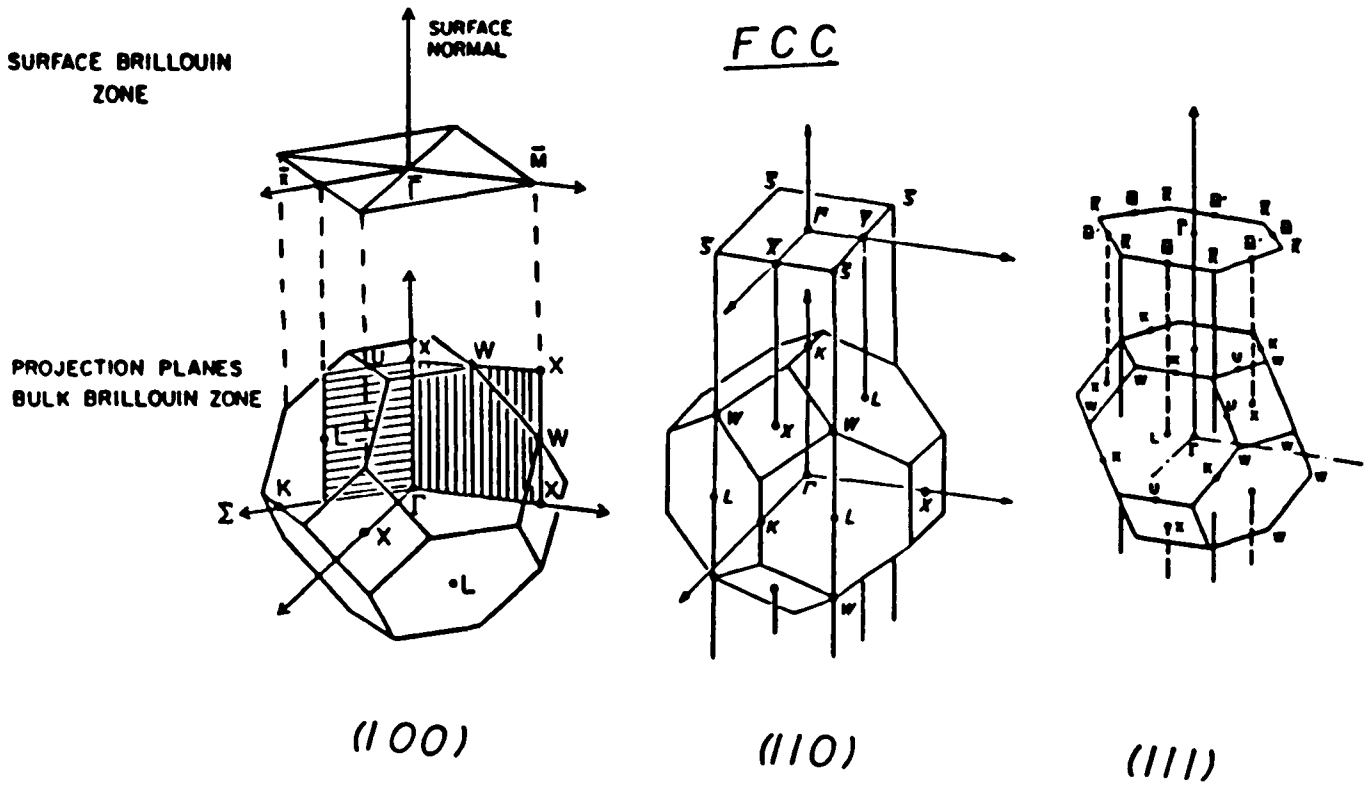

Figure 4.2. Projections of the bulk Brillouin zone onto surface Brillouin zone for three low index surfaces of a face-center-cubic (FCC) system.

4.2.1 A Brief Overview - Bulk electronic band structure of Al has been calculated using various techniques including some sophisticated self-consistent methods[78-84]. It is shown that the bands in Al are free-electron-like except near the Brillouin-zone boundary where the degenerate free-electron-states are split by the weak periodic crystal potential and hence introduce band gaps at these boundaries. This nearly-free-electron nature is primarily due to the characteristic atomic configuration of Al, *i.e.* , the conduction bands are filled or half filled with two s -electrons and one p -electron per atom. However, because of trivalency band gaps appear below the Fermi level. This causes severe modification of the density of states(DOS) from that of a pure electron gas. When projected onto a surface 2D BZ, part of the gaps remains in the surface electronic band structure, and induces some localized surface states and surface resonant states[85-89].

De Haas-van Alphen[56], Compton scattering[110], positron annihilation[3,111] and other experimental techniques have revealed the nearly-free-electron like Fermi- surface of Al some time ago. Recently, direct experimental mapping of the band structure away from the Fermi surface has been achieved through the use of energy- and angle-resolved photoemission and synchrotron light sources[103]. For a single crystal Al, the occupied portion of the bands displays a dispersion in qualitative agreement with the nearly-free-electron[79] model and self-consistent band calculations[83]. The measured occupied band width is 10.6eV, which is 0.5 eV smaller than calculated[83], due to electron-electron interactions. The measured gaps at X is 1.68eV wide, 0.35eV wider than the theoretical value, and centered at 1.99eV below the Fermi energy, 0.5 eV higher compared with the calculated gap center.

A common method of solving for the surface electronic structure is to use a thin slab of the order of 5-10 layers. The method involves matching the wave function inside the slab subject to some periodic boundary condition to the decaying wave functions in the vacuum region on both sides of the slab. Any surface states present are obtained automatically along with all the bulk states from these calculations. Thin slab calculations[85-87] were first to predict the existence of the surface states and surface resonant states in the projected energy gaps of these three Al surfaces. These predictions have been confirmed by a number of angle-resolved photoemission

experiments[101-105], and by some more advanced self-consistent calculations [87-89].

4.2.2 Projected Band Structures - To obtain the projected bulk Al bands, we have used the bulk band structure of Al calculated by M. Weinert using Harrison's bulk Al pseudopotential and a plane wave basis[80]. For each face we setup a mesh in the irreducible portion of the standard surface Brillouin zone(Fig. 4.1) and then for each $\vec{k}$-mesh point we vary k_z in the 3D Brillouin zone(Fig. 4.2) to generate the projected bands. Fig. 4.3 are the results of the projections on the high symmetry lines for each of these surfaces. There exist substantial gaps below and above the Fermi level, especially in the (100) and the (110) projections. With the assistance of Fig. 4.2 the origin of these gaps can be easily tracked back to the gaps at the boundaries of the 3D Brillouin zone[78-89]. For instance, the gap around $\bar{\Gamma}$ (also from $\bar{\Gamma}$ to $\bar{X}$ and from $\bar{\Gamma}$ to $\bar{M}$) of the (100) face is associated with the gap at the zone boundary across X and perpendicular to ΓX, which is also responsible for the gap around the $\bar{X}$ point of the (110) face. As mentioned before, localized surface states are found to exist in all the gaps. The true surface states appear close to the bottom of the gaps and form a two dimensional parabolic dispersion which extends into the resonant region. As an example we show in Fig. 4.4 the results of the angle-resolved photoemission experiment reported in Ref.[102]. The shaded area is the gap(also shown in Fig. 4.3), the chain-dotted curves and the dashed curves are the surface states and resonant states, respectively. The solid curve will be discussed later. For clarity, the surface states existing inside the two narrow gaps of Al(111) presented in Ref.[105] are not shown.

In general, from the free electron nature we would anticipate that projected gaps exist in the off high symmetry directions as well, and occupy some domains in the 2D Brillouin zone. In Fig. 4.5 we plot the projections(shaded) on the irreducible portion of the 2D Brillouins zone of the gap around $\bar{\Gamma}$ in the (100) face and the gap around $\bar{X}$ in the (110) face. For the (111) face we only project the gap at 3/4 of the way from $\bar{\Gamma}$ to $\bar{M}$ moving up to Fermi level. The projection within the whole zone can easily be mapped out by unfolding these portions throughout the zone. As suggested by these projected band gaps we would expect that surface states and surface resonant states exist elsewhere in the gaps in addition to the high symmetry lines(Fig. 4.3), even though

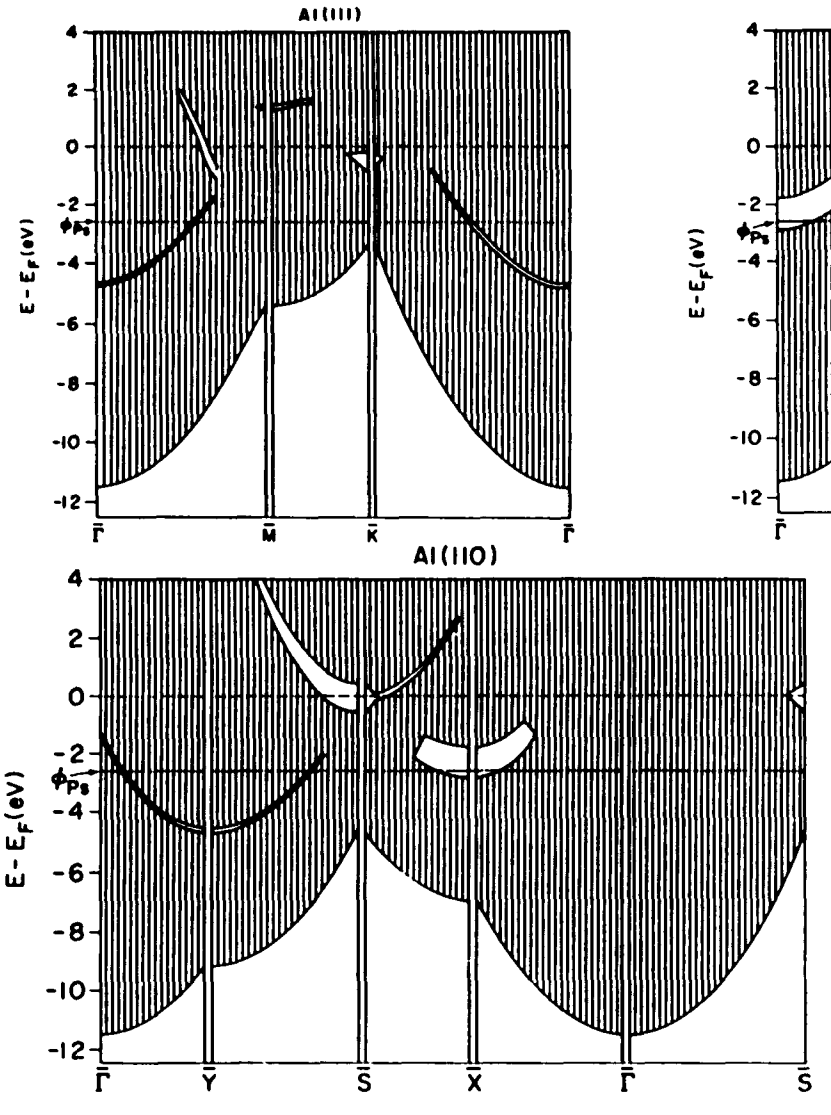

Figure 4.3. Projected aluminum band structure along high symmetry lines in the surface Brillouin zones shown in Fig. 4.1-Fig. 4.2. The bulk Al band structure is calculated using Harrison's pseudopotential and a plane wave basis(Ref.[80]).Also marked is the positronium work function ϕ_{P_s}, above which the occupied states are accessible for Ps formation at the surface.

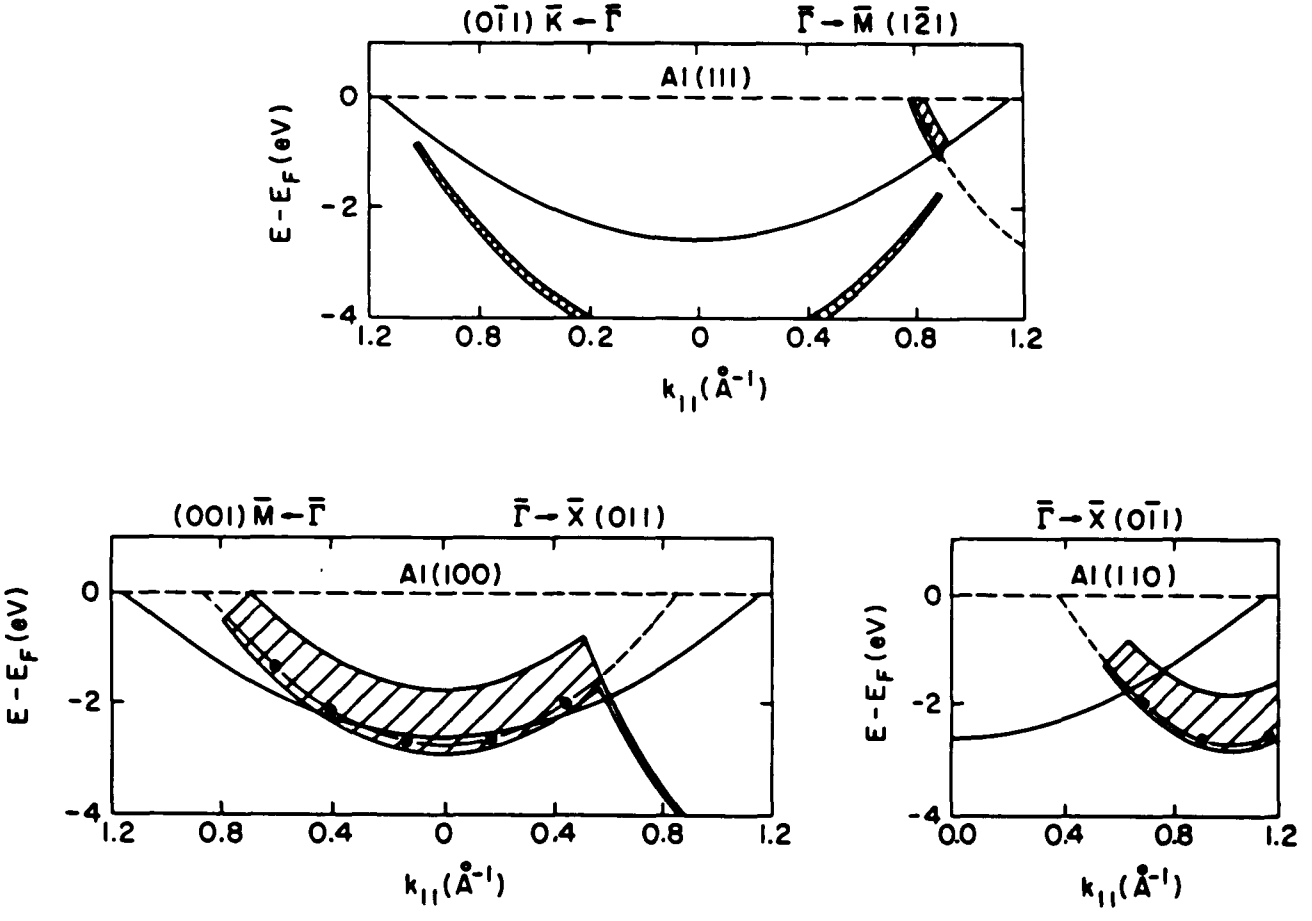

Figure 4.4. Shaded areas are the projected band gaps reproduced from Fig. 4.3. The dot-chained and dashed curves are, respectively, the dispersions of the true surface state and surface resonant state given in Ref.[102]. Solid curves are the dispersion of the lowest occupied states that can form Ps atoms.

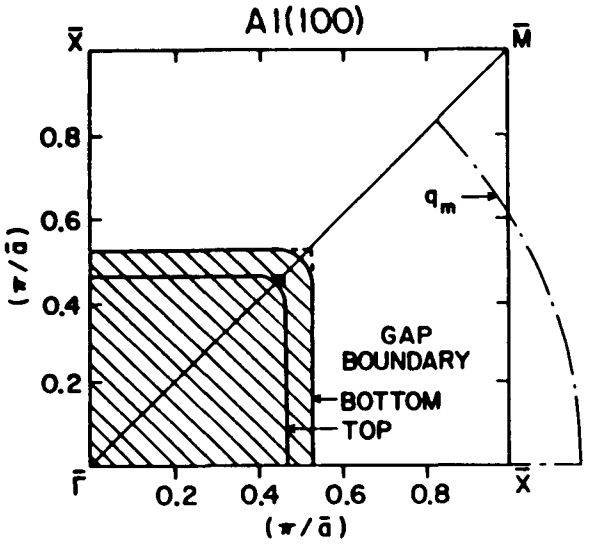

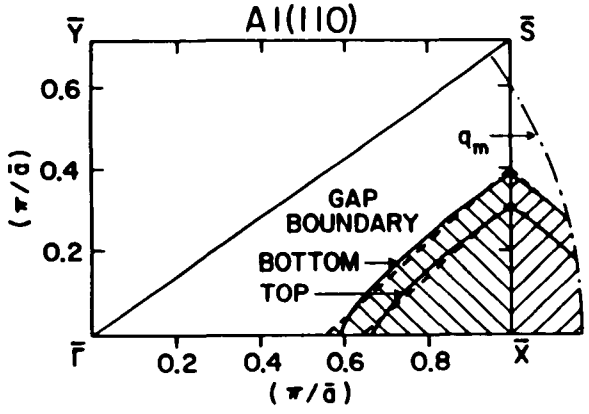

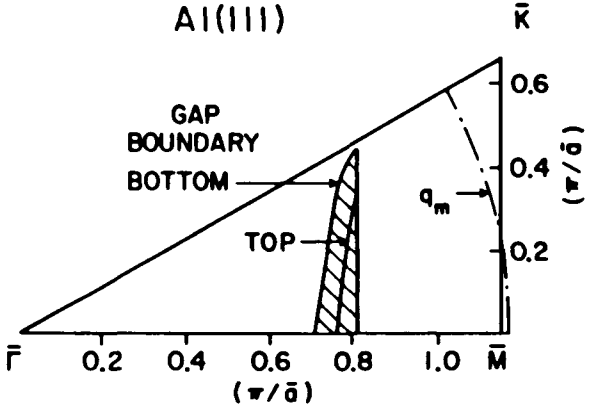

Figure 4.5. Shaded areas are the projections of the gaps in the projected surface band structure. The solid lines represent the gap boundaries. For the (111) face gap is projected up to Fermi level, the lower narrow gaps and the gap at $\bar{K}$ are not projected. The dot-chained curves indicate the maximum allowed Ps parallel momentum or electron parallel momentum in the extended zone scheme. $\bar{a}$ is defined in Fig.4.1.

neither theoretical predictions nor experimental evidence have been reported explicitly.

§ 4.3 Oxidation Process of Al Surfaces

The initial oxidation process of Al surfaces is face dependent. Experiments[95-96,98,106-107] have established that a well-defined chemisorbed phase exists on the Al(111) surface at low oxygen exposure, and that after higher exposure($>$150L) Al-oxide formation takes place. On the other hand, oxygen atoms are incorporated at the very onset exposure into the Al(100) surface layer, and oxide islands are formed without a precursing chemisorbed stage[65,66]. The different behavior is the direct consequence of their surface structures. Oxygen atoms chemisorbed on the Al(111) surface form a $p(1\times1)$ overlayer[98] occupying the threefold hollow sites with out an Al atom directly below in the second interior layer. The distance between oxygen overlayer and metal surface layer was deduced[107] to be 0.70 Å from the O-Al bond length of 1.79 Å . The latter is shorter than the 1.97 Å O-Al bond length in bulk Al_2O_3, but greater than 1.65 Å in-plane distance between the threefold center and its adjacent Al atoms so that penetration through this most compact surface is more difficult. The O-O length is found to be 2.90 Å consistent with the O-O distance in a $p(1\times1)$ structure. For the more open structure surface of Al(100) covered with a monolayer of oxygen, the Al-O bond length is found[109] to be 1.98 Å, which is consistent with oxygen atoms are being at the in-plane fourfold hollow sites, leading to a bond length of 2.02 Å . The Al atoms immediately below the hollow site act as traps for oxygen atoms and stop further diffusion[66]. The observed change of the electron work functions ϕ_-[65] due to the oxygen exposure are consistent with these pictures. For Al(111) surface at a monolayer coverage, ϕ_- increases by 0.1eV, while for Al(100) surface ϕ_- decreases almost linearly with oxygen coverage to a saturation differences of 0.5-0.8eV. The increase/decrease in ϕ_- is caused by the additional inward/outward dipole layer formed due to the outward/inward charge transfer from the metal substrate to electronegative adatoms. In contrast to the (111) and the (100) faces, less is known about oxide formation on the (110) face. Auger electron spectroscopy(AES) studies[65-66] showed that the (110) face has highest oxygen sticking probability, the (111) next and the (100) least. The

reported zero coverage sticking probabilities[65] for the (111) and (100) faces are respectively 0.03 and 0.015 monolayer/L. For the (110) face ϕ_- remains almost constant up to a monolayer coverage of oxygen, but the oxidation signal grows rather rapidly[64,66]. These might suggest a combined process of chemisorbed and oxidation at the same time.

Several theoretical calculations have been carried out to study the aluminum oxidation[90-95]. In particular, self-consistent linearized augmented plane wave calculations[90] were performed on Al(100) and Al(111) surfaces by assigning oxygen atoms to be located at the above mentioned positions. These calculations yielded good agreement with the experimental data of work function, Al2*p* core level shifts and the configuration of the oxygen atoms with respect to the substrate. The important electronic properties revealed in these calculations are: (i) For the (100) face, charge transfer after oxygen adsorption only happens within the nearest coplanar metal atoms to the adatoms, which results in the formation of a dipole moment opposing the usual surface dipole layer and hence reduces the electron work function by 0.5eV, consistent with experiment; (ii) For the (111) face, charge density of active surface states associated with the clean surface is responsible for outward electron transfer to O atom, resulting in a small additional inward dipole layer and the increases in ϕ_- by 0.7eV(larger than the experimental value of 0.1 eV); (iii) For both surfaces O2*p* electrons localize in the surface layer and produce low-lying bands as shown in Fig. 4.6, the surface states of clean surfaces are washed out in the (111) face, and for Al(100) they are replaced by the oxygen-induced surface resonance near the Fermi level.

§ 4.4 Previous Positron Studies on Al

High precision 2D-ACAR data of single crystal Al first appeared about 10 years ago[3,111]. It was concluded that the Fermi surface(FS) of Al is spherical within 1% in the extended zone scheme. The averaged FS radius measured at 100°K is $6.73\times10^{-3}mc$, in good agreement with the free-electron value of $6.78\times10^{-3}mc$. It was shown that the OPW calculation can account well for the observed zone face interactions and high-momentum components(umklapp annihilations) having an amplitude of a few percent of the zero order peak intensity. In addition, the e^+–e^-

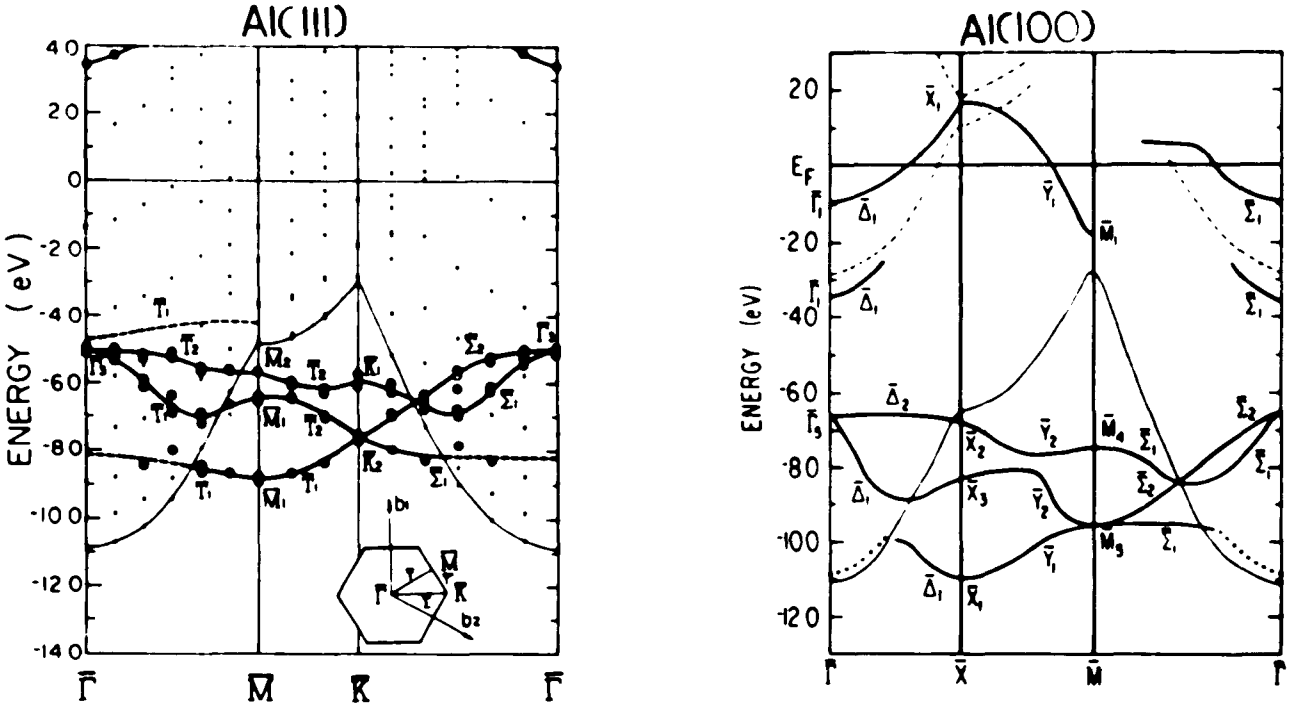

Figure 4.6. (From reference 90). Left: self-consistent electronic band structure of the oxygen chemisorbed five layer Al(111) film. The filled circles denote the state with 60% or more charge in the surface layer and vacuum regions. The thin solid line represents the bottom of the bulk Al conduction band. Dashed lines are the energy center of the states with large O2p_z components. Right: surface state and surface resonance state for the O/Al(100) slab. The thin solid line is the bottom of the Al conduction band. Dashed lines represent the surface state for the clean Al(100) slab. the dotted lines indicate states interacting with the Al substrate.

Table 4.1 Positronic properties of three low index surfaces of aluminum(selected from Table 5.1 in Ref.[1], ϕ_{P_s} and E_b are defined by Eq.(1.13) and (1.15), the remainders are experimental values).

	ϕ_- (eV)	ϕ_+ (eV)	ϕ_{P_s} (eV)	E_s (eV)	E_b (eV)	y_0	f_0
Al(100)	4.41(3)	-0.19(2)	-2.58(3)	0.64(2)	3.03(5)	0.21	0.62
Al(110)	4.28(3)	-0.05(5)	-2.57(6)	0.40(1)	2.92(4)	0.09	0.55
Al(111)	4.24(3)	-0.04(1)	-2.60(3)	0.34(3)	2.90(6)	0.14	0.68

many-body effect was shown to lead to a small extended bulge on the projected FS.

Slow positron reemission, direct formation and emission of Ps and thermal emission of Ps from all three low index surfaces of Al have been well established experimentally[1-2,8,14,22,32-34,37,39]. Some of the important positronic properties are summerized in Tbl. 4.1. The positron work functions ϕ_+ listed here are slightly negative and in reasonable agreement with theoretical values[17]. However, a small positive ϕ_+ for an Al(110) surface has also been reported[2]. The discrepancy is most likely due to the the variation of different surface conditions such as impurity level and surface roughness. In Tbl. 4.1 y_0 is the extrapolated positron remission fraction at zero positron incident energy. Previous measurements have shown that y_0 has negative temperature dependence and decreases as the oxygen contamination increases[2,37,112].

The Ps fractions, f_0, at zero incident positron energy were extrapolated from measurements at finite energies[1]. The branching ratio for Ps formation is much greater than that for slow positron emission for the Al surfaces. For an Al(111) surface, the maximum kinetic energy of Ps emission in the normal direction obtained from TOF measurement[22] is in good agreement with $-\phi_{P_s}$ derived from the measured ϕ_- and ϕ_+ according to Eq.(1.13). The same experiment showed that the velocity distribution of normal emission Ps from an Al(111) surface is consistent with the metal being left in an one hole excited state. A simple golden rule model with constant transition matrix element fits the data fairly well near $-\phi_{P_s}$.* Hence it is suggested that the Ps emission

* In the low energy range, instead of dropping off as the energy decreases, the TOF spectrum increases towards zero energy. This is claimed by the authors[22] to be the result of multiple scattering of the γ-photons in the detector slit, but is interpreted as the inelastic process by Ishii et al.[29,30].

spectroscopy may reflect the density of states near a metal surface.

Thermal desorption of Ps were observed to occur and increase as the sample is heated up to a threshold temperature T_v. Above T_v[2] Ps fraction drops as a result of trapping positrons by thermally activated vacancies. T_v reduces as the incident positron energy increases. For an Al(110) surface at very low incident positron energy (28eV) the Ps fraction is found to raise up to a saturation level close to unity at $\sim$ 700° K. At E=1.5keV, the threshold temperature is about 600° K. The activation energy E_a for these three faces extracted from the temperature-dependent Ps-fraction measurement using Eq.(1.14) are given in the table. The positron biding energy E_b are deduce according to Eq.(1.15). The thermally desorbed Ps energy spectrum from an Al(111) surface was shown by TOF measurement[34] to be an exponentially decreasing function of energy, and is consistent with Ps having a velocity-independent reflection coefficient.†

The effect of oxygen-exposed Al surface on Ps formation has been studied in detail[2,32,37,39,112]. For an Al(100) surface, only small changes in Ps fraction are observed up to $\sim$ 500L exposure, between 500L and 1000L Ps fraction increase rapidly and then falls as the exposure increase further. This is interpreted[2] as the shallowing of the positron surface state with the initial increasing oxygen exposure, thus the activation energy E_a is reduced and surface state positrons are desorbed as thermal Ps even at room temperature. The decrease in Ps fraction is associated with the formation of an amorphous-$Al_x O_y$ overlayer at higher exposure, which results in the trapping of positrons in the Al-oxide overlayer and possibly in the interface region as well.

The positron surface state is widely regarded as an image potential bound state[40]. A recent discrete-lattice calculation[41] of positron surface state properties on the low index surfaces of Al has yielded the anisotropic biding energies (E_b), which are in good agreement with the experimental values. It also showed that monovacancies play little or no role for positrons on Al surfaces, and that oxidation makes the surface state unstable with respect to the Ps emission. The latter is consistent with experimental observations. However the prediction of 400 psec positron

† For more detailed discussion, see §4.10.

lifetime at Al surfaces seems too short. The measured positron surface state lifetime at an Al(110) surface is 580±10 psec[39]. This discrepancy was attributed to the inconsistency from using the local-density-approximation(LDA) in the previous lifetime calculation. By assuming zero annihilation rate in the image potential region, the lifetime of 630 psec was obtained. On the other hand, estimations of the Ps thermal activation energies and the surface state lifetime for Al surfaces from the recently proposed physisorbed Ps model[46] are in reasonable agreement with experiments.

The largest inconsistency between the two models and experimental results is in the momentum distributions of the surface state annihilation. The image potential model[40-44] predict a large anisotropy in the momentum distribution: the perpendicular component with respect to the surface is $\sim$ 30% broader than the parallel component. The first 2D-ACAR study on an Al(100) surface has yielded an isotropic distribution of positron surface state annihilation. Thus the nature of positron surface state is still not fully understood. The ACAR projected Ps momentum spectra for both the Al(100) and the Cu(121) surfaces[7,8] showed isotropic distributions in qualitative agreement with a simple free-electron model. These new results have motivated some theoretical investigations on the Ps formation mechanisms[29,30,31]. We will discuss these results together with our new ACAR measurements in §4.9.

§ 4.5 2D-ACAR Results as Measured

In this section we show that much can be learned about various positron interaction processes at a surface from the directly measured 2D-ACAR spectra taken under different conditions, without applying the data separation procedures. To help understand the spectra shown in the present section, information connected to these figures are collected in table 4.2. The surface conditions are roughly divided as clean or oxygen-exposed. The clean surface implies that the total contamination is less than 0.01ML C for all three faces, and 0.03ML O for the Al(111) and Al(100), but it is $\sim$ 0.1ML O for the Al(110) surface owing to the higher oxygen sticking probability. Some common treatment of the spectra to be shown below are: (*i*). All the contours are the

Table 4.2 Collected information associated with Fig. 4.7a through Fig. 4.14c. $p_\perp$, $p_\parallel$, $p_\perp'$ represent the crystal orientations along these three directions(see Fig. 1.4 for the geometry). The meanings of the remaining symbols are: V_{tot}, total counts of the direct measured spectrum before applying momentum sampling function; E, incident positron energy; T, the sample temperature; O, total oxygen exposure; and f, the extracted Ps fraction(see Eq.(3.30)).

	$p_\perp$	$p_\parallel$	$p_\parallel'$	V_{tot} (10^3)	E (keV)	T ($^\circ K$)	O (L)	f (%)
Fig. 4.7a	111	$1\bar{2}1$	$10\bar{1}$	6976	^{22}Na	300		
Fig. 4.7b	111	$1\bar{2}1$	$10\bar{1}$	597	14.5	300		0
Fig. 4.7c	111	$1\bar{2}1$	$10\bar{1}$	388	1.5	300		35
Fig. 4.9a	100	011	$01\bar{1}$	426	1.5	300		33
Fig. 4.9b	100	011	$01\bar{1}$	247	1.5	600		65
Fig. 4.9c	100	011	$01\bar{1}$	383	5.0	750		7
Fig. 4.11a	110	$0\bar{1}1$	001	494	1.5	300		33
Fig. 4.11b	110	$0\bar{1}1$	001	654	1.5	300		40
Fig. 4.11c	100	001	010	463	1.5	300		32
Fig. 4.11d	100	011	$01\bar{1}$	510	1.5	300		34
Fig. 4.13a	100	011	$01\bar{1}$	402	1.5	300	150	38
Fig. 4.13b	111	$1\bar{2}1$	$10\bar{1}$	465	1.5	300	3×10^4	36
Fig. 4.13c	111	$1\bar{2}1$	$10\bar{1}$	852	1.5	300	1×10^6	0

smoothed version of the spectra as measured, the smoothing is accomplished by using 5 iterations Van Cittet's algorithm discussed in Chapter 3; (*ii*). Unless specified each spectrum is displayed with 14 contours, which is equivalent to displaying peak-normalized spectra with equal contour step; (*iii*). The single cuts at $p_\parallel$=0 or $p_\perp$=0 are made from the volume-normalized nonsmoothed spectra, by summing two nearest neighbouring channels, *i.e.*, -0.19 mrad and 0.19 mrad.

4.5.1. Incident Positron Energy Dependence- Fig. 4.7 shows three contour plots of the 2D-ACAR spectra for: (a). an Al(111)-^{22}Na-Al(111) sandwich sample; (b) an Al(111) surface bombarded with 14.5 keV incident positrons; and (c) the same surface bombarded with 1.5 keV positrons. A perspective view of the bulk spectrum (a) is shown in Fig. 1.5a. The cuts at $p_\parallel$=0 and at $p_\perp$=0 of these spectra are shown in Fig. 4.8. As it is well known[3,111], the bulk spectrum is close to the projection of a Fermi-sphere with a radius of ~6.8 mrad, reflecting the nearly-free electron

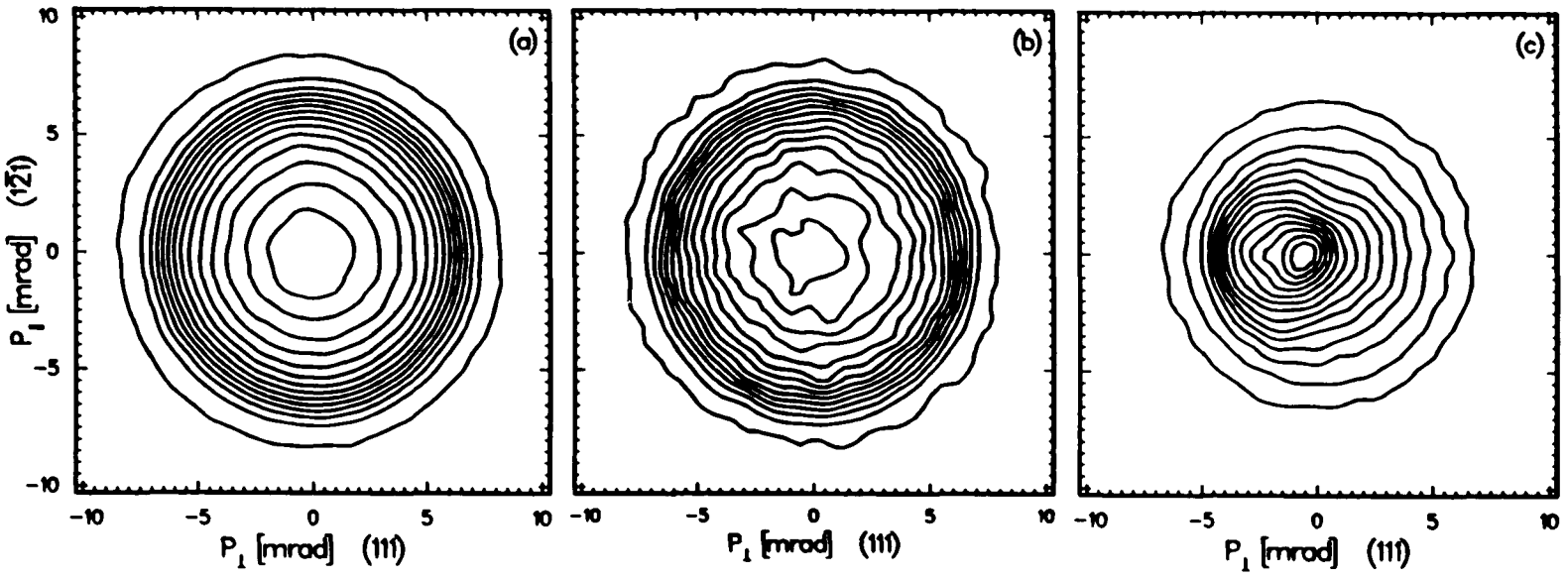

Figure 4.7. 2D contour plots of the directly measured ACAR spectrum for: (a). an Al(111)-^{22}Na-Al(111) sample; (b). an Al(111) surface bombarded with a 14.5keV positron beam; and (c). the same as (b), but the beam energy is 1.5keV.

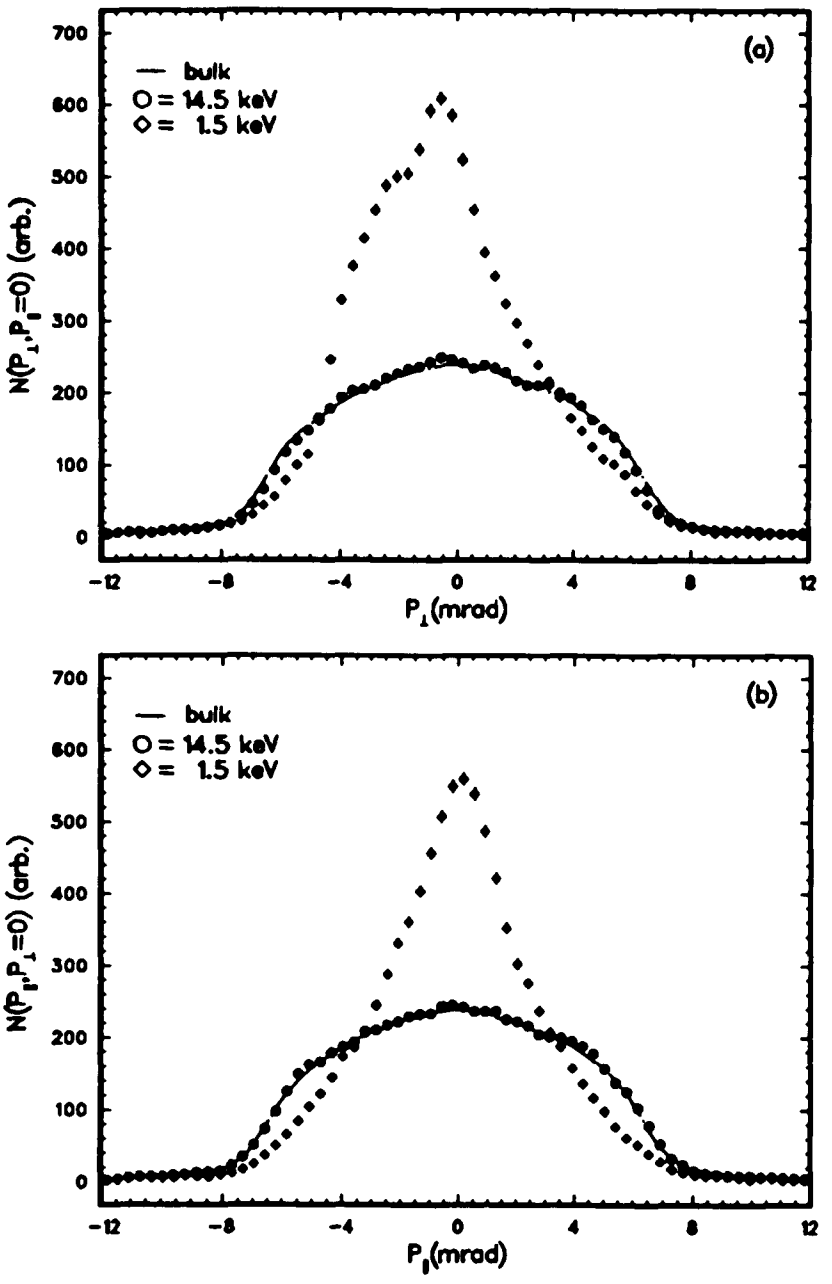

Figure 4.8. Cuts at (a). $p_{\parallel}$=0 and (b). $p_{\perp}$=0 of the three ACAR spectra shown in Fig. 4.7. The error bars for the 14.5keV curves are equivalent or smaller than the size of the symbols.

like conduction band structure of Al. We see that at E=14.5keV the spectrum (b) is almost the same as (a) except the central contours shift slightly towards the left due to a small fraction of Ps emission. Given the statistics and high incident energy, the small Ps fraction can not be estimated accurately from the measured spectrum. Estimation from Eq.(1.9) and Tbl. 1.1 gives 90% bulk annihilation and 10% Ps and surface state annihilation, which seems too large compared with our measurement. Fig. 4.8 shows a good quantitative agreement in their 1D cuts. This indicates that reliable position of $p_\perp$=0 can be obtained from a $\sim$ 15keV run. When the incident positron energy is reduced to 1.5 keV we observe Fig. 4.7c, which changes drastically from the high energy run. At this energy 70% of the incident positrons diffuse back to the surface and 35% of them form Ps and escape into vacuum. This leads to the antisymmetrical distribution with respect to the surface (or $p_\perp$=0). The effect of Ps emission can be seen more clearly from the cuts in Fig. 4.8a. In our coordinates Ps are emitted with negative $p_\perp$. The small plateau is associated with the Ps distribution and will be discussed in detail in latter sections. In $p_\perp$ >0 region, it mainly contains the positron surface state annihilation which is apparently much narrower than the bulk. The kinks at $\pm$ 5.5 mrad are the result of residual bulk annihilation.

Similar changes from Fig. 4.7b to Fig. 4.7c owing to the different incident positron energies have also been observed for Al(100) and Al(110) surfaces. These results are anticipated from previous slow positron beam experiments. The incident beam energy can be reduced further (200eV) to increase the surface signal and eliminate the bulk contribution. However, at lower energy nonthermal positron fraction is significant and will confuse the analysis of Ps spectra. Thus in all our surface measurements we select 1.5keV as the incident energy, at which the nonthermal fraction is about 2%[53].

4.5.2. Temperature Effect - Fig. 4.9 compares the measured ACAR spectra from an Al(100) sample at room temperature (a), 600° K (b) and at 750° K (c). The beam energy is 1.5 keV for (a) and (b), and 5 keV for (c). The perspective representations of (a) and (b) are shown in Fig. 1.5b and 1.5c. In order to see the intense peak structure graph (b) is plotted with 9 contours instead of 14 as there are in (a) and (b). Fig. 4.10 shows their cuts normal and parallel to the surface. The

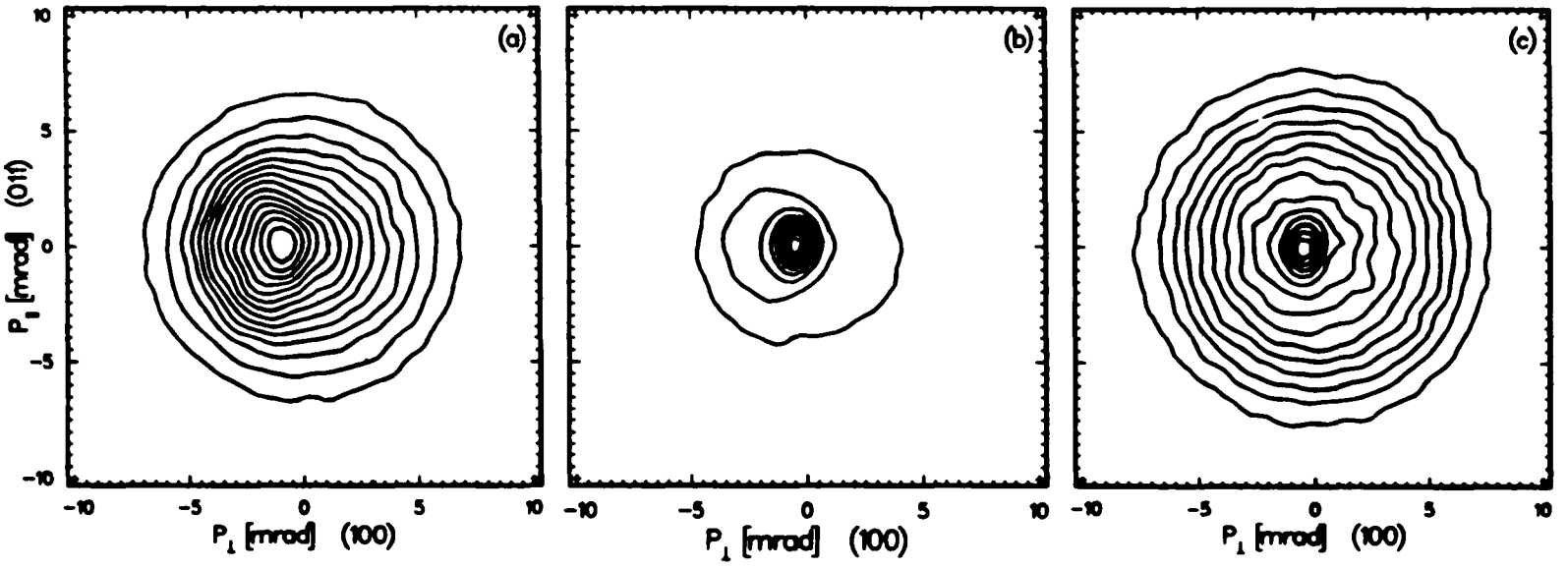

Figure 4.9. ACAR spectra for an Al(100) surface. The beam energy and sample temperature are: (a). 1.5keV, 300° K; (b). 1.5keV, 600° K; and (c). 5.0keV, 750° K. For clarity, (b) is plotted with 9 contours while (a) and (c) have 14 contours each.

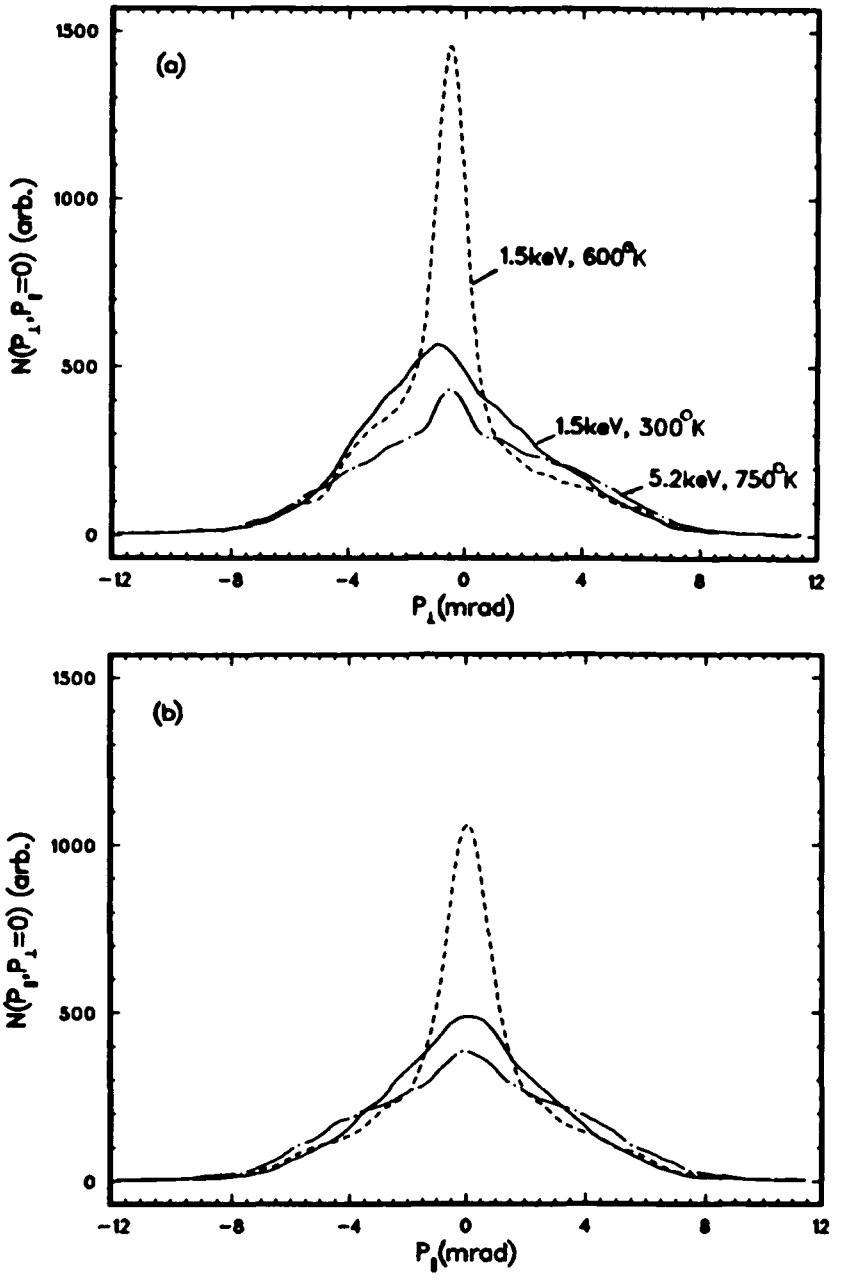

Figure 4.10. Cuts of the volume-normalized spectra of Fig. 4.9(a)-(c) at: (a). $p_{\parallel}=0$; and (b). $p_{\perp}=0$.

enormous change from (a) to (b) then to (c) clearly marks the change of the interaction mechanisms involved. The sharp narrow peak at $p_\perp$=-0.5 mrad indicates that a large fraction of thermal energy Ps are produced at the expense of a large reduction of positron surface state annihilation when the sample is heated to 600° K. Note that the temperature was chosen to be near T_v for Al at 1.5keV incident beam energy, so that the maximum thermal Ps fraction was obtained in accordance with Ref.[2]. The total Ps fraction* estimated later in §4.10 is 65%, and $\sim$ 85% of the positrons trapped at the surface are released as Ps at this temperature.

The peak in Fig. 4.9b drops dramatically at higher temperature and higher beam energy as can be seen in Fig. 4.10. The Ps fraction reduced down to 7% at 750° K. This change is consistent with positrons being effectively captured into the thermally activated vacancies[2]. As expected the annihilation spectrum is narrower than the bulk(Fig. 4.7a).

4.5.3. Crystal Orientation Dependence - We first inspect the azimuthal dependence of the surface ACAR spectrum taken with the 1.5keV beam. The spectra (a) and (b) in Fig. 4.11 are associated with the Al(110) surface being azimuthally rotated 90 ° with respect to each other(see Fig. 1.4). Namely, the projections were taken along the $\bar{\Gamma}\bar{X}$ or $(0\bar{1}1)$ for (a) and along $\bar{\Gamma}\bar{Y}$ or (001) for (b). Likewise for an Al(100) face, we show (c), projected along $\bar{\Gamma}\bar{X}$ or (001), and (d), the 45° rotation ($\bar{\Gamma}\bar{M}$ or $(01\bar{1})$ projection). The differences between (a) and (b) and between (c) and (d) are clearly small. They are most probably due to the small variations in the surface impurities rather than the azimuthal rotations.

Fig. 4.12a-c are the surface ACAR spectra taken at 1.5keV incident energy for Al(111), Al(100) and Al(110) surfaces. The projected and resolved directions parallel to the surfaces can be found in Tbl 4.2. They are the symmetrized version† of Fig. 4.7c, Fig. 4.9a and Fig. 4.11a, respectively. As can be seen that the symmetrization improves the statistics but maintain the original structures. It is clear that the right halves($p_\perp>0$) of (a)-(c) are similar to each other. On the left side($p_\perp<0$), the Al(111) spectrum (a) is closer to the Al(110) (c) but the two are very different

* The total Ps fraction is four times the para-Ps fraction which is measured in our ACAR experiment, also see §3.2.6.

† The symmetrization is two fold as defined by Eq.(3.19), also see §3.2.3.

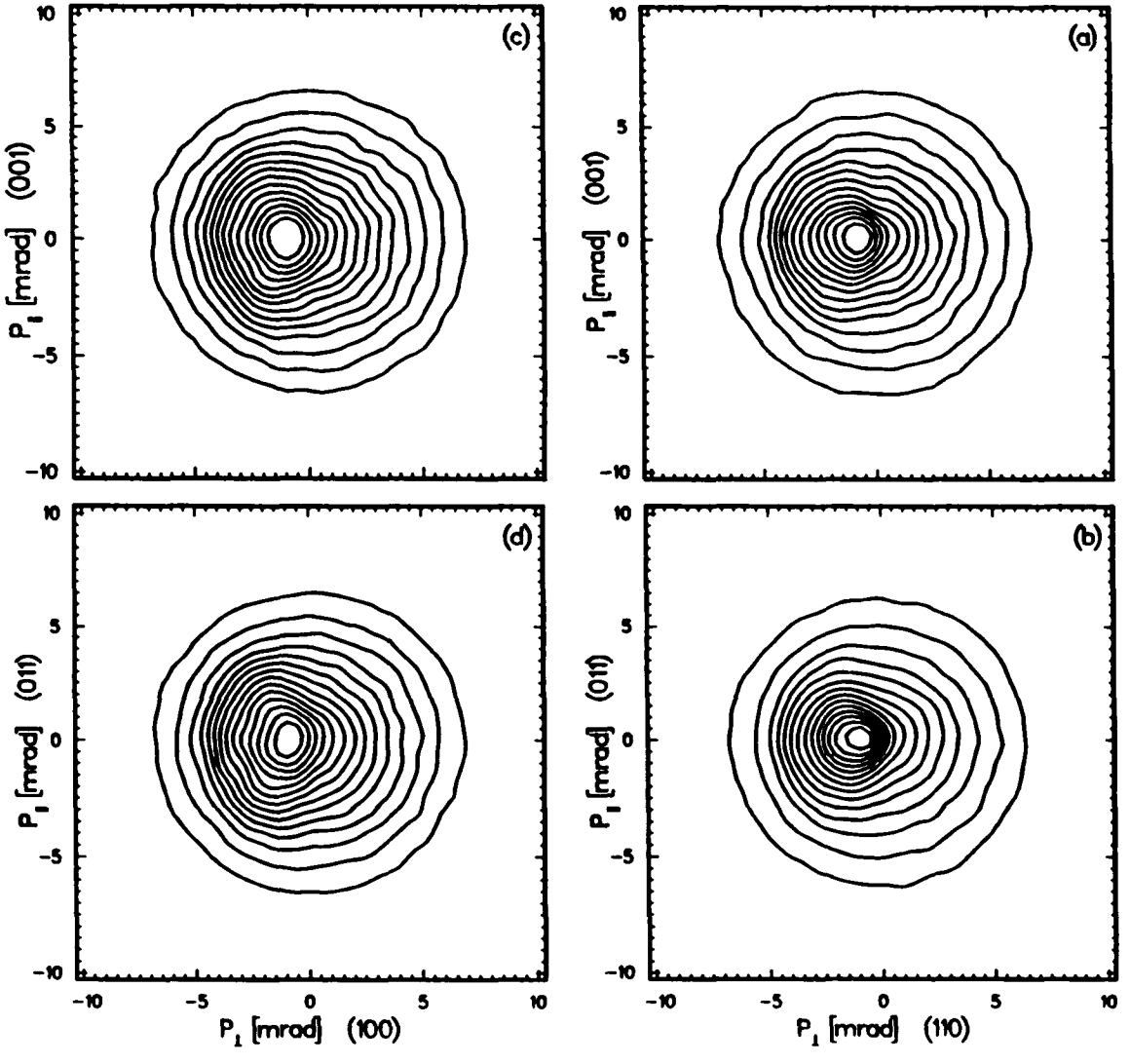

Figure 4.11. ACAR spectra for: (a). an Al(110) surface; (b). 90° azimuthal rotation of the Al(110) surface; (c). an Al(100) surface; and (d). 45° azimuthal rotation of the Al(100) surface. The beam energy is 1.5keV for all the runs.

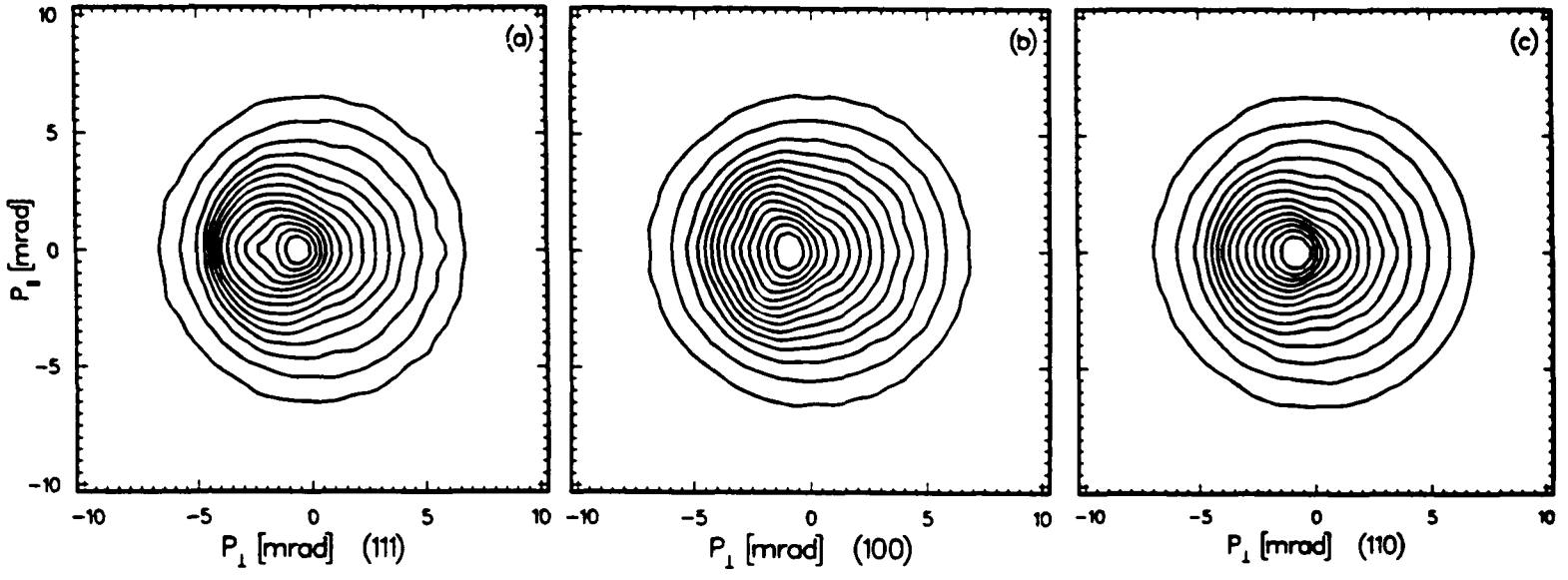

Figure 4.12. Symmetrized ACAR contour plots for clean surfaces of: (a). Al(111); (b). Al(100); and (c). Al(110). Spectra were taken at room temperature and 1.5keV incident energy. The unsymmetrized version of (a)-(c) are Fig. 4.7c, Fig. 4.9a and Fig. 4.11a, respectively.

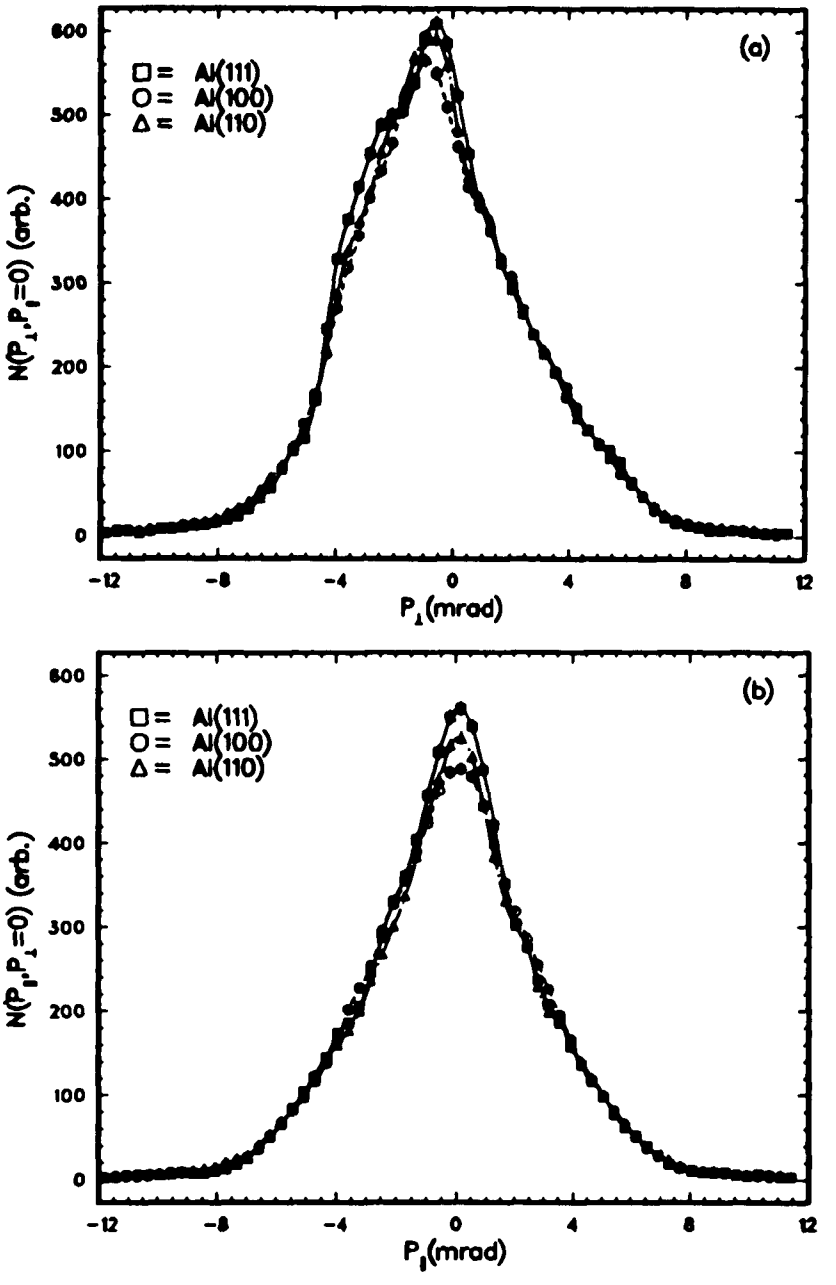

Figure 4.13. Cuts of the unsymmetrized versions of the spectra in Fig. 4.12a-4.12c at: (a). $p_{\parallel}=0$; and (b). $p_{\perp}=0$.

from the Al(100) spectrum (b). The (100) spectrum displays two side lobes that are absent in both the (111) and the (110) spectra. These similarities and differences can also be seen in their cuts at $p_{\parallel}$=0 and $p_{\perp}$=0 in Fig. 4.13. We see in Fig. 4.13a that the right hand shoulder coincides with each other. However, between $p_{\perp}$=-4.5 mrad and $p_{\perp}$=1.0 mrad there are statistically significant differences. These comparisons suggest that the Ps momentum distribution is much more strongly depends on the crystal orientations than the positron surface state annihilation. It will be shown that these structural differences can be attributed to the differences among the projected electronic band structures, and to a lesser extent, to the deviations of surface contaminations.

4.5.4. Oxygen Exposure - The ACAR results for three oxygen exposure on Al surfaces are shown in Fig. 4.14: (a). 150L on Al(100); (b). 3×10^4L on Al(111); and (c). 1×10^6L on Al(111). Again, we show their cuts at $p_{\parallel}$=0 and at $p_{\perp}$=0 in Fig. 4.15. For comparison a pair curves for the clean Al(100) spectrum(Fig. 4.9a) is also plotted in Fig. 4.15. Comparing the contour plots we see that the three lobes in Fig. 4.12a disappear when the Al(100) surface is exposed to 150L oxygen(Fig. 4.14a). The latter also results in a narrowing in the Ps distribution and in a 5% increase in total Ps emission fraction. Since this exposure leads to only a monolayer coverage the structure associated with the clean Al(100) sample is a surface effect. Fig. 4.14b shows that the Ps contribution is even sharper and narrower at high exposure. In this case overlayer Al-oxide is grown on the Al(111) surface the Ps spectrum mainly reflects the electronic property of the oxide rather than the metal substrate. When the exposure is increased to 1×10^6L, the spectrum (Fig. 4.14c) changed completely. Ps emission is almost zero. This is a clear indication of positrons being trapped in the disordered oxide layers or possibly in the interface region due to the increased thickness of the Al-oxide layer ($\sim$ 10 Å), and is in good agreement with the earlier studies[2].

In summary, we have demonstrated that the surface 2D-ACAR spectrum of Al has a strong dependence on the incident positron energy, sample temperature and oxygen coverage, but weaker on crystal orientations. We have also confirmed at least qualitatively some of the established processes such as positron diffusion, direct Ps emission, thermal desorption of surface state positron as Ps, trapping by thermally activated vacancies and by disordered oxide layers. All these

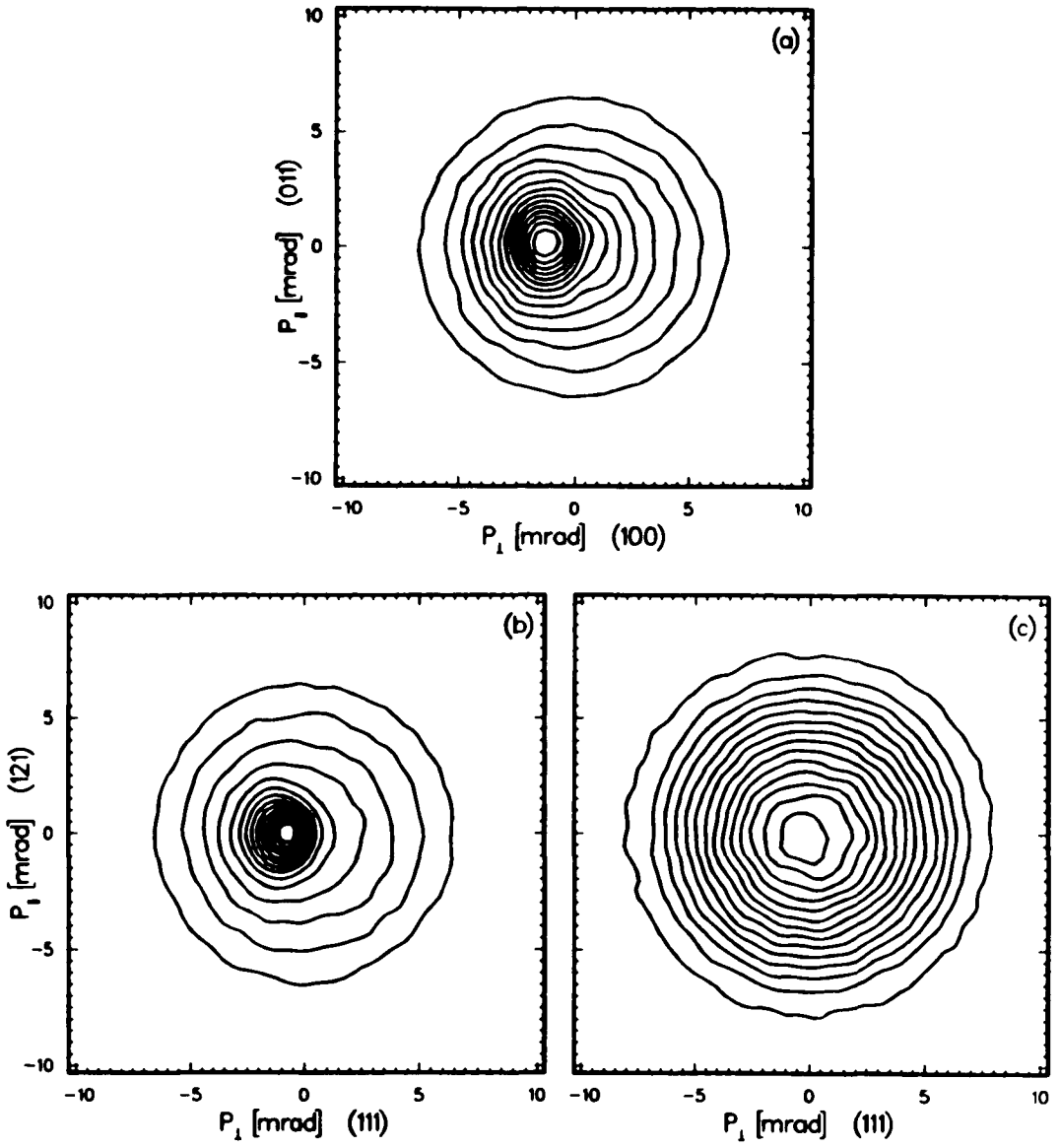

Figure 4.14. Contour plots of the ACAR spectra for oxygen exposed Al surfaces: (a). 150L/Al(100); (b). 3×10^4L/Al(111); and (c). 1×10^6L/Al(111). The beam energy is 1.5keV for all runs.

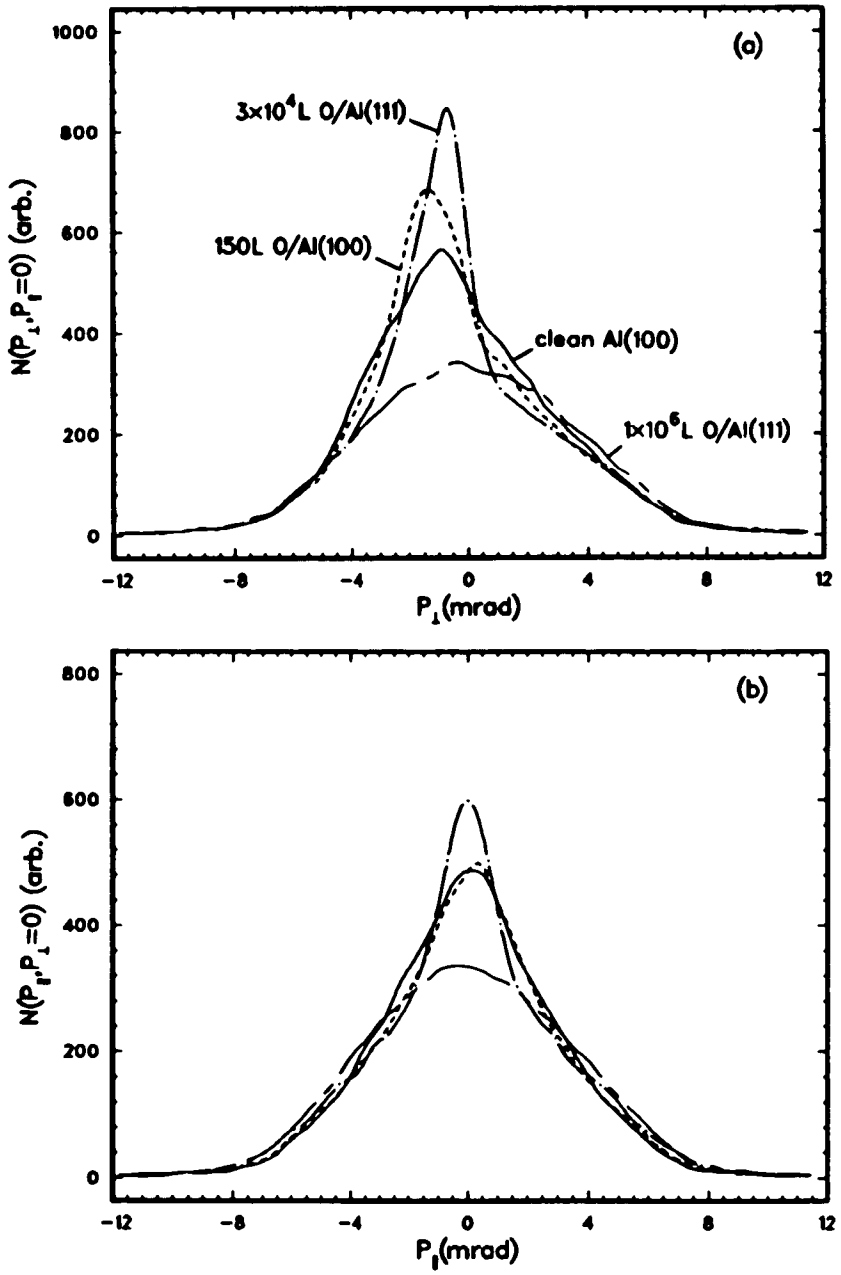

Figure 4.15. Cuts of the volume-normalized spectra of Fig. 4.9a and Fig. 4.14(a)-(c) at: (a). $p_{\parallel}=0$; and (b). $p_{\perp}=0$.

surface processes can be well studied by the ACAR technique. We shall now turn to a more quantitative analysis of our results.

§ 4.6 Positron Surface State Annihilation

4.6.1 Experimental Results - The technique of data separation has been described in detail in Chapter 3. Fig. 4.16 illustrate the original and the decomposed spectra in their one dimensional cuts at $p_{\parallel}$=0 for an Al(100) run using the 1.5keV beam. In Fig. 4.16(a) the triangles represent the total measurement, circles are the generated symmetrical distribution and diamonds are the differences between the total and the symmetrical distributions, *i.e.*, the separated Ps spectrum. The identity between the total and the symmetrical in the region $p_{\perp}>0.5$ mrad and $p_{\perp}<$ -6 mrad reflects the reliability of our data separation technique and the accuracy of our zero $p_{\perp}$ determination. The deconvolution step assures that the symmetrical curve turns over to the left in a natural way, as expected from the finite detector resolution, to avoid the unphysical sharpness at $p_{\perp}$=0 otherwise. The Ps distribution terminates at $\sim$ -5mrad. This is expected since the -2.6eV Ps work function converts to a maximum allowed Ps momentum of q_M=4.5mrad and our apparatus resolution is about 1mrad FWHM. We shall restrict ourselves to the surface state annihilation in the present section and leave the Ps spectra for §4.8.

Note that the symmetrical spectrum still contains some fraction of the bulk annihilation. For an incident energy of 1.5keV, we estimated from Eq.(1.9) and Eq.(3.36) that the symmetrical spectrum contains 30 vol% bulk contribution. Since the bulk spectrum is essentially isotropic(the umklapp annihilation intensity is much smaller), we choose to subtract the high statistical bulk data(Fig. 4.7a) from all the 1.5keV symmetrical spectra to obtain the surface state spectra. Fig. 4.16(b) shows the three curves: the symmetrical in circles, the 30 vol% bulk in crosses, and the difference in diamonds. The 2D contours of the symmetrical spectra before and after the removal of the 30 vol% bulk spectrum are plotted in Fig. 4.17(a)-(b), respectively. Remember that the left half is made up from rotating the right half by 180°, hence the spectrum shows an absolute inversion symmetry. We can see that after removing the bulk component the surface state spectrum

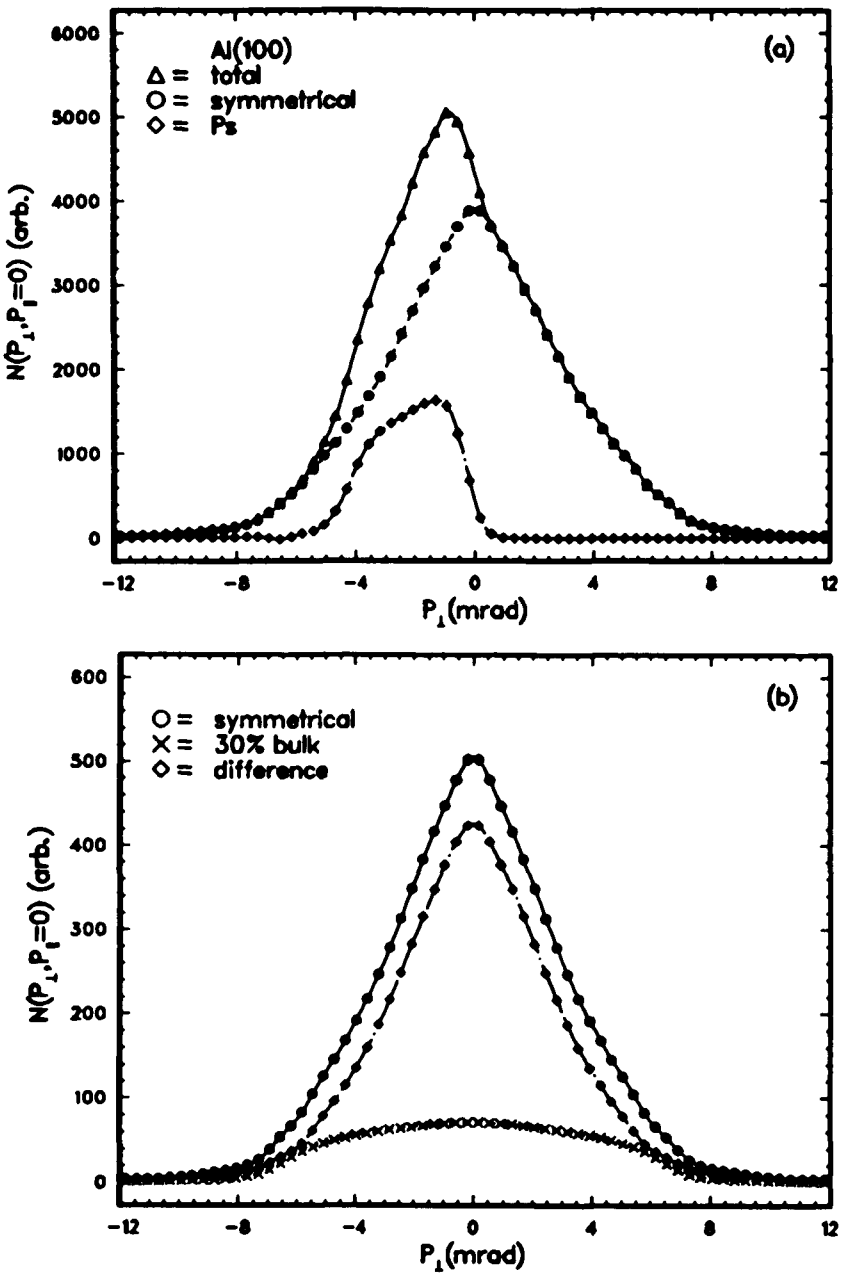

Figure 4.16. (a). $p_{\parallel}=0$ sections of the direct measured spectrum(triangles), the separated symmetrical part(circles) and the separated Ps spectrum(diamonds) for an Al(100) surface taken at 1.5keV beam energy. (b). Sections at $p_{\parallel}=0$ of the above symmetrical spectrum, a 30% bulk Al spectrum and their difference, i.e. the surface state spectrum.

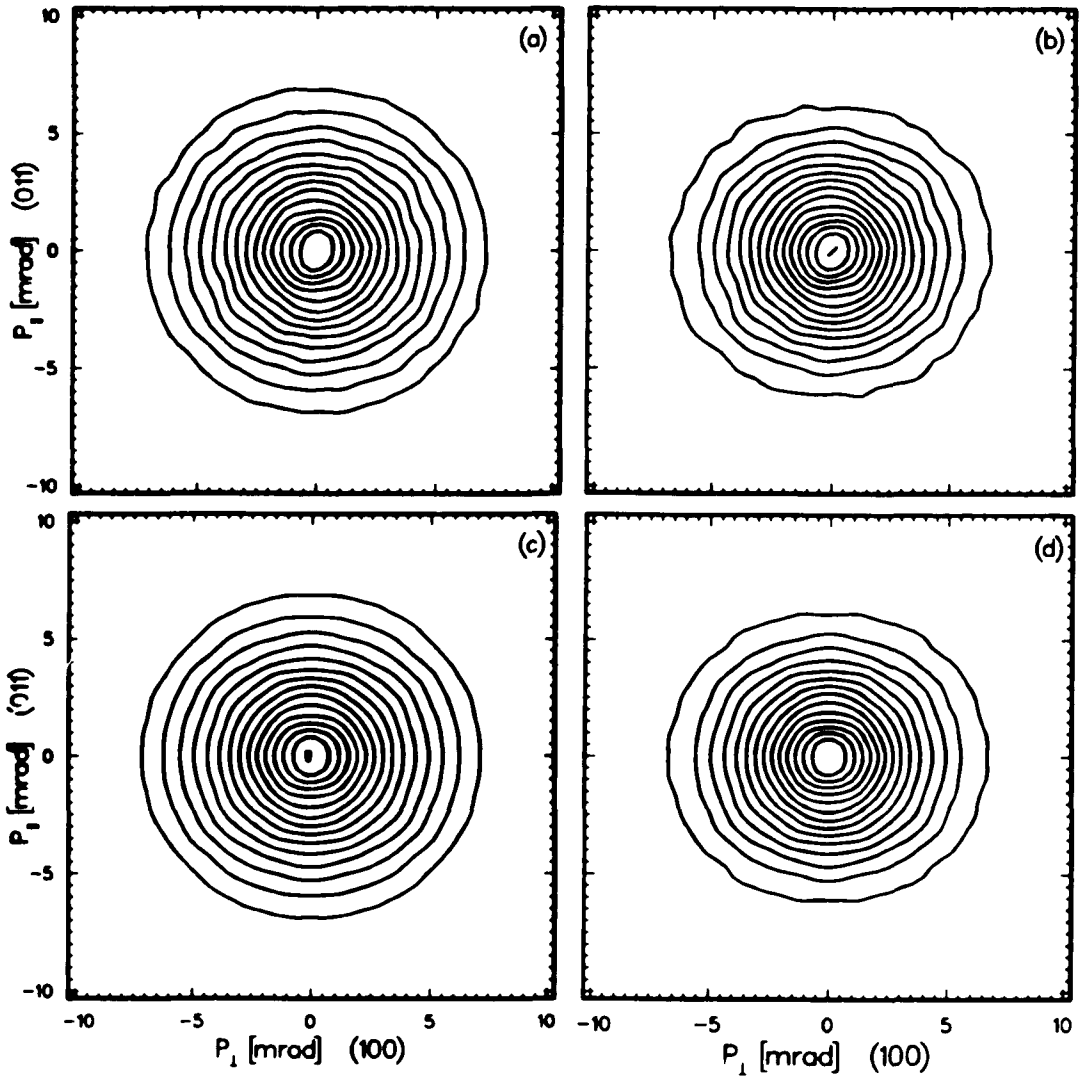

Figure 4.17. Contour plots of (a). the symmetrical and (b). surface state spectra extracted from an Al(100) surface run with a beam energy of 1.5keV. Frame (c) and (d) are the corresponding contour plots generated from the symmetrized version of the same run as (a) and (b). Their cuts at $p_{\parallel}=0$ are shown in Fig. 4.16.

(b) shows a small elongated shape in the outer contours. The $p_\perp$ direction is slightly longer than the $p_\parallel$ direction. These can be seen more clearly in Fig. 4.17(c)-(d), which are the corresponding spectra of (a) and (b) extracted in an identical manner from the symmetrized original spectrum. The symmetrized version provides a better way of displaying the structure of interest. Thus in the remainder of this section we shall only present symmetrized spectra for 2D contour plots.

In Fig. 4.18 we collected a set of surface state spectra taken for the three surfaces at room temperature bombarded with the 1.5keV positron beam. The index in the up-left corner of each frame indicates the crystal orientation along the resolved parallel momentum direction. They are labeled as: (a). for an Al(110) surface(from Fig. 4.11b); (b). for the same surface rotated by 90° (from Fig. 4.11a); (c). for an Al(100) surface (from sum of Fig. 4.9a and 4.11d); (d). for the same surface rotated by 45° (from Fig. 4.11c); (e). for sum of three contaminated Al(100) surface runs($\sim$ 0.1ML oxygen), azimuthal angle being mixed; (f). for an Al(100) surface exposed to 150L oxygen, corresponding to 1ML coverage(from Fig. 4.14a); (g). for an clean Al(111) surface(from Fig. 4.7c); and (h). for the same surface exposed to 3×10^4L oxygen(from 4.14b). As can be seen (a)-(d) and (g) are very similar, despite the fact that Al(110) runs are not as clean as the rest). They all demonstrate a small anisotropy along the outer contours($|p|$: 4 $\sim$ 7 mrad). Spectrum (e) is estimated to have oxygen contamination increased to 0.1ML, but it shows little change from the two clean surfaces (c) and (d). When the Al(100) surface is exposed to 150L oxygen the spectrum (f) becomes flatter on the top and more isotropic with a slight increase in width. The overlayer Al-oxide spectrum (h) changes even more. The outer contours are fairly circular and inner ones become elongated in the opposite directions as compared with the spectrum (g).

To examine the anisotropy between the normal and parallel distributions we first compare the long slit projection along these two directions. Fig. 4.19 shows a set of peak-normalized long slit curves in one to one correspondence with the spectra in Fig. 4.18 according to their alphabetical labels. In the region between ±4 to ±7 mrad, curve (a) through (g) display a slightly narrower distribution in the direction parallel to the surface(diamonds) compared with the distribution normal to the surface. The difference in the oxygen exposed Al(100) curve (f) is smaller than

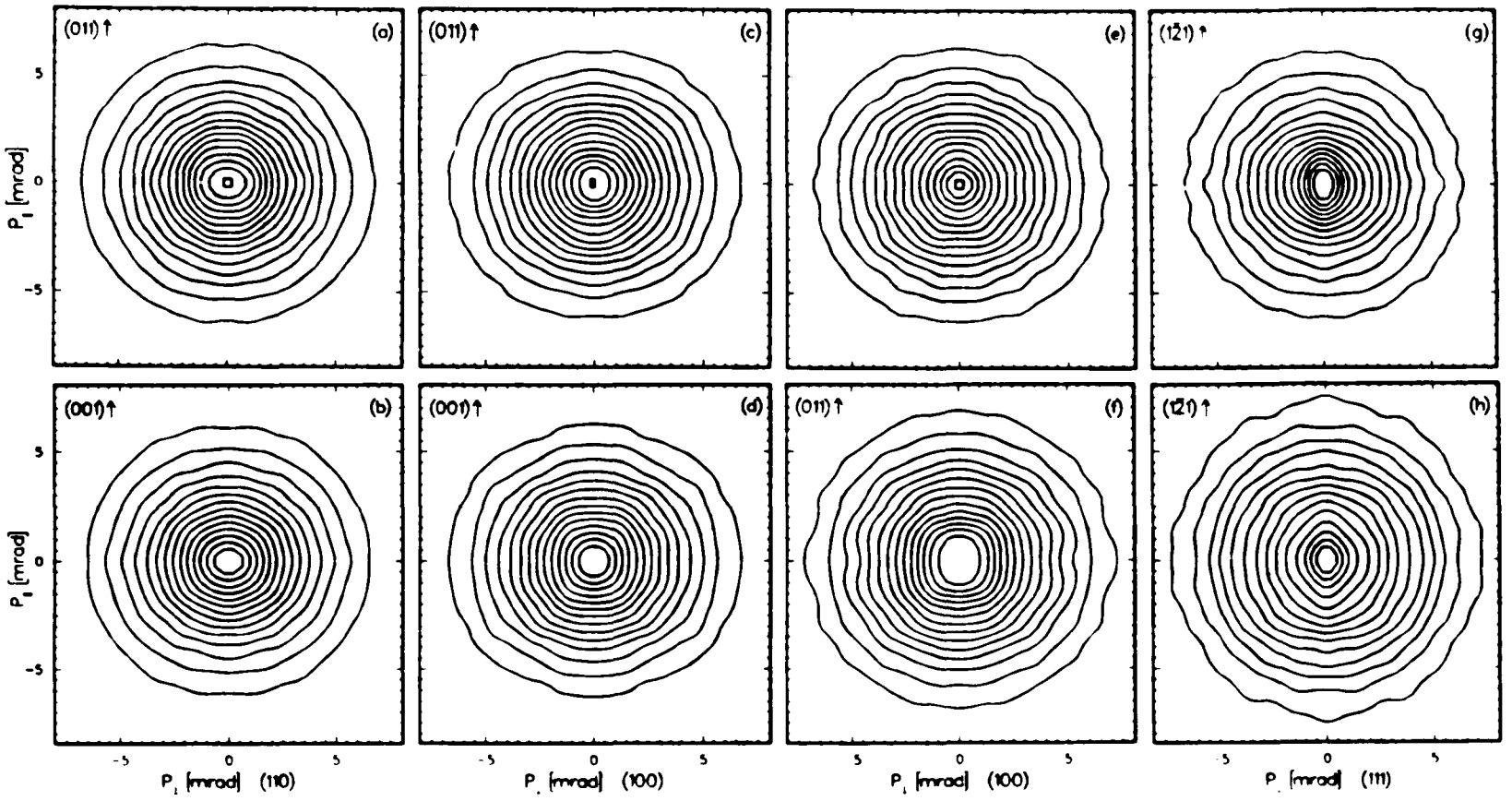

Figure 4.18. Contour plots of positron surface state ACAR spectrum for: (a). an Al(110) surface; (b). the Al(110) surface rotated by 90° azimuth; (c). an Al(100) surface; (d). the Al(100) surface rotated by 45° azimuth; (e). a contaminated Al(100) surface($\sim$ 0.1ML oxygen); (d). an Al(100) surface exposed to 150L oxygen; (e). an Al(111) surface; and (d). the Al(111) surface exposed to 3×10^4L oxygen.

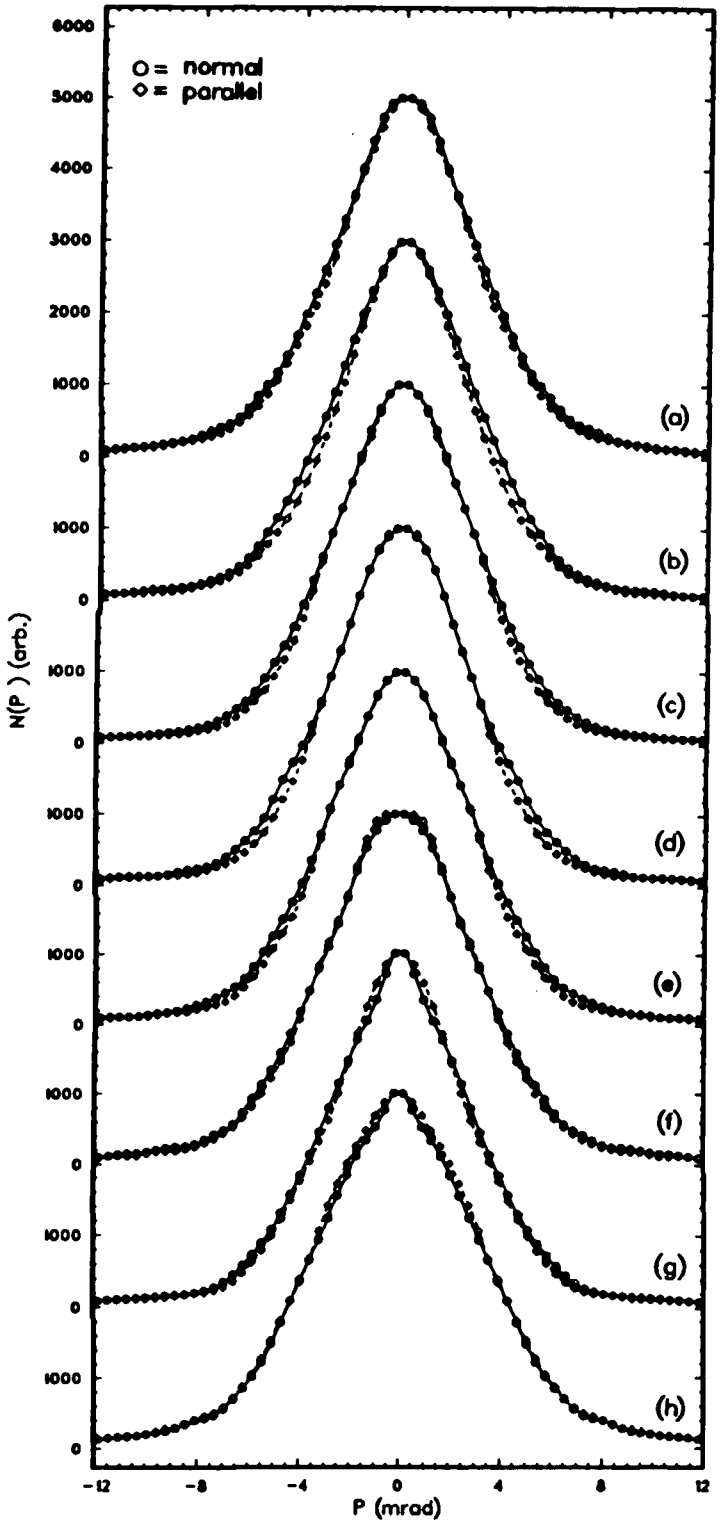

Figure 4.19. Peak-normalized long-slit spectra generated from the 2D-spectra shown in Fig. 4.18. The labels are in one-to-one correspondence.

that associated with clean surface (c) and (d) and with the contaminated surface(e). In this region the difference in (g) disappears when overlayer oxide is grown on the Al(111) surface (h). On the lower momentum side (0 to ± 4 mrad), some deviations can be observed amongst the curves. In curve (a) and (b) the small anisotropy persist while for curve (c),(d) and (e) the distributions in the two directions are almost the same. For the oxygen exposed surface, curve (f) shows more flattening on the parallel direction than the normal. For curves (g) and (h) the small anisotropy occur in the opposite order. Single cuts at $p_{\parallel}$=0.19mrad and at $p_{\perp}$=0.19 mrad are also generated similarly in Fig. 4.20. The extraction of error bars is explained in chapter 3. The data points are correlated due to the data separation thus appear more smoother than the error bars represent. All the features identified in Fig. 4.19 can also be found in Fig. 4.20.

Note that in Figs. 4.19-4.20 a small distortion from a true surface state distribution in the vicinity of $p_{\perp}$ =0 may still retained, even though our data separation technique appears to work very well. Fortunately, the detector smearing of Ps distribution into $p_{\perp}>0$ region can extend no more than $\sim$ 1.5mrad(3σ). Beyond that the direct measured spectrum is purely from the surface state annihilation, and thus it is important to inspect this region as well. Fig. 4.21 compares the single cuts made at $p_{\parallel}$=1.7mrad(circles) and $p_{\perp}$=1.7 mrad(diamonds) from the original measured spectra minus 27 vol%(see Eq.(3.35)) of the high statistical bulk spectrum. The inset in the left frame shows the cut positions. We notice that near the zero($p_{\perp}$=0), the normal curves are always higher than the parallel, indicating the smearing effect of the Ps spectrum. Again, in the large momentum region we observe the similar deviations shown in the Fig. 4.18-Fig. 4.20 But in the low momentum region it is not clear that there are statistically significant difference between the normal and parallel distributions.

One important point should be borne in mind when one is comparing the width between the normal and parallel distributions. The uncertainty in the position of $p_{\perp}$ origin will result in a linear deviation in the normal distribution, which could affect the width. In the present case, we see in Figs. 4.18-4.21 that matching the normal and parallel distributions in the large momentum region will require to offset the normal distribution by $\sim$ 0.2 mrad which is 5 times the uncer-

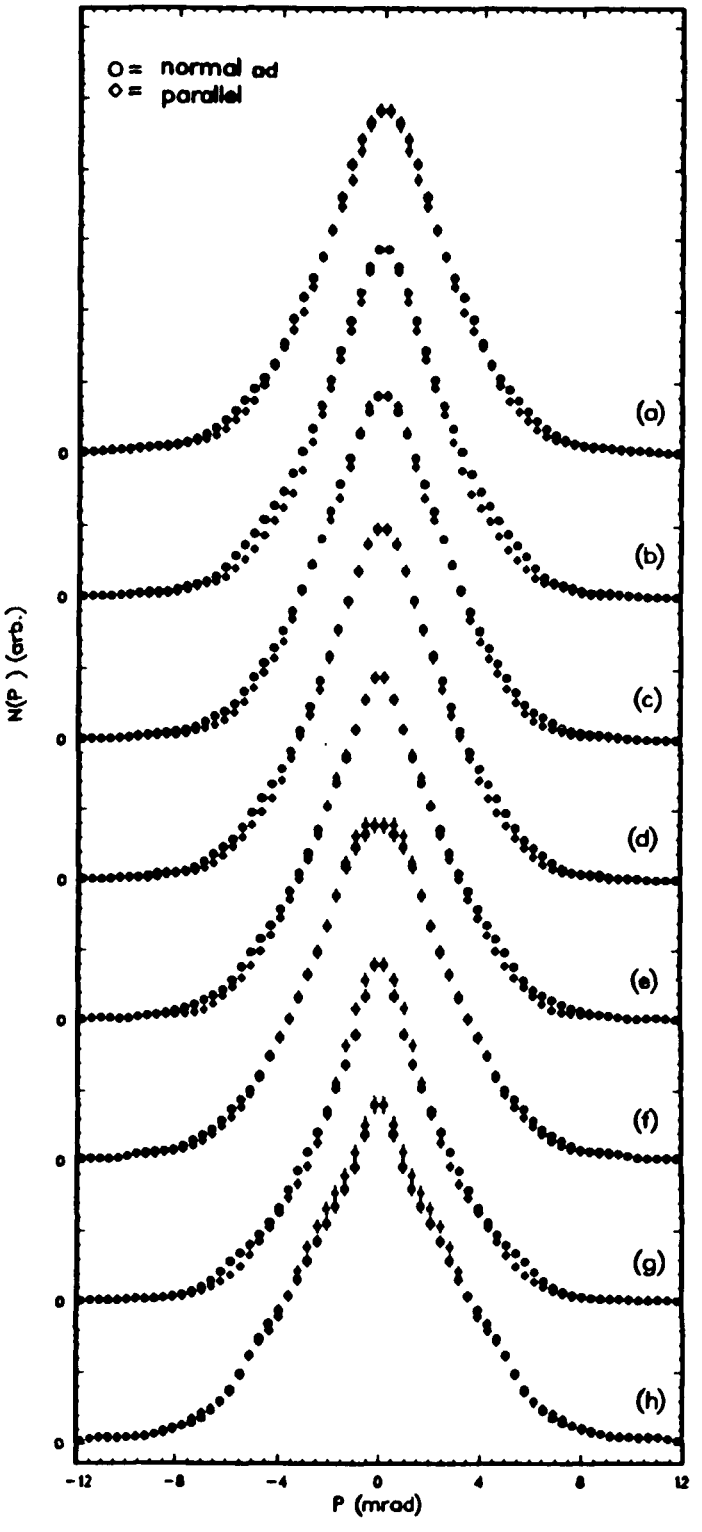

Figure 4.20. Cuts at $p_{\parallel}$=0 and $p_{\perp}$=0 for each of the surface state spectrum shown in Fig. 4.18. The labels are in one-to-one correspondence.

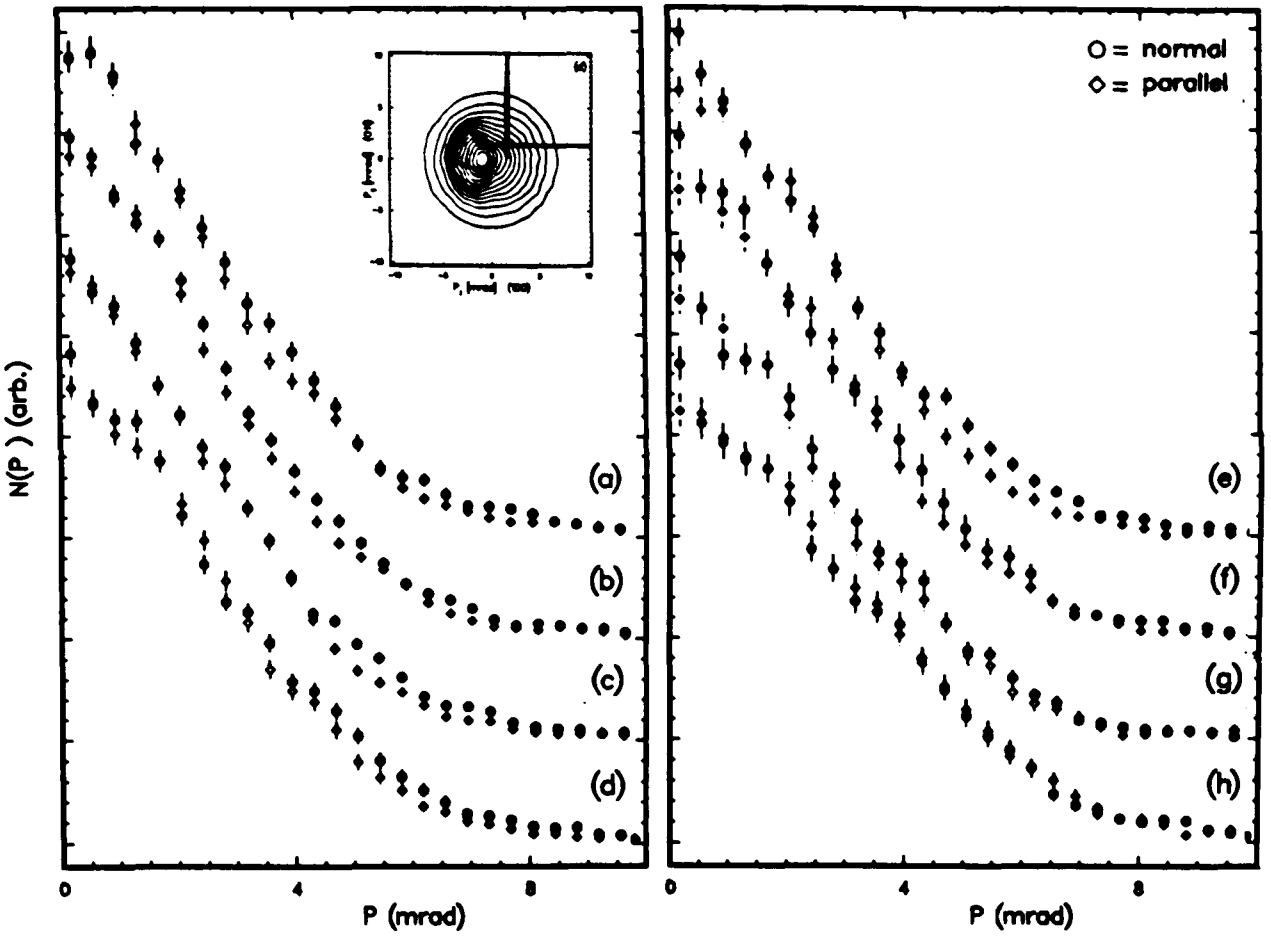

Figure 4.21. Cuts at $p_{\perp}$=1.68 mrad and $p_{\parallel}$=1.68 mrad(shown in the inset) of the original spectrum for each of the surface state spectrum shown in Fig. 4.18. The labels are in one-to-one correspondence.

tainty of the $p_\perp$ origin. This attempt will inevitably introduce an anisotropy in the low momentum region, and produce a Ps spectrum with momentum greater than q_M and with a too large total fraction. Further more taking into account the sample size effect will only result in narrowing the parallel distribution slightly and thus enchance the anisotropy shown in the above figures. Thus it is appropriate for us to conclude that for three low index surface of Al, positron surface state annihilation spectrum exhibits only a small anisotropy in the momentum region From ± 4 to ± 8 mrad.

Comparisons between the different spectra in Fig. 4.18 are shown in Fig. 4.22 and Fig. 4.23 for the long slit spectra and for the zero cuts, respectively. The perpendicular distribution is plotted on the right while the parallel are plotted on the left. The symbols are labeled alphabetically in one to one correspondence with each frame in Fig. 4.18. Curves (*i*) to (*iii*) are volume-normalized for the purpose of comparing the three crystal orientations; two different projections of the Al(100) surface and the Al(110) surface. That the parallel momentum curves higher than the normal curves is consistent with the previous observations that the parallel distributions are slightly narrower. Curves (*iv*) and (*v*) are peak- normalized in order to better compare the widths. Curve (*iv*) compares clean Al(100) spectrum with the contaminated ($\sim$ 0.1ML oxygen) and the 150L oxygen exposed Al(100) surface($\sim$ 1ML). The effect of oxide layers grown on an Al(111) surface is shown in curve (*v*). The following conclusions can be drawn: 1). for three low index surfaces of Al, the positron surface state annihilation spectrum weakly depends on the crystal orientation and the azimuthal projection angle; 2). the averaged FWHM of the clean spectra is 5.3 mrad, less than half of the width in the bulk annihilation; 3). monolayer oxygen coverage on Al(100) surface leads to a 10% increase in the width of surface state spectrum; and 4). overlayer Al-oxide on an Al(111) surface broaden the spectrum by 1mrad.

4.6.2 Comparison with Theory - Two positron surface state potentials(Fig. 1.3a), the classical static image potential[40,41] and the screened static image potential[41], have been described in §1.2.5. Based on these models Nieminen and Manninen[41] have calculated the 2γ-angular correlation spectrum for the long-slit detector geometry. They predicted a large anisotropy

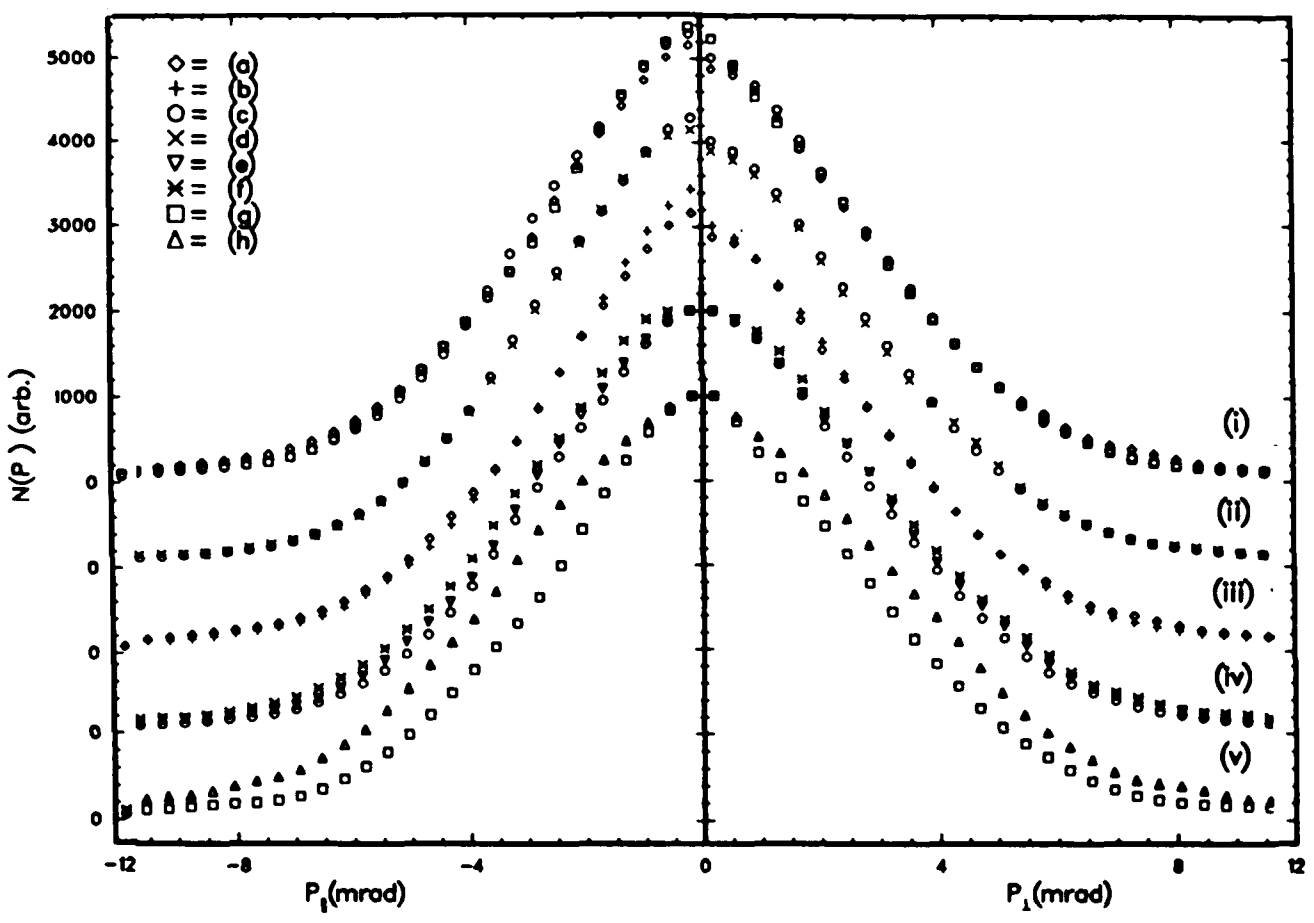

Figure 4.22. Long-slit spectra: the perpendicular momentum component on the right and the parallel momentum on the left. Each symbol is related through the same label to the surface state spectrum shown in Fig. 4.18. (i) to (iii) are area normalized and (iv) and (v) are peak normalized.

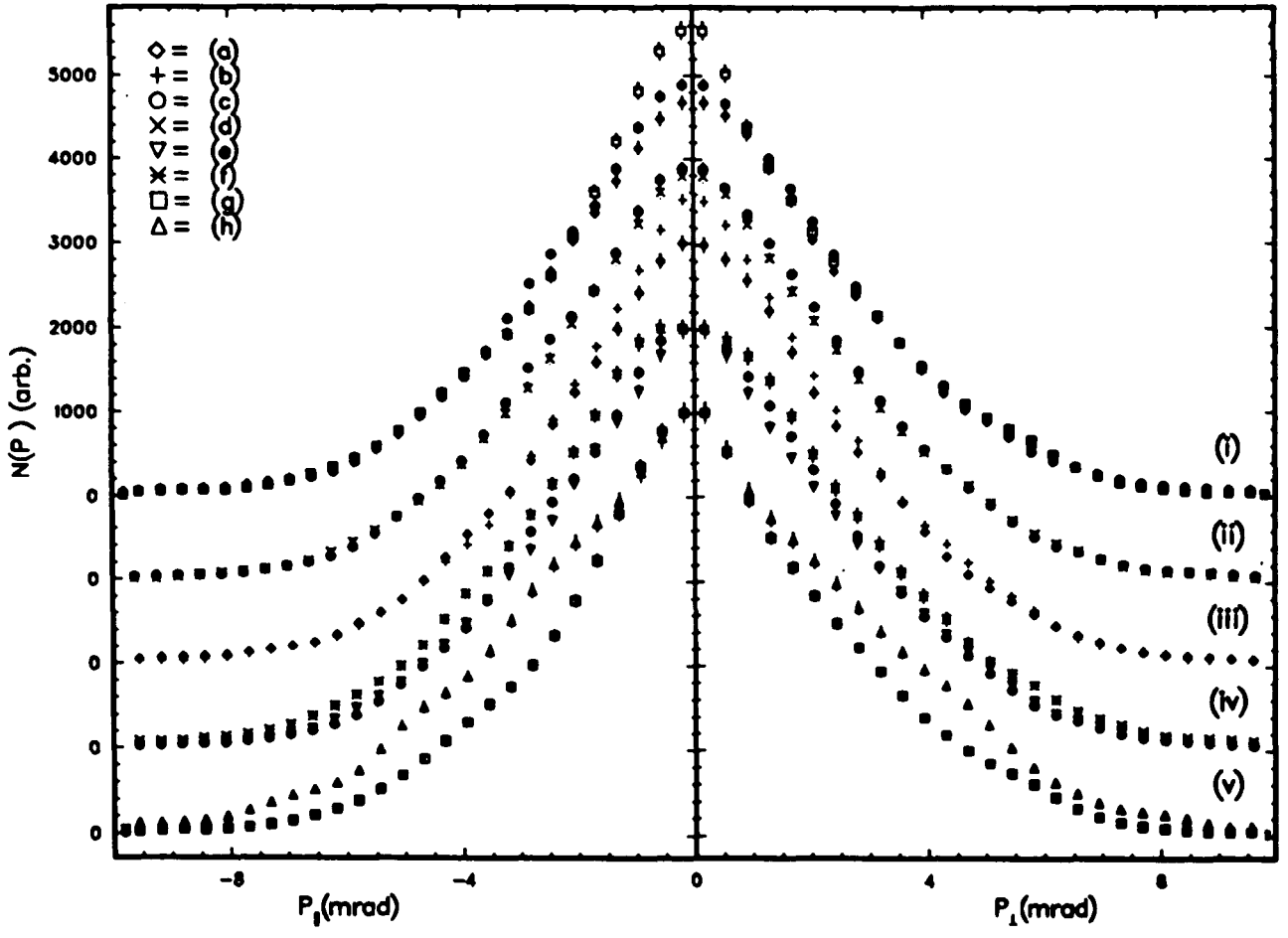

Figure 4.23. Single cuts at $p_{\parallel}$=0(on the right) and at $p_{\perp}$=0(on the left) of the surface state spectra shown in Fig. 4.18. Each symbol is related through the same label to the spectrum shown in Fig. 4.18. (i) to (iii) are area-normalized and (iv) and (v) are peak-normalized.

between the distributions of the momentum components parallel and perpendicular to the surface. When the long-slit spectra are area-normalized the peak height of the parallel distribution is twice that of the normal, indicating a substantial broadening in the normal momentum component due to the positron localization perpendicular to the surface. This result was found to be independent of the model potentials; (they also included the dynamic nature of the image interaction[41]). A separate jellium model calculation[42] showed that using a $\sim$ 1 Å wide square potential well for the positron state, the averaged positron momentum contributes to half of the total width in the normal distribution.

Similar calculations have been repeated[44] using the above two potentials and various surface electron density after the first two reports of the surface ACAR measurements on an Al(100) surface and a Cu(121) surface[7,8]. It was shown[44] that the mixed-density approximation (MDA) yields less anisotropy than the IPM, and the 2γ-angular correlation spectrum has a strong dependence on the form of the potential, which is in contradiction to the Nieminen and Manninen's conclusion[41]. In the upper-right frame of Fig. 4.24 comparisons of the long-slit spectra from the MDA calculation[44] using the Lang-Kohn electron density are reproduced. Curves 1 are the results of the screened potential while curves 2 are for the simple static potential. The solid curve is the free electron bulk spectrum. On its left plotted three corresponding experimental spectra(not numbered) for an Al(100) surface and for a bulk Al. For comparing the widths the perpendicular distribution of curves 1 on the right is also shown on the left. Curve 3 will be discussed later. The lower figure shows the 2D contours of the measured surface state spectrum(left) and the theoretical spectrum of the simple potential. Although the simple potential (2) produces much less anisotropy compared with the screened potential (1), the disagreement with the experiment is still large. In addition to the substantial anisotropy, the widths of curves 2 are too large compared with the measured spectra. The normal distribution of curves 1 is in good agreement with the measurement but its parallel momentum component is much too narrow, and it results in a large anisotropy. The calculated positron binding energy is 2.37eV for the classical potential (2), and 4.05eV for the screened potential (1). The effective image plane induced in potential (1)

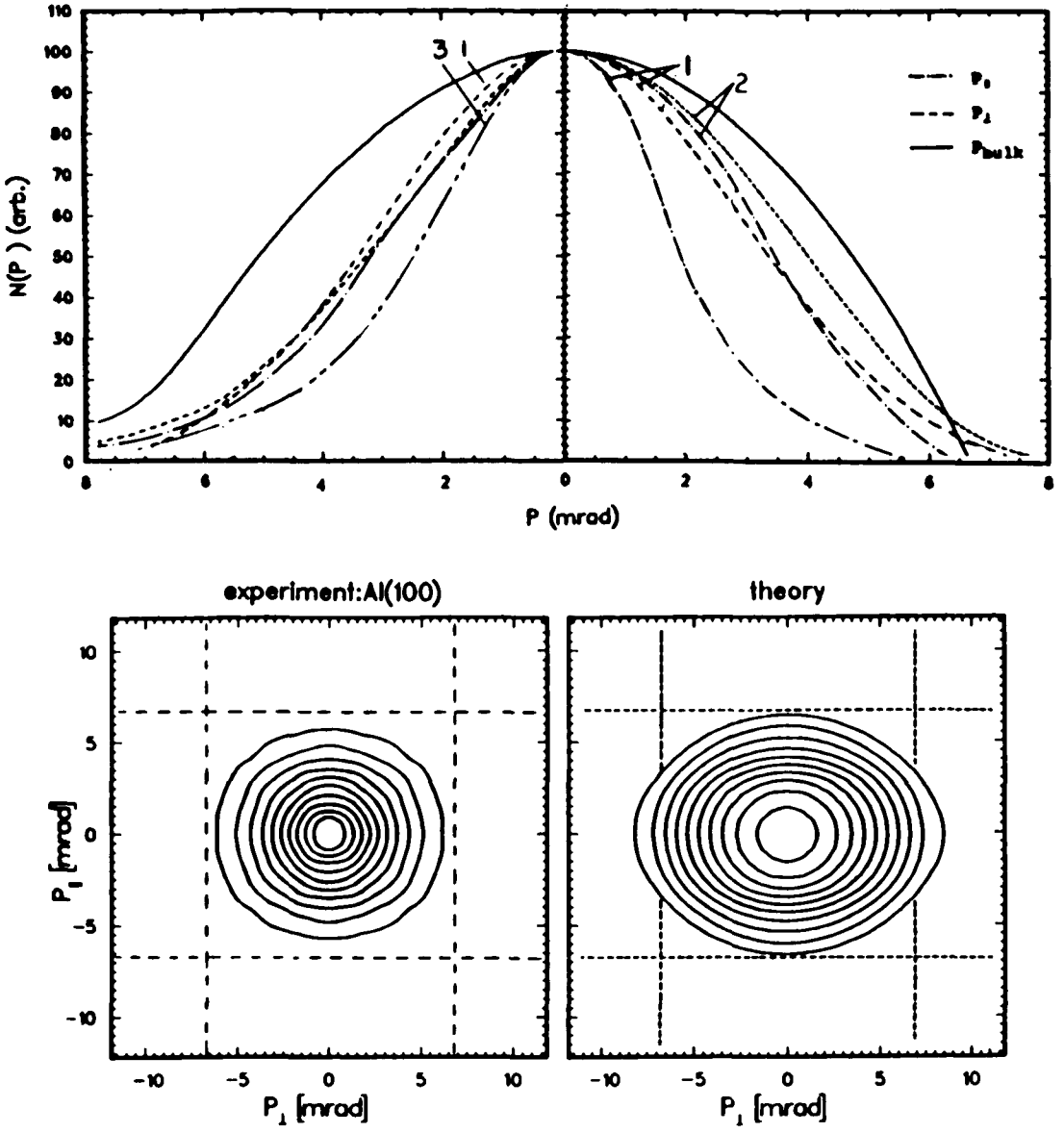

Figure 4.24. Top-right: long slit spectra of the Al positron surface state from MDA calculations(after Ref.[44]) using the Lang-Kohn electron density and a screen static image potential(curves 1), or the classical static image potential(curves 2); the solid curve is the free-electron long slit spectrum for bulk Al. Top-left: unnumbered are the experimental spectra for an Al(100) surface and for a bulk Al corresponding to those shown on the right; dashed curve 1 on the left is the same as the right; curve 3 is the prediction of the physisorbed Ps surface state on Al(Ref.[46]). Bottom: 2D-contour plots of the experimental surface state spectrum and the theoretical surface state spectrum for the static image potential(from Ref.[44]).

is responsible for the deeper bound state, which in turn leads to an narrower annihilation momentum distribution, especially in the parallel momentum component. Nevertheless, these theoretical calculations do demonstrate narrower surface state distributions compared with the bulk state(solid), characterizing the inhomogeneous electron density at the surface.

In the physisorbed Ps picture of Platzman and Tzoar[46](see Fig. 1.3b in §1.2.5), the 2γ-angular correlation distribution reflects the center-of-mass(CM) motion of the weakly bound Ps atom. Normal to the surface, this model yields approximately a Lorentzian squared long-slit distribution with a full-width of 4.8 mrad, which is shown as curve 3 in the upper-left frame. It is about 20% narrower than the experimental results. Parallel to the surface, the angular correlation arises from the recoil momentum of the CM due to the emission and re-absorption of a surface plasmon via a higher order virtual process. Consequently, the width is comparable with the normal width and the total spectrum is isotropic. The in-plane recoil effect is introduced to avoid the large anisotropy if the physisorbed Ps atom is to be thought as a free moving object in the surface plane.

In his variational calculation[48], Cuthbert has compared the above two distinct surface states using a hydrodynamic(HD) model for deriving the image potential from the positron(Ps)-plasmon interaction. It is concluded that the Ps state cannot be ignored in HD calculation of positron binding to a surface. It is argued that because of the positron's very reduced overlap with the bound electron(the consequence of the HD model), the dominate contribution to the decay rate arises from its overlap with the plasma, thus annihilation is expected to occur predominately through 2γ-decay, and angular correlations are expected to reflect the momentum distribution of electrons in the plasma. However no quantitative prediction for the angular correlation is given. We note that in low density insulator crystals(*e.g.* , quartz, ice), Ps atoms are formed and annihilate in a large fraction via a pickoff process[26], in which the positron of an ortho-Ps annihilate with a host electron of opposite spin. Similar process may also need to be consider in the surface Ps state model.

The lack of a substantial anisotropy in our measured positron surface state ACAR spectra

suggest that the positron surface state is not extended in the surface plane. It is pointed out in Ref.[8] that localised surface states could be induced by some surface defects, or by impurity adatoms. Further theoretical investigations are needed to understand what type of complete localized state would be much more stable than the image potential induced surface state for a positron at the surface. From their discrete-lattice calculation[41] of the image induced positron surface state, Nieminen and Puska concluded that monovacancies play little or no role for positrons on Al surfaces. Using a fixed effective image plane(§1.2.5), they also predicted that the surface diffusion constant $D_+=1.4cm^2/sec$ for Al surfaces. This, together with the measured surface state lifetime of 580 psec for the Al(110) surface[39], corresponds to a lateral diffusion length of $\sim$ 3000 Å. If the positron surface state was to be localized in the surface plane, it then indicated that the up limit of the surface defect concentration is $\sim$ 1/3000 Å. This would not be unrealistic for the Al surfaces, if the defects were steps or ledges[63]. In our analysis, it is found that small contamination(0.01-0.1ML) of oxygen does not change the surface state spectrum noticeably. This is somewhat surprising since the theoretical calculation[90] showed that the O2p electron are highly surface localised and they form lowlying bands(Fig. 4.6) with a width of $\sim$3eV. We might expect some observable effect due to the positron annihilation with these localized O2p electrons.

To date no theoretical computations have been performed using a realistic electronic band structure. As shown in Fig. 4.3-4.5, the projected band structures of three low index surfaces of Al are very different. More projected gaps appear in the (100) and the (110) face electronic band structures. However, our measurement showed very little variations among the positron surface state ACAR spectra of these surfaces. A possible explanation for this is that the total occupied states are much greater than the gaps and the localized surface states. It should be important to see whether or not theoretical model would predict any anisotropy in this regard.

§ 4.7 Annihilation in Near Surface Defects

The behavior of positron at the presence of vacancies, dislocations and voids in bulk Al has been studied in some detail[25,113,114]. We have shown in Fig. 4.9 and Fig. 4.15 that the surface

ACAR measurement is sensitive to the near surface defects: thermally activated vacancies and disodered oxide layers. It should be mentioned here that these two runs were partially explored to obtain the symmetrical spectra in a shorter runing time, owing to the narrower distributions, for the determination of the $p_\perp$=0 position. Thus in this section we will only briefly analyse these spectra and make comparison with the surface state annihilation.

In Fig. 4.25a we replot the contours of the ACAR spectrum (Fig. 4.9c) collected at 750° K and with a beam energy of 5keV after it is symmetrized and 7% positronium is removed. Since there are essentially no Ps formation and emission from the 10 Å oxide layer covered Al(111) surface, its spectrum in Fig. 4.14c is symmetrized in both normal and parallel direction and is shown in Fig. 4.25b. Within statistical fluctuation the two spectra are essentially circular. This has also been confirmed by checking the normal and parallel cuts. Comparing with the bulk spectrum of Fig. 4.7a and the Al(100) surface state spectrum of Fig. 4.17d, we see that Fig. 4.25a-b are narrower than the bulk spectrum but broader than the surface state spectrum. Fig. 4.25c shows the parallel cuts at $p_\perp$=0 of these four spectra which are peak-normalized. Curve (i) is from the bulk spectrum of Fig. 4.7a, (ii) and (iii) are from frame(a) and (b) in the same figure, and curve (iv) the surface state spectrum in Fig. 4.17d. From (i) to (iv), the FWHM changes from 11.8 mrad to 9.4 mrad, 8.7 mrad and 5.3 mrad, characterizing four different environment surrounding the positron.

We note that curve (ii) has two shoulders. Similar structure has been observed in previous bulk measurements[113,114], which also demonstrated a progressive weakening of the umklapp or higher momentum components as the temperature is raised until at $\sim$ 900° K the spectrum becomes essentially isotropic and the humps diminish. These are an unambiguous manifestation of the transformation of a positron from a delocalized Bloch state to a vacancy-trapped state. The spectrum taken at 900° K[114] has a FWHM of $\sim$ 10 mrad, narrower than our 750° K run. This may be puzzling at first glance. From the monovacancy formation entropy, enthalpy(H_{1V}^F=0.62eV) and the specific trapping rate given in Ref.[2] we estimate that at 750° K sample temperature $\sim$ 10% of the annihilation inside the bulk are from the delocalized Bloch state. This will broaden the spectrum compared with the case of saturated trapping at 900° K. On

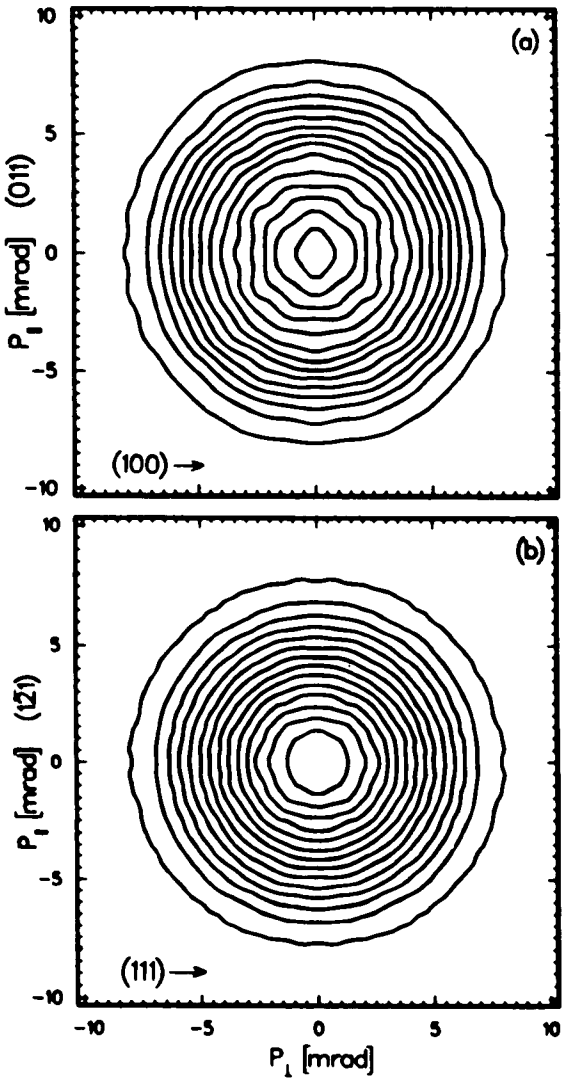

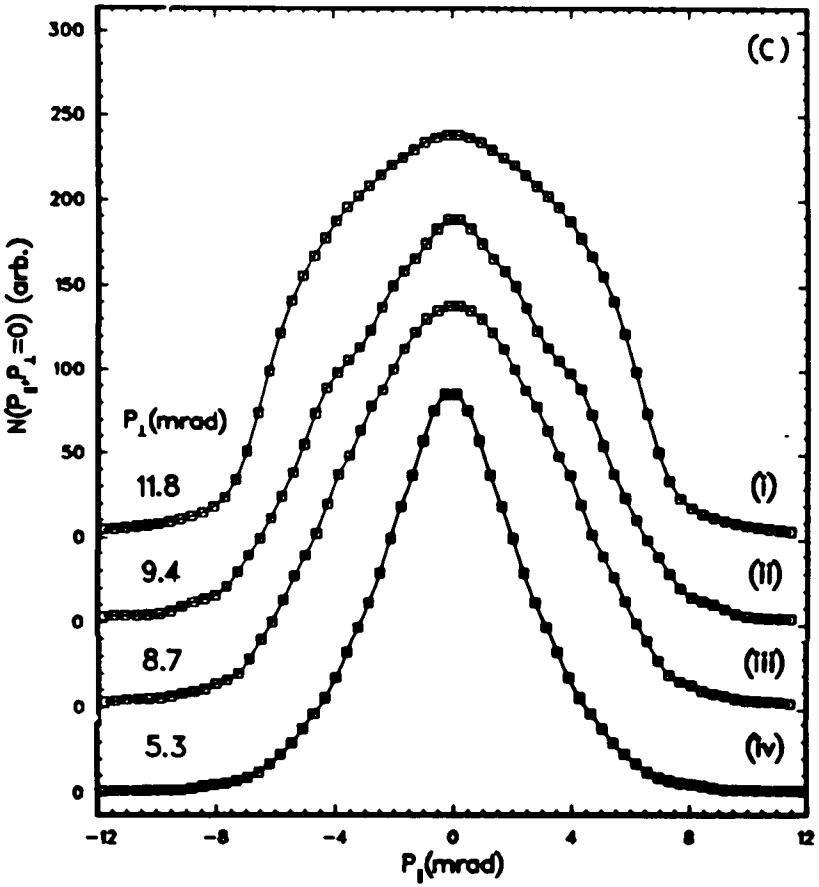

Figure 4.25. (a). Contour plot of Fig. 4.9c after the removal of the Ps component; (b). Four-fold symmetrized version of Fig. 4.14c. (c). Sections at $p_\perp$=0 for: (i). the bulk spectrum of Fig. 4.7a; (ii). spectrum (a) on the left; (iii). spectrum (b) on the left; and (iv). the surface state of Fig. 4.17d; the FWHM is indicated for each curve.

the other hand, 7% Ps emission at 5 keV incident positron energy suggests that $\sim$ 9% incident positrons are captured in the exterior surface state which narrows the total symmetrical spectrum. Thus the combination of these two factors is responsible for the narrower width as well as for the shoulders.

The Al-oxide spectrum(Fig. 4.25b) was obtained with a beam energy of 1.5keV, in frame (c) the clear distinction of curve (iii) from (i) and (iv) implies that most of the implanted positrons are trapped in the amorphous oxide layers. Although 1×10^6 oxygen exposure leads to $\sim$ 10 Å oxide layer and at 1.5keV the mean implantation depth is $\sim$ 250 Å , the smooth and narrower distribution compared with the bulk distribution (i) indicates that very little(if any) thermalized positrons are reflected from the interface back to the bulk and annihilate with the bulk characteristic. However, it is possible that some of the incident positrons could be trapped in the interface region. Since in the case of overlayer Al-oxide, most of the positrons reach the exterior surface, we feel that trapping of positrons in the Al-oxide and Al substrate interface region can not be a dominating process here.

We may wish to make some connections of the interior localized states with localized states in the external surface. In fact, the image induced surface state model was historically proposed[40] to describe the trapping of positrons in voids, named internal surface state. Obviously if a void is large enough the properties of the metal-void interface must be similar to those of an exterior metal surface. Namely, the trapped positron is strongly localized perpendicular to the void walls but essentially delocalized along the walls. However, the annihilation spectrum for the above two type of defects is much broader than the external surface state annihilation spectrum. Therefore, their physical environment differs from the exterior surface.

§ 4.8 Positronium Momentum Distribution

Fig. 4.26 shows a set of separated Ps spectrum contours. Each spectrum contains $\sim 4\times10^4$ counts. In order to improve the statistics and to better display the structures, the spectra are obtained from the symmetrized versions of the original measurements (see §3.2.3). The crystal

orientations along the two resolved momentum directions are indicated in the lower left corner and the total Ps fractions are given in up left. A conservative estimate of the error bars associated with these calculated Ps fraction is ±3%. Note that the contours are rotated 90° clockwise from the previous presentations. All the spectra shown here are taken with a beam energy of 1.5keV. Frame (a)-(c) are for Al(111), Al(100) and Al(110) surfaces, respectively. Frame (d) is for the clean (111) surface (a) exposed to 3×10^4L oxygen. Frame (e) is for the same clean Al(100) surface (b) but with a 45° azimuthal rotations, and (f) is for the Al(110) surface (c) rotated by 90° azimuth. Frame (g) and (h) are for, respectively, an Al(100) surface exposed to 150L oxygen or contaminated with oxygen up to $\sim$ 0.1ML during the run. The sections through $p_{\parallel}=0$ and $p_{\perp}=-1.7$ mrad of the spectrum (a)-(c), (g) and (d) are plotted in Fig. 4.27. For clean surfaces all the runs started with less than 0.06ML carbon and 0.01ML oxygen impurities. At the end of measurements the carbon level remains the same and the oxygen increased to $\sim$ 0.05ML for the Al(111) and Al(100) surface, but to $\sim$ 0.1ML for the Al(110) runs since this face has highest oxygen sticking coefficient. The 150L oxygen exposed Al(100) surface is estimated to have 1ML coverage.

The Ps spectra in the first row vary significantly from one face to another. While both Al(111) and Al(110) spectra(a and c) display isotropic† distributions the Al(100) spectrum (b) shows a clear anisotropy characterized by the three statistically significant lobes. The common feature appear in all three spectra is the sharp rise near the origin, especially for the Al(110) spectrum. The two spectra in the right column corresponds to the same Al(110) surface but with two different projection angles. Their structures are very similar, except the lower one has higher Ps fraction and is slightly more peaked which is due to more oxygen contamination as a result of 3 hours longer data collection time. Similarly, the first two spectra in the middle column are for an Al(100) surface projected along (011) and (010) directions, respectively. The 45° azimuthal rotation(e) does not change the Ps spectrum appreciably. However, the three lobes present in the Al(100) spectra disappear when the surface is exposed to 150L oxygen(g) or when the surface is contaminated with $\sim$ 0.1ML oxygen(h). The thin oxide layer covered Al(111) produces a much

† Here the meaning of "isotropic" is with respect to the structures in the spectrum, and is not to be confused with its use in the previous section, since Ps is always emitted asymmetrically.

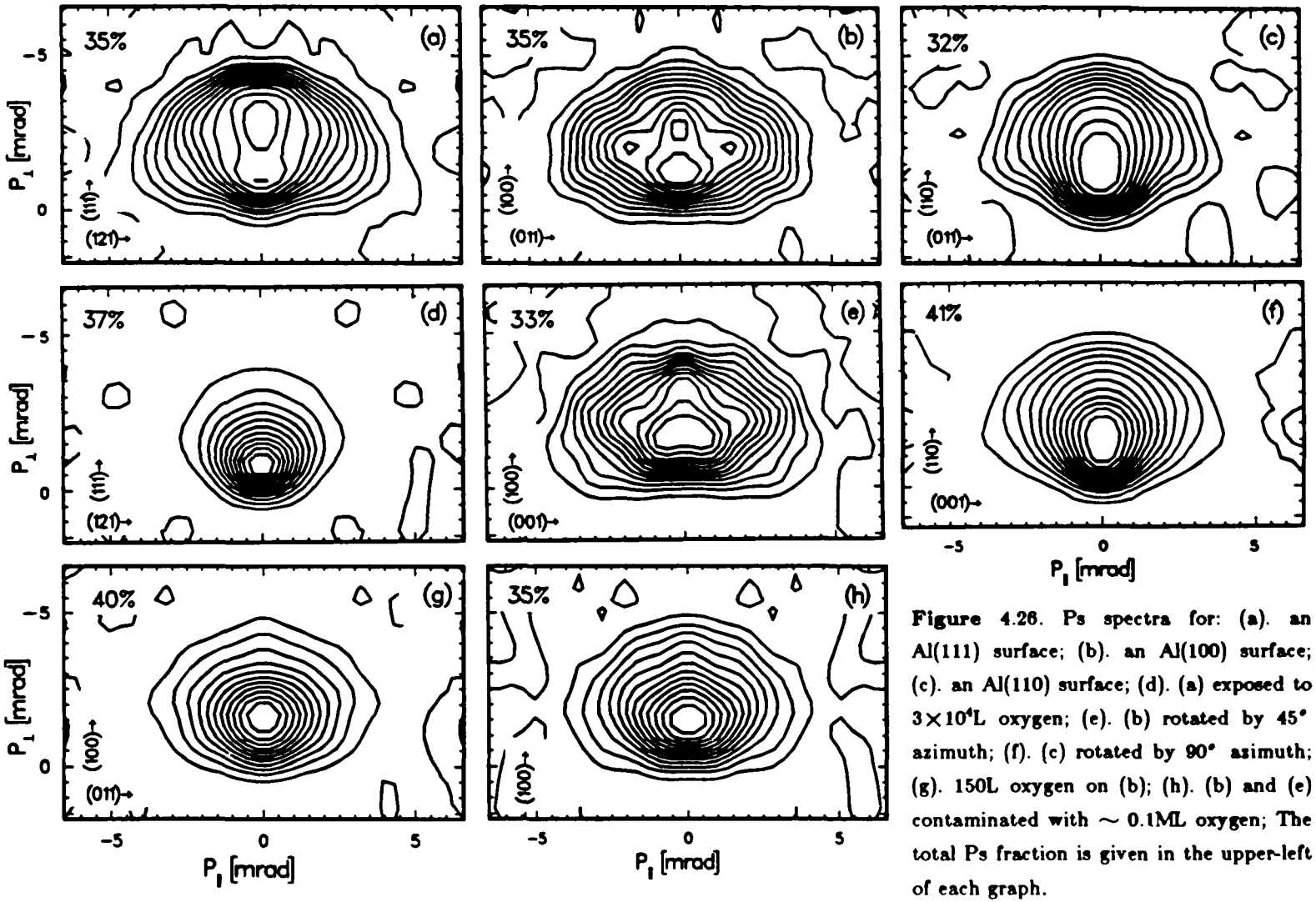

Figure 4.26. Ps spectra for: (a). an Al(111) surface; (b). an Al(100) surface; (c). an Al(110) surface; (d). (a) exposed to 3×10^4L oxygen; (e). (b) rotated by 45° azimuth; (f). (c) rotated by 90° azimuth; (g). 150L oxygen on (b); (h). (b) and (e) contaminated with $\sim$ 0.1ML oxygen; The total Ps fraction is given in the upper-left of each graph.

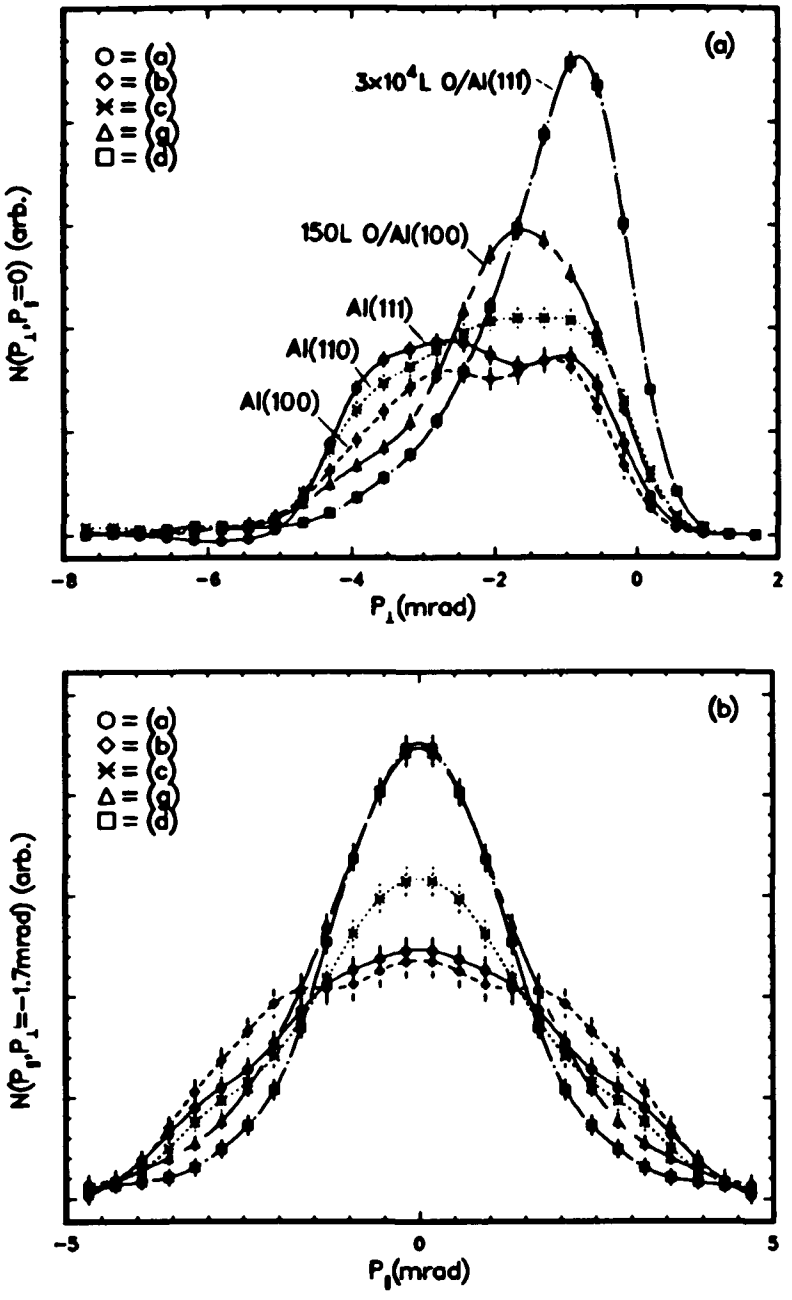

Figure 4.27. Sections through: (a). $p_{\parallel}=0$; and (b). $p_{\perp}=-1.7$ mrad of the volume-normalized Ps spectrum in frame (a),(b),(c),(d) and (g) of Fig. 4.26.

narrower Ps spectrum (d) with a most probable momentum of $\sim$ 1 mrad (*i.e.*, a most probable energy of $\sim$ 130 meV).

The three lobes appear in the clean Al(100) Ps spectra are directly connected to those appeared in the direct measured spectra shown in Fig. 4.12. This structure was reproduced from the resputtered and repolished Al(100) surfaces, but never appear in the other two faces of Al, Si surfaces or a Ni surface. The lobes are very sensitive to the oxygen impurity in the surface, whose presence tends to destroy this structure. Therefore, it becomes evident that this feature is associated with the clean Al(100) surface only. To show that the three lobes are indeed present independent of the symmetrization, we plot in Fig. 4.28 the unsymmetrized version of Fig. 4.26b and a set of parallel cuts.† The anisotropy seen in the cuts persists in a range of at least 2 mrad. Thus we believe that the anisotropy of the data is established without a doubt.

Fig. 4.26h and 4.26g shows that the effect of accumulating $\sim$0.1ML oxygen on a clean Al(100) surface during the run is very similar to that of oxygen exposure to the clean surface up to a monolayer. To study this effect in more detail we have performed a sequential run with three hours each following the initial preparation of the Al(100) sample. The results are shown in Fig. 4.29, where each spectrum contains a total counts of $\sim 1\times10^4$. We note that the anisotropy present in frame (a) gradually diminishes and the momentum distribution narrowers as we move to frame (d), which is statistically the same as Fig. 4.26g. The detail of this effect can be seen more clearly from the normal and parallel sections shown on the right. The weight of a narrower component peaked at $\sim$ $p_\perp$=-1.5 mrad increases progressively as we progress from (a) to (d). After the first run the contamination was roughly the same as it was initially, $\approx$0.006ML C and $\approx$0.01ML O as determined by a double-pass cylindrical mirror Auger analyzer. After the fourth run (frame d) the C level was unchanged, but the O was found to have increased to 0.12ML. Thus we can attribute the above effect to the an increasing oxygen contamination.

To investigate further the nature of the observed structures in the Ps momentum distribu-

† It should be mentioned that the data points are correlated as a result of the decomposition, hence the error bars appear too large with regard to the data points(see §3.4).

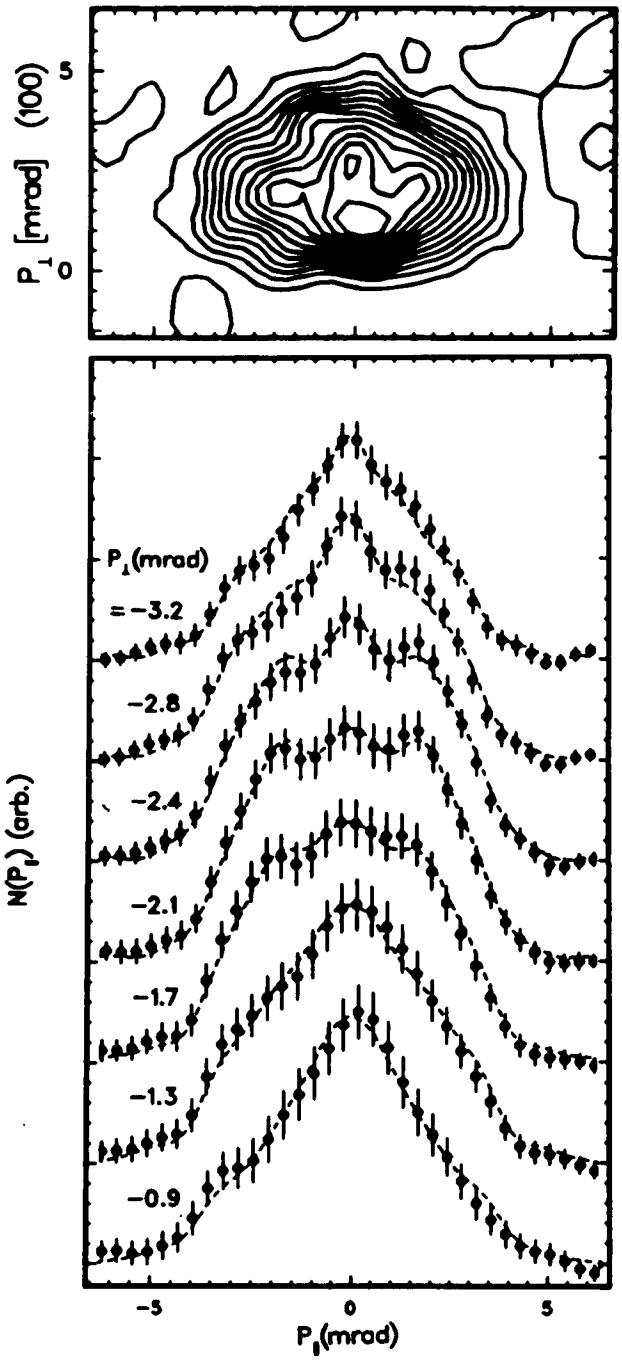

Figure 4.28. Top frame: contour plot of an unsymmetrized Ps spectrum for an clean Al(100) surface, its symmetrized version is shown in Fig. 4.26b, the three statistically significant lobes are shown in the text to reflect the shape of the projected band gaps in the 2D BZ; Lower frame: parallel sections of the upper spectrum, the value of $p_\perp$ for each curve is given, dashed curves are for the symmetrized spectrum.

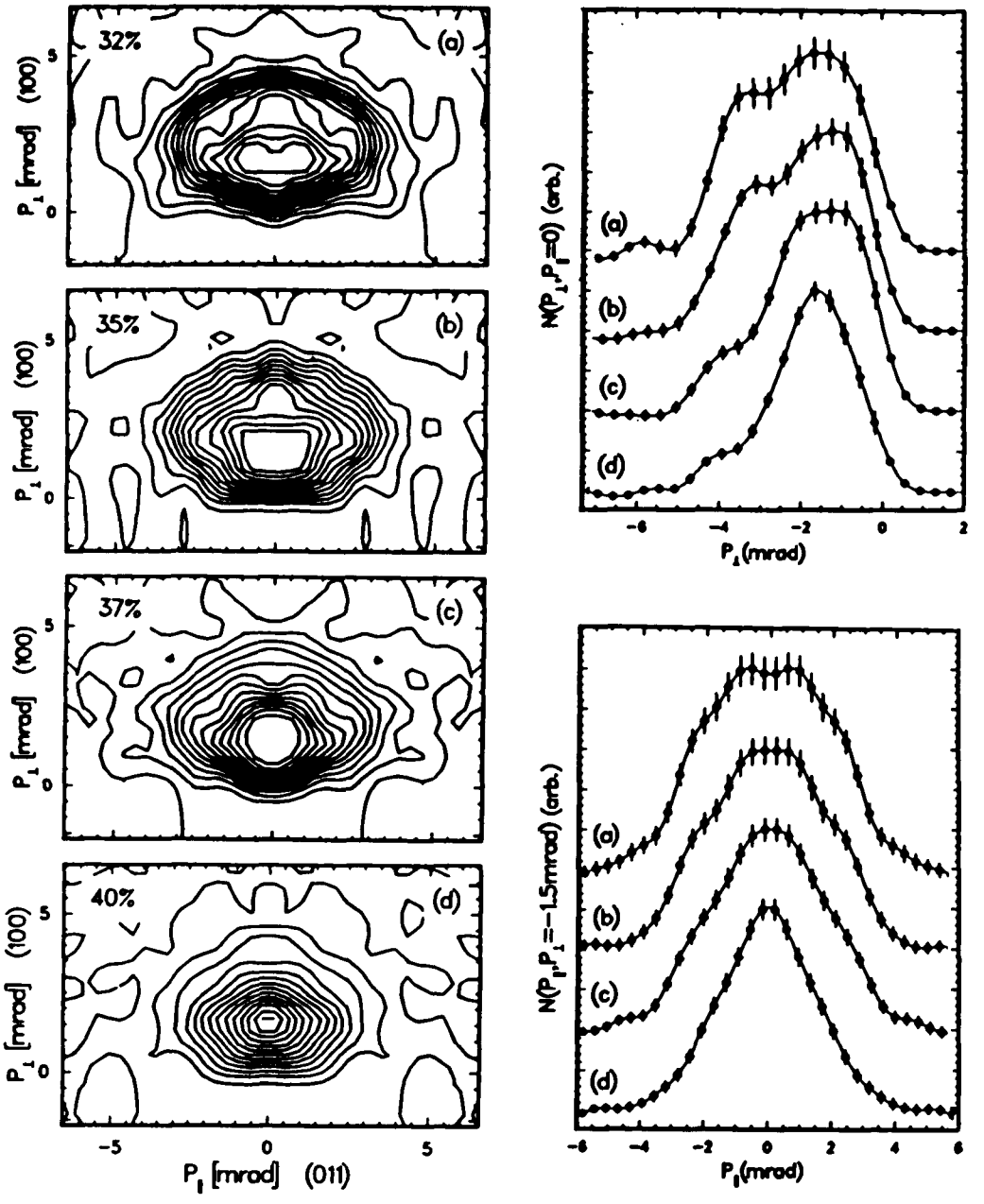

Figure 4.29. Left: contour plots of four sequential measurements for an initial clean Al(100) surface, time duration for each spectrum is 3 hours, the observed change is due to the oxygen contamination of the surface as a function of time; Right: sections through $p_{\parallel}$=0 (top frame), and $p_{\perp}$= -1.5 mrad (lower frame); the alphabetical label corresponds to each frame on the left.

tions, we shall now turn to some theoretical discussion.

§ 4.9 Nearly-Free-Electron Model

4.9.1 Constant Transition Matrix Element Approximation - When the transition matrix element can be assumed to be constant, the Ps momentum distribution, Eq.(1.51), derived from the Fermi golden rule and the IPM approximation in §1.5.3 becomes:

$$\rho_{Ps}(\mathbf{q}) = const \cdot \sum_{\vec{k},i,\vec{g}} n_i(\vec{k},q_\perp)\delta(\vec{q}-\vec{k}-\vec{g})\delta(E(\mathbf{q})+(E_F-E_i(\vec{k}))+\Phi_{Ps}). \tag{4.1}$$

This expression can be derived alternatively from a simple kinematic method based on the conservation of energy, momentum parallel to the surface, and the number of particles. The latter requires

$$\rho_{Ps}(\mathbf{q})d^3\mathbf{q} = \rho(\mathbf{k})d^3\mathbf{k}, \tag{4.2}$$

where $\rho(\mathbf{k})$ is the electron density. Therefore the Ps momentum density

$$\rho_{Ps}(\mathbf{q}) = \rho(\mathbf{k})\frac{d^3\mathbf{k}}{d^3\mathbf{q}}. \tag{4.3}$$

The ratio of the volume elements is governed by the conservation of the energy and the momentum parallel to the surface.

4.9.2 Free Electron Approximation - To proceed further we first regard the electrons as independent particles confined to a Fermi sphere. Since the positron is in thermal equilibrium, its thermal momentum and energy can be neglected as compared with that of electrons. Using the parabolic dispersion for the free electrons and Ps, the conservation of the parallel momentum and energy can be written respectively as:

$$\vec{q} = \vec{k} \tag{4.4}$$

$$\frac{1}{4}q^2 = -\Phi_{Ps} - (E_F - \frac{1}{2}k^2), \tag{4.5}$$

where atomic units have been used. In a free electron gas the electron density in the momentum space is constant. Substituting Eq. (4.4)-(4.5) into Eq. (4.3) yields

$$\rho_{Ps}(\mathbf{q}) = const \cdot n(\mathbf{k}) \cdot q_\perp \left[q_\perp^2 - q_\parallel^2 - q_\parallel'^2 + 4(E_F + \Phi_{Ps}) \right]^{-1/2}. \tag{4.6}$$

The two dimensional projection of $\rho_{P_s}(\mathbf{q})$ is obtained via the integration of Eq.(4.6) over $q_\parallel'$, yielding

$$\rho_{P_s}(\vec{q}) = const \cdot \arcsin\left(\left[\frac{-4\Phi_{P_s} - q_\parallel^2 - q_\perp^2}{4(E_F + \Phi_{P_s}) - q_\parallel^2 + q_\perp^2} \right]^{\frac{1}{2}} \right), \qquad (4.7)$$

which is the same as obtained in Ref.[7]. Care has to be taken while performing the integration. For the maximum Ps momentum $q_M = \sqrt{-\Phi_{P_s}} \leq k_F$, the step function $n(\mathbf{k})$ in Eq.(4.6) is irrelevant, however for $q_M > k_F$ a cutoff occurs at $|\vec{q}| = k_F$ instead of q_M.

Since Al has a nearly-free-electron like band structure, Eqs. (4.6)-(4.7) are expected to give a reasonable approximation. The contour plot of the expression Eq. (4.7) using $E_F = 11.7eV$ [56] and $\Phi_{P_s} = -2.6eV$ is shown in Fig. 4.30a. This free electron model shows a characteristic semi-circular cut-off† at $q_M = \sim 4.5 mrad$, corresponding to the maximum kinetic energy $-\Phi_{P_s}$. In order to make comparison with the experimental spectrum we convolute Eq. (4.7) with a two dimensional Gaussian function, representing the detector resolution function (see discussion in § 3.2.3). The convoluted theoretical spectrum is shown in Fig. 4.30b, which contains twice the number of contours than those of frame (a) on the left. We see that the spectrum becomes slightly enlarged due to the smearing of the finite detector resolution.

Two comments on the above derivation should be made here:

(1). We have assumed a constant transition matrix element. A simple correction is to consider that the number of electrons reaching the surface per unit time is proportional to k_z. Including k_z leads to the cancellation of the denominator in Eq. (4.6) and $\rho_{P_s}(\mathbf{q})$ becomes simply proportional to $q_\parallel$. On the other hand, since the Ps formation takes place at the surface one might think that the formation probability is inversely proportional to k_z, which then cancels the former and leaves Eq.(4.6) unchanged.

(2). Since Ps is formed near the surface, we might imagine that the electron is pulled over the potential barrier by the positron. It is then intereasting to compare the Ps formation with the

† The two sharp corners at $p_\perp = 0$ and $p_\parallel = \pm 4.5$ mrad are rounded-off by the contour plotting routine(see Ref.[7]).

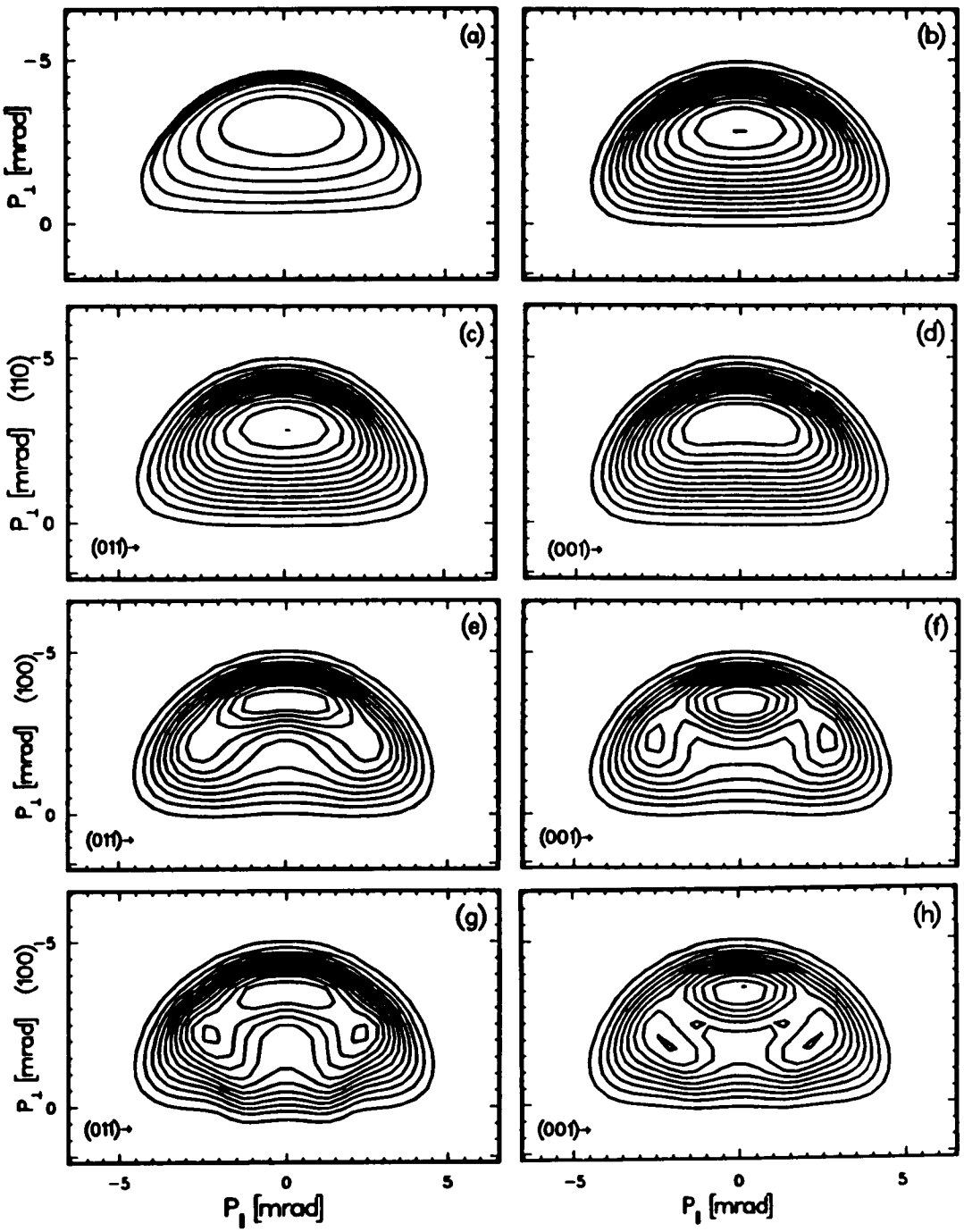

Figure 4.30: Theoretical predictions for: (a). a free electron model; (b). (a) convoluted with detector resolution(as are c-h); (c). a nearly-free electron model on Al(110); (d). same as (c) but rotated by 90°; (e). a nearly-free electron model on Al(100); (f). same as (e) but rotated by 45°; (g). same as (e) with 20 vol% surface state electrons added; (h). same as (f) with 20 vol% surface state electrons added.

escaping of photoelectrons in the 'three-step' model[115]. There it is argued that after transferred to the surface only those excited electrons whose normal component of the kinetic energy is greater than the surface barrier can escape into vacuum, known as the cone emission. Such a restriction would lead to a 45° cone emission of Ps atoms regardless the surfaces so long as the the Φ_{Ps} is negative. This is inconsistent with the experimental results shown in the previous section. In the case of Ps formation, there is a positron present, and the attractive Coulomb interaction between e^+-e^- produces a strong screening. Therefore the surface barrier does not affect the quasi-neutral-Ps atoms in the same way as it does the photoelectrons.

4.9.3 Nearly-Free-Electron Approximation - In § 4.2 we have shown that the projected band structures of the three low index surfaces of Al contain significant amount of energy gaps. More importantly, large gaps appear in the range from the Fermi level E_F down to $E_F+\Phi_{Ps}$ (2.6eV below the Fermi energy), which is crucial for Ps formation(marked in Fig. 4.3) and hence may make the real Ps momentum distribution differ substantially from the pure free electron prediction of Eq. (4.6). In addition to the energy conservation, parallel momentum conservation needs to be considered at the same time. From Eqs.(4.4)-(4.5) we see that the electron energy required for Ps formation is least when $q_\parallel$=0, i.e. Ps atoms are emitted parallel to the surface. In this case

$$E(\mathbf{k}) = E_F + \Phi_{Ps} + \frac{1}{4} \mid \vec{K} \mid^2. \tag{4.8}$$

This minimum dispersion is plotted in Fig. 4.4(solid lines). Together with the Fermi level they determine an accessible region for Ps formation. Clearly a large portion of the projected gap in the Al(100) surface is present in this region, and it will affect significantly the Ps formation. In contrast, for the (110) face only a small fraction of the band gap appears in this accessible region, and for Al(111) the effect is even smaller. Our view is not complete without inspecting these effects throughout the whole 2D Brillouin zone. Going back to Fig. 4.5 we see that within the circle of radius q_M, the maximum Ps momentum, the (100) BZ contains largest projected-gap area around the $\bar{\Gamma}$ point, and according to Fig. 4.4 $\sim$ 90% of the gap is in the accessible region;

Table 4.3 Fitted parameters for band gap boundaries. $\omega \approx 1+sin^2\phi$, where ϕ is the angle with respect to $\bar{X}\bar{\Gamma}$ and the origin is at $\bar{X}$. Parameters for Al(111) are averaged.

	$E_g - E_F\,(eV)$		$k_g\,(\pi/a)$		$m^*\,(m_e)$	
	top	bottom	top	bottom	top	bottom
Al(100)	-1.76	-2.89	0	0	1.02	1.00
Al(110)	-1.79	-2.86	1	1	1.02ω	1.00ω
Al(111)	-1.77	-2.88	$2/\sqrt{3}$	$2/\sqrt{3}$	0.60	0.58

although the (110) face also contains large amount of gaps, they center around the $\bar{X}$ point; most of them are below the minimum dispersion curve, thus should produce only small effect; again the (111) face is least affected. This analysis provides us the reason for the Al(100) Ps spectrum being very different from those of the other two faces.

Quantitatively, we insert these gaps as predicted by the Harrison's pseudopotential calculation into the free electron Fermi sphere to form a more realistic local electron density function $\rho(\mathbf{k})$. In principle, the presence of these gaps will cause an increase in the electron density in the occupied region if the Fermi radius stays the same. We assume the change is uniform and $\rho(\mathbf{k})$ remains constant. The top and bottom gap boundaries(Fig. 4.3-4.4) can be formed using the parabolic dispersion:

$$E_g(\vec{k}) = E_g + \frac{(\vec{k} - \vec{k_g})^2}{2m^*}, \tag{4.9}$$

where m^* is the effective mass. At the edge they are joined by a straight line. All the parameters, E_g, $\vec{k}_g$ and m^* are obtained from fitting this parabolic curve to the projected band structure in the whole 2D BZ. They are listed in table 4.3. To simplify the computation the dashed curves in Fig. 4.5 are used as the boundaries.

Our nearly-free electron predictions of the Ps spectrum are plotted in Fig. 4.30. Frame (c) is for an Al(110) surface projected along the $\bar{\Gamma}\bar{Y}$. Close inspection shows that it is slightly more forward at small $p_\perp$ compared with frame (b), the free electron prediction. This can be understood because the gap is near E_F (Fig. 4.5) and is projected on the large $|p_\parallel|$ region. When the surface is subject to a 90° azimuthal rotation the projection becomes along the $\bar{\Gamma}\bar{X}$, the gap affects a small

region around $p_{\parallel}=0$ and $p_{\perp}\approx-\frac{2}{3}q_M$, and causes a small flattening on the top of the spectrum as observed in frame (d). Convoluted with our detector resolution function both Al(110) spectra (c) and (d) are similar to the free electron prediction (b). Frame (e) and (f) are for an Al(100) surface projected along the $\bar{\Gamma}\bar{X}$ and $\bar{\Gamma}\bar{M}$, respectively. As might have been expected from the above discussion, these two spectra for the Al(100) surface differ considerably from the free electron prediction (b). The predicted Al(111) spectrum is essentially indistinguishable from (b). To better visualize the structure of these predictions, Fig. 4.31 plots the perspective views of the three frames (b),(e) and (f) of Fig. 4.30. Both Al(100) spectra show three characteristic lobes, that are absent in the gap-free picture (b). The 45° azimuthal rotation causes a small change in the ratio of the heights of the center lobe to the side lobes.

A comparison between the measured spectra and the predictions for two Al(100) runs and one Al(111) run is made in Fig. 4.32. They are in qualitative agreement for: (i). an isotropic distribution is predicted for the Al(111) surface and the three lobes anisotropy for the Al(100) surface; and (ii). azimuthal rotation by 45° causes only small changes. Therefore, we conclude that the anisotropy in the Al(100) spectra stems from the shape of the projected energy gaps centered at $\bar{\Gamma}$ in the 2D BZ. However, all the experimental spectra exhibit dense contour lines around the origin indicating an enhanced low momentum component of Ps emission, while the theoretical spectra are more peaked towards the maximum Ps momentum. This discrepancy will be discussed in detail latter. The Al(110) spectra in frame (c) and (f) of Fig. 4.26 are similar to the Al(111) in (a), except the intensity of the low momentum component is higher in the Al(110) spectra. This is most likely due to the faster oxygen contamination of this face[64], and hence makes it difficult to compare them with the theoretical predictions Fig. 4.30c-d for this surface.

The theoretical prediction of the positions and relative shape of the lobes in the Al(100) Ps spectra depends on the width and the positions of the gaps in the surface band structure. It is noted that recent angle-resolved photoemission experiment[103] showed that the mapped width of the gap at X point(projected onto the $\bar{\Gamma}$ point) is about 0.5eV wider than the theoretical prediction[83]. These observations may need to be taken into account when more precised quantitative

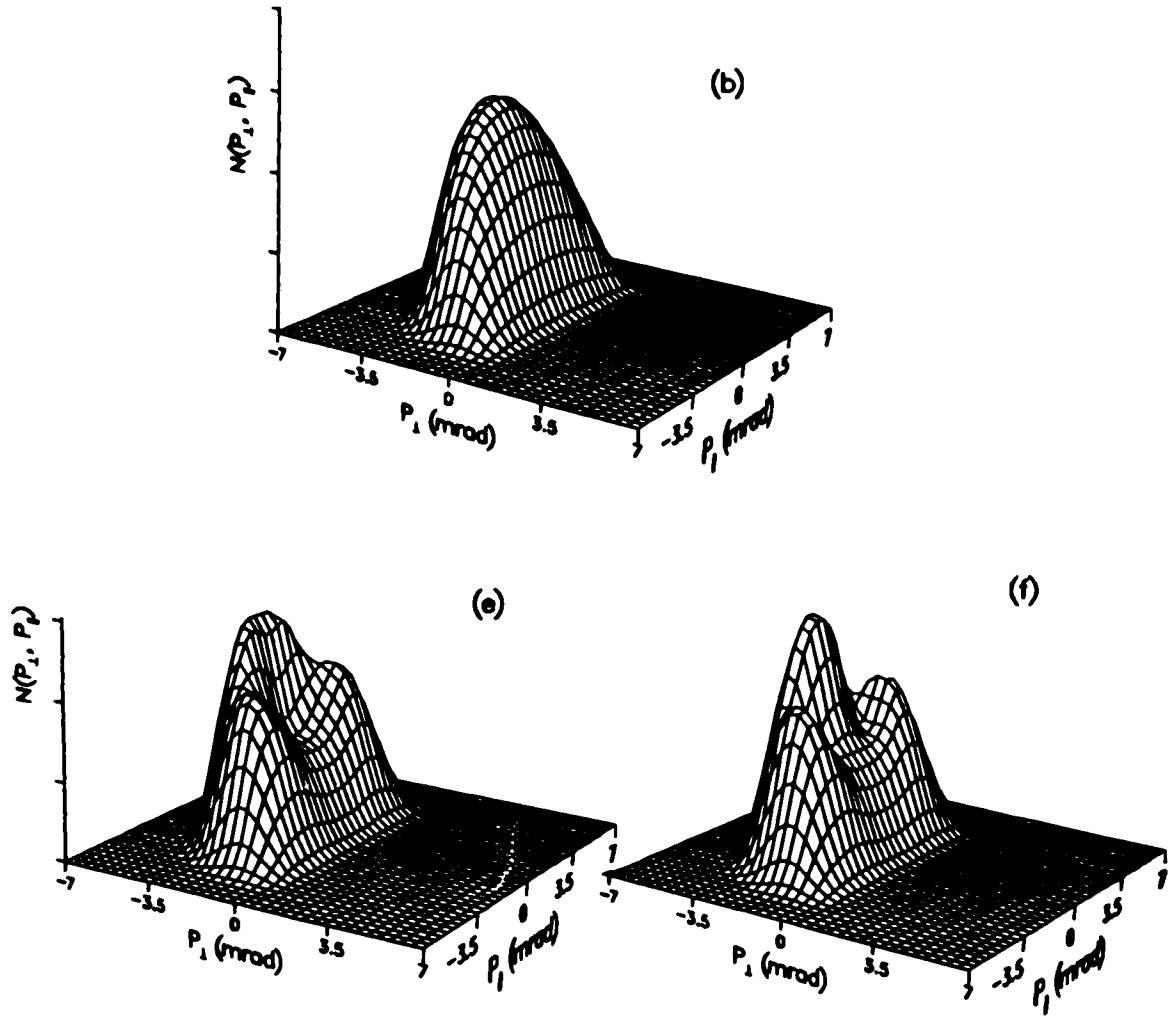

Figure 4.31. Perspective view of Fig. 4.30b, Fig. 4.30e, Fig. 4.30f, correspondingly. The three lobes in the Al(100) spectra are clearly visible in (e) and (f).

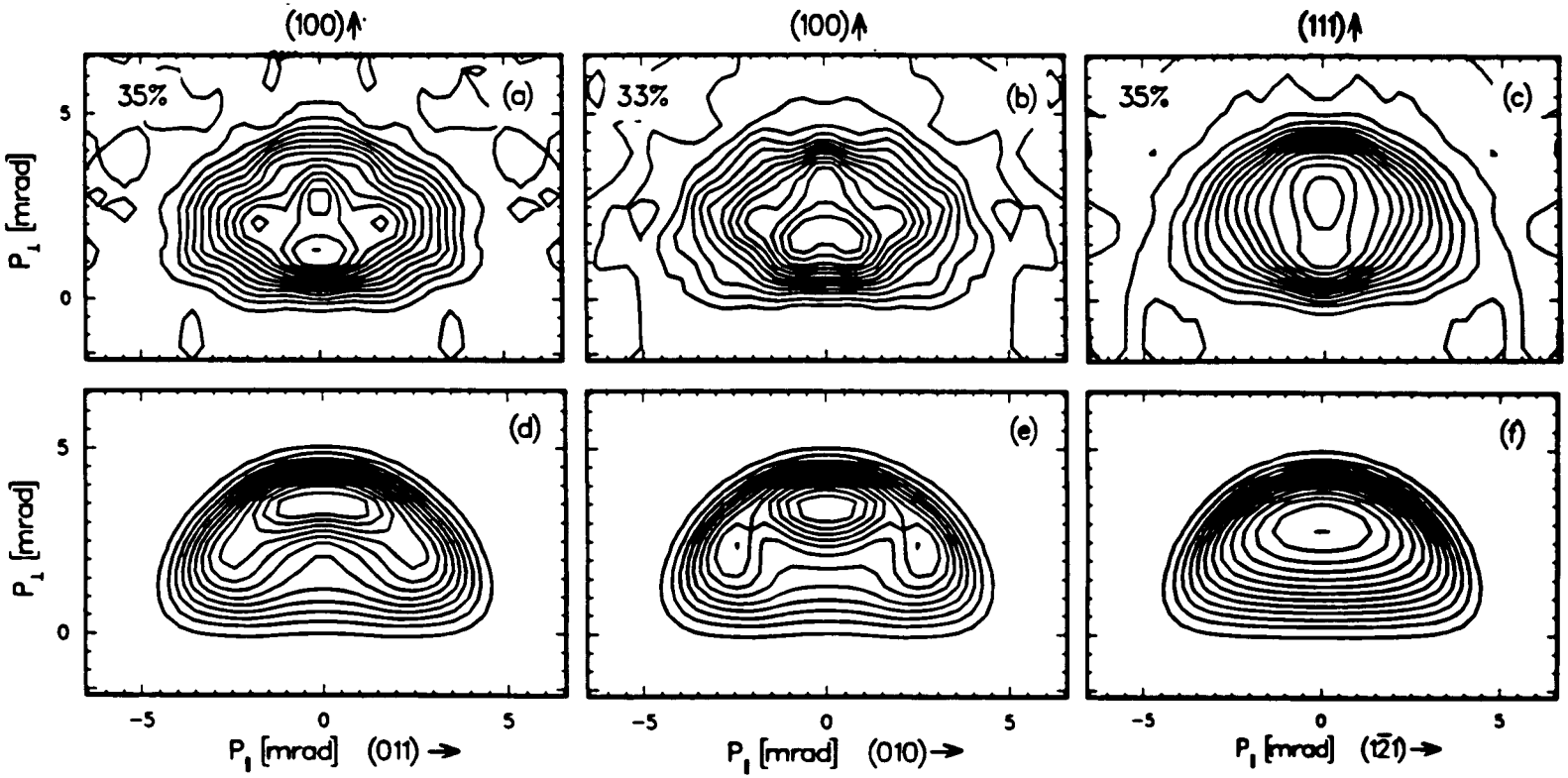

Figure 4.32. Comparison between experimental data(up part) and the nearly- free electron predictions(lower part). Left column: for an Al(100) surface; Middle column: for the same surface but rotated by 45° azimuth; Right column: for an Al(111) surface.

prediction is desired.

4.9.4 Electron Surface State - Electron surface states have been observed for all three Al surfaces by a number of angle-resolved photoemission experiments[101-105]. Since they are localised at the surfaces one may expect them to have significant effect on the Ps formation, though the total number of surface localized electrons are much smaller than the regular bulk-like electrons extended into vacuum. To include this in our model we use the result of Ref.[102] which shows the surface states are essentially located at the bottom of the projected band gaps (Fig. 4.4). We assume a 0.1eV width of these states and the same effective mass in all directions. Fig. 4.30(g)-(h) are the results of adding 20 vol% surface state electron's contribution into the nearly-free-electron predictions(e) and (f). We see the effect of the surface state electrons is to enhance the two side lobes and bring them a little closer. The agreement with the measured spectra improved only slightly. However, the fraction of surface state electrons added was somewhat arbitrarily. Thin slab surface electronic structure calculations[88] showed that the bulk- and surface-state wave functions are in fact very similar, and that the differences between them are mainly on the atoms themselves; hence for Al the experimental anisotropy should be mainly dominated by the bulk projected density of states.

4.9.5 The Low Momentum Component - Despite the reasonableness of the theoretical predictions, a discrepancy exists between the theoretical spectra and the measured in the low momentum region. This is shown clearly in Fig. 4.33 which compares the sections through $p_{\parallel}$=0 and $p_{\perp}$=-1.3 mrad of the volume-normalized Ps spectra for the three surfaces. The possible origin of the measured low momentum component are: (i). the effect of oxygen contamination of the sample surface; (ii). momentum dependence of the transition matrix element; and (iii). some inelastic processes involved in the Ps formation. We now discuss these three aspects in the present and following two sections.

We have shown in Fig. 4.29 that the Ps spectroscopy has a remarkable sensitivity to oxygen contamination on Al surfaces. The presence of the oxygen atoms is clearly prompt by the appearance of a low momentum component. The sensitivity may in fact be high enough to detect less

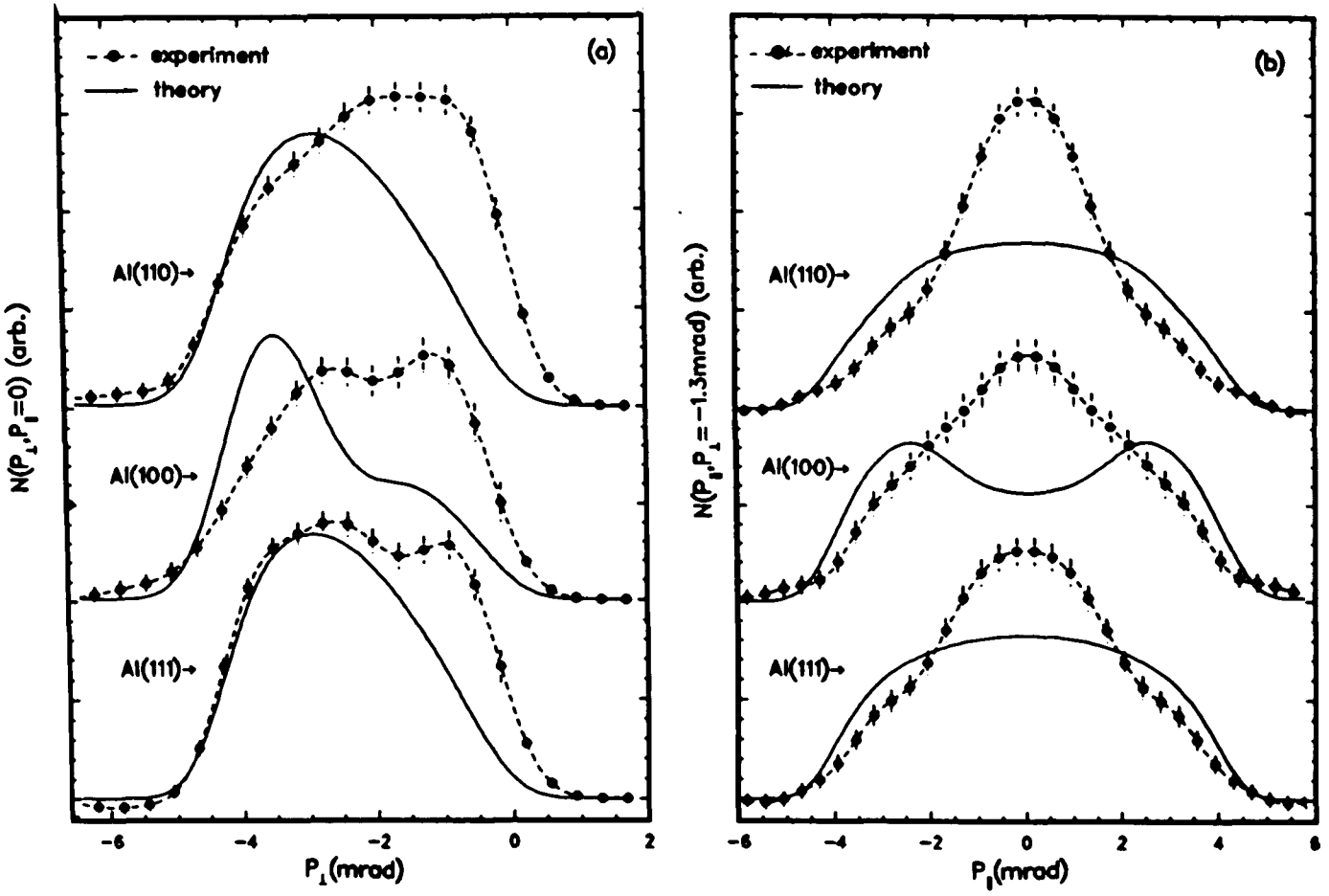

Figure 4.33. Sections of the volume-normalized experimental(dashed) and theoretical(solid) Ps spectra for the three low index surfaces of Al. The experimental curves are from Fig. 4.26(a)-(c), the theoretical curves from Fig. 4.30(b),(c) and (e). The parallel sections(left) are at $p_{\parallel}=0$, the perpendicular(right) at $p_{\perp}=-1.3$ mrad.

than 0.01ML oxygen coverage. To explore the possibility that the difference between the theory and experiment is due to the oxygen impurities, we subtract the clean Al(100) run by 40 vol% of the 150L oxygen-exposed Al(100) surface run. The result is displayed in Fig. 4.34. Similar result is also obtained from subtracting Fig. 4.29d from Fig. 4.29a. Fig. 4.34a shows clearly the three lobes close to those in Fig. 4.31e or Fig. 4.31f. The cuts in Fig. 4.34b and 4.34c also show reasonable quantitative agreement between the theory and the 'oxygen-component-subtracted' Al(100) spectrum.

Form the theoretical point of view, the fact that oxygen contamination produces low momentum Ps can not be an electronic effect alone. It was shown[90] that for chemisorbed oxygen on Al(111) and Al(100) surfaces, all the O2p electrons are lying below 5eV from the Fermi level(Fig. 4.6), thus can not participate in the Ps formation. The presence of the oxygen atoms in or on the surfaces of Al also leads to some charge transfer from Al atoms towards O atoms, and as a result ϕ_- increases by 0.1eV for Al(111) and decreases by 0.5-0.8eV for Al(100) surface. For Al(100) surface it also induces some new surface resonant states, which replaces the surface states existing in the clean surface. The change of the dipole potential will cause an opposite effect on ϕ_+ (Eq.(1.12)) and therefore will not affect the direct Ps formation process(Eq.(1.13)). The enhanced low momentum Ps emission from oxygen contaminated Al surfaces can not be explained by the change of surface states either, because otherwise we should see a high momentum component in the Ps emission from Al(100) surface owing to the induced surface resonant state near the Fermi level(Fig. 4.6).

Nieminen and Puska[41] have shown theoretically that the ordered chemisorbed monolayers of oxygen on Al surfaces(§4.3) make the image induced positron surface state unstable with respect to positronium emission. For an Al(100) surface, oxygens lower the positron binding energy E_b only by less than 0.1eV. This together with the 0.5-0.8 eV decrease of ϕ_- leads to zero or negative activation energy E_a (see Eq.(1.15)), hence drives the positron surface state unstable. A different mechanism operates on Al(111) since the measured ϕ_- hardly changes in the chemisorbed phase. The same oxygen configuration, which leads to the result shown in Fig. 4.6, lowers

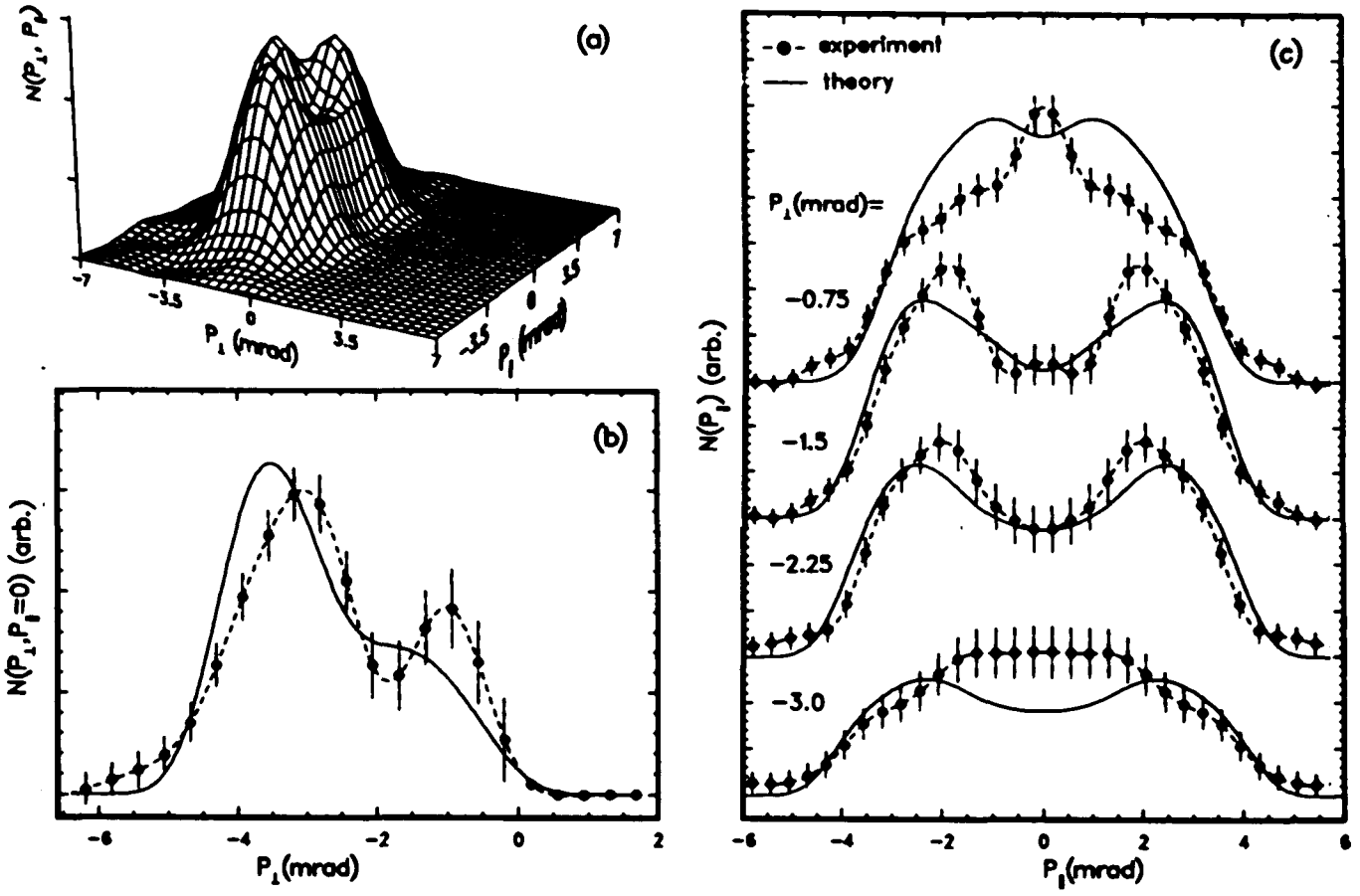

Figure 4.34. Ps spectrum of a clean Al(100) surface run minus 40 vol% of a 1ML oxygen on Al(100) run: (a). a perspective view; (b). section through $p_{\parallel}$=0(dots); and (c). sum of two nearest parallel sections at different $p_{\perp}$ given in the figure. Solid curves are from the nearly-free electron prediction of Fig. 4.30e.

the binding energy E_b substantially so that $E_s \approx -0.2eV$. Thus it seems reasonable to assume that for oxygen chemisorbed Al surfaces positron surface states serve as some intermediate states for low energy Ps formation and emission. On the other hand, it seems difficult to explain at the same time why the monolayer oxygen on Al(100) surface only increases the total Ps fraction by 5%, while the total Ps thermal desorption from a clean Al(100) surface at 750° K reaches 38%(see §4.10).

4.9.6 The Transition Matrix Element - To include the possible momentum dependence of the transition matrix element in the Ps formation theory, more complete theory is required. Recently, Walker and Nieminen have attacked this problem[31]. They calculated the matrix element using Eq.(1.44) and a screened e^+–e^- potential

$$U(|\mathbf{r}^+-\mathbf{r}^-|) = \frac{e^{-\beta|\mathbf{r}^+-\mathbf{r}^-|}}{|\mathbf{r}^+-\mathbf{r}^-|}. \tag{4.10}$$

Their final state is the same Ps wave function ψ_{P_z} as in Eq. (1.46). The electron wave function ψ_- and positron wave function ψ_+ for the initial state are obtained by assuming that electrons are confined by an infinite barrier a small distance($\frac{3}{8}\pi k_F$) from the semiinfinite jellium edge, and that positrons see a step potential specified by $|\phi_+|$ ($\phi_+<0$). The overlap between the initial state and final state is restricted to the surface region. Their result convoluted with a resolution function of 1.5mrad FWHM is shown in Fig. 4.35b, in comparison with our free electron prediction (a) and experimental results for an Al(111) surface (c). We see that their matrix element enchances the small $p_\perp$ and shift the most probable Ps distribution toward the lower $p_\perp$ by $\sim$ 0.5mrad. However this does not remove the discrepancy in the low momentum region exhibited in Fig. 4.34, and in the high momentum region it worsens the agreement. It should be mentioned that their treatment is the first-order time independent perturbation, and it ignores the possibility of electron-hole pair creation or the scattering of Ps once formed.

4.9.7 Positron Neutralization Model - That charged particles of the same velocity take similar interactions with electrons at a surface in spite of the differences in mass and kinetic energy has stimulated some work[29,30] in extending the ion neutralization theory to the description of

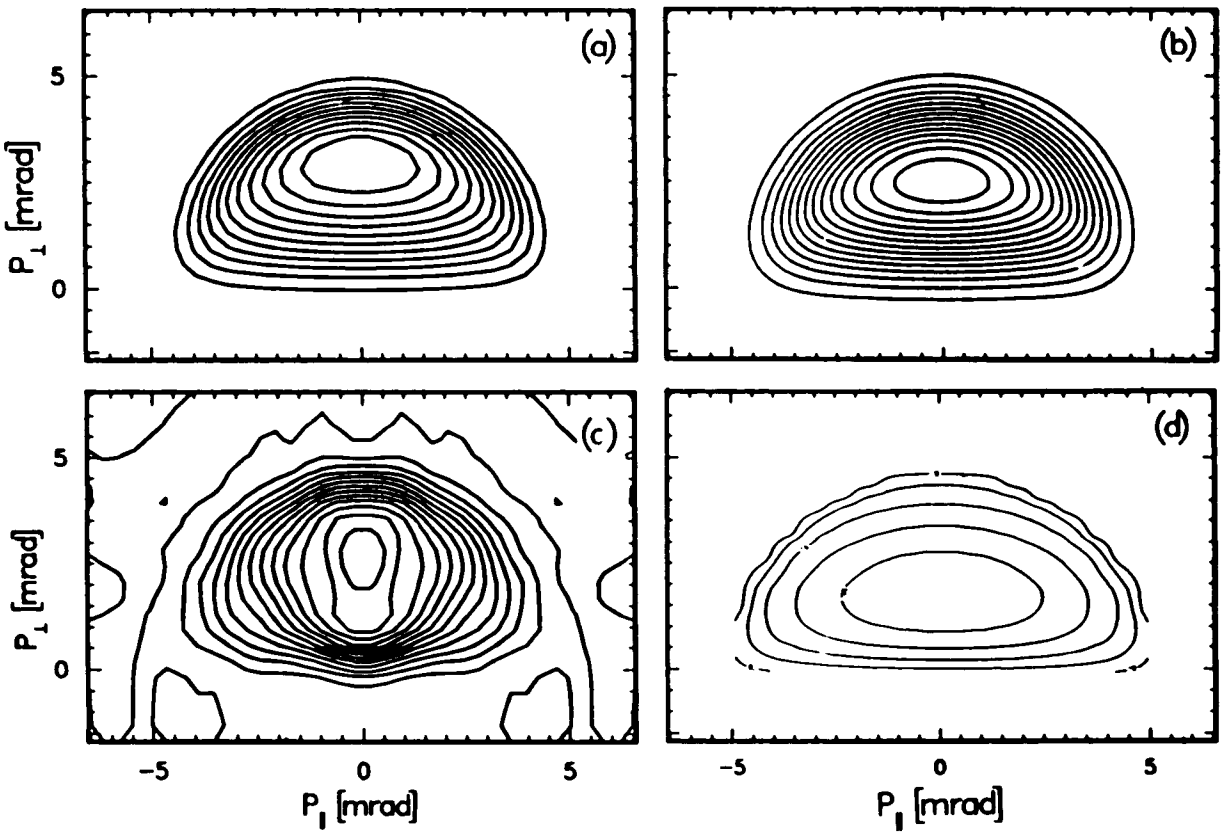

Figure 4.35. Theoretical predictions of the Al Ps spectrum from: (a). the present nearly-free model; (b). Walker and Nieminen(Ref.[31]); and (d). Shindo and Ishii(Ref.[30]). (c): experimental spectrum for an Al(111) surface.

Ps formation at metal surfaces. Here one regards the electrons as hopping between the surface and the Ps atom on the vacuum side of the surface. The transition matrix element from surface to the Ps state (or vise versa) is similar to that of Walker and Nieminen[31]. But instead of confining the overlap of ψ_{P_s} with ψ_- and ψ_+ in the a small surface region, a spatial factor $\beta \cdot exp\,[-\beta(\,|\,z^+ + z^-\,|\,/2 - z_0)^2]$ is multiplied to the ψ_F, of Eq.(1.44) and β is taken to be ∞ to describe the Ps center-of-mass motion(z_0). In addition, an exponentially decaying dynamical factor is introduced to account for the decreasing transition magnitude in an increasing distance between the Ps atom and the surface. This classical trajectory approximation is then used in solving the time dependent Schrodinger equation, in which the interaction Hamiltonian includes both the formation and dissociation of Ps. It is emphasized by Isii and Isii *et al.* [29,30] that including the dissociation term is essential in order to avoid the divergence at large angle emission , which one encounters in the first order Born approximation($\approx 1/v_z$). The dissociation term allows the electron to hop back from the Ps atom to an unoccupied state in the surface. It is shown[29] that the transition matrix element is essentially constant, but the dynamical interaction enhances the small momentum emission and smears the electron density of states near a metal surface. The weak dependence of the transition matrix element on the angle and energy substantiates the assumption made in our simple kinematical model(§4.9).

In the above classical trajectory approximation, the distance s between the Ps atom and the surface can only be estimated using the final(rather than instant) Ps velocity: $s = t \cdot v_z$. This is invalid at high velocity. The full quantum mechanical treatment of this resonant charge transfer theory for Ps formation has been derived by Shindo and Ishii[30]. Their starting point is the golden rule formula of Eq.(1.44), except the matrix element is separated into the inner freedom part and the center-of-mass part. The latter is treated quantum mechanically , and is the analogue of the classical trajectory approximation. It is obtained from an optical potential method, which is in parallel to the above semi-classical treatment.

A prediction of the 2D-ACAR spectrum for an Al(100) surface with free electron bands from this theory is shown in Fig. 4.35d. It is similar to the semi-classical prediction given by Isii in

Ref.[29]. We see that the most probable momentum appears at much smaller $p_\perp$ and the detailed shape is in disagreement with the experiment. It is argued by these authors[29,30] that the over enhancement of the low $p_\perp$ emission arises from the wide-band approximation utilized in their derivations. Although it is widely used in ion-neutralization problems, this approximation seems to be inadequate for Ps formation. It allows electrons to return to too wide unoccupied bands in the surface, thus overestimating the Ps dissociation. Isii and Shindo[29] have substituted some model bands for the 'wide-band' to test their semi-classical theory and found that the energy and angular dependence of the Ps emission spectrum is indeed sensitive the band width and band structure. Clearly, applying these theory to a more realistic Al electronic band structure would be desirable, so that comparison with the observed anisotropic Ps distribution for the Al(100) surface will be possible.

§ 4.10 Thermally Activated Positronium

We have shown earlier in Figs. 4.9-4.10 that when an Al(100) surface is heated to 600° K , a sharp narrow peak near zero momentum on the negative $p_\perp$ side emerges in the ACAR spectrum with a large reduction of the positron surface state annihilation component. This is taken as the first ACAR experimental evidence for the established picture that positrons captured at the surface states are thermally desorbed as Ps atoms. Note that the thermal peak in Fig. 4.10 has a width comparable with the detector resolution and it's center appears almost at the origin. This implies that the thermally desorbed Ps energy is indeed on the order of $K_B T$, thus the width of the peak is dominated by the apparatus resolution($\sim$ 1mrad). In fact, it is for this very reason our inversion-subtraction data separation technique fail to decompose the spectra accurately. The deconvolution procedure is not capable of transferring all the thermal Ps contribution smeared into the positive $p_\perp$ side back to the negative region.

To investigate further the projected thermal Ps momentum distribution the following approximation is made: at the present sample temperature the bulk, surface state, and directly formed Ps annihilation spectra do not change substantially from that at room temperature.

Therefore, the room temperature spectra, when properly normalised, can be used to remove approximately their corresponding hot components from the high temperature measurement, to obtain the thermal Ps distribution. This is reasonable since the thermal momentum is much smaller than the Fermi momentum, and ϕ_-, ϕ_+ and ϕ_{P_s} do not change appreciably compared with the most probable energy($\sim$ 1eV) of the directly emitted Ps[22]. However, at 600°K vacancies are thermally activated ($C_v \approx 10^{-5}$)[113] and about 10%[2] of the implanted positrons are trapped and annihilate in these vacancies producing a spectrum with a width lying between the extended bulk state and external surface state as shown in Fig. 4.25. Fortunately this is a small fraction and we will not attempt to make any correction here. The contribution from each component can be estimated in a self-consistent manner. The yield of the thermal desorbed Ps should be equal to the reduced fraction of positrons captured in the surface states, assuming the temperature effect on the surface branching ratios is of higher order. Furthermore the normalization factors can be adjusted so that the intensity of the difference spectrum just approaches negative values which is of course unphysical.

Figs. 4.36-4.37 illustrates this method with the perpendicular and parallel sections through the peak. The normalization factors indicated in the figures are the volume-percentage with respect to the solid-curve spectrum. It is seen in Fig. 4.36 that the symmetrical component(dashed curve) consisted of 25 vol% surface state and 43 vol% bulk spectra obtained at room temperature gives a good approximation. The small deviation is attributable to a small broadening at high temperature, and more likely to the thermal vacancies trapping positrons. The difference curve(dots) is the extracted total Ps spectrum which clearly shows a cutoff at $\sim$ 5mrad as expected from the discussion in § 4.8. That the room temperature Ps spectrum coincides well in the large momentum region with the extracted total Ps spectrum seen in Fig. 4.37 confirms our earlier argument. From the normalization factors we estimate f_{bulk}=22%, $f_{s.s.}$=13%, and f_{P_s}=65% in which 38% are thermal Ps. Thus the bulk fraction remains almost the same as the room temperature fraction, the direct formation of Ps is reduced by $\sim$ 5% and $\sim$ 84% surface state positrons are thermally desorbed as Ps.

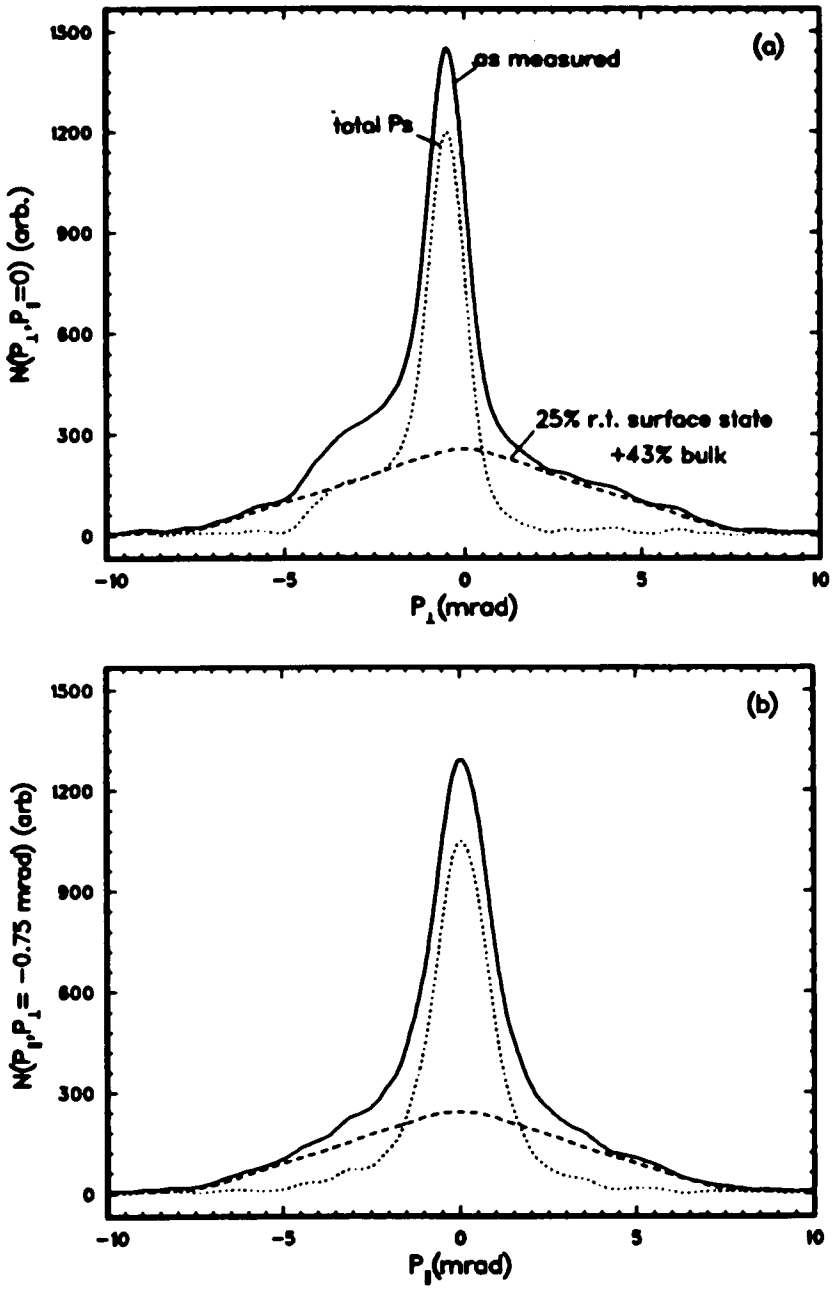

Figure 4.36. Sections through (a). $p_{\parallel}$=0, and (b). $p_{\perp}$= -0.75 mrad of three ACAR spectra. Solid curve is a total measurement for an Al(100) surface at 600°K with a 1.5keV beam. the dashed curve is a composed symmetrical spectrum containing 25 vol% room temperature surface state spectrum and 40 vol% room temperature bulk spectrum. The dotted curve is the difference.

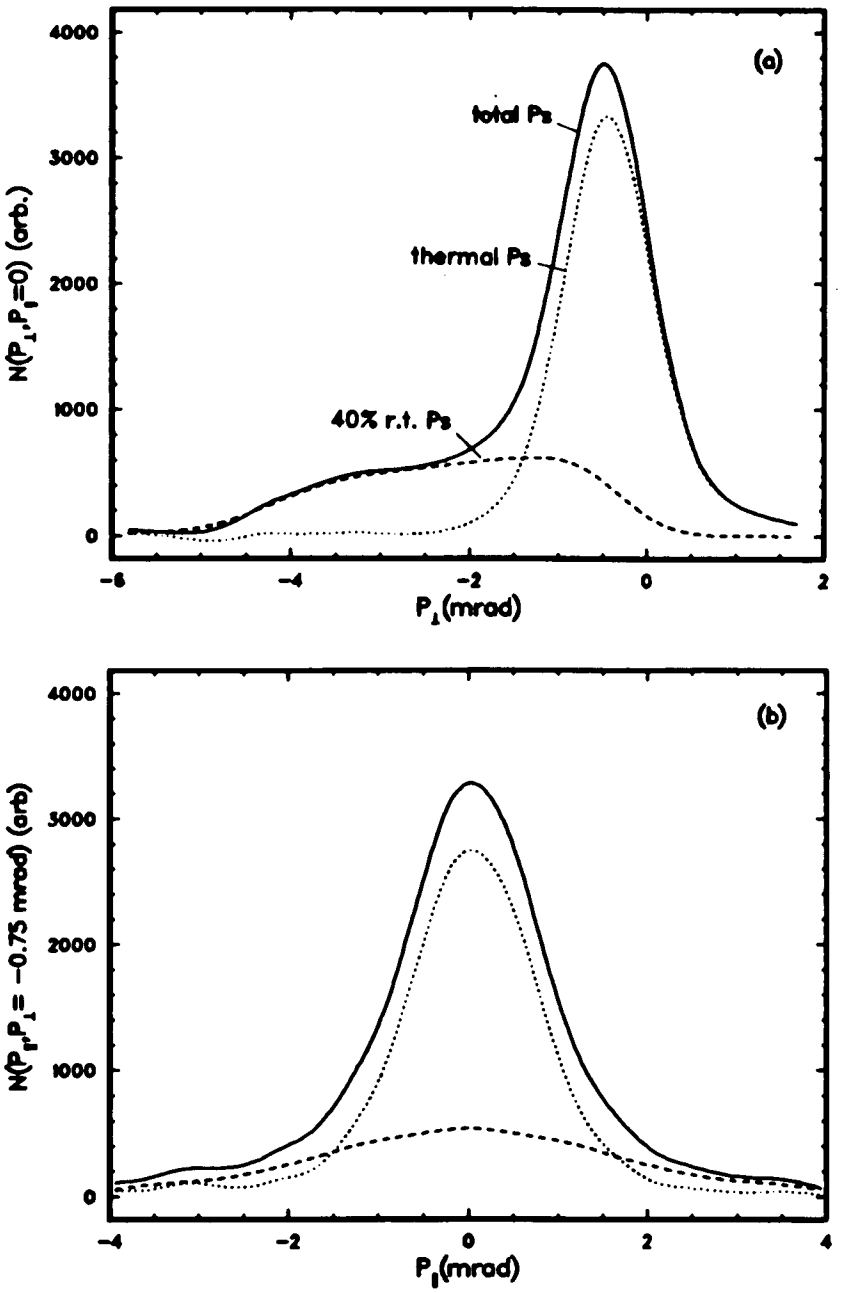

Figure 4.37. Sections through (a). $p_{\parallel}$=0, and (b). $p_{\perp}$= -0.75 mrad of three ACAR spectra. Solid curve is the extracted total Ps spectrum(dotted curve in Fig. 4.36); dashed curve is 40 vol% room temperature Ps spectrum with respect to the total Ps; and the dotted curve is the difference, the deduced thermal desorbed Ps spectrum.

The Ps thermal activation process has been treated in terms of thermodynamics[34,35] similar to those leading to the Richardson-Dushman equation, for ordinary thermionic electron emission. In this model, the positrons are confined to the surface, the electrons may be in both surface and bulk states, and the Ps forms a classical ideal gas in the vacuum. The condition that the three species be in thermal equilibrium requires the chemical potential of the Ps being equal to the sum of that of the positron and electron, which are exchanging with the Ps via the formation of a bound state. By detailed balance and assuming electrons are at the Fermi level, this leads to the Ps thermal emission rate

$$z = z_0 T exp\,[-E_a/K_B T]\,(1-<r>), \tag{4.11}$$

where $z_0=4K_B/h$, K_B and h are respectively the Boltzmann and Planck's constants, and $<r>$ is the average of the Ps reflection coefficient $r(q_\perp)$ for the surface over the distribution of the Ps thermal velocities. The same derivation also yields the momentum(or velocity) distribution of the thermal Ps atoms:

$$\rho^r_{Ps}(\mathbf{q}) = exp\,[-q^2/4mK_B T]\,(1-r(q_\perp))\cos\theta, \tag{4.12}$$

where the Knudsen's cosine law has been included and the reflection coefficient is in general the function of the normal component of the momentum. Pendry has calculated $r(q_\perp)$ with a model that assumes the Ps moving towards the surface first encounting an absorbing barrier with a reflecting step immediately behind. The step height is $-(E_+ + E_{Ps} + E_-)$, where E_{Ps} is the Ps vacuum binding energy, E_- and E_+ are the electron and positron surface state energies. It is found that to the lowest order in $q_\perp$,

$$1-r(q_\perp) = q_\perp. \tag{4.13}$$

In their TOF study for the normal emission thermal Ps from an Al(111) surface, Mills *et al.* [34] fit, with a good χ^2, Eq.(4.11)-(4.12) to their data and obtained $E_a = 0.344$eV, (1-<r>)=0.21 and T to be within 10% of the sample temperature. Their data also showed that $r(q_\perp)$ is essentially constant and hence is at variance with Eq.(4.13).

The probability of converting a positron in the surface state to a free thermal Ps is $z/(z+\gamma)$, where γ is the positron surface state annihilation rate. Using the above fitted parame-

ters for an Al(111) surface and γ=1.72$nsec^{-1}$ for an Al(110) surface as reported by Lynn *et al.*, we estimate that at 600° K 62% surface state positron are thermally activated. This is about 20% lower than our measurement for an Al(100) surface. The earlier Ps fraction study by Mills, *et al.*, which yielded the activation energies listed in Tbl. 4.1, did not include the linear temperature term in Eq.(4.11), and obtained $(1-<r>)z_0/\gamma = 3.5\times10^6$ for an Al(100) surface. In this way we arrive at $z/(z+\gamma)$=93%, with which our measurement agrees well within the uncertainty of estimation.

Our ACAR data provide the first comparison between experiment and the angular-dependent theoretical distribution of Eq.(4.12). To do so we project Eq.(4.12) and convolute it with a Gaussian resolution function:

$$N^r_{P_s}(q_\parallel, q_\perp) = \int d\,\mathbf{p}'\ \rho^r_{P_s}(\mathbf{q}')\, exp\,[-((q_\parallel' - q_\parallel)^2/2\sigma_\parallel^2 + (q_\perp' - q_\perp)^2/2\sigma_\perp^2)], \tag{4.14}$$

where $\sigma_\parallel$ includes the finite sample size effect. The result of Eq. (4.12) and Eq.(4.14) using a constant Ps reflection coefficient $r(q_\perp)$ is plotted in Fig. 4.38 against the extracted thermal Ps spectrum(dots). They are normalized to have the same peak intensity. We note that the agreement is excellent. A few remarks should be made: (i). When the sample size effect in not included in the resolution function the agreement between the theory and data is much poorer in the parallel sections, this is due to the very narrow distribution of the thermal Ps. (ii). The preference of a constant Ps reflection coefficient is consistent with TOF study of Mills *et al.* [34], substitution of Eq.(4.13) in Eq.(4.12) results in a too much forward distribution compared with the measurement. (iii). The distribution function of Eq.(4.12) is less sensitive to the variation of temperature, no appreciable difference can be observed within ±50° K. At present condition, the width of the detector resolution dominates the spectrum width. Clearly, higher precision study awaits for better detector resolution. Further more measurement with a lower energy beam can avoid thermal vacancy complications and leads to more accurate thermal Ps yield estimation from which E_a and $<r>$ can be extracted.

Quantum mechanical treatment of the Ps thermal desorption has been described by Levine and Sander[38], and by Isii[29]. The process is the same as the quantum tunneling. The rate is cal-

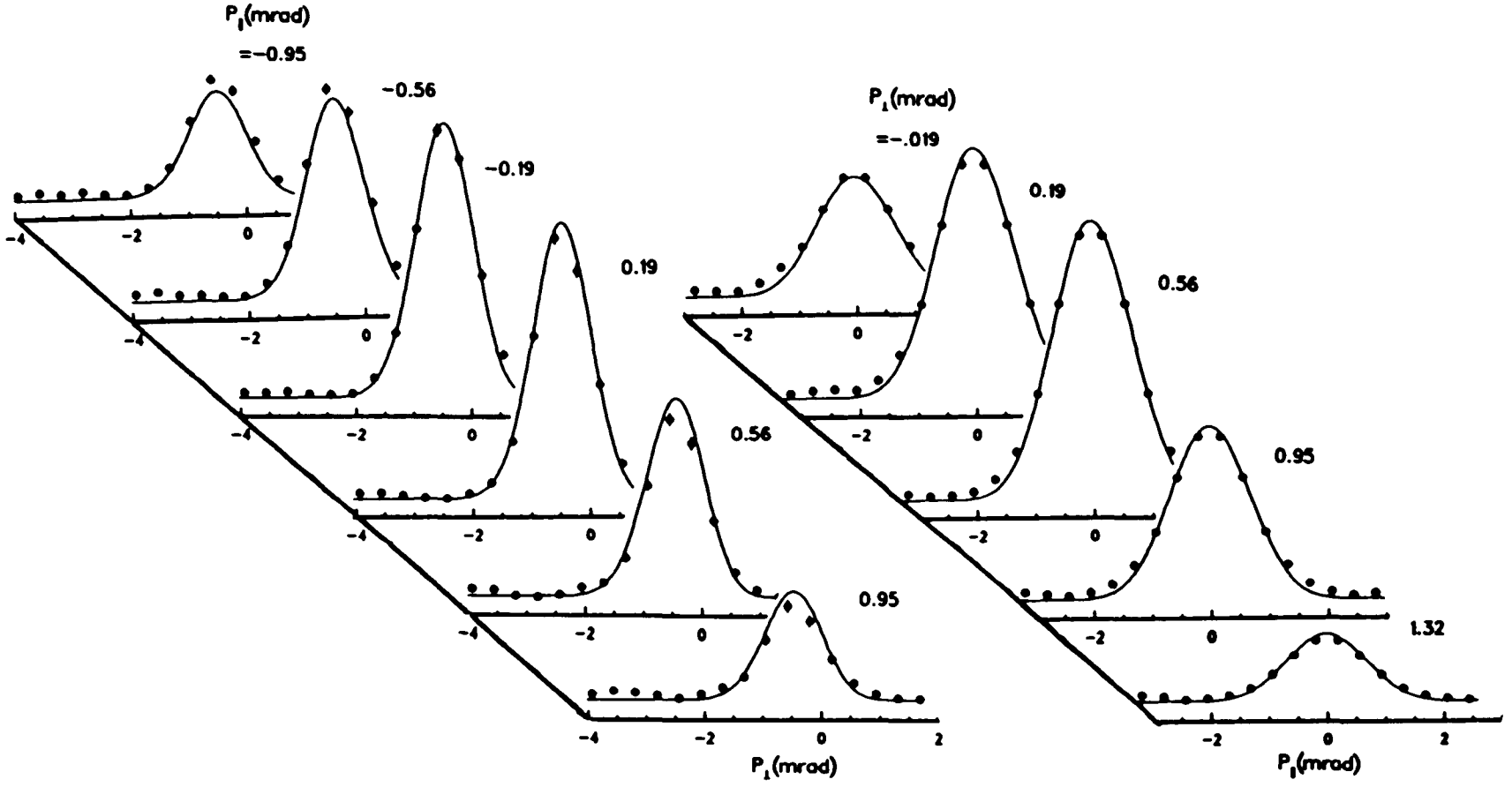

Figure 4.38. Theoretical prediction of Eq.(4.12)-(4.14) (curves) versus the extracted thermal Ps spectrum(dots) at 600°K. They are normalized to have equal peak intensity. A constant reflection coefficient is used in Eq.(4.12).

culated from solving the time dependent Schrodinger equation. The temperature dependence of the tunneling rate arises from the initial positron state. This description is similar to that for the spontaneous Ps emission, except the initial positron state is an bound state. Isii, again, included the dissociation term in the Hamiltonian and treated it similarly with the ion neutralization theory discussed in §.4.9.7. The dissociation of Ps has the equivalent effect as the 'reflection coefficient' in the thermodynamic theory of Chu, *et al.* [35]. The total desorption rate obtained by Ishii[29] is essentially the same as Eq.(4.11), but with a weak temperature dependent 'reflection coefficient'.

Chapter 5. 2D-ACAR Measurement on Si Surfaces

§ 5.1 The Motivation

One of the unique properties of positron annihilation in crystalline materials is the occurrence of the high momentum component (HMC or umklapp component), which arises from the delocalized nature of both the positron and electrons in a periodic system. This can be clearly visualized in the IPM derivation of §1.4. This effect is enhanced when delocalized Ps atoms are formed and annihilate inside single crystal quartz and ice[26], owing to the narrow distribution of the center of mass motion. In Fig. 5.1 we replot the results of 2D-ACAR measurements on an Al crystal(a) [3] and on a quartz crystal(b)[4]. For Al the HMC becomes visible only after we scale up the spectrum. In contrast the quartz spectrum clearly exhibits first and second order satellite peaks on top of a broader distribution which is due to the pickoff process[26]. These satellite peaks are shown[116] to be a necessary consequence of HMC in the para-Ps decay which arises from the orthogonalization of the the positronium and the valence electron wave functions. The presence or absence of the HMC in an angular correlation spectrum thus provide us a unique signature of whether a positron or Ps state is delocalized or localized in the system under study. We note, unfortunately, that in both cases the intensity of the HMC decreases rapidly as we go to higher order G, and hence makes these effects less significant in most of the cases. In the application to the surface study(see §1.5), however, advantages of surface reconstructions could be taken to make this effect potentially more observable. A reconstructed surface often possesses a larger 2D unit cell with respect to the substrate structure. This in turn leads to a reduction of the 2D reciprocal lattice unit cell and to an enhancement of the HMC of the annihilation due to delocalized surface state positrons(if it indeed exists). A surface-delocalized image potential induced positron surface state or a physisorbed Ps state at a surface will then become the two dimensional analogues of the above two bulk examples.

Of the many reconstructed surfaces discovered to date, Si(111)-(7×7) is the most appealing

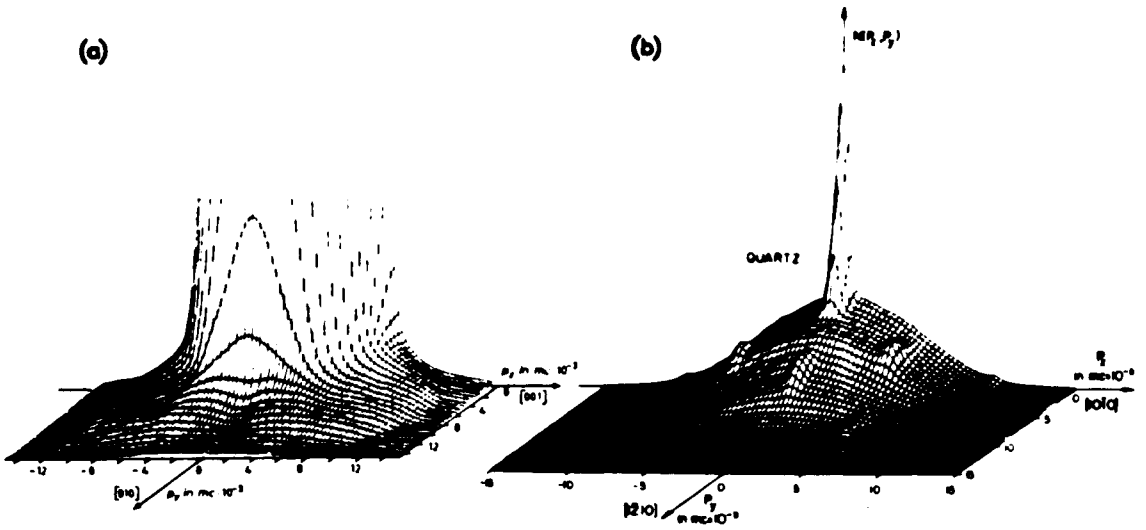

Figure 5.1. 2D-ACAR spectrum for: (a). positron umklapp annihilation in a single crystal Al(from Ref.[3]); and (b). Ps umklapp annihilation in a quartz crystal (from Ref.[4]).

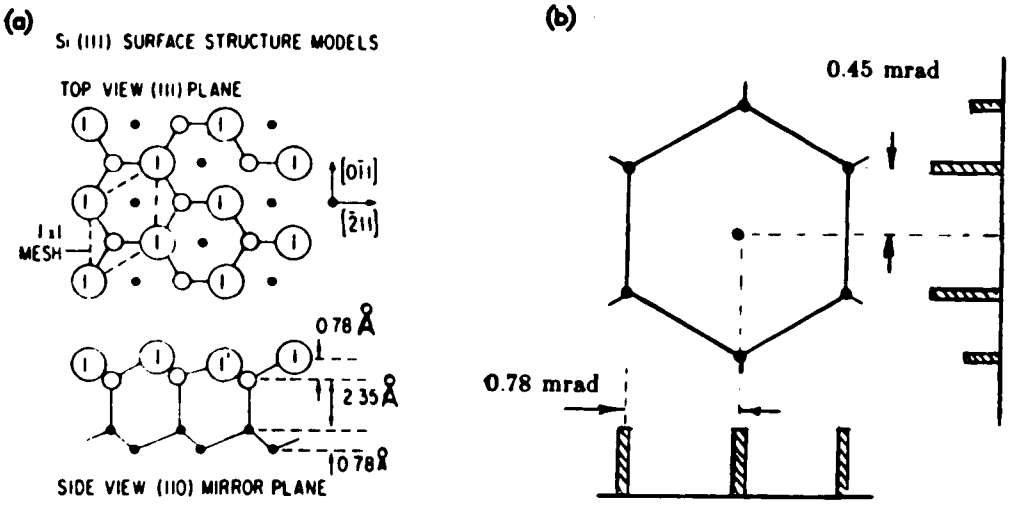

Figure 5.2. (a). Model structure for the perfect termination in the (111) direction of a silicon crystal, the circle size is larger for closer atoms; (b). Projection of the first order umklapp components for a Si(111)-(7×7) surface reciprocal lattice, the bar height is proportional to the number of the reciprocal lattice vectors projected.

to our interest for its extraordinary large unit cell containing 49 atoms[69,117]. The bulk Si bond length(Fig. 5.2a) is $a_B = 2.35$ Å and the dimension of the conventional cubic unit cell(8 atoms) at room temperature is $a_0 = 5.431$ Å. The layer spacing in the (111) direction is 0.78 Å between the outer double layers and is 2.35 Å (Si-Si bond length) for second-to-third layer. The side of the unit mesh of a perfectly terminated surface in the (111) direction is $a_{1\times1} = 3.84$ Å[69]. The unit length of the corresponding reciprocal lattice vector $|\vec{g}|_{7\times7}$ is equal to 0.866 *a.u.*. For the (7×7) reconstructed surface of Si(111) the unit cell expands by a factor of 7 in both independent directions and the corresponding unit cell of the reciprocal lattice is reduced by the same factor, which leads to $|\vec{g}|$=0.124 *a.u.* or 0.903 *mrad*. Fig. 5.2b illustrates the projection of the first order HMC along $(\bar{2}11)$ and $(01\bar{1})$ direction. The bar height is proportional to the number of the reciprocal lattice vectors projected. Thus if we were to see the HMC in the ACAR spectrum of Si(111)-(7×7) surface they would appear every 0.78 *mrad* in the $(01\bar{1})$ projection and every 0.45 *mrad* in the $(\bar{2}11)$ projection. Within the same order, the relative intensities of these HMC would very in accordance with the number of the contributing reciprocal lattice vectors. By comparison, the Si(100) is reconstructed with a (2×1) unit mesh and two sets of (2×1) domains along the [011] and $[0\bar{1}1]$ directions[118]. The dimension of the unit square mesh of the unreconstructed Si(100) surface is 3.84 Å. Thus for Si(100)-(2×1) reconstructed surface, the first order HMC might appear at 3.16*mrad* in a $(01\bar{1})$ projection. Note that in the present geometry shown in Fig. 1.4, HMC would only occur in the parallel distribution with respect to the surface.

Our work was naturally motivated in part by the fundamental and technological importance of Si surfaces. Despite that considerable efforts and significant progress have been made over the past 30 years these surfaces continue to generate broad interest because of many remaining uncertainties. We have learned in the study of Al surfaces that Ps spectroscopy reflects electron density of states near the surface, and that positron surface state annihilation is sensitive to various surface conditions. This recently extended technique might allow us to yield new complementary information about the electronic structures of these surfaces. The understanding of these analogous mechanisms on semiconductor surfaces, whose electronic structure differs greatly from metals

due to the presence of the fundamental band gaps between the filled valence band and empty conduction band(at T=0), is an important constituent of a more complete picture of the behavior of positrons in surfaces. These studies would give us an insight into what contributions can the 2D-ACAR technique offer to the surface physics.

We have carried out measurements on Si(111)-(7×7), hydrogenated Si(111)-(7×7), and Si(100)-(2×1) surfaces. As we shall see our preliminary results bear some strong resemblance between the symmetries of the surface momentum density and the bulk momentum density. The similarity is enchanced when the Si(111)-(7×7) surface is saturated with atomic hydrogen. Although the ACAR spectra exhibit some oscillations it is difficult at present time to assign them to HMC without introducing any controversy. It is not surprising that for such complicated systems, it is impossible to fully understand our data, or more general the interaction of positrons with these surfaces, without more comprehensive measurements as well as a close interplay with theoretical investigations. Thus it is more appropriate to regard the remainder of this chapter as the initial exploration of these surfaces rather than to provide unambiguous solutions to various questions raised during these studies.

§ 5.2 Two Reconstructed Si Surfaces

The reconstructions of silicon surfaces form a remarkable rich class of geometrical structures[69,117,118]. Depending upon the treatment various surface atom configurations can be fabricated. For Si(111), the most frequently obtained structure following sputtering and thermal annealing is the (7×7) reconstruction[119]. Cleaved Si(111) surface displays a (2×1) reconstruction[120]. Unreconstructed Si(111)-(1×1) surface can be prepared by impurity-stabilizing or quenching the Si(111)-(7×7) surface[121]. A recent scanning tunneling microscope(STM) experiment[122] further exploited that c(4×2) and (2×2) regions populate the ordered parts of the Si(111) surface directly after laser annealing, and that subsequent partial thermal anneals result in a surface containing (5×5), (7×7), (9×9), and other intermediate structures. For Si(100), the simultaneous presence of (2×1) and (1×2) domains is the most abundant structure, while c(4×2) and (2×2) domain are also observed[118,123]. It is reported[124] recently that phases with (2×n)

structure($6 < n < 10$) can be formed on Si(100) by rapid quenching from high temperature. An unreconstructed (1×1) structure is also obtainable by H-stabilization[125]. In our measurement only the common Si(111)-(7×7) and Si(100)-(2×1) structures were obtained. We will, therefore, restrict the following discussion to these two surfaces.

5.2.1 Si(111)-(7×7)- The atomic structure of Si(111)-(7×7) reconstructed surface is, perhaps, the most mysterious structure encountered in surface science. It took thirty yeas of persistent research to finally resolve this challenging problem.† The model, which is supported by most of the experimental and theoretical studies and hence seems universally accepted, is the Dimer-Adatoms and Stacking-fault (DAS) model introduced by Takayanagi *et al* [126]. Fig. 5.3a shows the top view of this DAS model unit cell, in which the size of the circles is larger for the closer atoms. Fig. 5.3b is the side view along the long diagonal, i.e. atoms on the $(10\bar{1})_d$ lattice plane. The (7×7) unit cell encircled by the solid line is divided in two equilateral triangles. In the right half of the cell, the crystal maintains the normal cubic diamond stacking sequence up to the last complete atomic layer. In the left half, however, the surface contains a stacking fault that is due to a rotation of the bond directions in the outer layer by 60°. The faulted and unfaulted regions of the unit cell are 'zipped' together by dimer bonds along the edges of the two triangles. On top of this structure, 12 adatoms are located at the three-fold hollow sites(having atoms beneath in the second layer). Each adatom is bonded to the three surface atoms below, resulting in a reduction of two dangling bonds per adatoms. Additional dangling bonds are present on the six so called restatoms in the underlying layer and on 1 atom inside the hole at the corner of the unit cell. The reduction of dangling bonds from 49 to 19 is the driving force for the surface reconstruction.

The electronic structure of this surface is strongly influenced by this complicated reconstruction. In addition to the regular bulk band electrons, photoemission and angle-resolved photoemission experiments[121,127] have revealed three surface states associated with the (7×7) reconstruction. As shown in Fig. 5.4 these surface states(open circles) appear at $\approx0.2(S_1)$, $\approx0.8(S_2)$, and

† This was achieved after we started this work.

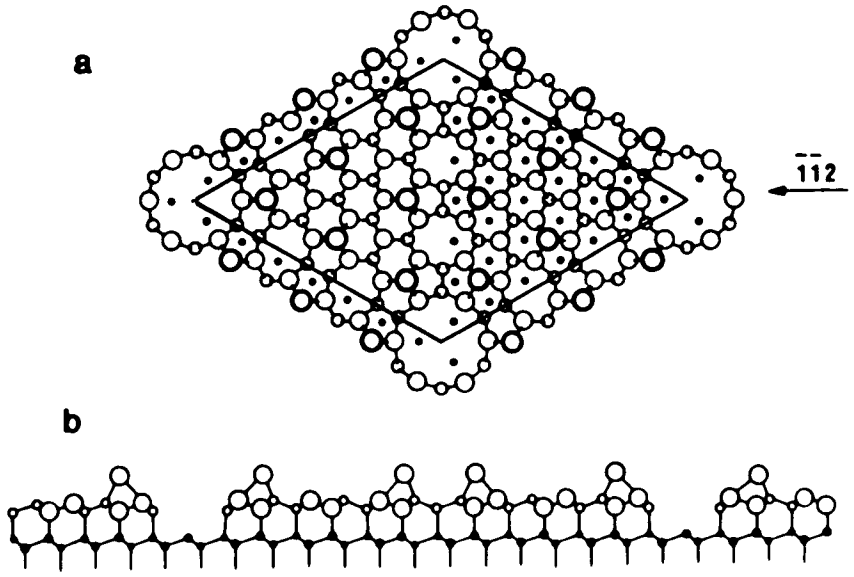

Figure 5.3.(form Ref.[126]). The dimer-adatom-stacking-fault(DAS) model for the Si(111)- (7×7) reconstructed surface: (a). top view; (b). the $(10\bar{1})_d$ lattice plane along the long diagonal of the 7×7 unit cell(solid line). Nearest atoms enlarged. The stacking fault layer is on the left triangle(see b).

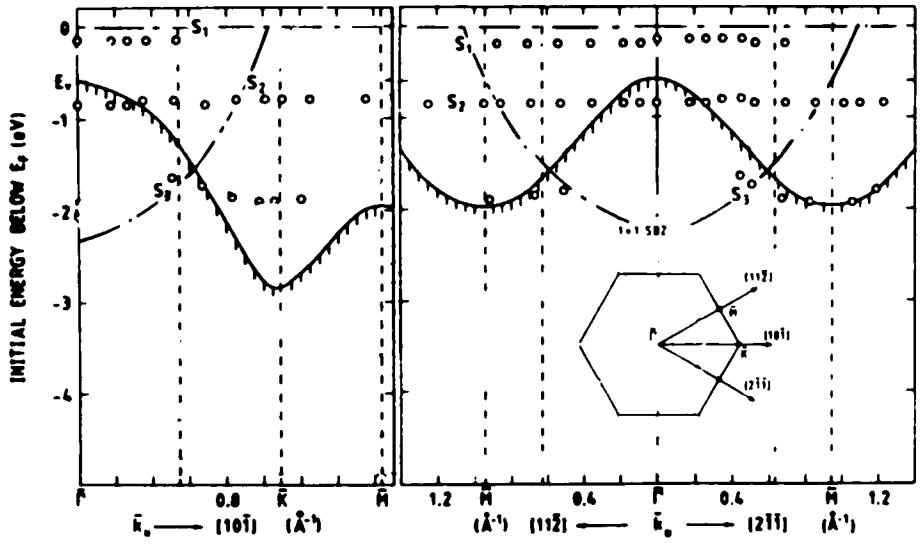

Figure 5.4. Circles: dispersions of the measured surface states S_1, S_2, and S_3 in a 1×1 SBZ for a Si(111)- (7×7) surface; Shaded solid lines: the top of the projected valence band; Dot-chained lines: the minimum Ps dispersion curve(see §5.4).(after Ref.[127]).

$\approx 1.8(S_3)eV$ below the Fermi level. Only the S_3 state exhibit dispersion with a narrow band width of $\approx 0.3\ eV$. The S_1 and S_2 states are sensitive to gas adsorption and thus are assigned to dangling bonds while S_3 is assigned to back-bonds or to the dangling bonds. More specific information has been obtained by STM studies[128], which shows that S_1, S_2 and S_3 states are directly associated with the dangling bonds on the adatoms, dangling bonds on the restatoms and the back-bonds, respectively. These observations are in good agreement with the first-principle pseudopotential calculation[129] using a simplified adatom model. Since the S_2 state is lower than S_1 state, electrons are transferred from the adatoms to the restatoms to fill the S_2 manifold leaving 6 out of 24 of the S_1 manifold filled. Consequently, Si(111)-(7×7) is weakly metallic.

5.2.2 Si(100)-(2×1)- A number of distinct models have been proposed for Si(100)-(2×1) reconstruction[118]. They are, as shown in Fig. 5.5 with the ideal unrelaxed surface(a), the symmetric dimer model (b), vacancy(or missing row) model (c) and (d), conjugated-chain model (e), double conjugated-chain model (f), and the asymmetric (or buckled) dimer model(g). Among the various surface structural geometries the dimer configuration appears to explain most of the experimental results. In bulklike terminated surface(a) each of the first-layer atoms is bonded to two atoms in the second layer, leaving two dangling bonds on each surface atom. Dimerization reduces one dangling bond per surface atom and leads to the lowest total energy as compared with other models shown in Fig. 5.5. The optimal dimer geometry is, in fact, the asymmetric dimer geometry(g), in which the two buckled atoms(1&2) have a small vertical displacement. It is shown[123] that the surface has a rather large number of defects in addition to the symmetric and asymmetric dimers. Recent pseudopotential total-energy calculations[130], however, indicated that the dimer-plus-chain model proposed for the $c(4\times2)$ has a lower energy than the (2×1) dimerized surface.

Two surface states are often found for the two domain Si(100)-(2×1) reconstructed surface[131-133]. One is at 0.7eV below E_F, and it is assigned to the dangling-bond band, while the other ranges between 2 and 3eV below E_F and is assigned to the dimer bond. Tight-binding calculations[133], reproduced in Fig. 5.6 for the asymmetrical model, has demonstrated a dimer-

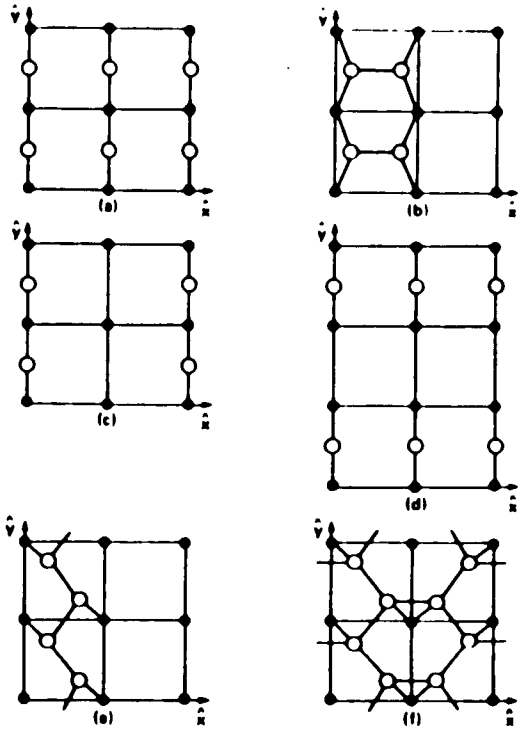

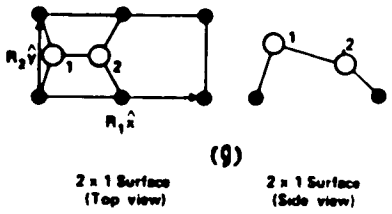

Figure 5.5. Proposed models for 2×1 reconstructed Si(100) surface: (a) ideal, unrelaxed surface; (b) symmetric dimer; (c) and (d) vacancy models; (e) conjugated-chain model; (f) 'double' conjugated model; (g) asymmetric dimer model. Surface atoms are shown as open circles and second layer atoms as dark circles.(after Ref.[118]).

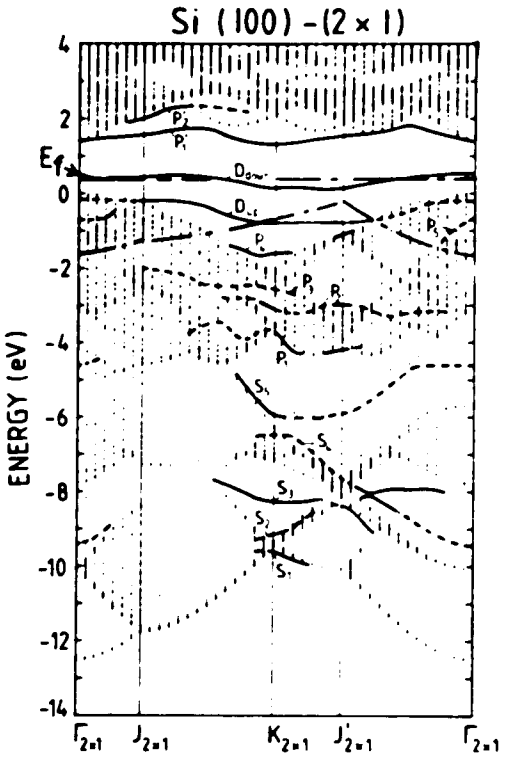

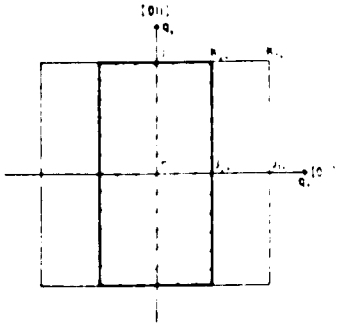

Figure 5.6. Right: Surface Brillouin zones of the ideal 1×1 and the reconstructed 2×1 surfaces of Si(100); Left: Surface-band structure of Si(100)-(2×1) for the asymmetric dimer model. E_F is 0.35eV above the top of the valence band. The dot-chained curve is the minimum Ps dispersion. For the labeled surface state bands see discussion in the text and in Ref.[133].

bond band P_3, a fully occupied dangling-bond states, D_{up}, at atom 1(Fig. 5.5g) and an empty dangling-bond state, D_{down}, at atom 2. The calculated dispersion, band width and the energetic position of these states are in good agreement with experiments(not shown in the figure). The presence of the D_{up} dangling-bond state as a result of the asymmetrical dimerization is the origin of the semiconducting property of this surface.

§ 5.3 Bulk and Surface Annihilation Spectra

5.3.1 Experimental Results - A typical result obtained for a Si(111)-(7×7) surface bombarded with 200eV positron beam is shown in Fig. 5.7. Figure 5.7b and 5.7c are, in the same scale, the separated Ps and surface state spectra from the original spectrum of Fig. 5.7a. Their perspective views are similar to those plotted in Fig. 3.8. We have shown in §1.2.1 that at 200eV incident energy 99% of the implanted positrons diffuse back to the surface and the bulk annihilation at this energy is essentially zero. Thus the symmetrical spectrum obtained from separation is pure surface state and no subtraction of residual bulk component is needed in contrast to the 1.5keV Al runs. Two special features are worth noting. (i). The surface state only possesses an inversion symmetry, but no reflection symmetry with respect to the surface; (ii). The surface state spectrum is hexagon-like in the outer contours, but not exactly hexagonal.

For all the silicon surface measurements we have used 200eV incident energy, which henceforth is implied in all the surface data to be shown below and will not be mentioned latter for simplicity. For convenience, we list in table 5.1 the useful information associated with the data to be discussed. Some of the previously established electronic and positronic properties are summerized in table 5.2.

Fig. 5.8 shows the contour plots of a set of high energy runs(left) and the corresponding surface runs(right). (a)-(b) are for a Si(111)-(7×7) surface projected along $(01\bar{1})$; (c)-(d), a Si(111)-(7×7) surface projected along $(\bar{1}2\bar{1})$(*i.e.* 30° azimuthal rotation of (a)-(b)); and (e)-(f), a Si(100)-(2×1) surface projected along the $(01\bar{1})$. The beam energy is 15keV for (a), 14keV for (b), and 13keV for (e), which are reflected by the increasing amount of Ps components appeared in these

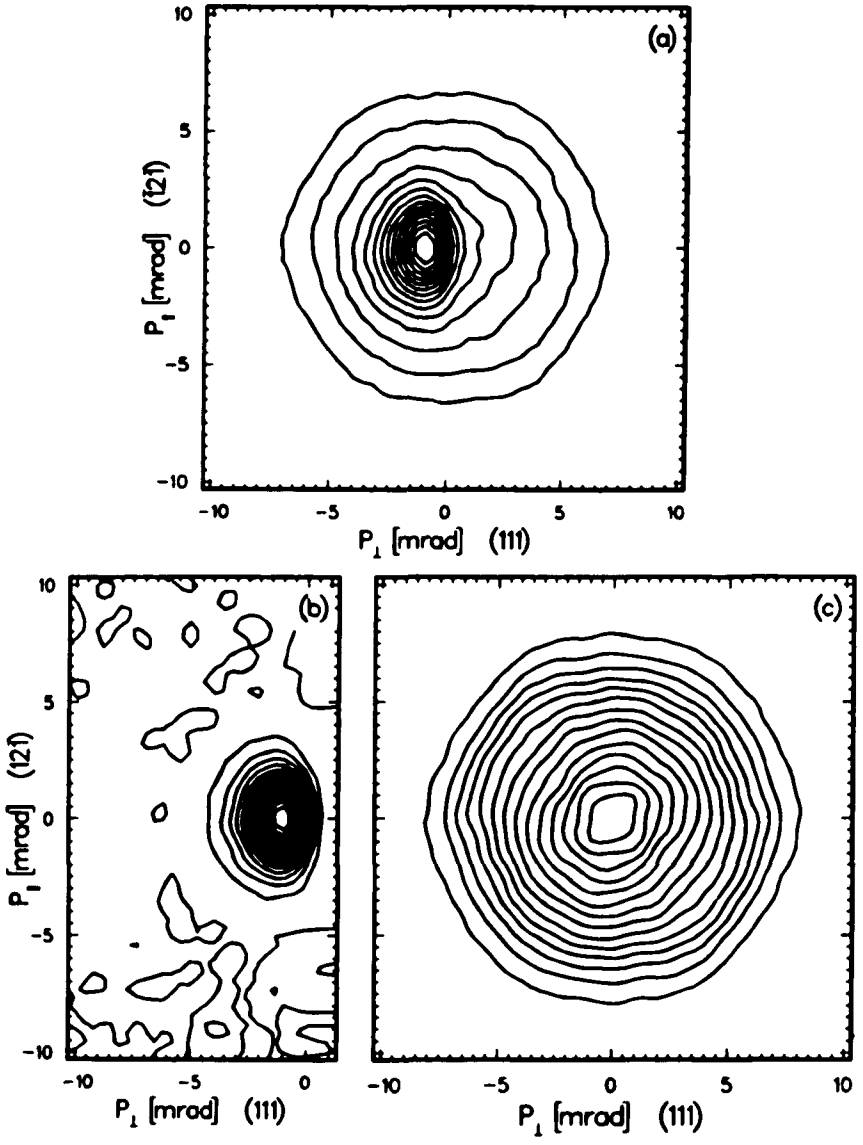

Figure 5.7. Contour plots of the 2D-ACAR spectrum for a Si(111)-(7×7): (a) as measured; (b) separated Ps component; and (c) separated surface state component. The incident positron energy is 200eV and sample is at room temperature.

Table 5.1 Collected information associated with figures in chapter 5. $p_\perp$, $p_\parallel$, and $p_\parallel'$ represent the crystal orientations in these directions; V_{tot}, total counts of the direct measured spectrum before applying momentum sampling function; E, incident positron energy; T, the sample temperature; H, total hydrogen exposure and f, extracted Ps fraction(See Eq.(3.30)).

	p_x	p_y	p_z	V_{tot} (10^3)	E (keV)	T ($^\circ K$)	H	f (%)
Fig. 5.8a	111	$\bar{1}2\bar{1}$	$01\bar{1}$	865	15	300		
Fig. 5.8b	111	$\bar{1}2\bar{1}$	$01\bar{1}$	261	0.2	300		43
Fig. 5.8c	111	$01\bar{1}$	$\bar{1}2\bar{1}$	446	14	300		
Fig. 5.8d	111	$01\bar{1}$	$\bar{1}2\bar{1}$	356	0.2	300		45
Fig. 5.8e	100	011	$01\bar{1}$	484	13.5	300		7
Fig. 5.8f	100	011	$01\bar{1}$	762	0.2	300		55
Fig. 5.9a	111	$\bar{1}2\bar{1}$	$01\bar{1}$	947	0.2	300		43
Fig. 5.9b	111	$\bar{1}2\bar{1}$	$01\bar{1}$	647	0.2	300	monolayer	29
Fig. 5.14a	111	$\bar{1}2\bar{1}$	$01\bar{1}$	138	14	870		4
Fig. 5.15a	111	$\bar{1}2\bar{1}$	$01\bar{1}$	167	0.2	870		83

Table 5.2 Positronic properties of $Si(100)$-(2×1) and $Si(111)$-(7×7) surfaces (selected from Tbl. 5.1 in Ref.[1]). ϕ_- and E_F-E_v are from Refs.[127,131,132], ϕ_{P_s} and E_b are defined by Eq.(1.13) and Eq.(1.14), the remainders are experimental values).

	ϕ_- (eV)	E_F-E_v (eV)	ϕ_+ (eV)	ϕ_{P_s} (eV)	E_a (eV)	E_b (eV)	y_0	f_0
$Si(100)_{2\times1}$	4.85	0.35			0.17(3)	2.06(7)		0.63
$Si(111)_{7\times7}$	4.60	0.63	-1.0(2)?	-3.2?	0.49(5)	2.69(7)	0.1	0.44

contour plots. Some major crystalline orientations are indicated in the figure. We see that the three surface state spectra display a resemblance to the symmetry of their bulk counter parts. In particular, the relative rotation of $\sim50^\circ$ between (a) and (e) can also be observed in (b) and (f), except for some differences near the centers. The reflection symmetries exhibited in these spectra with respect to some low index axes are required by the crystal symmetry.

Fig. 5.9 shows with equal peak intensity the cross sections through $p_\parallel=0$ (top) and $p_\perp=0$

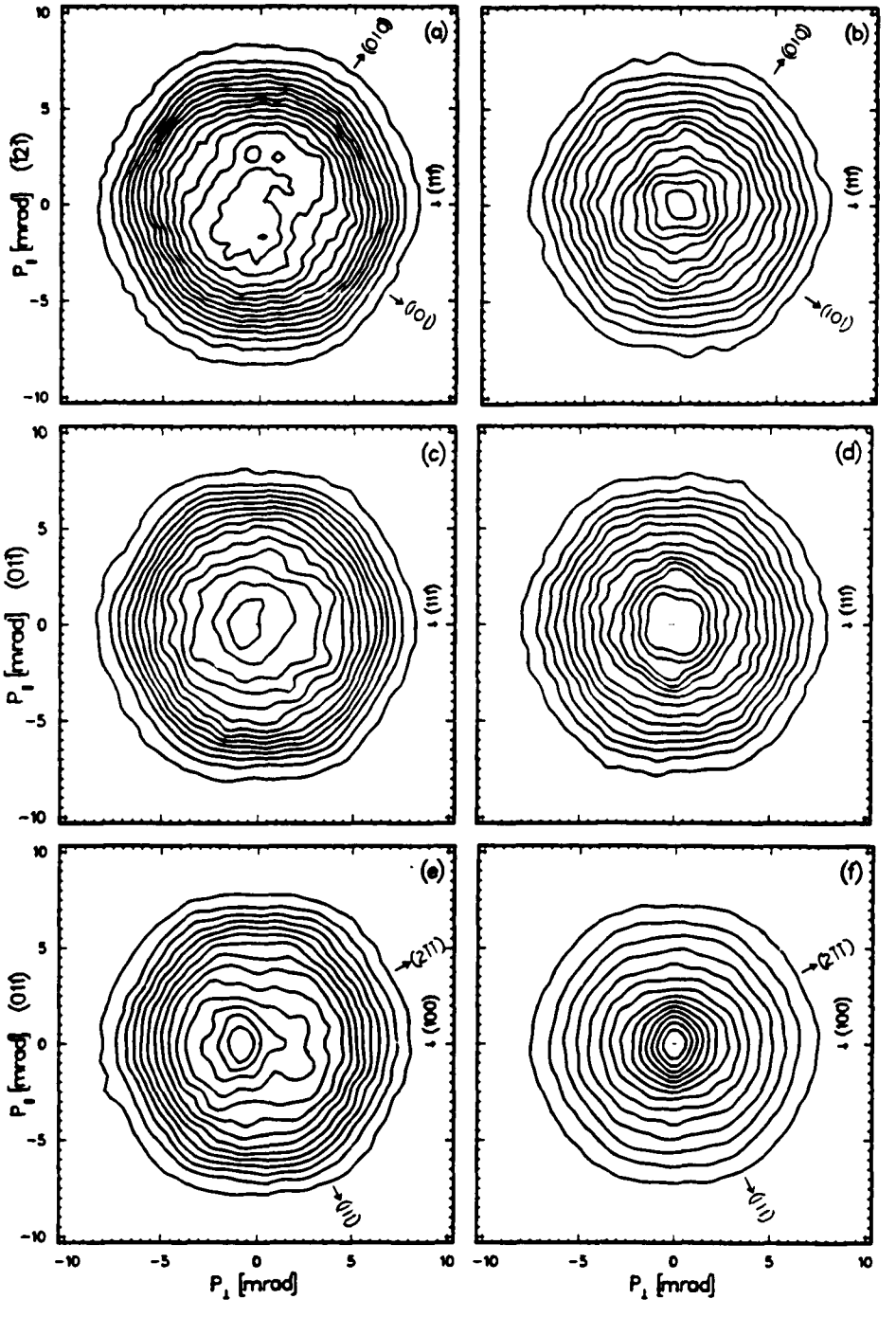

Figure 5.8. High energy(left column) and surface state(right column) 2D-ACAR spectrum for a Si(111)-(7×7) (a to d) and for a Si(100)-(2×1) (e and f). The beam energy is: 15keV for (a); 14keV for (c); and 13keV for (e); and 200eV for all the surface runs(b,d,f). (c)-(d) are the 30° azimuthal rotation of the (a)-(b) surface.

(bottom) of these six spectra in Fig. 5.8. For each surface the high energy run is shown on top of the surface run for comparison. The columns from left to right corresponds to the rows from top to bottom of Fig. 5.8. The dashed curves lying under the upper curves are from the same high energy spectrum after the removal of the Ps component. That the Ps fraction increases(from left ot right) as the beam energy decreases from 15keV to 13keV are clearly seen in these cuts. The surface state curves are much narrower than the bulk, though their contour symmetry are similar. The curves very from one orientation to another and there are oscillations and breaks in these curves, especially in the parallel cuts of the surface spectra. We defer our discussion regarding these structures.

A higher statistical surface data is generated by summing three independent runs. Similar cuts at $p_{\parallel}=0$ and at $p_{\perp}=0$ for this summed surface state spectrum are shown in the lowest portion of Fig. 5.10(in diamonds). We see that the oscillations become much weaker, but still visible. On top of these two curves we plot a set of same cuts for a H-saturated Si(111)-(7×7) surface run. The small oscillation for the clean surface are replaced by two large bulges on each side of both curves, as a result of monolayer hydrogen coverage. Fig. 5.10a and 5.10b are two contour plots of the ACAR data for the clean and H-saturated Si(111)-(7×7) surface, respectively. The effect of hydrogen adsorption reflected in the 2D contour plots (b) is seen to produce a flatter distribution near the top of the spectrum, leading to a closer similarity to the bulk symmetry(Fig. 5.8a).

Due to the complicated structure of these 2D-ACAR spectra verification of possible anisotropic distributions is made from comparing the long-slit spectra of both surface and bulk distributions(after Ps component being removed). These long-slit spectra are shown in Fig. 5.11. The FWHM of the normal distribution for each spectrum is indicated in the figure. Spectra (a) to (c) are generated from the high energy runs of Fig. 5.8a, 5.8c, 5.8e; spectra (d) is from the hydrogenated Si(111)-(7×7) of Fig 5.10b; and spectra (e) to (f) are from surface runs of Fig 5.8b, 5.8d, and 5.8f. We see no sign of anisotropy in all the surface spectra. The normal widths of three bulk spectra(a-c) are almost the same. The (100) bulk spectrum(c) shows some anisotropy as expected from the earlier inspection of its 2D contour plots(Fig. 5.8e). However this anisotropy

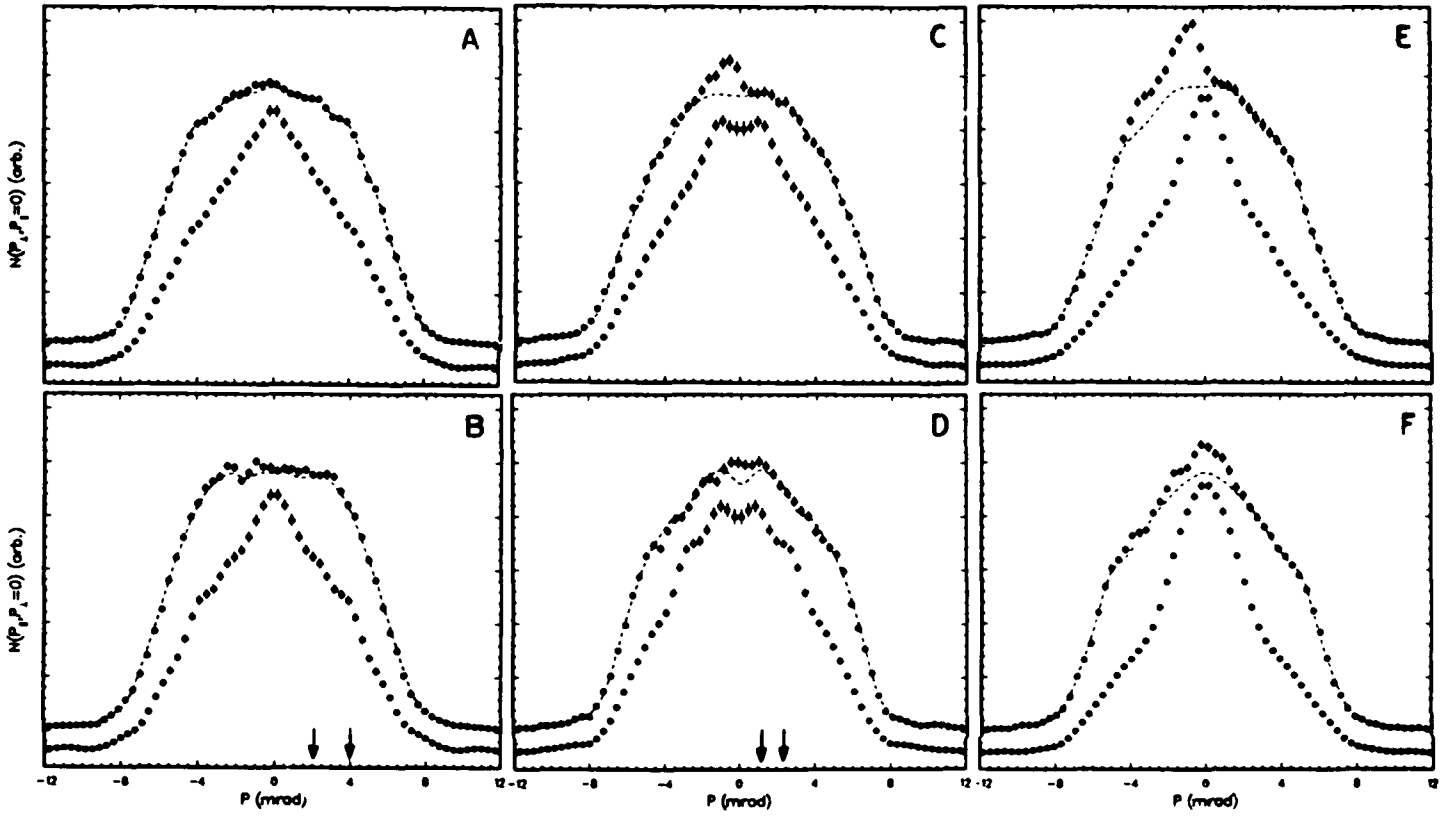

Figure 5.9. Sections at $p_{\parallel}$=0 (upper) and $p_{\perp}$=0 (lower) of the spectra shown in Fig 5.8. High energy spectra are plotted on top of the surface state spectra. Dashed curves are the same bulk spectra after remove the small Ps component. Columns from left to right correspond to rows from top to bottom in Fig. 5.8.

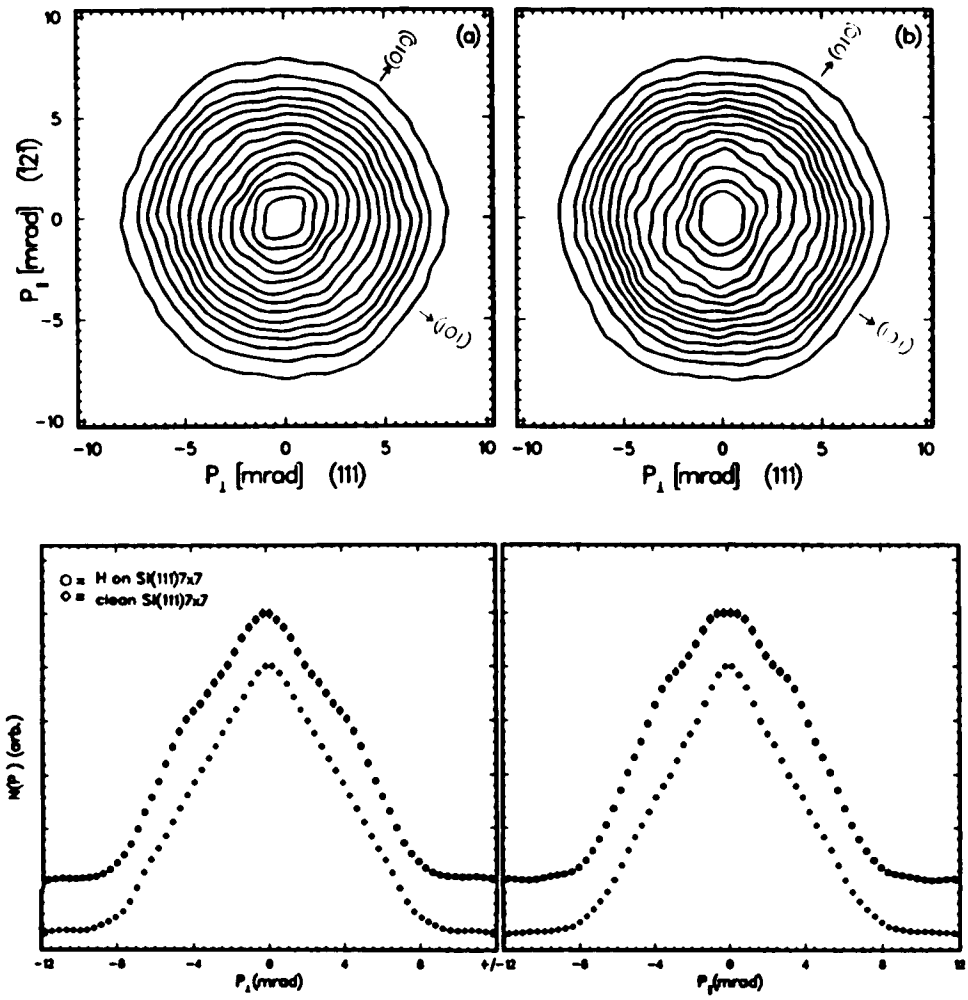

Figure 5.10. Top: contour plots of the 2D-ACAR spectra for: (a) a clean Si(111)-(7×7) surface; and (b) monolayer hydrogen covered Si(111)-(7×7) surface. Bottom: cuts at $p_{\parallel}$=0(left) and $p_{\perp}$=0(right) of the above two surface state spectra. The clean surface spectrum(under) is the sum of three independent runs.

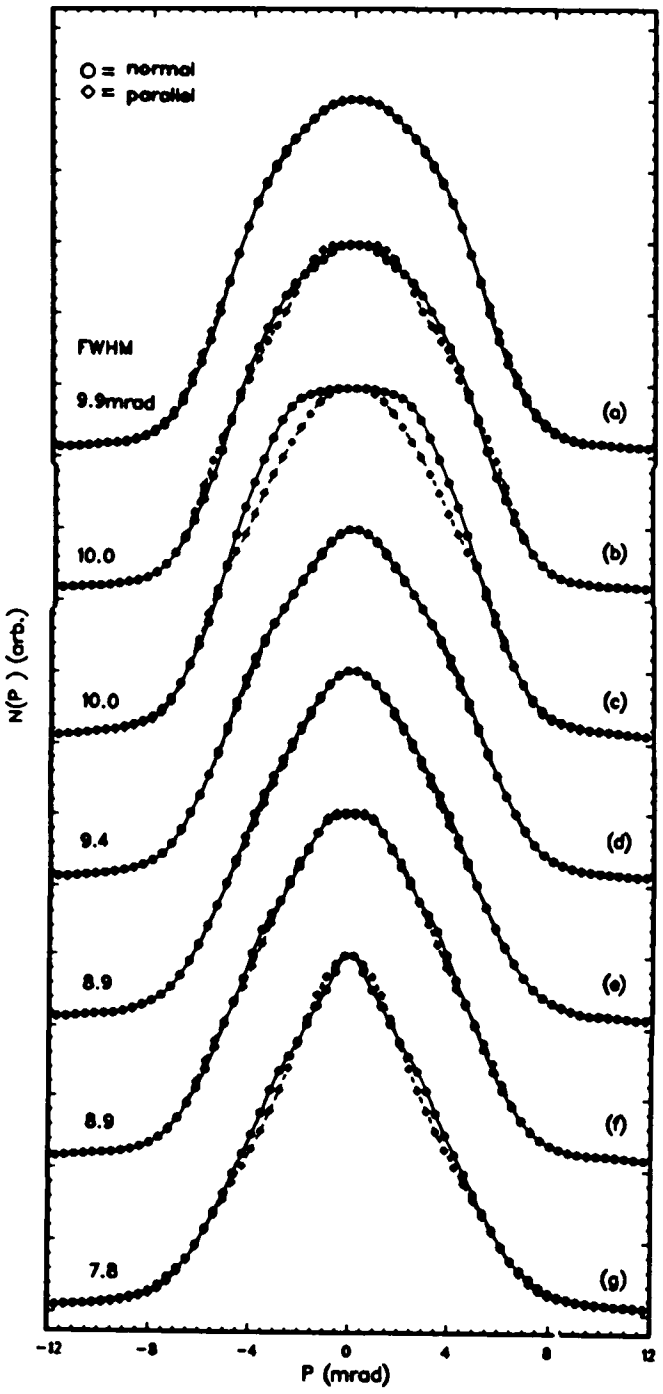

Figure 5.11. Peak-normalized long-slit spectra. (a) to (c) are generated from the bulk spectra (a), (c), (e) in Fig. 5.8; (d) from the hydrogenated surface spectrum of Fig. 5.9b; (e) to (g) from clean surface spectra (b), (d), (f) in Fig. 5.8. The FWHM is given for each of the normal distribution.

diminishes in the surface spectrum (g). Two Si(111)-(7×7) surface spectra(e and f) have the same width, which is 1.1mrad larger than that of Si(100)-(2×1), but is 0.5 mrad narrower than the monolayer hydrogen covered Si(111)-(7×7) surface spectrum.

5.3.2 Discussion - Our measurements at 13-15keV(Fig. 5.8a, c, e) are in good agreement with those obtained from standard bulk ACAR measurement[134]. Fig. 5.12a shows an example for comparison. In fact these Si data are very similar to the results of Ge[135,136]. It is shown[137] that the hexagon-like outer contours are closely related to the Jones zone, but the exact origin of the warped shape in the central part of the spectrum is not fully understood yet. The warped shape near the center of spectrum Fig. 5.8a can be better visualized from its perspective presentation in Fig. 1.6a. We note that similar warped shapes appear in the surfaces of constant energy of the valence bands in k-space[138]. More quantitative connection of these band structures with the observed bulk ACAR data is currently being considered[134].

It may first appear exciting that some oscillations are present in the Si(111)-(7×7) surface spectra(Figs. 5.9b and 5.9d). However, they can not be directly identified as the HMC associated with the (7×7) reconstruction, because the oscillations are separated by ≈ 2 *mrad* for the $(01\bar{1})$ projection(5.9b) and by ≈ 1.25 *mrad* for the $(\bar{1}2\bar{1})$ projection(5.9d), roughly three times our predicted values in §5.1. It is noted that in the DAS model(Fig. 5.3) between every two corner holes there are two eight-sided rings along the unit cell boundary and along the short diagonal. These eight-sided rings and the corner holes may be viewed as surface voids. Two additional voids can be found at the center of the six adatoms on each triangle(Fig. 5.3b). Together they form a (3×3) sub mesh of voids in the (7×7) unit cell. It is well known that due to the ion-core repulsion positron wave functions tend to peak in the low atomic density regions, e.g. vacancies, dislocation lopes, voids, *etc.*. Thus one may imagine that for a positron residing at the surface the apparent reconstruction of the Si(111) surface is (3/7×3/7). We would then arrive to a new prediction: the unit cell of the reciprocal lattice would have to be tripled and the observed oscillations would be consistent with the projection of the first order HMC associated with this corrugated surface voids net. Unfortunately, the following facts seem to be problematic with the above hypothesis:

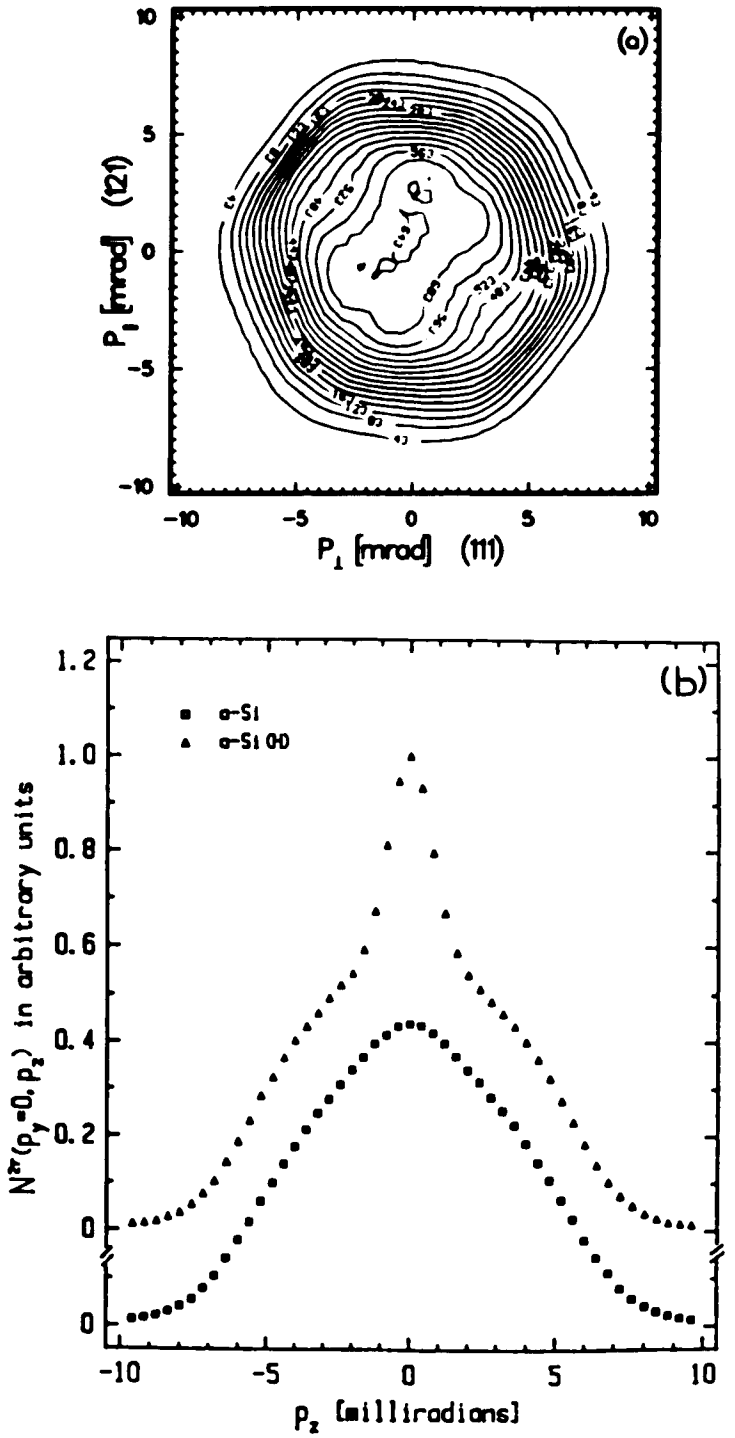

Figure 5.12. (a). Contour plot of the bulk Si ACAR spectrum(from R. N. West, unpublished data). (b). Cross section through the 2D-ACAR spectra at $p_y = 0$ for an amorphous silicon($a-Si$) and a hydrogenated amorphous silicon ($a-Si(H)$). (from Ref.[135], He *et al.*).

(1). The HMC is a long-range effect and requires the positron or Ps to be in a delocalized state in the surface plane. This is in contradiction with the lack of anisotropy in the long-slit spectra shown in Fig. 5.11, which is most likely due to the localization of the positron in the surface plane. Angle-resolved photoemission experiments[121] have shown that the S_2 and S_3 surface state of the Si(111)-(7×7) remain unchanged when the surface is converted to the impurity-stablized (1×1) phase or quenched (1×1) phase. Only the partially filled adatom dangling bond states S_1 are removed. STM images[139] showed that the (7×7) reconstruction persists essentially undistorted right up to the single atomic step. These observations indicated that the reconstruction itself depends on very-short-range , local interactions, and might suggest weak umklapp annihilation of surface positrons, although the reconstructed unit cell is very large.

(2). STM images[123,139] reveal that reconstructed Si surfaces contain sufficient amounts of defects, in particular for the Si(111)-(7×7), $(\bar{1}\bar{1}2)$ steps(parallel to $(\bar{1}10)$) and missing adatoms are found to be considerable[139]. It is unlikely that a delocalized positron will survive in this environment without been captured in defects. Further more, the fact that both projections of the Si(111)-(7×7) surface produce the same isotropic ACAR spectra(Fig. 5.11e-f) indicates that the surface state positron can not be a one dimensional delocalized wave propagating along the corner of the steps either.

(3). These oscillations could possibly be attributed to insufficient statistics and complicated structure of the ACAR spectra[Fig. 5.8]. This alternative is suggested based on the correlation between the bulk and surface spectra compared in Fig. 5.9. We note the normal cuts of the surface spectra in the left and middle columns also exhibit small oscillations which can not be explained by HMC. When the cuts are taken sequentially across the spectrum the positions where the oscillation occurs vary in a similar trend to those associated with the corresponding bulk spectrum. Moreover, summation of three independent measurements results in much weaker oscillations(Fig. 5.10).

Clearly more conclusive evidence for verifying the 'ordered' surface voids hypothesis requires better detector resolution and higher statistical data.

In contrast to the Si(111)-(7×7) spectra, Si(100)-(2×1) spectrum(Fig. 5.9e-f) shows a break in the normal and parallel sections at $\sim \pm 2$ *mrad*, possibly suggesting that the spectrum might consist of a narrower distribution on top of a broad distribution. We note that their widths would be comparable with that of the physisorbed Ps state[46] and that of a positron image induces surface state[40,41], respectively. Should this be the case the data would imply, apart from the lack of anisotropy, the coexistence of both the image potential induced state and the physisorbed Ps state. Again, it is not certain whether or not these breaks are correlated to the ones appearing at $\sim \pm 4.5$ *mrad* in the 13keV run for the same surface. It is also noted that the Si(100) sample contains a p-dopant with a resistivity of $15\text{-}30 ohm \cdot cm$, while the Si(111) sample is an detector-grade intrinsic crystal. This precludes the conclusion that the difference between their positron surface state spectra is a pure effect of the different surface reconstruction. Further systematic measurements with different dopant and with various level of dopant are needed to elucidate this question.

It is somewhat striking that the surface state spectra carry such strong resemblance of the bulk symmetry[Fig. 5.8]. This implies that despite of the complicated reconstructions of Si(111) and Si(100) surfaces, positrons residing at these surfaces still interact strongly with the valence electrons. It also suggests that the effect of the dangling bonds on the positron at the surface is relatively weak. In fact, a qualitative estimation is possible via the comparison of the results for the clean and hydrogenated Si(111)-(7×7) surface given in Fig. 5.10. Since all the dangling bonds are saturated by the hydrogen atoms and the Si-H bond is considerablely stronger than the Si-Si bond[140], the interaction of the surface state positron with the valence electrons is enchanced, giving rise to an even more bulk-like ACAR spectrum. This unique resemblance can serve as a guide for constructing some adequate theory describing the interaction of positrons with these surfaces, which in turn should provide us new insight into the electronic structure of these surfaces.

He *et al.* have performed ACAR and lifetime experiments on amorphous silicon($a\text{-}Si$) and hydrogenated amorphous silicon($a\text{-}Si:H$)[134]. Their ACAR data is replotted in Fig. 5.12b. In these samples positron annihilation occurs in the small voids, or the internal surface state. We see

that the cross section of the $e^- Si$ spectrum is almost the same as our surface spectrum. A narrow Ps component(~1.8 mrad) appears in the $e^- Si:H$, in which the dangling bond density is considerably reduced by the hydrogenation. As we will see the hydrogenated Si(111)-(7×7) surface produces less Ps than the clean surface. A better understanding of this different behavior could be approached by conducting temperature dependent study on the H-saturated Si(111)-(7×7) surface and comparing the results with those given by He et al.[134].

§ 5.4 Ps Momentum Distribution

Fig. 5.13 shows the Ps spectrum for: (a). Si(100)-(2×1); (b). Si(111)-(7×7); (c). 30° azimuthal rotation of (b); and (d). monolayer hydrogen covered Si(111)-(7×7). The crystalline orientations in the resolved momentum directions are given in the lower-left corner of each frame. The spectra (a)-(d) are extracted from the same measurements as in Fig. 5.8(f),(b),(d), and Fig. 5.10(b), respectively. The normal and parallel sections through $p_{\parallel}$=0 and $p_{\perp}$=-1.1 mrad of these Ps spectra are depicted in Fig. 5.14. The alphabetical labels for the four distinct symbols are in one-to-one correspondence with Fig. 5.13. We observe in these two figures very small difference among the four spectra. However the total Ps fraction indicated in the up-left corner of each frame in Fig. 5.13 varies substantially. The Si(100)-(2×1) reemits 10% more Ps than the Si(111)-(7×7) surface. The effect of hydrogenation of the Si(111)-(7×7) surface leads to a ~ 15% reduction of the total Ps fraction and slight broadening of the Ps distribution.

These results can be semi-quantitatively interpreted using our simple kinematical model and the surface projected band structures shown in Fig. 5.4 and Fig. 5.6. Here we use the Si(111)-(7×7) as an example for our discussion; parallel discussion can be carried out for the Si(100)-(2×1). We first need to determine ϕ_{P_s} for these two surfaces. Note that table 5.1 shows that the ϕ_+ is still uncertain(surprisingly). There has been one publication(to our knowledge), which reported $\phi_+ = -1.0(2) eV$ for a Si(100) surface. This value gives rise to $\phi_{P_s} = -3.2\ eV$, or the maximum Ps momentum $q_M = 5 mrad$, which is clearly in disagreement with our Ps momentum distribution(Fig. 5.14). A recent study[141] indicates that the '-1.0eV' does not represent the posi-

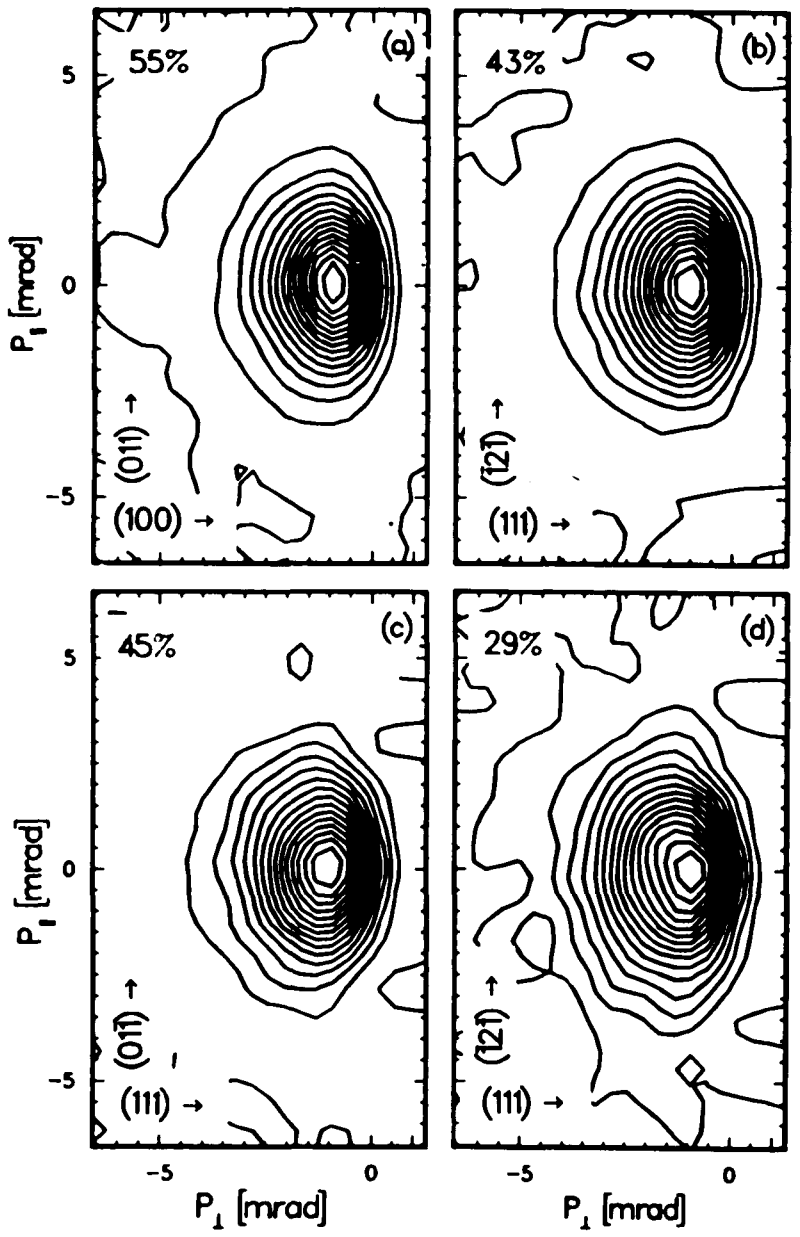

Figure 5.13. Ps 2D-ACAR spectrum for: (a) Si(100)-(2×1); (b) Si(111)-(7×7); (c) same as (b) but rotated by 30° azimuth; and (d) hydrogen saturated Si(111)-(7×7). Crystal orientations are indicated in the lower-left corner, and total Ps fraction at 200eV incident energy is in the up-left corner.

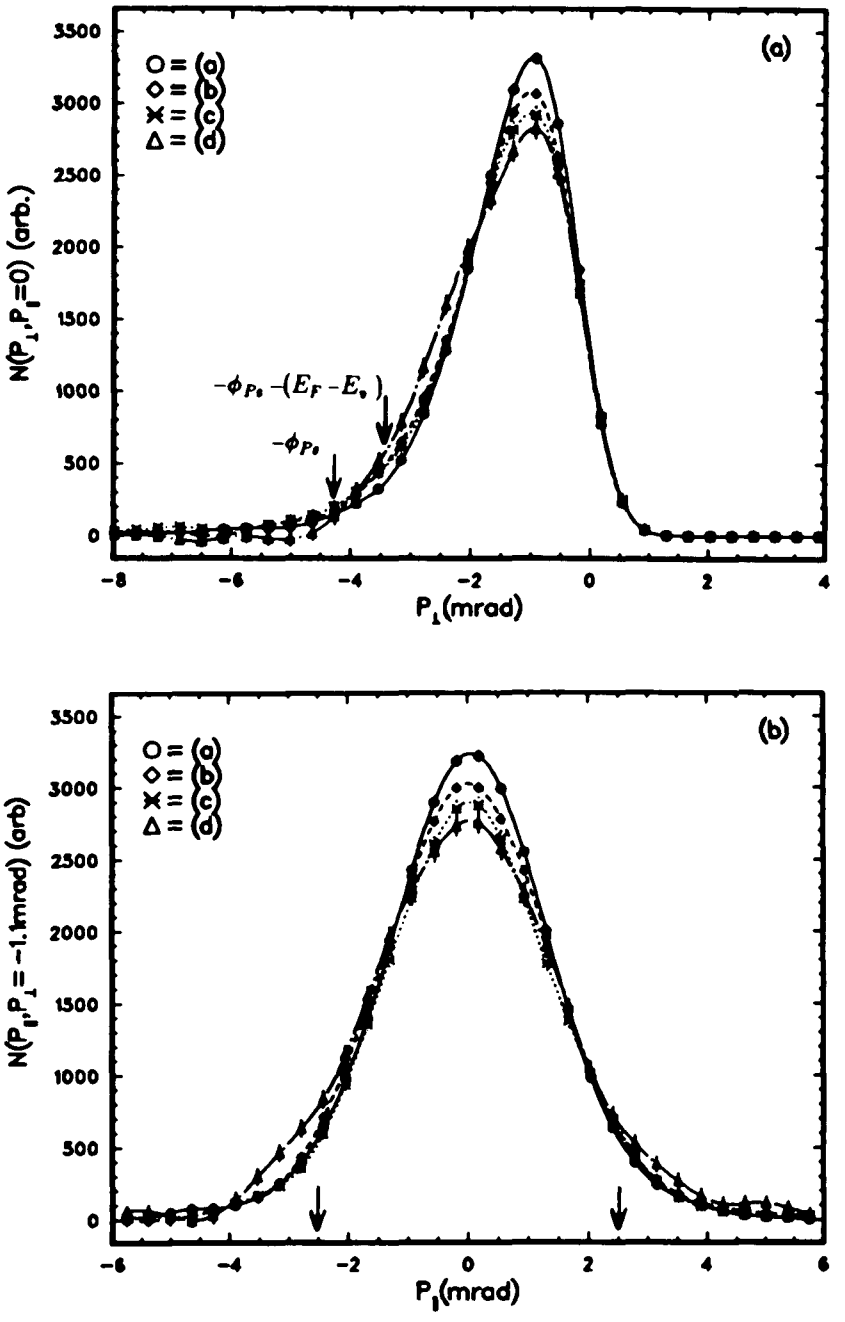

Figure 5.14. Cuts at $p_{\parallel}$=0 (a), and at $p_{\perp}$= -1.1 mrad(b) of the four Ps spectra shown in Fig. 5.13. The alphabetical labels are in one to one correspondence.

tron work function of the silicon surface, but reflects the band gaps of silicon crystal by the emitted nonthermalized positrons. From these new measurements it is estimated that $\phi_+ \approx 0$. This results in $\phi_{P_s} \approx -2.2eV$ and $q_M \approx 4.15mrad$, which is consistent with our Ps momentum distributions. We note that by definition ϕ_{P_s} is associated with electrons of Fermi energy. For a semiconductor, however, the Fermi level appears at the gap between the edge of the valence band and the edge of the conduction band. At room temperature the density of the occupied states is only significant in the valence band for intrinsic or lightly doped silicon crystals(used for present study). Thus the cutoff of the Ps distribution should be at $-\phi_{P_s}-(E_F-E_v)$ with a thermal smearing. In Fig. 5.14a we mark the two positions of $-\phi_{P_s} = -4.5mrad$ and $-\phi_{P_s}-(E_F-E_v) = -3.51mrad$ for the Si(111)-(7×7). We note that the Ps momentum distribution offers us a good way of measuring the *positive* positron work function for materials with $(E_F-E_v) \leq -\phi_{P_s}$, which can not be obtained by any other existing technique(TOF is equivalent to the momentum distribution).

To further understand the shape of the distribution, which is very different from that of simple metal Al, we return to Fig. 5.4. There the shaded curve is the projected valence band along three high symmetry lines. The dot-dashed curve is the lowest electron state available for Ps formation. Two important conclusion can be drawn from this figure. (i). The minimum dispersion curve intersects the top of the valence band at $\vec{k} \approx 0.65/$ Å. The parallel momentum conservation then requires a maximum parallel Ps momentum not to exceed $\sim$ 2.5mrad. These two positions are marked in Fig. 5.14b, and appear to be in good agreement with the measurement (remember our detector resolution is $\sim$ 1mrad FWHM). (ii). The accessible region(Fig. 5.4) between the minimum dispersion curve and the Fermi level for the Ps formation is cut off by the top of the projected valence band, above which is the band gap and no states are available for Ps formation. This is in contrast to the case of Al, and is responsible for the narrower Ps distribution peaking at $p_z \approx 1mrad$, corresponding to a most probable normal emission energy of $\sim$ 130 mV. This value is $\sim$ 0.67eV lower than the intersection of the minimum dispersion(dot-chained curve) with the top of the valence band(shaded curve), where a maximum area in the $\vec{k}$-space is pro-

jected in the ACAR spectrum. It, therefore, implies that the density of states in the projected 2D BZ is not constant, or that the matrix element favors the low momentum component, or a combination of the two. A more rigorous quantitative comparison requires the incorporation of a detailed band calculation. Nevertheless the above qualitative discussion has demonstrated a simple method to probe the top of the valence band and to estimate the dispersion of the projected valence band using the cutoff of the Ps momentum distribution.

A similar argument can be made to interpret the Si(100)-(2×1) spectrum using Fig. 5.6. It is noted that this spectrum has a slightly narrower distribution, which may suggest a small($\sim$ 0.3eV) positive positron work function.

We have not taken into account the dangling bound surface states, the S_2 band for Si(111)-(7×7) and the D_{sp} band for Si(100)-(2×1). These surface bands could affect the Ps formation because they are about 0.7 eV below the Fermi level. Since these bands are almost dispersionless, the associated Ps atoms would distributed in a hemispherical shell of a radius $\sim$ 1.5eV, and their projection parallel to the surface becomes a semi circular disk. Should these bands take part in the Ps formation we unlikely would be able to identify them because of the isotropic distribution. In addition, we feel that the S_3 state at -1.8eV below E_F in Si(111)-(7×7) can not be responsible for the small probable Ps momentum, because it is away from the $\bar{\Gamma}$ point and it is associated with the back-bonds.

The 10% increase in Ps fraction may be attributed to less surface defects trapping of Si(100)-(2×1) compared with the Si(111)-(7×7). This argument is consistent with the small difference in their Ps distributions but larger in their surface state spectra. Two scenarios may be invoked to explain the 15% decrease in Ps fraction as a result of the H-saturation of the dangling bond on the Si(111)-(7×7) surface. (i). Hydrogen coverage induces larger surface voids and hence enchance the trapping; (ii). Since the H-Si bond is much more stronger than the Si-Si bond, it is not a energetically favorable process for a positron to strip an electron off the Si-H bond, thus the Ps formation with dangling bond electron is restricted upon the H-adsorption. The second scenario implies that the dangling bonds play an important role in the Ps formation and emission

from the Si(111)-(7×7) surface. We recall that there are 19 dangling bonds per unit cell, which is 10% of the total bonds of the 49 surface atoms.

§ 5.5 Measurement at 870° K†

ACAR measurements for a Si(111)-(7×7) surface at 870° K were performed with 14keV and 200eV positron beam. Fig. 5.15a is the contour plot of the 14keV spectrum which has been smoothed with a Gaussian resolution function. The basic structure of the room temperature measurement(Fig. 5.8a) is retained, but a small increase of the Ps component is clearly observed. Fig. 5.15b shows the perpendicular section of the unsmoothed spectrum with $p_{\parallel}$ being integrated from -2 *mrad* to 2 *mrad* . The dashed curve is generated from the symmetrical spectrum used to deduce the Ps spectrum. The Ps peak indicates 4% total Ps fraction, which is increased from the room temperature value owing to the contribution of thermal desorbed Ps from the surface state. To see the high temperature effect we plot under the dashed curve a 93 vol% room temperature spectrum integrated over the same number of channels. Higher percentage leads to the excess of the room temperature curve with respect to the symmetrical curve in the two wings. The comparison here shows that going to 870° K only results in a small change in the bulk annihilation. This is in good agreement with the recent lifetime measurement for the vacancy formation in silicon[142]. The authors of Ref.[142] concluded that the monovacancies are formed above 1450° K with an activation enthalpy of 3.6 ±0.2eV, and that no evidence for divacancy formation could be found. Their result suggest that the small difference between the room temperature and 870° bulk annihilations spectra can not be caused by thermally activated vacancies.

The contour plot for the 200eV spectrum is shown in Fig. 5.16a. Its perspective view can be found in Fig. 1.6. It exhibits a dramatic change from the room temperature spectrum (Fig. 5.7a). This change is expected since most of the positrons residing at the surface at room temperature are thermally activated at 870° *K* [33]. We have applied the same method discussed in §4.10 to extract the thermal desorbed Ps component. Fig. 5.16b demonstrates the first step. Since the

† This was the maximum temperature which could be obtained from our heater stage.

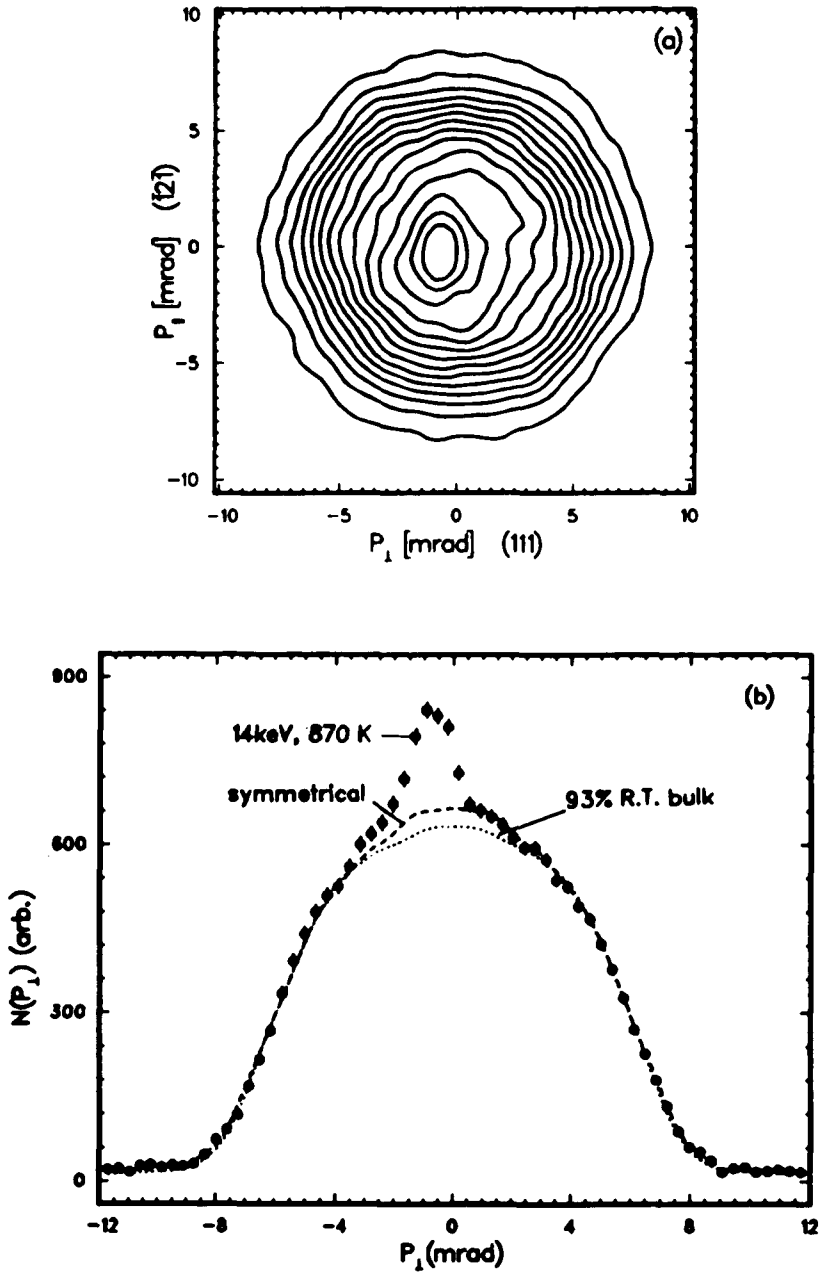

Figure 5.15. (a) Contour plot of the 2D-ACAR spectrum for a Si(111)-(7×7) surface at 870° K, the beam energy is 14keV; (b) Normal distribution of spectrum (a) integrated over -2 mrad $< p_{\parallel} <$ 2 mrad. Dashed curve is the same as the circles but with Ps removed. Dotted curve is 93 vol% room temperature bulk spectrum.

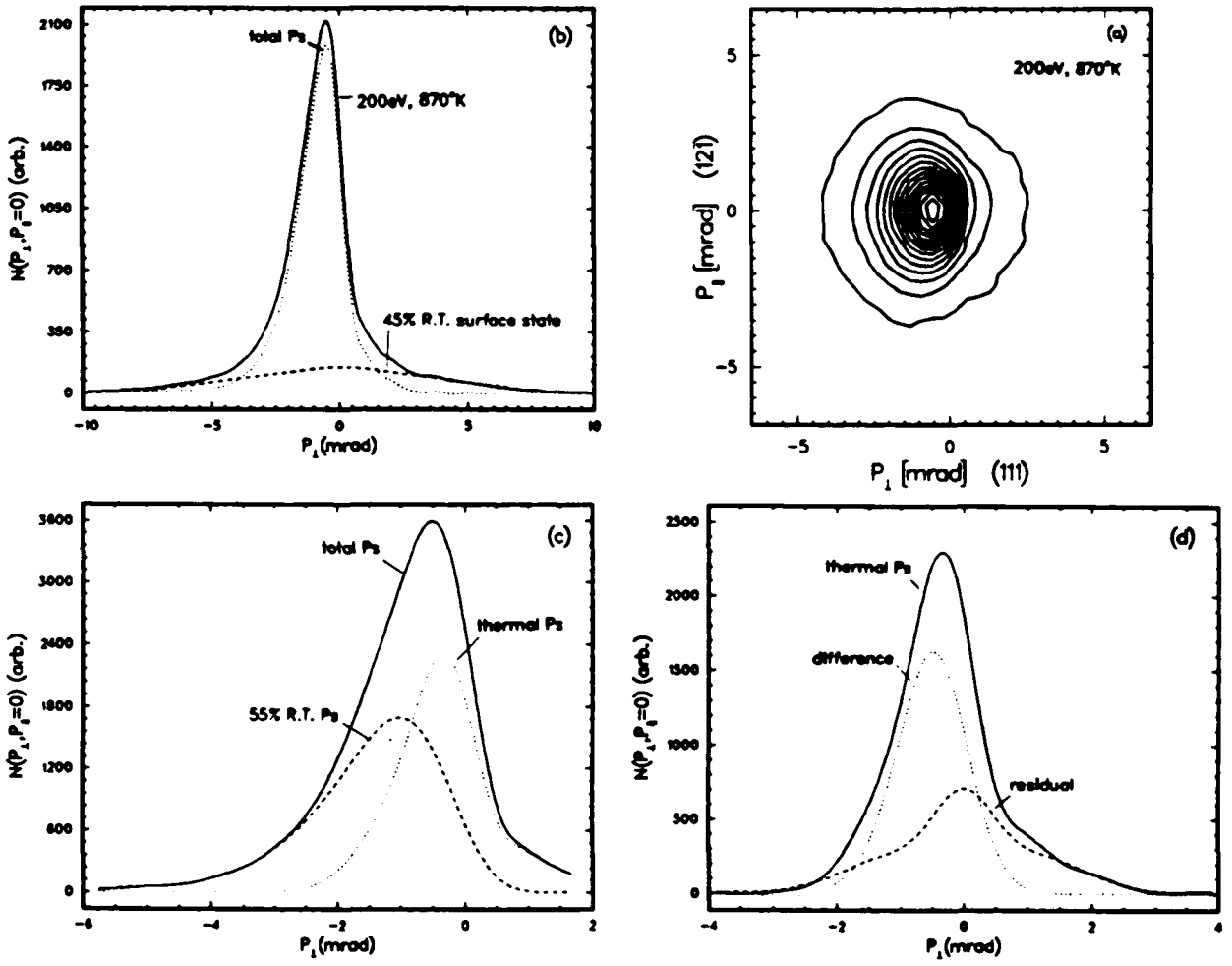

Figure 5.16. (a) Contour plot of the 2D-ACAR spectrum for a Si(111)-(7×7) surface at 870° K, the beam energy is 200eV; (b) to (c) illustrates the separation of various components, see discussion in the text.

bulk annihilation can be ignored at 200eV incident energy, we used the room temperature surface state spectrum for subtraction. A 45 vol% of the room temperature spectrum fits the 870° spectrum well at $p_\perp > 3$ mrad, but under subtracts the region at smaller $p_\perp$. This can be visualized more clearly as we progress to step 2 for removing the energetic Ps component shown in Fig. 5.16c. There 55 vol% room temperature Ps spectrum fits the extracted total Ps spectrum very well at $p_\perp < -3$ mrad. The resultant thermal Ps spectrum, however, contains too high intensity in the positive $p_\perp$ region, which can not be accounted for by the apparatus resolution. Consequently, Eqs.(4.12)-(4.14) do not fit this spectrum well. To analyze our data further we employ our separation technique to remove the symmetrical residual component, which is shown in Fig. 5.16d. In Fig. 5.17, the difference spectrum(dots) is compared with the result generated from Eqs. (4.12)-(4.14) at T=870° K. The theoretical spectrum is normalized to optimize the agreement. Like in case of Al, a constant reflection coefficient is preferred. As we can see the agreement is excellent.

From the above analysis we find that at 870° K, 17% incident positrons remain in the surface state, the direct formation Ps is the same as the total room temperature fraction of 45%, and the total thermally activated Ps is 38%. This indicates that 70% of the surface state positrons at room temperature is boiled off the surface at 870° K. The 38% extracted thermal Ps component is divided into a 10% symmetrical and a 28% thermal distribution. Explanation for this 10% 'symmetrical' component awaits for more systematic temperature dependent measurement. We have difficulty in correlating this component with the small deviations observed in the 14keV run since the latter contains insufficient counts. It is interesting to note that some previous studies[143,144] showed that a degenerate *p*-type layer may be formed in Si at high temperature, causing an electric field in the surface region. If this would be the mechanism responsible for our observed temperature effect, ACAR measurement of the positron residing at a hot Si surface should become an sensitive probe for this type of studies.

§ 5.6 Comparison with the Results of Al

We have observed that the results of the ACAR measurements on Si surfaces are substan-

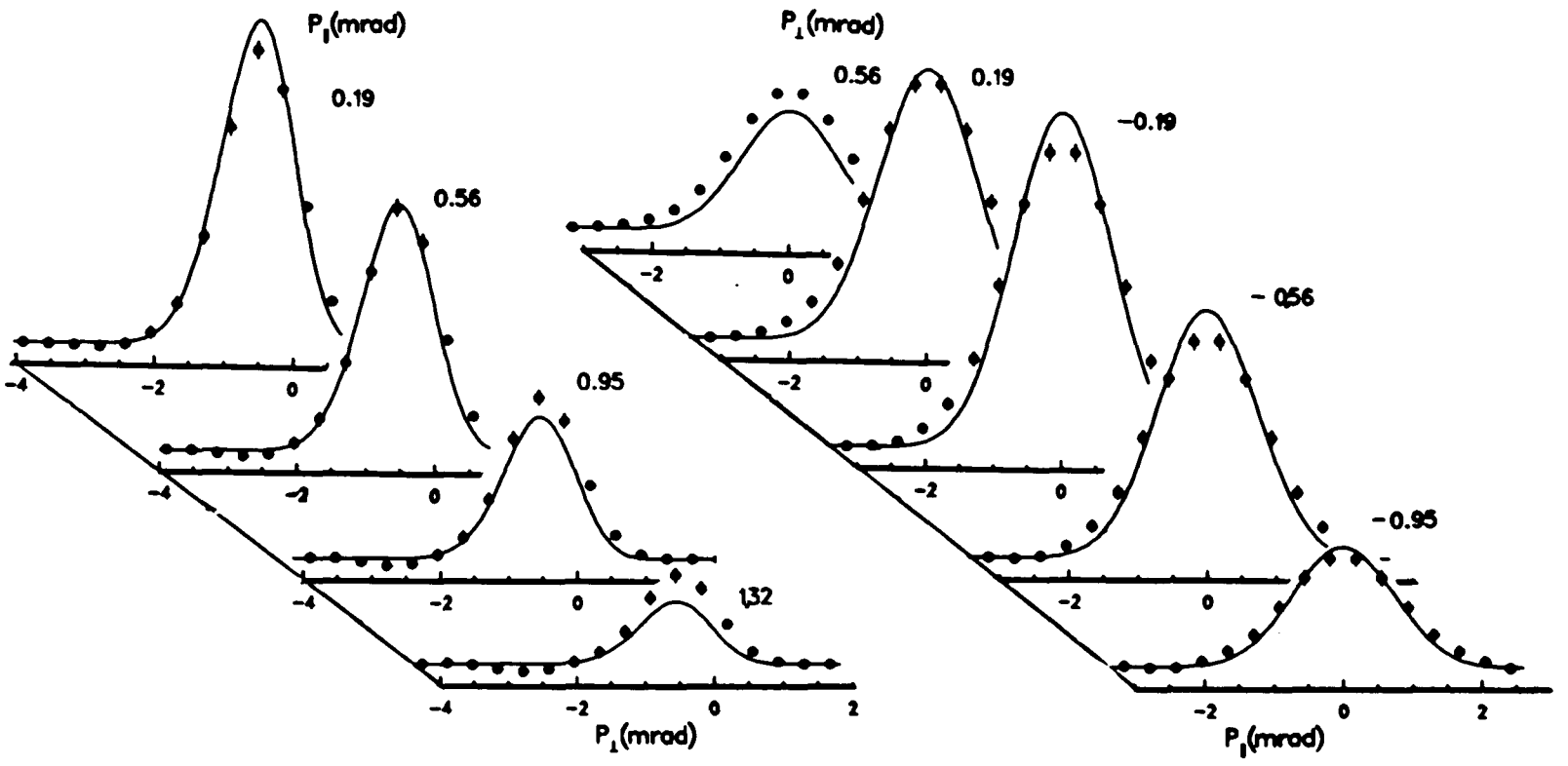

Figure 5.17. Comparison of the generated difference spectrum(dots) with the theoretical prediction of Eq.(4.12) and Eq.(4.14) using a constant reflection coefficient $<r>$ and T=870° K. The peak of the theoretical curve is varied to optimize the agreement.

tially different from those presented in Chapter 4 for the three low index surfaces of Al. This is not surprising because the two types of material represent two very different categories in the periodic table, a simple metal versus a semiconductor. These differences confirm the sensitivity of the ACAR technique for the study of electronic structures and properties of materials. As an example, we show in Fig. 5.18 four Ps spectra(a) and two surface state spectra(b). It is noteworthy that for the Al surface the Ps momentum distribution is much more sensitive to oxygen adsorption than the surface state annihilation; in contrast, for the Si surfaces it is the surface state annihilation that exhibits much change upon the hydrogenation of the surface, in comparison with the Ps momentum distribution.

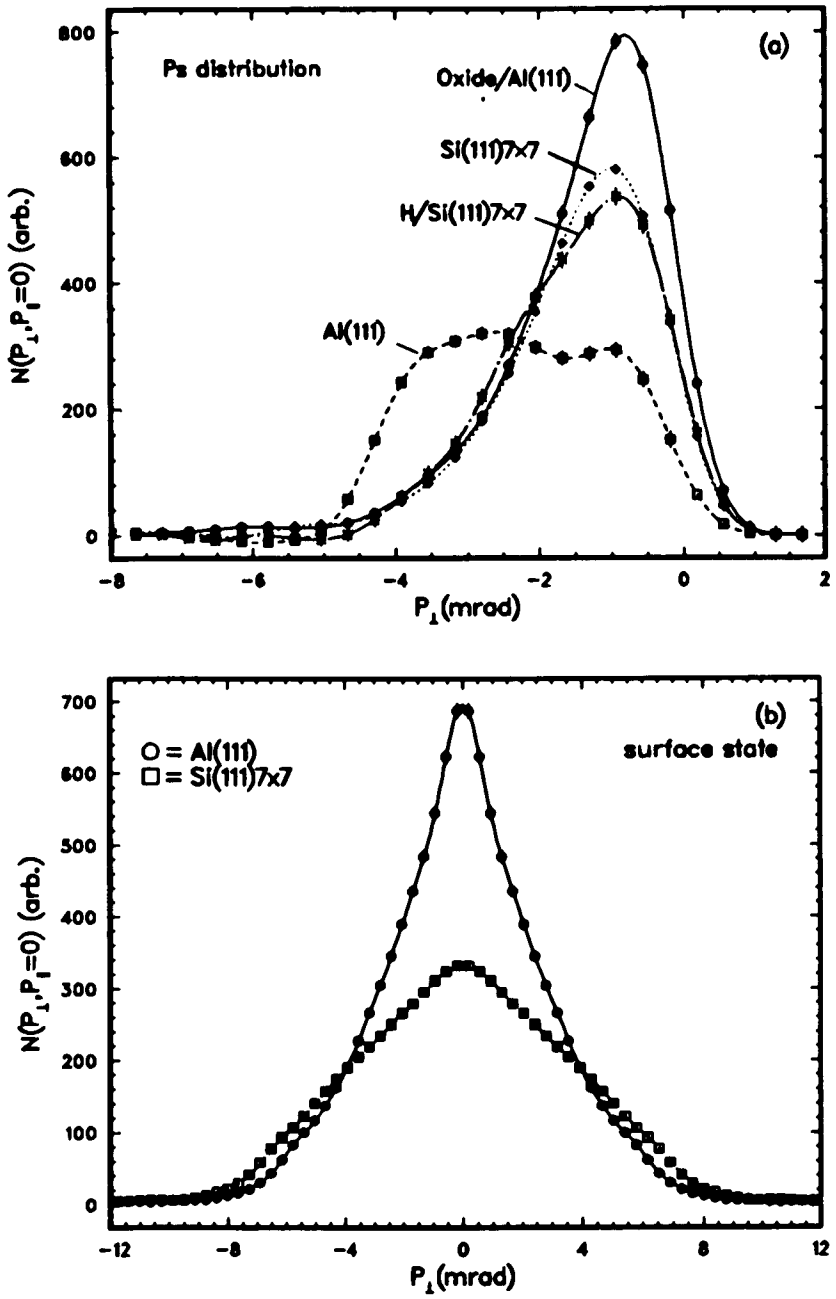

Figure 5.18. Cuts at $p_{\parallel}$=0 of selected Ps(a) and surface state(b) spectra for comparison between the results of Al and Si.

Chapter 6. Summary

Using a high intensity slow positron beam and an UHV surface chamber constructed at Brookhaven National Laboratory, we have successfully applied the well established 2D-ACAR technique to study the interactions of positrons with three low index surfaces of aluminum, Si(111)-(7×7), and Si(100)-(2×1) surfaces. Effects of the adsorption of oxygen on aluminum surfaces and hydrogen on a Si(111)-(7×7) surface have also been explored. Our measurements confirmed three important processes: spontaneous Ps formation and emission, positrons bound in a surface state, and thermally desorbed as Ps atoms. Based on the inversion symmetry of the bulk and surface state momentum density functions, an 'inversion-subtraction' data decomposition technique employing the Van Cittert's deconvolution algorithm has been developed to accurately separate the Ps component and the surface state component from the directly measured spectrum. In previous five chapters we have presented the first systematic discussion of these experimental techniques, the data analysis method, our measurements, and some simple theoretical models. We shall now summarize these discussions and give some suggestions for future studies.

Our measured annihilation spectrum for the positron surface state is considerably narrower than the extended bulk state. This change characterizes the surface inhomogeneous electron density and the localization of positrons at the surface. However, we obtained essentially an isotropic surface state annihilation spectrum for all the studied surfaces of Al and Si. This is inconsistent with either the image induced positron surface state model[40,41], or the physisorbed Ps surface state model[46]; both predicting large anisotropy due to the localization perpendicular to the surface and delocalization parallel to the surface of the bound positron or Ps. Although the emission of a surface plasmon can lead to an isotropic distribution of the bound Ps surface state annihilation, the theoretical width is too narrow in comparison with our measurement. The lack of an anisotropy in the experimental data suggests a lateral localization of the positron, as a consequence of trapping by surface defects or impurities. This conjecture needs to be verified in further studies. On the theoretical side, it is important to understand what type of surface

defect(ledges, steps, *etc.*) or impurities would induce a much more stable state than the image potential. From the experimental point of view, we need to search for more ideal surfaces that can be well prepared and characterised. At present time measurement on a graphite surface has been initiated[145], this surface has been confirmed by STM[146] to contain large defect-free domains. Soon these new results, in comparison with our Al and Si data, should provide us some new information about the nature of positron surface state.

We have demonstrated that the Ps momentum distribution reflects the electron density of states near the surfaces. In particular, it reveals the projected band gaps in Al surfaces with the strong face dependent, directional anisotropies; and exhibits much a change when we go to Si surfaces. These results imply that P: 2D-ACAR spectrum might offer us as a new angle-resolved surface spectroscopy. Since the final state of the Ps formation is well defined(e^+-e^- bound state), this technique has an advantage over the angle-resolved photoemission which has to assume free electron final states in order to map out the band dispersion of the initial states. Clearly, the feasibility of the angle-resolved Ps spectroscopy crucially depends on whether or not it is significantly contaminated by some complicated inelastic effects or by higher order transitions. We have seen that the measured Ps spectra for Al contains an enhanced low momentum component which can not be explained by the simple nearly-free electron model. Future measurement with improved experimental conditions needs to determine whether this enhancement is due to the oxygen and other impurities, or is intrinsic to Ps formation mechanism.

Although convincing evidence for surface umklapp annihilation has not been obtained from our preliminary results of Si surfaces, the idea discussed in §5.1 is an important one, and is worth being exploited further. The finding of the umklapp annihilation associated with some surface reconstruction would provide us with an definitive answer to the existence of a delocalized positron or Ps surface stat:. We also note that a two dimensional umklapp spectrum like the quartz spectrum in Fig. 5.1b can be obtained by changing our geometry(Fig. 1.4) so that surface normal becomes the integrated direction and two resolved momentum components are parallel to the surface. This should help us to identify any umklapp components in our observations, and reduces

our uncertainty(*e.g.* , in the case of Si(111)-(7×7)). In addition to the reconstructed semiconductor surfaces, it would be important to study some reconstructed metal surfaces and metal overlayer on reconstructed semiconductor surfaces, which are more dependent of long-range order interactions[147].

The Ps momentum spectroscopy is limited by energy conservation to a narrow energy band of $\sim$ 2eV($-\phi_{P_s}$) below the Fermi level for most of the metals(except alkali metals) and semiconductors. This suggests that to further understand the Ps formation mechanism measurement on *d*-band metals is of great importance, because the density of states(DOS) near the Fermi level are considerably increased due to the *d*-electrons. A preliminary measurement[145] indeed showed an enhanced Ps momentum intensity near the cutoff compared with the Ps spectrum of Al. However, the structures in the DOS for the majority and minority states can not be identified, and are most probably smeared out by the limited detector resolution. These experiments need to be repeated when higher resolution detectors are available. In addition, the induced localized surface state electron wave functions are quite distinct[80] from the bulk conduction electron wave functions at the surface and might play an important role in the Ps formation, as contrasted with the electron surface states in Al. Energy conservation also restricts the formation and emission of the umklapp Ps atoms(Eq.(1.51)) for most of the unreconstructed surfaces. We note, however, that ϕ_{P_s} is close to -5eV for a W surface[1] ($\sim$ -4 eV for Cr). In addition, W surfaces reconstruct (*e.g.* , c(2×2) for W(100))[147]. Thus it could be a good candidate for demonstrating the umklapp Ps formation effect.

In our present experiment, A small fraction reemitted slow positrons eventually return to the biased sample surface, and take part in either the surface state annihilation or the Ps formation. It is important to know whether or not these returning positrons form Ps via some different mechanism. For example they may form Ps while approaching the surface from vacuum, which then would be connected to the Ps formation by glancing angle scattering or back scattering[51]. This effect can be easily studied by selecting materials which have large slow positron emission yield such as Ni, W, Cu, *etc.*

In this thesis we present the first two dimensional momentum distributions of the thermally desorbed Ps. The ACAR spectra *directly* demonstrate the fact that these thermal Ps are indeed originated from the positrons trapped in some surface states at lower temperature($< 300°K$). These thermal Ps momentum distribution are shown to agree well with the theoretical description of the thermodynamical emission process[35]. However the sensitivity of our measurement to the temperature is clearly limited by the present detector resolution. Although our analysis indicates that a constant Ps reflection coefficient produces better agreement with experimental data, we do not have systematic measurements to verify the temperature dependence of the reflection coefficient. The establishment of this parameter would provide us some insight into the detail desorption mechanism[29,35,36]. High precision ACAR study on this subject requires detectors has a resolution better than 0.5 mrad FWHM. We recall the difficulty that we encounter in analyzing the high temperature Si(111)-(7×7) surface data. The origin of the residual 'symmetrical' component also need to be clarified in future systematic temperature measurement.

As has been shown throughout this thesis, our data separation technique is accurate except for high temperature surface data which is dominated by the large fraction of thermal Ps. Theoretical calculations[1, 29] and experiment[148] have indicated that for alkali metals $\phi_{P_s} > 0$, hence spontaneous Ps emission is forbidden. For these surfaces the asymmetric Ps component, therefore, will not appear in the measurement, and it is interesting to observe the obvious inversion symmetry of these spectra.

It is clear that a lot of our uncertainties in the above discussions can be removed once a more intense slow positron beam is available. Owing to Mills and Gullikson's recent discovery[149] of the new condensed solid-Ne moderator, it is anticipated that the slow positron beam intensity can be increased by two orders of magnitude. We have reason to be optismistic that by a combination of an increased source strength, a solid-Ne moderator, a laser isotope separation, and higher counting rate and better resolution Auger cameras[145], we will yield more exciting results in the near future.

List of References

[1] A. P. Mills, Jr., in *Positron Solid State Physics*, edited by W. Brant and A. Dupasquier (North Holland, New York 1983); and references therein.

[2] K. G. Lynn, *ibid.*

[3] S. Berko, *ibid.*; and references therein.

[4] S. Berko and H. N. Pendleton, Ann. Rev. Nucl. Part. Sci. **30** , 543 (1980).

[5] R. N. West, Adv. Phys. **22** , 263 (1973).

[6] K. G. Lynn, A. P. Mills, Jr., L. O. Roellig, and M. Weber, *Electronic and Atomic Collisions*, edited by D. C. Lorents, W. E. Meyerhof, and J. R. Peterson, (North-Holland, New York, 1986).

[7] R. H. Howell, P. Meyer, I. J. Rosenberg, and M. J. Fluss, Phys. Rev. Lett. **54** , 1698 (1985).

[8] K. G. Lynn, A. P. Mills, Jr., R. N. West, S. Berko, K. F. Canter, and L. O. Roellig, Phys. Rev. Lett. **54** , 1702 (1985).

[9] A. F. Makhov, Sov. Phys. -Solid State **2** , 1934 (1961).

[10] A. P. Mills, Jr., and R. J. Wilson, Phys. Rev. A **26** , 490 (1982).

[11] S. Valkealahti, and R. Nieminen, Appl. Phys. A **32** , 95 (1983); *ibid.* **35** , 51 (1984).

[12] R. M. Nieminen, and J. Oliva, Phys. Rev. B **22** , 2226 (1980).

[13] Bent Nielson, K. G. Lynn, A. Vehanen, and Peter J. Schultz, *ibid.* **32** , 2296 (1985).

[14] A. P. Mills, Jr., P. M. Platzman, and B. L. Brown, Phys. Rev. Lett. **41** , 1076 (1978); C. A. Murray, and A. P. Mills, Jr., Solid State Commun. **34** , 789 (1980).

[15] N. D. Lang and W. Kohn, Phys. Rev. B **1** , 4550 (1970); *ibid.* **3** , 1215 (1971).

[16] B. Y. Tong, Phys. Rev. B **5** , 1436 (1972).

[17] C. H. Hodges and M. J. Stott, Phys. Rev. B **7** , 73 (1973); R. M. Nieminen and C. H. Hodges, Solid State Commun. **18** , 1115 (1976).

[18] K. G. Lynn, D. M. Chen, Bent Nielsen, R. Pareja and S. Myers, Phys. Rev. B **34** , 1449 (1986).

[19] D. A. Fischer, K. G. Lynn, and W. E. Frieze, Phys. Rev. Lett **50** , 1149 (1983); D. A. Fischer, K. G. Lynn, and D. W. Gidley, Phys. Rev. B **33** , 4479 (1986).

[20] A. P. Mills., Jr., Appl. Phys. **23** , 189 (1980).

[21] W. E. Frieze, D. Gidley and K. G. Lynn, Phys. Rev. B **31** , 5628 (1985).

[22] A. P. Mills, Jr., L. Pfieffer and P. M. Platzman, Phys. Rev. Lett. **51** , 1085 (1983).

[23] A. P. Mills, Jr., Phys. Rev. Lett **46** , 717 (1981); **50** , 671 (1983).

[24] H. Kanajawa, Y. H. Ohtsuki, and S. Yanagawa, Phys. Rev. **138** , A1155 (1965).

[25] M. Doyama, in *Proc. 5th Int. Conf. on Positron Annihilation*, edited by R. R. Hasiguti and K. Fujiwara (Japan, 1979).

[26] A. Dupasquier, in Ref. 1; and references therein.

[27] *Proc. 3rd Int. Workshop on Positron(Electron)-Gas Scattering*, edited by W. E. Kanppila, T. S. Stein and J. M. Wadehra (World Scientific, Singapore 1985).

[28] M. Eldrup, A. Vehanen, Peter J. Schultz, and K. G. Lynn, Phys. Rev. Lett. **51** , 2007 (1983); P. Sferlazzo, S. Berko, and K. F. Canter, to be published in Phys. Rev. B (1987).

[29] Akira Isii, Surf. Sci. **147** , 277; 295 (1984); *ibid* **163** , 498 (1985); Akira Ishii, to be published.

[30] Shigeru Shindo, and Akira Ishii, to be published.

[31] A. B. Walker, and Nieminen, J. Phys. F **16** , L295 (1986).

[32] K. G. Lynn, Phys. Rev. Lett. **43** , 391 (1979).

[33] A. P. Mills, Jr., Solid State Commun. **31** , 623 (1979).

[34] A. P. Mills, Jr., and L. Pfeiffer, Phys. Rev. Lett. **43** , 1961 (1979); Phys. Rev. B **32** , 53 (1985).

[35] S. Chu, A. P. Mills, Jr., and C. A. Murray, Phys. Rev. B **23** , 2060 (1981).

[36] J. B. Pendry, in Ref.[1].

[37] K. G. Lynn, Phys. Rev. Lett. **44** , 1330 (1980); Peter J. Schultz, K. G. Lynn, and Bent Nielsen, Phys. Rev. B **32** , 4732 (1985).

[38] R. Y. Levine, and L. M. Sander, Solid State Commun. **42** , 5 (1982).

[39] K. G. Lynn, W. E. Frieze and P. J. Schultz, Phys. Rev. Lett. **52** , 1137 (1984).

[40] C. H. Hodges and M. J. Stott, Solid State Commun., **12** , 1153 (1973).

[41] R. Nieminen and M. Mannien, *ibid.* **15** , 403 (1974); R. M. Nieminen and M. J. Puska, Phys. Rev. Lett. **50** , 281 (1983); **53** , 1298 (1984).

[42] J. Garner, and R. Benedek, J. Phys. F. **16** , L165 (1986).

[43] B. Rosenfeld, K. Jerie and W. Swiatkowsk, ACTA Physica Polonica A **64** , 93 (1983).

[44] A. P. Brown, A. B. Walker and R. N. West, to bo published.

[45] N. D. Lang and W. Kohn, Phys. Rev. B **7** , 3541 (1973).

[46] P. M. Platzman and N. Tzoar, Phys. Rev. B **33** , 5900 (1986).

[47] P. Sferlazzo, S. Berko, and K. F. Canter, Phys. Rev. B **32** , 6067 (1985).

[48] A. Cuthbert, J. Phys. C **18** , 4561 (1985).

[49] A. H. Weiss, I. J. Rosenberg, K. F. Canter, C. B. Duke and A. Paton, Phys. Rev. B **27** , 867 (1983); I. J. Rosenberg, A. H. Weiss, and K. F. Canter, Phys. Rev. Lett. **44** , 1139 (1980).

[50] R. Mayer, Chun-Si Zhang, K. G. Lynn, W. E. Frieze, and F. Jona, to be published in Phys. Rev. B (1987).

[51] R. H. Howell, I. J. Rosenberg, and M. J. Fluss, Phys. Rev. B **34** , 3069 (1986); D. W. Gidley, W. E. Frieze, R. Mayer, and K. G. Lynn, submitted to Phys. Rev. Lett..

[52] A. Vehanen, J. Makinen, P. Hautojarvi, H. Huomo, and J. Lahtinen, Phys. Rev. B **32** , 7561 (1985); B. Nielsen, A. van Veen, and K. G. Lynn, in *Positron Annihilation*, edited by P. D. Jain, R. M. Singru and K. P. Gopinathan (World Scientific, Singapore, 1985).

[53] Bent Nielsen, K. G. Lynn and Yen-C Chen, Phys. Rev. Lett. **57** , 1789 (1986); K. G. Lynn, and Nielsen, Phys. Rev. Lett. **58** , 81 (1987).

[54] E. M. Gullikson and A. P. Mills, Jr., *ibid.* **57** , 376 (1986).

[55] R. A. Ferrell, Rev. Mod. Phys. **28** , 308 (1956); Chang Lee, Sov. Phys. JETP **6** , 281 (1958).

[56] Neil W. Ashcroft and N. David Mermin, *Solid State Physics*, (Saunders College, Philadelphia, 1976).

[57] S. Berko, and J. S. Plaskett, Phys. Rev. **112** , 1877 (1958).

[58] L. J. Clarke, *Surface Crystallography*, (John Wiley & Sons, New York, 1985).

[59] M. Weber, K. G. Lynn, L. O. Roellig, A.P. Mills, Jr, W. E. Frieze and A. R. Moodenbaugh, to be published.

[60] K. F. Canter, private communication; J. D. Jackson, *Classical Electrodynamics*, **§12.6** , (John Wiley & Sons, New York, 1975).

[61] M. Thompson, M. D. Baker, A. Chrislie, J. F. Tyson, *Auger Electron Spectroscopy*, (John Wiley & Sons, New York, 1985).

[62] *Auger Hand Book*, (Physical Electronics, 1983).

[63] J. K. Grepstad, P. O. Gartland and B. J. Slagsvold, Surf. Sci. **57** , 348 (1976).

[64] W. Eberhardt and C. Kunz, Surf. Sci. **75** , 709 (1978).

[65] P. O. Gartland, Surf. Sci. **62** , 183 (1977).

[66] C. W. B. Martinson and S. A. Flodstrom, Surf. Sci. **80** , 306 (1979).

[67] F. Jona, J. Phys. Chem. Solids **28** , 2155 (1967).

[68] A. Biaconi, R. Z. Bachrach, S. B. M. Hagstrom, and S. A. Flodstrom, Phys. Rev. B **19** ,

2837 (1979).

[69] D. E. Eastman, J. Vac. Sci. Technol. **17** , 492 (1980); and references therein.

[70] G. Schulze and M. Henzler, Surf. Sci. **124** , 936 (1982).

[71] R. J. Culbertson, L. C. Feldman, P. J. Silverman and R. Haight, J. Vac. Sci. Technol. **20** , 868 (1980).

[72] H. Froitzheim, V. Kohler and H. Lammering, Surf. Sci. **149** , 537 (1985).

[73] R.N. West, J. Mayer and P.A. Walters, J. Phys. E **14** , 478 (1981); *Positron Annihilation Detector Head Manual,* (Dept. of Phys., Univ. of East Anglia, 1984).

[74] M. Lax, *Symmetry Principles in Solid State and Molecular Physics* , (John Wiley & Sons, New York, 1974).

[75] *Deconvolution with Applications in Spectroscopy,* edited by Peter A. Jansson, (Academic Press Inc., 1984).

[76] G. K. Wertheim, Rev. Sci. Instrum. **46** ,1414 (1975); and reference therein.

[77] Philip R. Benvington, *Data Reduction and Error Analysis for the Physical Science,* (McGraw-Hill, New York, 1961).

[78] B. Segall, Phys. Rev. **124** , 1797 (1961).

[79] N. M. Ashcroft, Philos. Mag. **8** , 2055 (1963).

[80] M. Weinert, private communication; W. A. Harrison, *Electronic Structure and Properties of Solids* , (Freeman, San Francisgo, 1980).

[81] J. R. Anderson, and S. S. Lane, Phys. Rev. B **2** , 298 (1970).

[82] S. P. Singhal, and J. Callaway, Phys. Rev. B **16** , 1744 (1977).

[83] J. Callaway, and D. G. Lanrent, Phys. Lett. **84A** , 499 (1981).

[84] F. Szmulowicz, and B. Segall, Phys. Rev. B **21** , 5628 (1980).

[85] D. S. Boudreaux, Surf. Sci. **28** , 344 (1971).

[86] E. B. Carathers, L. Kleinman and G. P. Alldredge, Phys. Rev. B **8** , 4570 (1973); *ibid.* B **9** , 3325 (1974); 3330 (1974).

[87] J. R. Chelikowsky. M. Schluter, S. G. Lowis, and M. L. Cohen, Solid State Commun. **17** , 1103 (1975).

[88] H. Krakauer, M. Posternak, and A. J. Freeman, Phys. Rev. Lett. **41** , 1072 (1978); Ding-Sheng Wang, A. J. Freeman, H. Krakauer, and M. Posternak, Phys. Rev. B **23** , 1685 (1981).

[89] M. Seel, Phys. Rev. B **28** , 778 (1983).

[90] H. Krakauer, M. Posternak, A. J. Freeman, and D. D. Koellig, Phys. Rev. B **23** , 3859 (1981); Ding-sheng Wang, A. J. Freeman, and H. Krakauer, Phys. Rev. B **24** 3092; 3104; 3614 (1981).

[91] N. D. Lang, and A. R. Williams, Phys. Rev. Lett. **34** , 531 (1975); *ibid.* B **18** , 616 (1978).

[92] R. P. Messmer, and D. R. Salahub, Phys. Rev. B **16** , 3415 (1977); D. R. Salahub, M. Roche, and R. P. Messmer, *ibid.* B **18** , 6495 (1978).

[93] J. Harris, and G. S. Painter, Phys. Rev. Lett. **36** , 151 (1976); G. S. Paiter, Phys. Rev. B **17** , 662 (1978).

[94] I. P. Batra, and S. Ciraci, Phys. Rev. Lett. **38** , 774 (1977).

[95] D. M. Bylander, Leonard Kleinman, and Kenneth Mednick, Phys. Rev. Lett **48** , 1544 (1982).

[96] J. R. Noonan, and H. L. Davis, Phys. Rev. B **29** , 4349 (1984).

[97] A. L. Teston, and P. C. Stair, Surf. Sci. **171** , L491 (1986).

[98] S. A. Flodstrom, C. W. B. Martinsson, R. Z. Bachrach, S. B. M. Hagstrom, and R. S. Bauer, Phys. Rev. Lett. **40** , 907 (1978).

[99] P. Hofmann, W. Wyrobisch and A. M. Bradshaw, Surf. Sci. **80** , 344 (1979).

[100] W. Eberhardt and F. J. Himpsel, Phys. Rev. Lett. **42** , 1375 (1979).

[101] P. O. Gartland, and B. J. Slagsvold, Solid State Commun. **25** , 489 (1978).

[102] G. V. Hansson, and Flodstrom, Phys. Rev. B **18** , 1562 (1978).

[103] Harry J. Levinson, F. Greuter, and E. W. Plummer, Phys. Rev. B **27** , 727 (1983).

[104] Peter Hofmann, and Kyozaburo Kambe, Phys. Rev. B **30** , 3028 (1984).

[105] S. D. Kevan, N. G. Stroffel, and N. V. Smith, Phys. Rev. B **31** , 1788 (1985).

[106] A. Bianconi, and R. Z. Bachrach, Phys. Rev. Lett. **42** , 14 (1979).

[107] L. I. Johansson, and J. Strohr, Phys. Rev. Lett **43** , 1882 (1979).

[108] S. Brennan, R. Jaeger, and J. Stohr, Surf. Sci. **105** , L297 (1981).

[109] M. L. den Boer, T. L. Einstein, W. T. Elam, Robert L. Park, L. D. Roelofs, and G. E. Laramore, Phys. Rev. Lett. **44** , 496 (1980).

[110] P. Pattison, S. Manninen, J. Felsteiner, and M. Cooper, Philos. Mag., **30** , 973 (1974).

[111] J. Mader, S. Berko, H. Krakauer, and A. Bansil, Phys. Rev. Lett. **37** , 1232 (1976).

[112] K. G. Lynn, and H. Lutz, Phys. Rev. B **22** , 4143 (1980).

[113] M. J. Fluss, S. Berko, B. Chakraboty, K. Hoffman P. Lippel, and R. W. Siegel, in *Positron Annihilation* , edited by P.G. Colman, S. C. Sharma, L. M. Diana, (North-Holland, New York, 1982).

[114] A. Alam, J. H. Kaiser, P. A. Walters, R. L. Waspe, and R. N. West, *ibid.*

[115] *Photoemission I & II,* edited by M. Cardona, and L. Ley, (Springer-Verlag, New York, 1978).

[116] C. H. Hodges, B. T. A. Mckee, W. Triftshauser, and A. T. Stewart, Can. J. Phys. **50,** 103 (1972).

[117] W. Monch, Surf. Sci. **86** , 672 (1979).

[118] D. J. Chadi, J. Vac. Sci. Technol. **16** , 1290 (1979).

[119] R. E. Schlier, and H. E. Farnsworth, J. Chem. Phys. **30** , 917 (1959).

[120] R. M. Feenstra, W. A. Thompson, and A. P. Fein, Phys. Rev. Lett. **56** , 608 (1986).

[121] D. E. Eastman, F. J. Himpsel, and J. F. Van der Veen, Solid State Commun. **35** , 345 (1980); F. J. Himpsel, D. E. Eastman, D. Heimann, B. Reihl, C. W. White, and D. M. Zehner, Phys. Rev. B **24** , 1120 (1981).

[122] R. S. Becker, J. A. Golovchenko, G. S. Higashi, and B. S. Swartzentruber, Phys. Rev. Lett. **57** , 1020 (1986).

[123] R. M. Tromp, R. J. Hamers, and J. E. Demuth, Phys. Rev. Lett. **55** , 1303 (1985).

[124] J. A. Martin, D. E. Savage, W. Moritz, and M. G. Lagally, Phys. Rev. Lett. **56** , 1936 (1986).

[125] S. J. White, and D. P. Woodruff, Surf. Sci. **63** , 254 (1977).

[126] K. Takayanagi, Y. Tanishiro, M. Takahashi, and S. Takahashi, J. Vac. Sci. Technol. A **3** , 1502 (1985).

[127] R. I. G. Uhrberg, G. V. Hanssen, J. M. Nicholls, P. E. S. Persson, and S. A. Flodstrom, Phys. Rev. B **31** , 3805 (1985).

[128] R. J. Hamers, R. M. Tromp, and J. E. Demuth, Phys. Rev. Lett. **56** , 1972 (1986).

[129] John E. Northrop, Phys. Rev. Lett. **57** , 154 (1986).

[130] John E. Northrop, Phys. Rev. Lett. **54** , 815 (1985).

[131] R. I. G. Uhrberg, G. V. Hansson, J. M. Nicholls, and S. A. Flodstrom, Phys. Rev. B **24** , 4684 (1981).

[132] F. J. Himpsel, and D. E. Eastman, J. Vac. Sci. Technol. **16** , 1297 (1979).

[133] M. Schmeits, A. Mazur, and J. Pollmann, Phys. Rev. B **27** , 5012 (1983).

[134] R. N. West, private communications.

[135] S. Berko, and J. Mader, Appl. Phys. **5** , 287 (1975); Y. J. He, M. Hasegawa, R. Lee, S. Berko, David Adler, and Ai-Lien Yung, Phys. Rev. B **33** , 5924 (1986).

[136] J. Mayers, J. D. McGervey, P. A. Walters, and R. N. West, in *Proc. 5th Int. Conf. Positron*

Annihilation, eds. R. R. Hasiguti, and K. Fujiwara, (Japan, 1979).

[137] James R. Chelikowsky, and Marvin L. Cohen, Phys. Rev. B **14** , 556 (1976).

[138] K. Seeger, *Semiconductor Physics*, (Springer-Verlag, New York, 1982).

[139] R. S. Becker, J. A. Golovchenko, E. G. McRae, and B. S. Swartzentruber, Phys. Rev. Lett. **55** , 2028 (1985).

[140] Joel A. Appelbaum, and D. R. Hamann, Phys. Rev. Lett. **34** , 806 (1975).

[141] W. Chen, and K. G. Lynn, private communication.

[142] S. Dannefaer, P. Mascher, and D. Kerr, Phys. Rev. Lett. **56** , 2195 (1986).

[143] F. G. Allen, J. Eisinger, H. D. Hagstrum, and J. T. Law, J. Appl. Phys. **30** , 1563 (1959).

[144] J. C. Rivier, in *Solid State Surface Science*, ed. M. Green, (Dekkerm, New York, 1969), Vol. 1, p. 179.

[145] P. Sferlazzo, A. Viescas, S. Berko, K. F. Canter, K. G. Lynn, A. P. Mills, Jr, L. O. Roellig, and R. N. West, unpublished data and private communication.

[146] C. F. Quate, *Physice Today*, **39** (8), 26 (1986).

[147] *The Chemical Physics of Solid Surfaces and Heterogeneous Catalysis* , Vol. **1** , edited by D. A. King, and D. P. Woodruff (ELSEVIER, New York, 1981).

[148] K. G. Lynn, private communication.

[149] A. P. Mills, and E. M. Gullikson, Appl. Phys. Lett. **49** , 1121 (1986).